Liquid Jet Impingement on Mesoscale Modified Surfaces for Power Electronics Cooling

by

Aaron Handley Smith

A dissertation submitted to the Graduate Faculty of
Auburn University
in partial fulfillment of the
requirements for the Degree of
Doctor of Philosophy

Auburn, Alabama
December 9, 2023

Keywords: jet impingement, single-phase, surface modification, spent fluid management, particle image velocimetry, power electronics

Approved by:

Sushil H. Bhavnani, Co-Chair, Henry M. Burt Jr. Professor Emeritus of Mechanical Engineering
Roy W. Knight, Co-Chair, Associate Professor Emeritus of Mechanical Engineering
Nicholas Tsolas, Assistant Professor of Mechanical Engineering
Nedret Billor, Professor of Mathematics and Statistics

Abstract

In each vehicular generation, active safety and comfort features are added and enhanced, increasing the power draw required to operate every feature. As a result, heat generation in the power electronics is increasing, and it is anticipated that traditional, passive heat sinks will be insufficient to maintain the devices within operating conditions. Due to limited space under the hood, jet impingement cooling is a promising approach for active thermal management. Jet impingement on the backside of the substrate, a region with no components, can be applied with minimal added components under the hood and at flow rates and pressure losses in the range of those already achieved in the radiator flow loops of the current automotive generation. In jet impingement cooling, one or more columns of a working fluid are directed normal to a heated surface, naturally mitigating the development of the thermal boundary layer. In doing so, jet impingement can achieve highly efficient, single-phase heat dissipation from the surface. To achieve best performance across a surface, an array of jets can be applied. Interactions between these jets can provide thermal improvements in regions away from the jets, but spent fluid must be managed appropriately, otherwise it will negatively impact downstream performance. The present effort investigates mesoscale cone and rib structures on the impingement surface engineered to promote desirable flow interactions while providing additional surface area for heat dissipation. Each of these modifications were applied under both a flat and angled confining wall, the latter of which allowed spent fluid to reach the outlet without affecting jets downstream. Each of these geometries were investigated experimentally using particle image velocimetry flow visualization to examine the effects of the modifications and wall angles on the flow behaviors. This was paired with a numerical model in ANSYS Fluent, which also provided insight on thermal performance across the surface.

Acknowledgements

First and foremost, I would like to thank the members of my advisory committee: Dr. Sushil H. Bhavnani, Dr. Roy W. Knight, Dr. Nicholas Tsolas, and Dr. Nedret Billor. Special thanks are afforded to Dr. Bhavnani and Dr. knight for their guidance and patient support throughout my research progress.

Thanks go to Dr. John F. Maddox for conceptualizing and actualizing the first stage of this research effort, laying the foundation upon which this effort was built, as well as his repeated assistance. Additional thanks are given to Michael Henry and Kayla Reid for continuing this research prior to my involvement and training me to begin my research.

I would like to thank my friends from Auburn, Larkin Crilly, Brian Torres, Justin Van Cleave, and Zane Oligee for their assistance and support. In particular, I would like to acknowledge my lab and office mate, Dr. Karthekeyan Sridhar, for his friendship as we worked together through the years.

Finally, I would like to thank my mother, father, and sister for their love, support, and encouragement. Knowing they were there to support me was an endless comfort through many days of struggle. I would also like to acknowledge and name my grandfather, Buell Smith, and grandmother, Grace Smith, both of whom passed away during by graduate career. I know they would be proud to finally see me graduate.

Table of Contents

List of Figures

List of Tables

Nomenclature

Acronyms

DNS	Direct numerical simulation
GCI	Grid convergence index
LES	Large eddy simulation
PCB	Printed circuit board
PIV	Particle image velocimetry
RANS	Reynolds-averaged Navier Stokes
SST	Shear stress transport
WEG	Water-ethylene glycol

English Letter Symbols

A	Area (m^2)
D	Diameter (m)
E	Energy
F	External body forces (N)
f	Friction factor
g	Acceleration due to gravity (m/s^2)
h	Surface heat transfer coefficient (W/m^2K)
I	Turbulent Intensity
J	Diffusion flux (mol/ m^2s)
K	Turbulent kinetic energy (J/kg)
k	Thermal conductivity (W/mK)
N	A value output from the numerical model
Nu	Nusselt number: $Nu = \frac{hD_j}{k_f}$
O	Order of the numerical method
P	Static pressure (Pa)
Q	Total heat dissipated (W)
q''	Heat flux (W/ m^2)
R	Relaminarization source term

r	Ratio
Re	Reynolds number
S	Source term
Sk	Stokes Number
T	Temperature (°C)
t	time
u	Velocity (m/s)
x	Location (m)

Greek Letter Symbols

Γ	Effective diffusivity (m^2/s)
γ	Intermittency
ε	Turbulence dissipation rate (m^2/s^3)
Θ	Surface temperature rise (°C or K)
μ	Dynamic viscosity (N/ m^2s)
ρ	Density (kg/ m^3)
σ	Turbulent Prandtl number
τ	Stress tensor (N/m^2)
Φ	Heat transfer performance parameter
ω	Specific dissipation rate (s^{-1})

Subscripts

A	Area effect only
avg	Average
B	Baseline surface
E	Enhanced
eff	Effective
H	Hydraulic diameter
h	Heat of chemical reaction
in	Inlet

j	Jet
K	Turbulent kinetic energy
l	Local
M	Modified
m	Mass
p	Particle
s	Surface
T	Total
t	Turbulent
w	Deionized water
0	Baseline
1	Small element mesh
2	Large element mesh
γ	Intermittency
θt	Momentum thickness Reynolds number
ω	Specific dissipation rate

Chapter 1: Introduction

1.1 Electronics Thermal Management

Modern developments in electronic devices have led to increased power consumption and decreasing form factor, drastically increasing the need for effective heat management [1]. Increased computational power and smaller packages combine to result in a highly increased heat generation rate. Meanwhile, advancements in heterogeneous integration and stacked electronics reduce the available area for cooling, necessitating more aggressive thermal management strategies [2, 3]. In heterogeneous integration, devices from multiple manufacturers are assembled in close proximity to operate in conjunction. Each device generates its own heat, and the closeness of all the devices reduces the area available for thermal management. Stacked electronics are composed of multiple devices packaged vertically, reducing the surface area available for thermal management relative to the volume of heat generation. These effects necessitate increasingly aggressive cooling mechanisms to maintain a functional device temperature.

As all heat generated by an electronic device must eventually be removed to the atmosphere, electronic waste heat historically been managed through finned heat sinks, which increase the surface area for heat dissipation directly to the air. An example of such a heat sink is shown in Figure 1-1 for cooling of devices on a motherboard. These heat sinks are reliable, low in cost and complexity, and require minimal components. However, they have many limiting factors, including the thermal properties of materials used, diminishing returns from increasing fin length, limited space, and geometric design requirements to ensure proper air flow [4]. These limiting factors prevent them from being applicable with the ever increasing heat generation observed in modern devices.

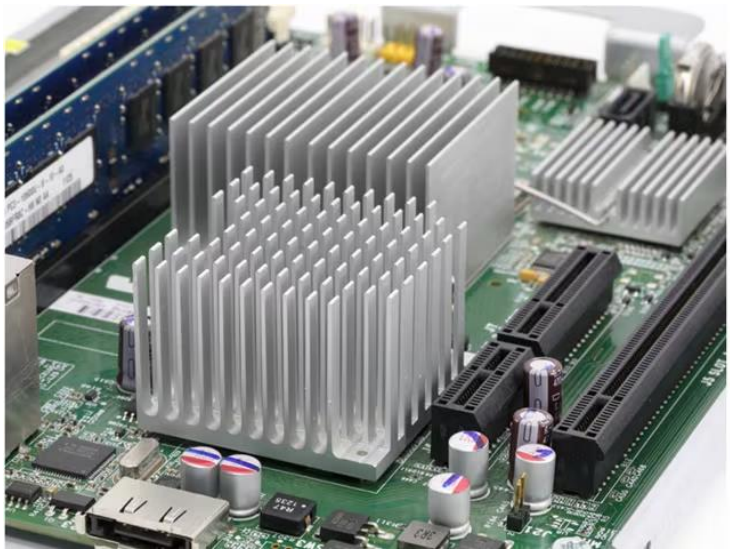

Figure 1-1: Finned heat sinks used to cool various devices on a motherboard [5]

As device heat generation approaches the limit of these heat sinks, active cooling solutions will become necessities; these methods dissipate the heat from the device using a working fluid, usually a liquid, rather than directly dissipating the heat to air. This heated fluid can then be directed to a larger heat sink, which may be located as close to or far from the device as needed. As liquids tend to have better thermal properties regarding heat dissipation, active cooling solutions can achieve higher heat transfer coefficients and heat fluxes [4]. However, this comes at an increased cost and complexity to the system, as an additional flow loop for the working fluid is needed, including a pump and a larger heat sink at a minimum.

1.2 Automotive Power Electronics Cooling

In modern vehicles, new active features are implemented with each generation while under the hood space is at a premium. As a result, power electronics are generating more heat with reduced space for thermal management. This will likely see an immense jump as development of autonomous vehicles continues. Furthermore, effective thermal management in electronic drive vehicles is essential to improving power density, performance, and reliability [6]. To maintain device performance, active cooling techniques, including jet impingement, microchannels, and spray cooling are being investigated [7].

While microchannels and spray cooling can achieve a higher heat flux or better surface temperature uniformity than jet impingement, they do so at much higher cost and complexity [8]. Implementing microchannels requires pumping a working fluid, usually a dielectric fluid, through engineered channels embedded in the substrate. This requires an additional flow loop for the new fluid and high pumping power to move the fluid through the small channels [7]. Depending on the application, two-phase microchannels, in which the working liquid boils through the microchannels, may be used to greatly increase the heat dissipation; this, however, comes at the cost of increased instability and equipment capable of handling a two-phase flow loop [9]. Spray cooling requires pumping a liquid through nozzles of small diameter to evenly spread small droplets across the surface, typically leading to the boiling of the fluid on the heated surface. Again, this requires a new flow loop for a new fluid, high pumping power to spray the fluid, and a complex system to handle the multi-phase flow [7].

While jet impingement has seen frequent use historically, usually in the cooling of turbine blades, its use in electronics thermal management is a relatively novel approach [2, 10]. Using the water-ethylene glycol (WEG) flow loop present in many commercial vehicles, power electronics may be cooled through jet impingement on the bottom side of the base plate, a region with no electronic components [7, 11]. As the flow will remain in the liquid phase and the pumping power and flow rates needed are of the same order of magnitude as those already achieved in the vehicles, jet impingement can be applied with minimal added components and slightly increased complexity. The primary downside to jet impingement is that, owing to its cooling performance being inherently tied to the motion of the fluid across the surface, temperatures across the surface will be less uniform than those achieved from microchannels or spray cooling. Thus, care must be taken in the design of the system to ensure that potential hotspots are managed appropriately.

1.3 Jet Impingement Characteristics

As the name suggests, jet impingement cooling is the motion of a jet of a cool working fluid against, usually normal to, a heated surface. The motion of the fluid has the natural effect of mitigating the development of the thermal boundary layer, which acts as a blanket to heat transfer. In doing so, jet impingement achieves the highest surface heat transfer coefficient possible without the introduction of a phase change. Furthermore, it is a highly flexible method, with wide variations

in scale, nozzle geometry, working fluids, impingement surface form factor, etc. Since the heat dissipation performance of jet impingement is inherently tied to the flow mechanics of the impinging jet(s), analyzing the performance and benefits of jet impingement requires an understanding of these flow behaviors.

1.3.1 Jet Classifications

The working fluid of an impinging jet may be a liquid or gas. The most common gas used is air, while a wide variety of liquids may be used. Certain classifications of impinging jets are defined based on which fluids are present in the impingement region, as shown in Figure 1-2. If the impingement region is flooded with the working fluid, it is referred to as a submerged jet. This definition applies to any liquid jet submerged in that liquid, as well as any air jet, as an air jet will naturally be surrounded by atmospheric air. If the working fluid is a liquid, but the region surrounding the jet is air, it is called a free jet. The viscous forces between the jet and surrounding fluid are significantly different in these two cases, resulting in varied performances. In many practical cases, space limitations require containment of the jet with a confining wall. In such scenarios, the jet may be referred to as a confined submerged jet or a confined free jet. This wall prevents the free flow of spent fluid from the surface, which affects the flow behaviors and thermal performance.

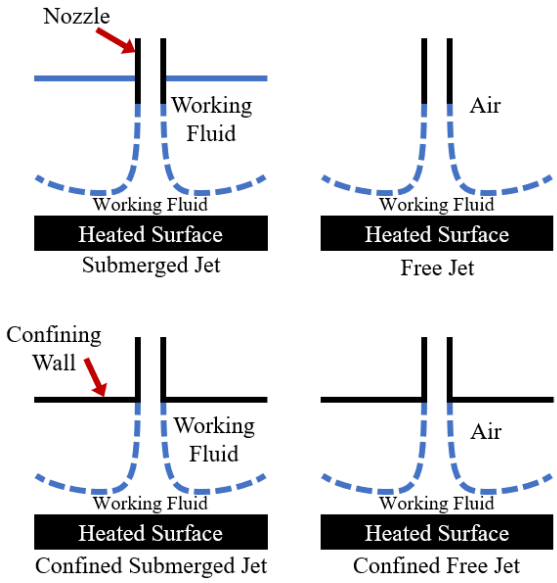

Figure 1-2: Classifications of impinging jets

1.3.2 Single Jet Characteristics

Figure 1-3 below depicts the typical flow behaviors seen for a single impinging jet. The jet exits the nozzle with some velocity profile which is dependent on the nozzle geometry and working fluid properties. As the jet moves through the surrounding fluid, viscous effects begin to affect this velocity profile, creating what is referred to as the shear layer. The internal region of the jet which has yet to be impacted by the shear layer is referred to as the potential core. With sufficient space between the nozzle and the surface, the shear layer will fully eliminate the potential core. As the jet approaches the surface, it decelerates as it is deflected peripherally. The region above the heated surface where the jet velocity approaches zero is referred to as the stagnation region. In this area, the downward fluid motion constantly displaces spent fluid with cool, fresh fluid, reducing the thermal boundary layer and promoting heat dissipation. When the fluid is directed peripherally by the surface, the fluid velocity becomes parallel to the surface, resulting in a region termed the wall jet. As the fluid motion is no longer normal to the surface, the thermal boundary layer is free to grow. As such, the heat transfer coefficient decreases with distance from the nozzle.

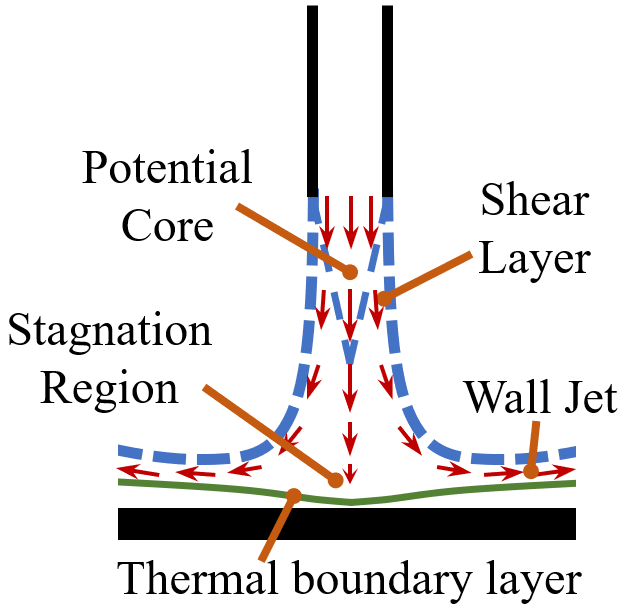

Figure 1-3: Characteristic flow behaviors of a single impinging jet

1.3.3 Jet Array Characteristics

In hotspot cooling, a single jet may be sufficient to maintain the spot at an acceptable temperature. However, in many practical situations, a large surface with distributed heating may need cooling. Since the performance of a single jet degrades with distance from the nozzle, a single jet will likely be impractical. To provide cooling across the surface, an array of smaller jets can be used across the surface. In an array, interactions between multiple jets become noteworthy and affect performance, as shown in Figure 1-4. The wall jet regions from two adjacent jets will meet between the jets, deflecting spent fluid away from the surface in a fountain-like motion. These fountains create mixing near the impingement surface, resulting in a long, slender region of increased heat transfer. While this region is small, these fountains occur away from the jets, aiding in surface temperature uniformity. As such, thermal performance can be enhanced by promoting these fountain interactions.

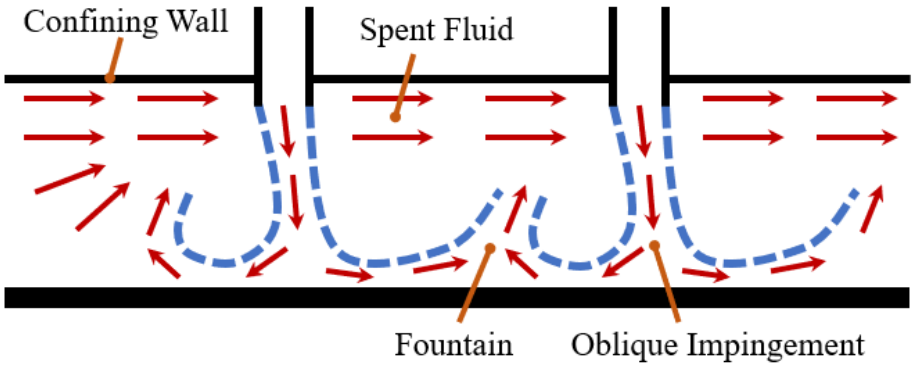

Figure 1-4: Characteristic flow behaviors of an impinging jet array

If a confining wall is used to contain the working fluid near the surface, the spent fluid from upstream jets must pass by all downstream jets. This has the undesired effect of deflecting the jets downstream, causing them to impinge on the wall at some angle less than 90°, referred to as oblique impingement. Due to the angle of impingement, the thermal boundary layer is not controlled as effectively as when the jet flows normal to the surface, thus resulting in reduced performance. To improve downstream performance, this spent fluid must be managed in some manner, such as fluid extraction from the impingement region. If the impingement array is sufficiently large and no spent fluid management is employed, then crossflow effects will eventually cause the downstream thermal performance to approach that of parallel flow in a channel.

This research effort is directed towards thermal-fluid improvements of arrays of confined submerged jets for application in cooling of automotive power electronics. Surface features will be implemented to promote interactions between jets and an angled confining wall will be utilized to aid in spent fluid management. The behavior of fountains will be closely studied, with emphasis regarding their promotion or suppression and their effects on thermal performance.

Chapter 2: Literature Review

Owing to the numerous classifications and configurations of jet impingement systems, many approaches have been and continue to be the subject of research efforts. Beyond the classes previously discussed, wide variations in orifice hydraulic diameter, orifice shape, jet spacing, nozzle-to-surface distance, impingement surface size, impingement surface shape, and many other variables are possible, depending on the application. The aim of this effort is to enable enhanced heat dissipation from automotive power electronics modified surfaces using an angled confining wall to mitigate crossflow effects and surface modifications to improve fluid mechanics and heat transfer. This effort will utilize submerged water impingement through circular orifices; thus, reviewed literature will typically fall into these categories, though many will examine different working fluids, orifice shape, and orifice scale, depending on the topic. Finally, previous work within the group will be reviewed, as past findings inherently connect to many decisions made during the completion of this research effort.

2.1 Jet Impingement in Electronics Thermal Management

Recent research efforts have examined the use of jet impingement in various electronics cooling applications. In 2020, Han et al. experimentally and numerically examined a water slot jet array for direct liquid cooling of a server processor [12]. The heat sink design made use of fluid extraction ports, referred to as drain slots in the study, to manage spent fluid and mitigate crossflow effects; these are engineered spaces in the nozzle plate through which spent fluid is drawn, rather than pulling the fluid out tangentially to the impingement surface. Combined with pin fins, the array was capable of cooling the surface to maintain acceptable temperature rises within 15°C under a heating power of 150W. Experiments and simulations agreed within 5%, indicating the accuracy of the model. In prior work, Han et al. also used a numerical model to analyze the use of jet impingement to stacked electronics packages, as shown in Figure 2-1 [13]. The design for this study also implemented fluid extraction but did not use fins. Application was examined within the substrate, on the top surface of the stack, and in both locations. Predictably, cooling in the substrate alone resulted in the highest temperatures while cooling on both sides yielded the lowest operating temperatures. The design was validated with experiments, suggesting jet impingement can be a feasible cooling method for stacked devices.

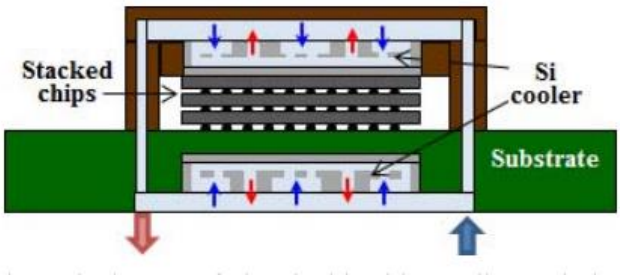

Figure 2-1: Jet impingement application on both sides of a stacked electronic package as examined by Han et al. [13]

Walsh et al. experimentally and numerically analyzed a microjet array of water embedded within an electronic substrate [14]. The array was designed such that it could be fabricated from industry-standard silicon microfabrication methods. As the array was embedded in the substrate, thermal resistances were significantly reduced. The numerical model was validated using micro-Raman thermography to measure the surface temperature profile, which yielded similar trends to the results calculated by the model. The array was shown to perform well, maintaining acceptable device temperature.

In 2019, Wei et al. experimentally and numerically investigated a microjet impingement cooler for high power electronic applications [15]. Cost efficiency was improved through fabrication of the array with polymer and micromachining, as opposed to more expensive materials such as ceramic or Si based fabrication. It was shown that the array was capable of achieving low thermal resistance of 0.25K/W without requiring exceptionally high pumping power. Furthermore, it was found that cooling with the jet array was more effective than using a single jet designed to accomplish the same task. For the same flow rate, the jet array achieved far lower thermal resistances on the periphery of the chip and improved surface temperature uniformity, reducing the range of temperature rises across the surface from 15°C under the single jet to 3°C under a four-by-four jet array with the same pressure drop.

Elsinger et al. completed a numerical grid-optimization with the jet diameter and nozzle-to-surface distance for a water microjet array [16]. The jet diameter was varied eight times from 40 to 600µm while, independently, the nozzle-to-surface distance was varied eight times also from 40 to 600µm, creating an eight-by-eight grid of 64 geometries. After verifying the model with a corresponding experimental setup, eight variations of each variable were examined, resulting in 64 unique cases. Of these, six were selected for more detailed analysis. Decreasing the jet diameter

and nozzle-to-surface distance was seen to result in increased heat transfer coefficients and pressure losses. The optimized geometry provided a 56% increase in the heat transfer coefficient and 60% reduction in the span of temperatures at the cost of a 152% increase in the pumping power.

Jörg et al. studied the applicability of water jet impingement in hotspot cooling of an insulated-gate bipolar transistor module using experimental and numerical methods [17]. A pin fin heat sink was compared to an array of impinging water jets, whose nozzles were located directly above the hotspots and had varying diameter. Both methods were found to be effective at reducing hotspots. IR-thermography was used to examine potential for thermal stresses, which revealed that impingement was highly effective in managing localized hotspots. A decrease in the nozzle diameter was effective at reducing the surface temperature and increasing the local heat transfer coefficient, but this came at the cost of increased pumping power. In this application, it was determined that the pin fin heat sink performed better regarding hotspot mitigation and thermal stresses.

Jones-Jackson et al. studied the potential use of jet impingement to cool an electric motor converter in 2021 [18]. The jet nozzle was varied as a circular nozzle with two diameters, a square nozzle, and a square nozzle with a chamfer. A numerical model was generated for a single impinging jet of water; the model was validated experimentally and yielded results within 2.4% of the experimental case. While little reduction of the surface temperature was observed due to the changing jet geometry, pumping power could be significantly reduced with minor changes to the geometry. The chamfered, square nozzle resulted in a 236% increase in pumping power when compared to the square nozzle with no chamfer. As such, it is seen that careful design and fabrication of the nozzle geometry is essential.

Agbim et al. numerically and experimentally analyzed a chip's temperature under a microjet array of impinging deionized water [19]. Jet impingement was applied directly to the backside of the direct-bond copper surface, as opposed to a conventional power module stack, in which the heat must also flow through layers of solder, an aluminum heat spreader, thermal grease, and a cold plate. Due to the additional layers between the chip and cooling fluid, the conventional stack saw diminishing returns in thermal resistance reductions as the heat transfer coefficient was increased. However, by applying jet impingement to the direct-bond copper surface, this limitation

was far less impactful, resulting in further reductions to the thermal resistance. By reducing the conduction resistances, improvements in the convective resistances became more effective and the efficiency of jet impingement was more impactful.

In 2018, Leena et al. numerically and experimentally studied application of a single row of irregularly spaced impinging jets of air for application in cooling electric devices [20]. Variations in jet Reynolds number, jet spacing, and nozzle-to-surface distance were examined. ANSYS Fluent was used in the numerical studies, which yielded results within 10% of a corresponding experimental setup. For the variables examined, it was found that variations in the jet Reynolds number resulted in the largest changes in the Nusselt number, which is to be expected. It was observed that, for the geometry examined, the single row of jets effectively acted as a single, slot jet at sufficiently low jet spacings. Only once the jets were spaced apart were their individual effects observable.

Incorporation of two-phase heat transfer with jet impingement provides potential for maximizing heat dissipation and achieving surface temperature uniformity, as investigated by de Oliviera and Barbosa Jr. [21]. A vapor compression cycle with R-134a as the working fluid was used in a system mimicking a device in operation. The compressor piston stroke, heat load, and nozzle diameter were each varied. The surface heat transfer coefficient varied more with a changing heat load than with the nozzle diameter, suggesting that boiling was the dominant heat transfer mechanism in the system. Because the smaller nozzle diameter required a higher pressure differential through the nozzles, two issues arose. First, compressor power consumption was higher to achieve the greater differential. Second, since the system pressure was higher, the saturation temperature of the liquid increased, resulting in a higher surface temperature. This displays the inherent complexity of combining aggressive thermal management mechanisms such as jet impingement and boiling.

One contributing factor to recent interest in jet impingement use in electronics thermal management is developments in additive manufacturing. Additive processes are capable of accurate generation of highly complex geometries that are impractical or impossible to manufacture through machining processes. In 2019, Paniagua-Guerra et al. numerically modelled a hybrid heat sink cooled with microjets for use in chip-scale, high power density electronic packages [22]. Intricate jet manifolds, shown in Figure 2-2 interweave inlet and outlet manifolds

to manage spent fluid in an effective manner. Designs with 16, 32, and 64 jet nozzles were examined for the same heated surface; depending on the design, jet diameters from 0.17 to 1.75mm were modelled. Arrays of such complexity would be infeasible were it not for recent developments in additive manufacturing. All designs achieved much lower thermal resistances than the specified base case, but with increased pumping power requirements. The 64-jet design provided the lowest temperature rises and best surface temperature uniformity.

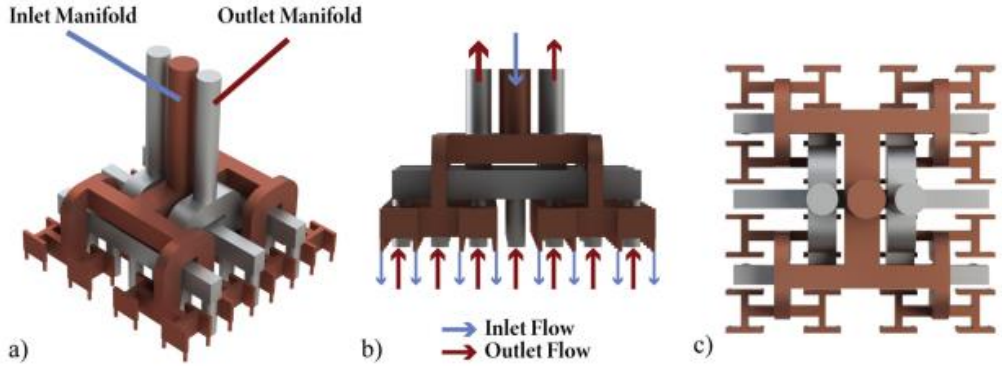

Figure 2-2: Jet array with interwoven inlet and outlet manifolds examined by Paniagua-Guerra et al. presented as a (a) isometric view, (b) side view and (c) top view [22]

Kaood et al. numerically modelled a water jet impingement array for thermal management of automotive devices [23]. The array was designed such that it could be manufactured as a single component using metal additive manufacturing and applied to an electronic heat source with a footprint of 2.5-by-2.5cm. Four designs were analyzed: a baseline array, an array with nozzles extending below the confining wall for downstream jets, an array with extended nozzles and a barrier in front of the furthest downstream row of jets, and an array implementing fluid extraction through the confining wall. The design with the barrier provided the lowest minimum surface temperature and lowest thermal resistance, but the fluid extraction design provided the best surface temperature uniformity and lowest pressure losses.

Kempers et al. experimentally and numerically analyzed a hybrid microchannel-microjet system created by metal additive manufacturing for application in electronics cooling [24]. Water was forced through 200-by-70μm slot jet nozzles, which nearly touch the surface. The fluid was exhausted through microchannels that lead to the outlet in paths that do not affect downstream jets. While the array was accurately fabricated, residue was deposited on the top surface of the jet nozzles while soldering the array to the inlet manifold, leading to disagreement between the model

and experiments regarding the pressure losses. Regardless, the experimental array was able to dissipate a heat flux of 1kW/cm^2 at a flow rate of 0.5L/min, resulting in a base temperature rise of 34°C.

Kwon et al. utilized additive manufacturing to cool a gallium nitride device through a complex system of impinging air jets in their 2010 study [25]. Two jets were used to cool two heat-generating devices. The effects of varying flow rate and device power on the transient device temperature were analyzed both experimentally and numerically. The jets were applied on the top side of the devices, on the other side of the printed circuit board (PCB), on both the top of the device and bottom side of the PCB, and on two sets of devices in a parallel configuration. In all cases, activating the jet array resulted in a rapid decrease in device temperature of up to 6.6°C/s, displaying the efficacy of this technique. Furthermore, many device and array configurations were analyzed, showing the repeatability of such additive manufacturing processes.

In 2021, Pappaterra et al. modelled an array of impinging jets to cool a high-performance processor and enable level 5 autonomous driving, using WEG as the working fluid [26]. A numerical model was generated to examine various design approaches. The final design implemented fin structures and fluid extraction in the impingement region. This array was created through metal additive manufacturing and analyzed in a testing system under operating conditions. Benchmarking comparisons made to finned heat sinks showed significant increases in heat dissipation with slight increases in pumping power.

Wei et al. directly compared micromachining to additive manufacturing by creating a similar array design through both processes and using them in an electronics cooling scenario using water as the working fluid [27]. While both processes yielded usable arrays, the additively manufactured array was less accurate, primarily in having nozzles with a slightly smaller diameter. Despite this, both arrays resulted in very similar thermal resistances. Furthermore, due to the ability of additive manufacturing to produce efficient internal geometries, pumping power was reduced by 24% when compared to the micromachined array, regardless of the smaller nozzles and a reduced form factor.

Thermal management of high-performance electronics devices necessitates increasingly aggressive cooling mechanisms as the power draw increases and the form factor decreases. Advances such as heterogeneous integration and stacked electronics reduce the area available for

cooling while compacting many devices together. Due to its flexibility and ability to effectively dissipate heat from a surface, jet impingement is the subject of many research efforts in these applications. Table 2-1 below summarizes the reviewed research efforts in which jet impingement was utilized in cooling electronic devices.

Table 2-1: Summary of past research on application of jet impingement in electronics thermal management

Principal author	Jet specifications	Application	Analysis method (model)	Key findings
Han (2020)	Water jet array	Data center server processor	Experimental and numerical (model not stated, likely laminar)	Maintained device temperature rises less than 15°C for a heating power of 150W
Han (2017)	Water jet array	Stacked electronics	Experimental and numerical (Laminar)	Impingement on both sides of the stack maintained chip temperatures within operating conditions
Walsh	Water microjet array	General high-power devices	Experimental and numerical (k-ω model)	Embedding microjets in the substrate reduces thermal resistances between the device and working fluid
Wei (2018)	Water microjet, single and array	General high-power devices	Experimental and numerical (Transition SST model)	For the same flow rate, the array achieved better temperature uniformity than the single jet
Elsinger	Water microjet array	General high-power devices	Experimental and numerical (Transition SST model)	An optimization study on the jet diameter and nozzle-to-surface spacing yielded a 56% increase in the heat transfer coefficient
Jörg	Water jet array	General high-power devices	Experimental and numerical (Laminar)	Placing a jet over a hotspot effectively cooled the spot and reduced thermal stresses
Jones-Jackson	Water jet array	Electric motor converter	Numerical (k-ω SST model)	Changes in the nozzle geometry had more effect on the pumping power than thermal performance
Agbim	Water microjet array	General high-power devices	Experimental and numerical (Spalart-Allmaras model)	Applying impingement to the direct-bond copper reduced conduction thermal resistances, allowing for greater improvements
Leena	Air jet array	General high-power devices	Experimental and numerical (k-ε model)	Jet orifices spaced closely together may act as a single jet; individual jet effects are not notable unless spaced apart

de Oliveira	Two-phase, single R-134a jet	General high-power devices	Experimental	A small nozzle diameter increased pressure losses, resulting in a higher saturation temperature and reduced performance
Paniagua-Guerra	Water microjet array	General high-power devices	Numerical (Laminar)	Many, small jets can improve temperature uniformity at the cost of increased pumping power
Kaood	Water jet array	Automotive electronics	Numerical (Transition SST model)	Complex internal geometries, including flow diverters and fluid extraction, can improve thermal performance and pressure losses
Kempers	Water microjet array	General high-power devices	Experimental and numerical (Laminar)	An additively manufactured, hybrid microchannel-microjet system dissipated 1kW/cm^2 with a measured base temperature rise of 34°C
Kwon	Two air jets	General high-power devices	Experimental and numerical (k-ε model)	Transient temperature reductions of up to 6.6°C were achieved when the jets were activated
Pappaterra	WEG jet array	High-performance vehicle computer	Experimental and numerical (k-ω SST model)	Additive manufacturing can enable accurate formation of highly complex geometries
Wei (2019)	Water jet array	General high-power devices	Experimental	Additive manufacturing can accurately create complex internal geometries, resulting in reduced pumping power versus a micromachined array of the same design

2.2 Spent Fluid Management and Crossflow Mitigation

In confined arrays of impinging jets, crossflow as spent fluid passes downstream jets suppresses normal impingement and fountain interactions, negatively impacting performance. As mitigating crossflow effects is necessary to achieve best performance, many research efforts have been dedicated to studying potential methods to mitigate its effects with a variety of approaches. In their 1987 study, Obot and Trabold experimentally analyzed the effects of crossflow on an impinging air jet array by allowing the fluid to exit through one, two, or four sides of a square array [28]. It was found that reducing the allowable exits, thereby increasing the crossflow, reduces the downstream Nusselt number. At a certain mass flow rate, this effect was more detrimental for

arrays with a high density of jets than for arrays with a sparce number of jets. Coupled with the finding that a higher jet density results in a higher heat transfer coefficient, this study displays the significance of effective spent fluid management, particularly for arrays with many jets.

Corvera and Mahjoob numerically modelled the use of various rectangular air jets experiencing crossflow for hotspot cooling applications in 2022 [29]. Rectangular jets of varying dimensions experiencing crossflow were used to cool a hotspot mimicking an electronic component. After verifying the model with literature, it was found that orienting a rectangular jet in the streamwise direction was effective at reducing effects from the crossflow, while orienting the jet in the transverse direction magnified crossflow effects. However, the square jet achieved the best surface temperature uniformity, though it was more affected by the crossflow. Following this, Corvera and Mahjoob continued their investigations by more directly examining the effects of crossflow on an air jet [30]. The cooling effects of crossflow alone, an impinging jet alone, and the jet in crossflow were examined. One examined case of the combined jet in crossflow angled the impinging jet with the crossflow and placed it slightly upstream, with the intent to direct the jet onto the hotspot more effectively. While the best thermal performance was achieved with the jet alone, the angled jet case yielded slightly only slightly higher surface temperatures with a reduced required pumping power, suggesting that adjustments to the jet array design to accommodate anticipated crossflow can provide beneficial results.

He et al. investigated the use of various crossflow diverters in a row of impinging air jets using a numerical model [31]. These diverters were placed between each jet such that fluid from all upstream jets were deflected towards the peripheral walls and away from the subsequent jet downstream, as shown in Figure 2-3. By diverting crossflow peripherally, downstream jets were shielded, allowing them to impinge normally, reducing deflection when compared to the baseline case. However, increased frictional losses resulted in unequal flow rates through each nozzle; downstream nozzles had notably higher fluid velocities due to a larger pressure difference between their entrance and exit. This improved performance downstream at the cost of slightly reduced performance upstream and increased supply pressure requirements. Regardless, a heat transfer performance parameter designed to combine heat transfer benefits and frictional losses increased by over 10% for all cases, suggesting that the tradeoff would be worthwhile. The parameter (Φ) was created by Fan et al. in 2009 and is shown in Equation 2.1, which is used to compare the

Nusselt number and friction factors for an enhanced case (subscript E) to a baseline case (subscript 0) [32].

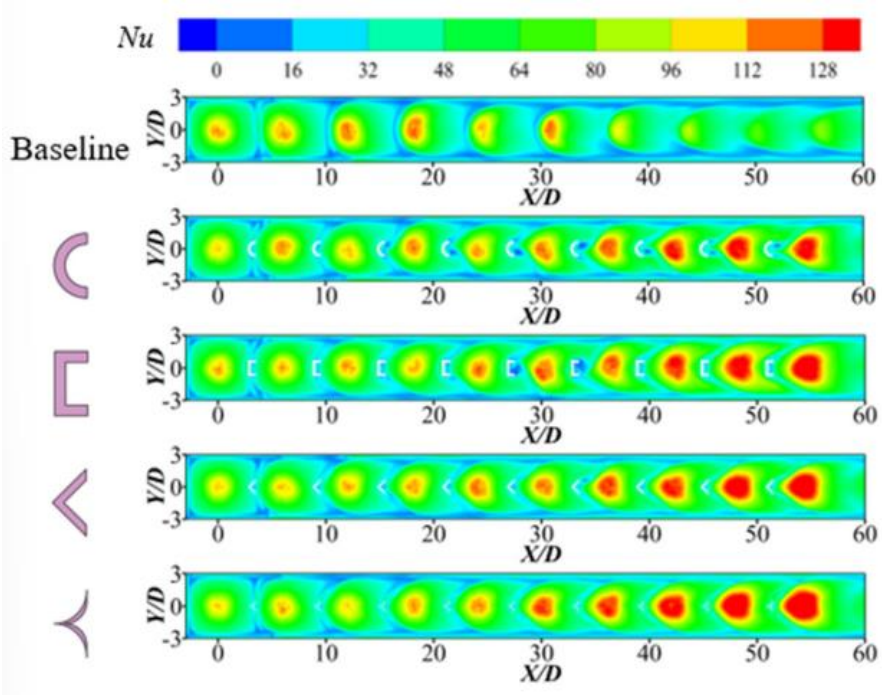

Figure 2-3: Surface Nusselt number contours for various crossflow diverters used by He et al. [31]

$$\Phi = \frac{Nu_{E,avg}/Nu_{0,avg}}{(f_E/f_0)^{1/3}} \tag{2.1}$$

In a similar fashion, Madhavan et al. examined U-shaped crossflow diverters in impinging air jet arrays in turbine blade cooling applications [33]. It was also found that such diverters shield downstream jets, allowing them to impinge normally. This increased the average Nusselt number by 15-30%, depending on the supplied pumping power. However, increased pressure losses resulted in uneven flow through the nozzles, reducing performance upstream.

Arens et al examined five jet arrangements intended to reduce crossflow effects in a numerical model [34]. These arrangements included variations in confining wall angle, nozzle diameter and nozzle spacing, with the latter two varying based on the radial location of a given nozzle. The center temperature of the surface was extrapolated from three temperature measurements made at known distances from the surface. It was found that increasing the nozzle diameter or density downstream improved thermal performance by 20% and 27% respectively when compared to an equivalent array with a constant diameter. However, the confining wall angle

provided inconsistent results. The angled wall was beneficial with a constant jet diameter and density but proved ineffective with an increased jet diameter downstream. It was concluded that further analysis of the angled wall was necessary.

In 2021, Forster and Weigand used experimental and numerical methods to model a row of air jets impinging on a gas turbine blade [35]. Across the surface, small holes were used to remove spent fluid to both reduce the thermal boundary layer and mitigate crossflow. Additional air flow upstream from the jets was supplied at varying flow rates to model increased crossflow effects. Independently, the nozzle height was also varied. An increase in crossflow resulted in decreased local and average Nusselt numbers, indicating how crossflow effects can reduce performance across the surface. In contrast, decreasing the nozzle spacing increased local and average Nusselt numbers. Even though the crossflow increased in velocity, the reduced spacing resulted in less deflection of the jets. Fluid extraction was used in all cases, so there was no baseline case with which to compare. It would likely be highly effective if compared as such, but it would be very difficult to apply to electronics cooling, as implementing extraction holes in the substrate would be very difficult and could likely only be used in very few applications.

Fluid extraction through the impingement surface is not applicable in most scenarios, as the object being cooled likely cannot accommodate extraction channels. While extraction through the nozzle plate requires complex design considerations, it is more likely to be applicable in any given application, since the surface does not require extensive internal machining. Onstad et al. applied fluid extraction through the nozzle plate for an array of impinging jets [36]. Flow visualization was achieved for a water jet array using magnetic resonance velocimetry, while an air jet array was used to examine heat transfer performance. Flow visualization measurements were taken at two Reynolds numbers, which yielded little difference in flow structures between the two flow rates. In one direction, a smooth transition from the nozzle outlet, through the stagnation region, and out the extraction port was observed with no indication of vortices. In the other direction, crossflow effects were observed to deflect jets on the periphery of the array, creating vortex structures and reducing performance. This was attributed to the design of the inlet manifold creating uneven flow through the nozzles in this direction. Heat transfer analysis was only completed with varying Reynolds number and compared to other results in literature. The average

Nusselt number increased with increasing Reynolds number, and the results were seen to agree with literature.

Hobby et al. also examined the use of fluid extraction ports, but in a micro-scale, laminar jet array of water [37]. The array was 3D printed using a photopolymer material and analyzed in operating conditions. It was found that the resulting Nusselt numbers had major differences between the numerical and experimental results. However, once adjustments were made to the numerical results due to regions not modelled, close agreement was found for the total system pressure drop between the computational prediction and experimental findings. In 2017, Rattner numerically modelled 1000 laminar microjet impingement cases with fluid extraction ports to generate correlations for a variety of cases [38]. Variations in the jet Reynolds number, Prandtl number, jet spacing, and nozzle-to-surface distance were examined. The numerical model was validated by comparing a simple jet without extraction to a previously existing experimental correlation. Fluid extraction was then added and each variation was modelled using the same methodology. Two correlations were generated using all the cases, one for the pressure loss and another for the average surface Nusselt number. The pressure loss correlation yielded results within 25% of the model's output for 94.8% of the cases, while the Nusselt number correlation did so for 96.5% of cases.

Mitigation of detrimental crossflow effects is a complex problem with a variety of solutions undergoing research. Simple approaches including adjustments to the nozzle design and placement of crossflow diverters have been shown as effective. Meanwhile, the more complex approach of fluid extraction are becoming increasingly feasible with advances in additive manufacturing. Table 2-2 below summarizes the findings of the examined crossflow research efforts.

Table 2-2: Summary of past research on mitigation of crossflow effects

Principal author	Jet specifications	Crossflow Mitigation Method	Analysis method (model)	Key findings
Obot	Air jet array	Additional outflow paths	Experimental	Increased crossflow degrades the downstream Nusselt number
Corvera (2022)	Single air jet in crossflow	Slot jets oriented with crossflow	Numerical (k-ε model)	Orienting slot jets in the streamwise direction reduces the impact of crossflow

Corvera (2023)	Single air jet in crossflow	Jet angle and location adjustments	Numerical (k-ε model)	Angling the jet with crossflow reduces the required pumping power with similar thermal performance
He	Air jet array	Crossflow diverters	Numerical (k-ω SST model)	Diverters shield downstream jets at the cost of increased pressure losses and uneven jet flow
Madhavan	Air jet array	Crossflow diverters	Experimental and numerical (k-ε model)	Diverters improved thermal performance by 15-30% across the surface, but increased pressure losses
Arens	Water jet array	Confining wall angle, jet diameter, jet spacing	Experimental and numerical (Unspecified SST model)	Increasing the jet density or diameter downstream can reduce crossflow effects
Forster	Air jet array	Fluid extraction	Experimental and numerical (k-ω SST model)	Fluid extraction through the surface reduces the thermal boundary layer and crossflow effects
Onstad	Water jet array for flow fields, air jet array for heat transfer	Fluid extraction	Experimental	Fluid extraction ports are able to allow normal impingement and extraction without creating circulation
Hobby	Water jet array	Fluid extraction	Experimental and numerical (Laminar)	Additive manufacturing was capable of creating a complex array with fluid extraction
Rattner	Microjet array of non-specific fluids ($1 \leq Pr \leq 100$)	Fluid extraction	Numerical (Laminar)	Accurate correlations for the pressure losses and Nusselt numbers for impinging jets with fluid extraction were formulated

2.3 Impingement Surface Modification

Research into applying modifications to the impingement surface is somewhat underdeveloped. A major problem with this approach is jet impingement's inherent reliance on its flow mechanics to maximize heat dissipation; if surface modifications inhibit preferential behaviors such as the stagnation region or fountain interactions, they can decrease performance

while also increasing pumping power requirements. In 2001, Ekkad and Kontrovitz examined the use of mesoscale, concave surface dimples under and between jets on the heat transfer characteristics of an air jet array [39]. The dimples were 1.27cm in diameter and had varied depths of 0.3175 and 0.15875cm; each size was also examined with each dimple located directly under a jet or between jets in the outflow direction. It was found that surface dimples reduced the local and average Nusselt numbers when compared to without dimples. This result was attributed to a "bursting phenomena". Fluid moving through the dimples would burst out from under the surrounding surface, negatively impacting the stagnation regions nearby. Downstream, as crossflow reduced the impact of the jets and the flow approached channel-like conditions, the dimples improved performance once jet flows became less impactful. It was concluded that these dimple structures were not advisable when impingement mechanics are the dominant driving force for heat transfer. Likewise, Kanokjaruvijit and Martinez-Botas investigated similar dimples with more parametric variations in their 2010 study [40]. In this case, dimples were examined with diameters of 4cm and 1.74cm with depths of 0.6, 1, and 0.55cm. Dimples were likewise examined both directly under and between jets. Experimentation revealed that dimples were more effective with crossflow, where channel flow effects dominated heat transfer. A similar conclusion was found when Trabold and Obot continued their research [41]. Square ribs were applied to the target surface perpendicular to the exhaust air flow. These were found to slightly reduce the Nusselt number upstream, where crossflow was minimal and impingement mechanics dominate. However, performance was improved downstream, where crossflow became more impactful and channel flow dominates.

El-Sheikh and Garimella investigated the use of pins of two heights under a single jet and multiple jets of air [42]. All pins had a diameter of 1.6mm and the height was varied at 12.7 and 25.4mm. A definition of the heat transfer coefficient was used in which the characteristic area was that of the base, not the total area of the modified surfaces. Under this definition, the heat transfer coefficients increased notably, though this definition does not differentiate the effects of increased surface area from altered flow mechanics. The heat transfer coefficient changed little between the short fins and the tall fins, despite the surface area doubling. For a given Reynolds number, the multiple jet array yielded higher heat transfer coefficients, but the single jet provided slightly higher heat transfer coefficients for a given flow rate.

Hansen and Webb applied fin and ring structures to an impingement surface under a single jet of air in their 1991 study [43]. The surface modifications investigated were square pin fins of three heights, pyramidal fins, and two annular ring designs. The square fins all had widths of 1.59mm with varied heights of 1.59, 3.18, and 4.76mm. The pyramidal fins had base widths of 3.18mm and heights of 1.59mm. One ring design used three rings of square cross-section, with side lengths of 1.59mm, each located at different distances from the jet, while the other was a single ring of rectangular cross-section, with a width of 3.18mm and height of 6.35mm, placed far away from the jet. In all cases, heat transfer was increased, though this was largely attributed to an increase in surface area. The ring designs were found to reduce the Nusselt number in all cases. The pyramidal and pin fins were found to increase the Nusselt number, with the pyramidal fins providing the highest improvement, followed by the short, intermediate, and tall square fins; this pattern indicates an increase in the Nusselt number as the modification form factor is reduced to provide less impact on the stagnation region. It was proposed that the portion of the surface area exposed to normal impingement, oblique impingement, and/or parallel flows was the primary reason for the differing results.

King and Chandratilleke numerically examined the use of conical surface modifications under a single impinging jet of air onto a surface of constant temperature [44]. Local heat flux was shown to improve up to 30% near the jet before decaying shortly downstream. Near the base of the cone, small recirculation regions were observed, as displayed in Figure 2-4. This was somewhat mitigated by applying a fillet to the base, reducing the size of this region. Otherwise, no negative affects on flow mechanics were observed. As such, it has been shown that surface protrusions under a single impinging jet can have positive effects on the overall heat transfer.

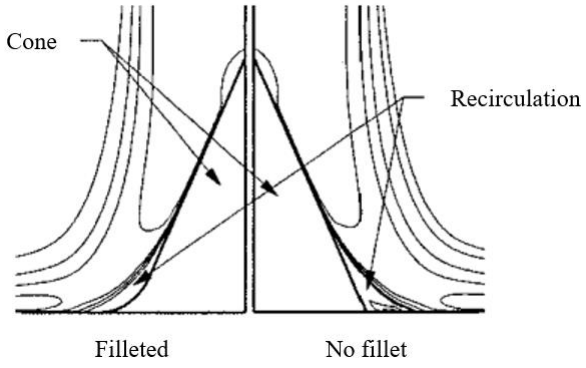

Figure 2-4: Velocity magnitude contours from King and Chandratilleke displaying recirculation at the base of a cone structure [44]

In 2023, Govindaraju et al. numerically modelled five mesoscale fin structures in a liquid jet array [45]. The structures analyzed were cones under each jet, cones under each jet surrounded by square pin fins, rectangular fins radially aligned from each jet, square pin fins, and rectangular pin fins. The model was verified using an experimental setup with the baseline surface. Each modification increased the heat transfer by increasing the surface area, but in all cases the heat transfer coefficient reduced due to negative impacts on flow behaviors. The cone modifications were used in a topology optimization study, which yielded a 9.3% improvement in the thermal performance, despite only increasing the surface area by 1.7%, indicating the potential improvements in jet impingement when desired flow interactions are promoted.

Gao et al. numerically modelled a variety of trapezoidal fins in a microjet array [46]. The study did not examine a control case without fins. Notably, the fins had nearly the same height as the nozzle-to-surface distance. As a result, these modifications did not directly impact the stagnation region which primarily drives heat transfer in jet impingement. Using these, temperature uniformity within 5.5°C was achieved for a supplied heat flux of 200W/cm^2. It is possible that the modifications may have magnified crossflow effects towards the outlet, but it cannot be definitively determined without an unmodified baseline case.

Cui et al. numerically modelled a jet impingement system for the cooling of multi-core integrated circuits with hotspots in their 2022 study [47]. Many parameters were examined, including jet diameter, number of jets, pin fin design, and inlet diameter. The pin fins examined were millimeter-scale, with one case having uniform fins across the surface and the other reducing the cross-sectional area of the fins and increasing the fin density only over the hotspot regions. The heat transfer coefficient for this study was also defined based on the base area, which yielded increasing values when the finned surfaces were applied, though much of this increase was likely caused by increasing the surface area. Temperature uniformity was improved using each of the finned surfaces. It was also concluded that increasing the jet number and diameter over the hotspots, but not the surrounding area, greatly improved heat dissipation from the hotspots. The optimized design, which made use of a finned surface, improved the temperature non-uniformity by 58%.

In 2011, Celik experimentally analyzed the use of a ring of mesoscale dimples surrounding an impinging air jet with circular and co-axial geometries [48]. The co-axial jet is a composite jet

created from two air streams departing from concentric nozzles. This co-axial nozzle was particularly effective, as the two independent air streams were able to mitigate some of the reduced performance that results from the development of the wall jet, where flow becomes parallel to the surface. The dimples created a disruption in the thermal boundary layer, improving performance away from the jet. Combining the co-axial jet and dimples resulted in a 27% increase in the average Nusselt number when compared to a cylindrical jet on a smooth surface, while the dimples alone created a 6% increase. These dimples were exclusively placed away from the stagnation region, suggesting that mesoscale or mesoscale surface modifications can be beneficial when applied in certain regions, rather than across the entire surface.

Madhavan et al. used high-porosity metal foams on the impingement surface to increase the effective surface area and promote mixing near the surface [49]. The aluminum foam was 3mm thick with a high porosity and pore density. Four surface cases were examined: a smooth surface, foam across the entire surface, striped foam between rows of jets, and striped foam under rows of jets. The intent of the striped cases was to mitigate increased pressure losses expected from implementing the foam surfaces. Increases in both the average surface heat transfer coefficient and pressure drop corresponded to the amount of the surface covered in the foam; an increased foam coverage resulted in increases in both heat dissipation and pressure losses. Weighing both the thermal improvements and increased pressure drops, it was determined that the case with full foam coverage yielded the best results of up to a 100% improvement in the thermal hydraulic performance than the baseline case. In this study, this was defined to mean that, at a given pumping power, the metal foam across the whole surface yielded a heat transfer coefficient 100% higher than the baseline surface.

To avoid the detrimental effects on flow frequently created by mesoscale surface modifications, microfins or surface roughening have been investigated. Because these modifications are on a much smaller scale than the flow behaviors, they have far less effect, allowing for increased heat transfer without negatively impacting preferred flow mechanics. Radmard et al. numerically investigated the use of jet impingement and micro pin fins for chip-level and hostspot cooling applications in their 2021 study [50]. Arrays of water jets with varying nozzle-to-surface distance and diameters impinged upon the finned surface. The fin height was set equal to the nozzle-to-surface distance. Increasing the height or diameter reduced the required

pumping power at the expense of decreased thermal performance. Thermal resistances around 0.015K/W were reported. It was then shown that additive manufacturing could be used to reliably create the finned surface.

Waye et al. utilized a microfinned impingement surface to increase the heat dissipated from an automotive traction drive inverter by an array of impinging WEG jets [51]. Impingement on the microfinned surface, impingement on a flat surface, and channel flow with no impingement were each analyzed experimentally and numerically with varied flow rate and device power. Jet impingement required additional pumping power but successfully reduced the thermal resistance from the surface, particularly from the microfinned surface. In particular, jet impingement on the microfinned surface improved the thermal performance by 17% while reducing the system's weight by 3kg, increasing the specific power by 36% as compared to the channel flow baseline. The thermal resistance was reduced by 5% when jet impingement was applied, and this was further reduced to 13% with application of the microfinned surface.

In 2013, Moreno et al. achieved thermal improvements using microstructures on the impingement surface for water impingement in both free and submerged conditions [52]. The microstructures examined were a microfinned surface, a microporous coating, and a spray pyrolysis coating. These were compared to a baseline smooth surface, surfaces roughened by sand blasting and sandpaper, and millimeter-scale pin and radial fins. In the free jet configuration, the fin structures performed best at low Reynolds numbers, but the roughened and microporous coated surfaces were more effective at high flow rates. In particular, the microporous coating provided a Nusselt number enhancement of 130% over the baseline, which was suggested to be caused by early transition from laminar to turbulent flow in the wall jet region. In the submerged jet configuration, this transition did not occur and the finned surfaces performed best at all Reynolds numbers examined. The microfinned surface increased the Nusselt number by 100% compared to the baseline, while the roughened and microporous coatings had little-to-no effect.

While almost any impingement surface modification can be expected to increase the heat dissipated, reduce thermal resistances, and/or reduce surface temperatures, these effects are typically due to increasing the wetted surface area. Mesoscale modifications can negatively affect desirable flow mechanics such as stagnation and fountain interactions or introduce fluid circulation near the surface which dampens heat transfer, causing a reduction in the surface heat transfer

coefficient. While microfinned surfaces avoid causing such interference, they may result in increased pressure losses and their scale limits their cooling potential. Table 2-3 below summarizes the findings of the impingement surface modification studies examined.

Table 2-3: Summary of past research on jet impingement surface modifications

Principal author	Jet design	Modification type and size	Analysis method (model)	Key findings
Ekkad	Air jet array	Dimples – diameter of 1.27cm, depths of 0.16-0.32cm	Experimental	Bursting behavior from dimples affects nearby jets
Kanokjaruvijit	Air jet array	Dimples – diameters of 1.74-4cm, depths of 0.55-1cm	Experimental	Dimples perform better in strong crossflow
Trabold	Air jet array	Ribs normal to outflow direction – height of 0.813mm	Experimental	Reduction in upstream Nusselt number due to ribs
El-Sheikh	Air jet, single and array	Pin fins – diameter of 1.6mm, heights of 12.7-25.4mm	Experimental	Changing short fins to tall fins yielded minimal thermal improvement
Hansen	Single air jet	Pin, pyramidal, and annular fins – varied by type; widths of 1.59-3.18mm, heights of 1.59-6.35mm	Experimental	Nusselt numbers increased by pyramidal and short square fins
King	Single air jet	Cone under the jet – dimensions not specified; aspect ratios of 0.5-2	Numerical (v^2f model)	Local heat flux increased by 30% near the cone, circulation at cone base inhibited performance
Govindaraju	Water jet array	Various pin fins and/or cones under jets – varied base designs, heights of 4.2-4.7mm	Experimental and numerical (Laminar or k-ε model)	Surface topology optimization provided a 9.3% performance improvement with a 1.7% increase in area
Gao	Water microjet array	Trapezoidal fins – height of 400µm, width of 200µm between the parallel sides	Numerical (k-ε model)	Making the fin height equal the nozzle-to-surface distance has little effect on stagnation

Cui	Water jet array	Pin fins – height of 1.5mm, widths of 0.25-0.5mm	Numerical (Re-Normalisation Group k-ε model)	Reducing the form factor of the fins on the hotspots improved performance
Celik	Single air jet	Dimples away from the jet – diameter and depth of 0.5mm	Experimental	Dimples disrupted the thermal boundary layer, increasing the Nusselt number away from the jet
Madhavan	Air jet array	High-porosity metal foam – thickness of 3mm, fiber diameter of 233μm	Experimental	Increased heat dissipation achieved at expense of increased pressure losses
Radmard	Water microjet array	Pin fins – height of 1-5mm, width of 0.4mm	Numerical (k-ε model)	Additive manufacturing was shown to be capable of creating the fin structure
Waye	WEG jet array	Rib fins – height not specified, width of 100μm	Experimental	Impingement on the finned surface improved thermal performance by 17% at a reduced weight when compared to the baseline
Moreno	Single water jet, free and submerged	Rib fins, two porous coatings – height of 725μm, width of 67μm	Experimental	The average Nusselt number increased by 130% for a coating under a free jet and 100% for the fins under a submerged jet

2.4 Past Efforts in Group

The present research effort is the third iteration of research into jet impingement by this group. First, Maddox et al. experimentally and numerically investigated a grid array of impinging water jets for use in cooling or vehicular power electronics [53]. To enable detailed analysis of a variety of jet geometries, a system was fabricated that could take 36 unique heat flux and surface temperature measurements across the surface. This was accomplished by enabling translation of the jet array across the heated surface to nine locations, where four measurements would be taken for each location. As a result, experimental visualization of surface contours on the impingement surface was enabled; and example set of these contours is shown in Figure 2-5.

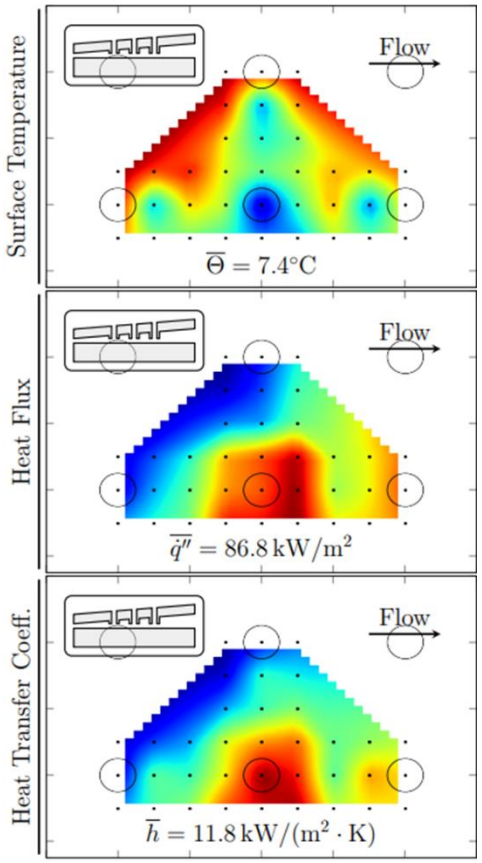

Figure 2-5: Example set of experimental contours generated by the system created by a research predecessor

Using this system, many parameters, including jet spacing, jet height, confining wall angle, and flow rate were examined. In all cases, deionized water was used as the working fluid. The results indicated that a confining wall angle was an effective spent fluid management strategy. By angling the wall upward in the direction of outflow, space was available to the spent fluid to bypass downstream jets without impacting their performance. Using this angled wall, a dimensionless jet spacing of four jet diameters was found to perform best in most cases, while a spacing of six performed better under a flat confining wall.

Henry et al. and Reid et al. took those findings and analyzed the use of staggered array designs and WEG as the working fluid [54, 55]. These staggered array designs are depicted in Figure 2-6.

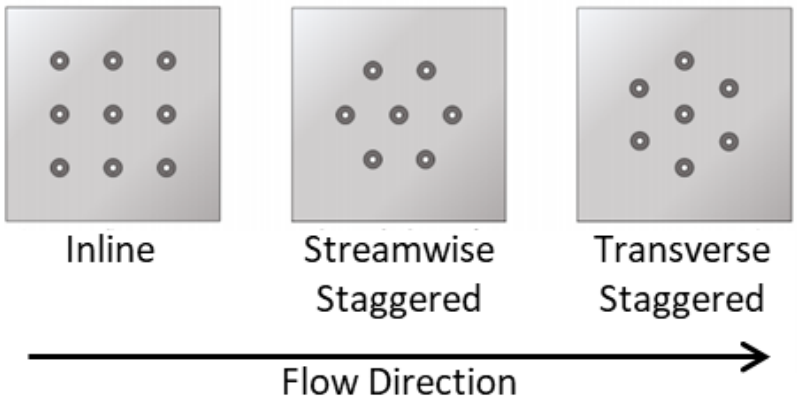

Figure 2-6: Array designs investigated by research predecessors

Comparing equivalent cases with each pattern showed that the inline array performed best, providing both the highest and most consistent heat transfer coefficients. The transverse staggered array magnified the detrimental crossflow effects, as two upstream nozzles would affect each nozzle downstream, as opposed to only one nozzle in the inline and streamwise staggered arrays; this resulted in the transverse staggered array having lower heat transfer coefficients than the others. While the streamwise staggered array did not suffer from this problem and attained comparable heat transfer coefficients to the inline array, the heat transfer was highly focused and poorly spread. From this, it was concluded that the inline array pattern performed best out of these three. Further investigation into the use of a WEG mixture with the same inline array and water in staggered arrays was completed. This was to investigate the effects of mixing antifreeze with water, as in the case of radiator flow loops currently present in commercial vehicles. The differing properties of the WEG mixture resulted in lower heat transfer coefficients than for deionized water and it was concluded that lower jet spacings were more practical for this fluid.

The present effort uses these past findings as a starting point to examine the use of mesoscale surface modifications to promote desirable jet interactions and manage spent fluid. These will be used in conjunction with the angled confining wall extensively examined in past work for a flat surface. By engineering the modifications to promote desired flow mechanics, improvements in thermal performance can be achieved without the detrimental effects observed in historical research.

Chapter 3: Methodology

3.1 Present Effort

Based on the results of the research predecessors, certain nozzle array parameters will be held constant in this effort. All cases utilize a three-by-three, in-line array of deionized water jets with a jet diameter of 3.18mm. Nozzles are spaced four jet diameters apart and the distance between the nozzle outlet and impingement surface is two jet diameters. The fluid will impinge on a surface with dimensions of 76.2-by-76.2mm, as is the case for past experimental cases. These parameters are displayed in Figure 3-1.

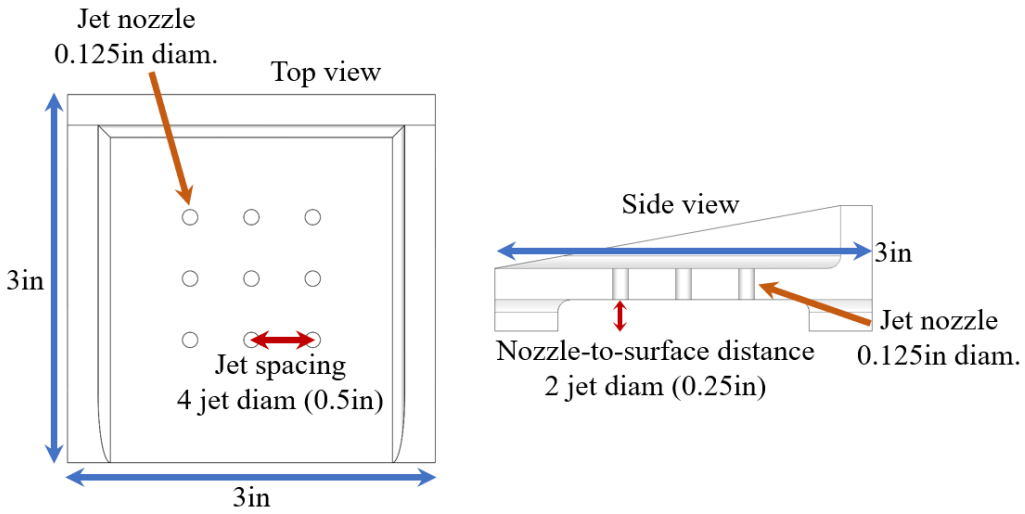

Figure 3-1: Constant jet array parameters for the present research effort

The present research effort investigates the use of engineered mesoscale impingement surface modifications with primary intent to promote desired flow characteristics. Four modifications were investigated, as shown in Figure 3-2 below. All modifications were either triangular ribs or cones, all with bases of one jet diameter and varied heights of one-half and one jet diameter. First, cone pin fins were placed under each jet with the intent to (a) promote equal deflection of the working fluid in all directions, avoiding preferential motion in one direction and (b) increase the surface area in the stagnation region, where heat transfer is most efficient. Henceforth, these cones under the jets will be referred to as jet cones. Next, triangular ribs were independently applied between each set of jet both parallel and normal to the outflow direction, respectively referred to as streamwise and transverse ribs. These were designed to promote deflection of spent fluid from the impingement surface and increase heat transfer from areas not

under the nozzles. Finally, based on previous results, it was decided to investigate cone modifications between jets in the outflow, or streamwise, direction. The goal of these was to shield downstream jets from crossflow effects, particularly under a flat confining wall.

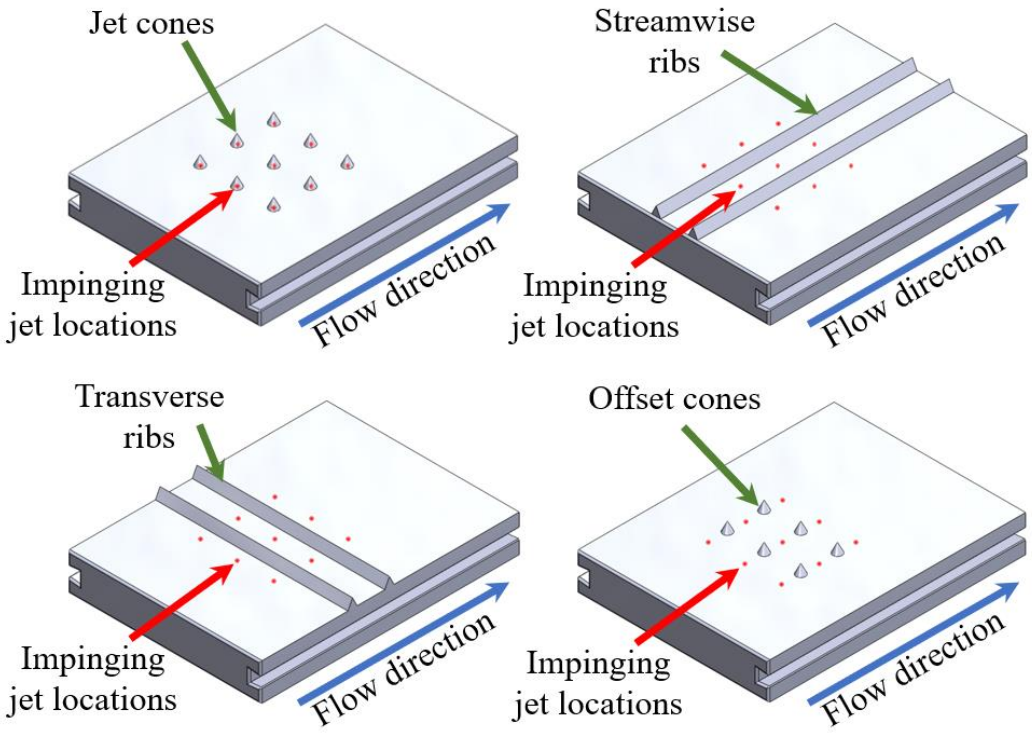

Figure 3-2: Impingement surface modifications under investigation

Each of these modifications have been examined both under a flat confining wall and an angled confining wall of 7.5°, as shown in Figure 3-3. The angled wall is designed to allow spent fluid to bypass downstream jets without impacting their performance. This spent fluid management method is relatively simple, requiring slightly more space to implement, as opposed to fluid extraction, which would complicate the system with an intricate nozzle plate design and tubes for extraction.

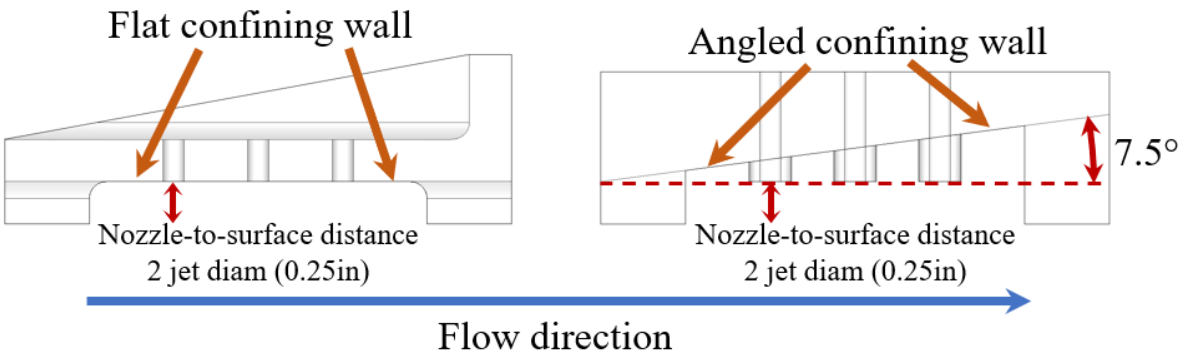

Figure 3-3: Flat (left) and angled (right) confining walls under investigation

All geometries have been examined both experimentally using particle image velocimetry (PIV) flow visualization and numerically using ANSYS Fluent. Through both methods, velocity fields in two areas of interest will be visualized, while the numerical model will also allow thermal effects to be examined. To examine the effects of the modifications and confining wall angle on the flow mechanics, velocity vector fields in two regions will be gathered with each method, as shown in Figure 3-4. The first location slices through the central row of jets, in what will be referred to as the jet plane. The other plane slices between rows of jets, termed the fountain plane.

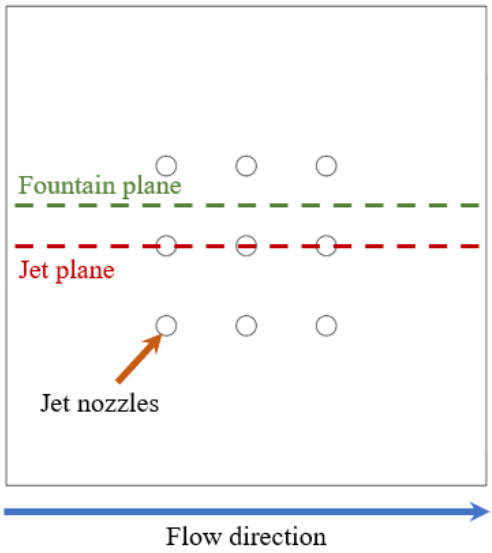

Figure 3-4: Regions of interest for flow mechanics investigated with both PIV and numerical modelling

Finally, all numerical cases were examined at jet Reynolds numbers of 5600, 8400, 11200, and 14000, as defined in Equation 3.1.

$$Re_j = \frac{\rho \bar{u}_j D_j}{\mu} \tag{3.1}$$

Preliminary testing, numerical modelling, and literature showed that fluid mechanics varied little with flow rate [36]. While the magnitude of the fluid velocity changed, the location and size of flow behaviors varied little. This trend is displayed for both the numerical and PIV flow fields in Appendix E. Since the PIV experiments only examined fluid motion, PIV results were only gathered at a volumetric flow rate of 2GPM, corresponding to a jet Reynolds number of 5600.

3.2 Particle Image Velocimetry (PIV) Flow Visualization

3.2.1 PIV Background

PIV flow visualization is an experimental method for generating vector fields for fluids in motion. Figure 3-5 below displays an example of such a system in operation. The fluid in motion is seeded with small particles. A laser sheet shines through the fluid as it does so, light is reflected off the particles. In the same instant, a synchronized camera facing normal to the laser sheet takes a snapshot, capturing only reflected laser light. Using two laser heads, two such snapshots are captured in rapid succession. Comparing these two images allows for local flow velocities to be calculated.

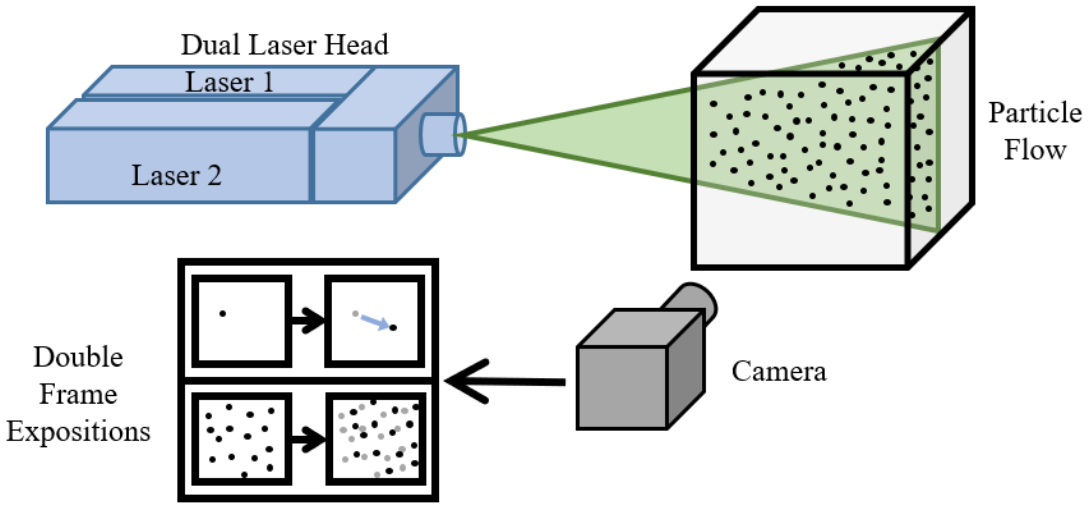

Figure 3-5: Example PIV system

The laser used for these experiments was a TSI YAG200-15-QT L laser sheet system. The fluid, deionized water, was seeded with small, glass spheres with a mean diameter of 55µm. For presented PIV contours, particle movement within interrogation windows approximately of size 0.5-by-0.5mm are examined; in other words, vectors in the velocity fields are spaced approximately 0.5mm apart. Each vector was calculated using cross-correlation, where the interrogation windows are stationary and do not follow the particles. As the flow was turbulent in all cases, ensemble correlation was utilized to find the steady-in-the-mean solution. This was accomplished by taking thirty pairs of snapshots and averaging the results to find the resulting vector fields. Finally, the time gap between snapshots was set as 80ms for the jet plane and 120ms for the fountain plane. The jet flows were much faster than the surrounding flows and required a smaller time gap, whereas the velocities in the fountain plane were slower and a larger gap could better capture the trends.

3.2.2 PIV Flow Loop

A flow loop schematic is displayed in Figure 3-6. Flow was generated by an Iwaki magnetic pump controlled by a Lenze SMVector variable frequency drive. The volumetric flow rate was measured using an Omega FTB4700 turbine flow meter, the output of which was measured by an Arduino Uno and displayed on a computer. Air bubbles were often entrained in the fluid when departing from the pump, so a vessel was placed between the pump and impingement chamber to

prevent these bubbles from entering the chamber, and thereby affecting the fluid motion reflecting laser light into the camera. The separator was a small vessel, 3D printed using resin, with the inlet at the top and the outlet at the bottom; the bubbles would rise in the separator, resulting in only water flow through the outlet. This water would then enter the impingement chamber, where it would be forced through the jet nozzles, impinge on the modified surfaces, then be directed to the outlet. A fluid reservoir was placed after the chamber to expose the system to atmospheric pressure. The fluid temperature was not controlled and remained near the ambient temperature.

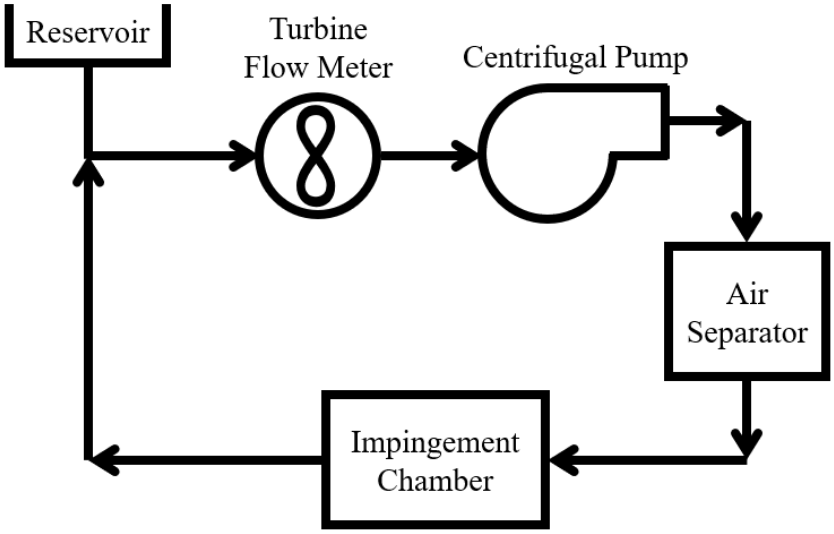

Figure 3-6: PIV flow loop

Figure 3-6 below displays the impingement chamber and its key components. Water first enters through the top and passes through a flow diffuser. The diffuser is a 3D printed component designed to spread the inlet flow throughout the chamber, avoiding any preferential flow through the nozzles if the inlet flow was unimpeded. The water is then directed through a modular nozzle array designed to enable creation of any combination of jet arrays or impingement surface under investigation. A removable wall allows the array to be changed between runs. The water is directed through the outlet on the backside of the chamber. Optical windows made of borosilicate glass are assembled on the front and side of the box for the laser and camera. Finally, a drain was added to the back to allow the fluid to be removed before disassembly.

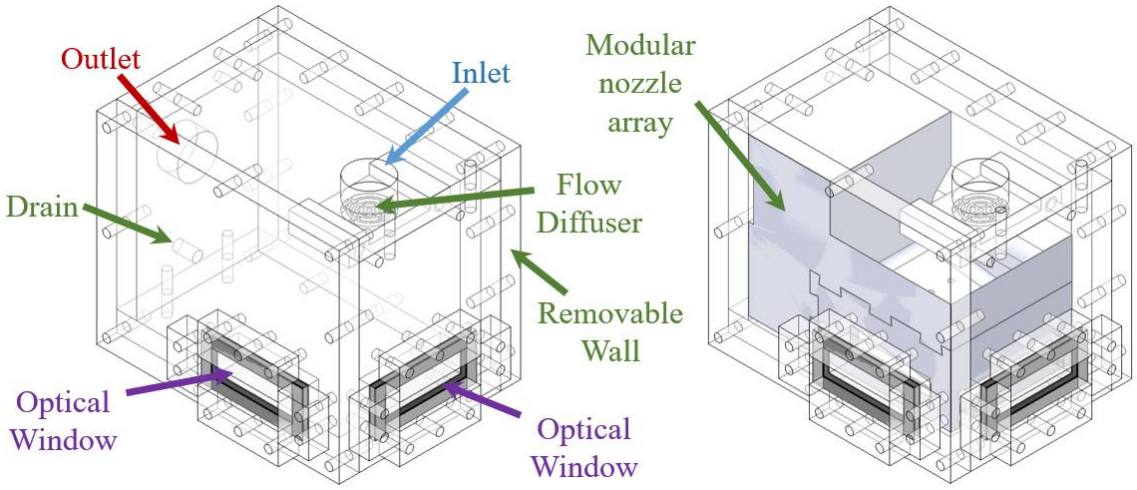

Figure 3-7: Empty impingement chamber (left) and assembled impingement chamber (right) with key features identified

Due to the many geometry combinations to be analyzed, a modular design was created. Dovetail grooves were used to combine different surfaces and nozzle arrays to a universal frame, as shown in Figure 3-8.

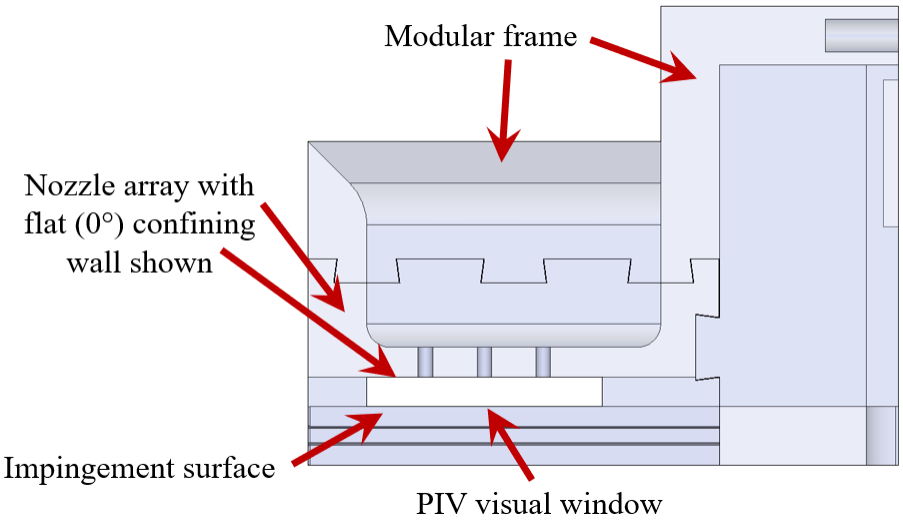

Figure 3-8: Modular nozzle array design

The frame and nozzle array were 3D printed with ABS plastic. The nozzles were reamed to an inner diameter of 3.18mm then smoothed using acetone. The upper confining wall was also smoothed using acetone. The impingement surfaces were 3D printed using a semi-transparent resin, as shown below in Figure 3-9.

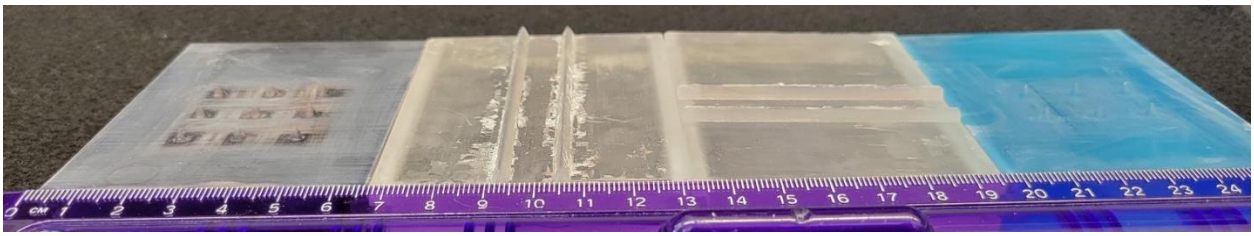

Figure 3-9: Modified impingement surfaces for use with the PIV system from left to right showing the jet cones, streamwise ribs, transverse ribs, and offset cones

The impingement surfaces were smoothed using a combination of sanding and acetone. The pictured assembly displays a flat confining wall, which frames the region the PIV system was able to analyze. This visual region was the same for the angled wall, as the laser could not illuminate above the lowest point in the nozzle array. Side views of the impingement chamber with and without the modular nozzle array inserted inside are shown in Figure 3-10.

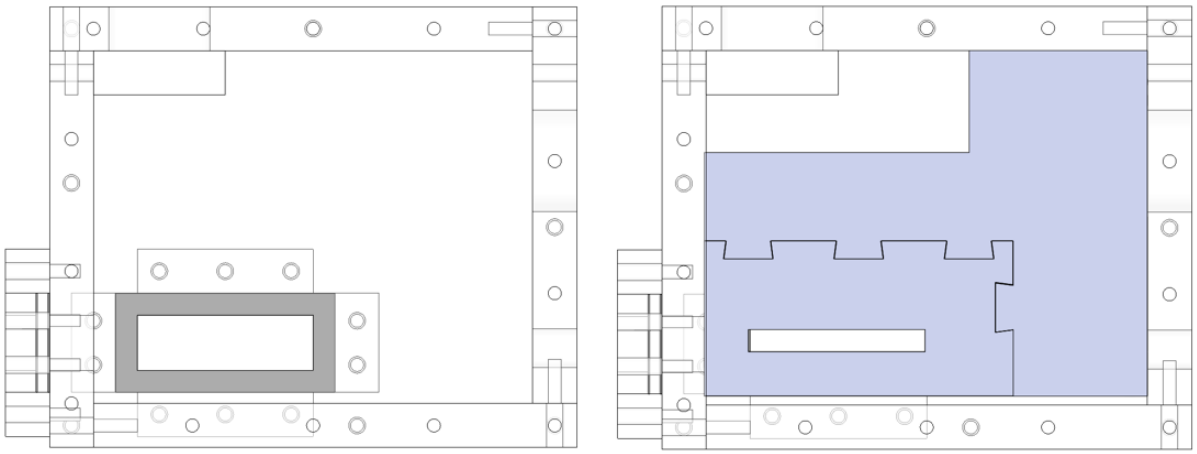

Figure 3-10: Side views of the impingement chamber without (left) and with (right) the modular nozzle assembly in place

3.2.3 PIV Process

Data collection began by assembling the modular impingement array with the desired combination of confining wall angle and surface. To reduce the amount of air in the impingement chamber, the assembly was inserted and affixed in the box while the box was filled with deionized water. The box was then sealed and the rest of the system was filled with water. Air bubbles trapped in the tubing and chamber were maneuvered out of the system and into the surroundings, minimizing the air in the system prior to startup. The box was then placed on a 3D printed stand designed to hold it at the height necessary to keep the optical windows level with the laser head.

As air trapped in the pump and various other locations in the system could not be removed prior or during assembly, a debubbling process would be completed prior to initiation of the PIV system. The top of the air separator was connected to a pipe with a ball valve at its end. This ball valve was placed in the reservoir located after the impingement chamber and opened. The pump was then activated, starting flow through the system. Water flow from the pump would be entrained with air bubbles. This mixture would reach the air separator and be separated. One path would travel up, through the tube and ball valve to the reservoir, while to other would travel down, through the impingement chamber. Buoyancy drove the air bubbles up, through the former path and into the reservoir, where they were released to the atmosphere and removed from the system, while only water would be driven through the impingement chamber. After some time, air bubbles would no longer depart from the pump. The ball valve was then shut, forcing all water flow from the pump through the impingement chamber.

Once bubble flow was eliminated, the laser head and impingement chamber were surrounded by a shroud of felt and the PIV system was activated. The synchronizer, camera, computer, and power supply and coolant to the laser head were activated. On the computer, the software Insight 4G was used to control the laser, synchronizer, and camera. As the laser head and impingement chamber were free-standing, alignment was necessary such that the laser sheet would illuminate parallel to the outflow direction, not at an angle. As the impingement chamber was manufactured with polycarbonate sheets, its walls were reflective. While wearing safety glasses designed to reduce the laser's intensity to the wearer, the laser sheet was activated and shone directly at the polycarbonate surface of the chamber. A paper sheet was held just above the laser head and the shroud was lifted just enough that the laser light reflected off the chamber's surface could be seen on the paper. If the laser was not hitting the chamber's wall normally, the reflection would be deflected to the side of the laser head. The laser was then deactivated and the chamber was rotated depending on the location of the laser reflection relative to the laser head. The laser would then be reactivated and this process iterated until the laser light was reflected back to the head. At this point, the laser and impingement chamber were rotationally aligned. The reflective surface of the impingement chamber were then covered with cardboard and the safety glasses were changed to another set designed for near-complete eye protection.

At this point, the fluid needed to be seeded. Seeding particles were introduced to the system via the reservoir located after the impingement chamber. These were mixed into the system by opening the ball valve and allowing flow from the top side of the air separator to the reservoir, similar to the debubbling process. To determine if the fluid was sufficiently seeded, images needed to be taken from the camera while illuminated from the laser. The system would be set to continuously capture images while the laser was activated, showing the images on screen. During this time, the camera was focused on the light reflected from the seeding particles and the aperture was adjusted until they were clearly visible. Seeding particles would then be added until they uniformly filled the space in the impingement region without being so dense that the laser light was overly dimmed downstream.

While the laser and chamber were rotationally aligned and the fluid was seeded properly, it was unlikely that the laser was illuminating the region of interest. The first region to be captured would be the jet plane, as the impinging jet flow was a very clear and reliable behavior to observe. If needed, the time gap between synchronized image pairs was set to 80ms. A set of five image pairs was then captured where the laser head initially rested, allowing a flow field to be generated by the processing portion of the software. The resulting flow field was observed, but a single case would not readily reveal in which direction or how much the laser head and impingement chamber were misaligned. Using translation knobs on the laser head, the laser was moved to illuminate a new region in the chamber. A set of images were then captured and processed at this new location. Based on the changes in the resulting flow field between the two locations, it could usually be determined in which direction the laser head needed to be moved to fall within the jet plane. The laser head location would then be adjusted by trial and iteration until it illuminated the region in which the jets were clearest and widest. Adjustments to the camera's focusing and aperture were done as needed if the laser head and impingement chamber were initially far out of alignment.

Upon completion of the alignment process, the pump was adjusted to the desired flow rate of 2GPM and a set of thirty pairs of images were captured for analysis. These were then processed within the software. The processing stage required five inputs: spatial calibration, a processing mask, a pre-processor, a processor, and a post-processor. The spatial calibration was completed by measurement. Within an image, the vertical distance illuminated by the laser sheet was measured by clicking the top and bottom of the illuminated region. The software then measured this distance

in pixels. This pixel value was then specified to be 6.35mm in length, which is the nozzle-to-surface distance of two jet diameters used for all cases. Using these values, the software would automatically convert distance measurements to mm and velocity measurements to m/s. The processing mask specifies the region in each image that the PIV analysis is to be completed. As the camera would capture blank spaces on the periphery of each image, a rectangle would be manually placed to specify the region of each image in which particles were visible. Finally, the pre-processor, processor, and post-processor were prefabricated within the software and were not adjusted between any sets of captured data. The purpose of all these components was to compare each pair of images, find spots of bright light representing the seeding particles, determine the direction and magnitude of movement of the particles in each region between images in a pair, exclude any bad measurements that resulted from few particles being present in a given location for an image pair, and output the final averaged result for the flow field. If this process resulted in a clear flow field with visible trends, the resulting flow field was exported to a text file for later analysis within Matlab. If there were issues with the quality of the results, adjustments to the flow rate, seeding particles, laser, or camera were completed until the results were legible.

Once data in the jet region was gathered, the laser head was translated to illuminate the region between sets of jets. A full rotation of the translation knob corresponded to a translation of 1mm, so the knob was rotated 6.35 times to rest between jet rows. The time gap between image pairs was set to 120ms and the data collection process was completed once again at the new location. Upon collection of data at both locations, the PIV system was deactivated, the flow loop was deactivated, the system was disassembled, and seeding particles were cleaned off the impingement chamber and nozzle array.

3.3 Numerical Modelling

In parallel with experimental efforts, numerical modelling of each case was completed using ANSYS Fluent 2021 R1.

3.3.1 Geometry

The model geometry is displayed in Figure 3-11. Water enters through the top face of the blue region, impinges on the copper surface, and departs out the back. Heat is generated in a rectangular region embedded in the copper block at a rate of $6.027*10^6$ W/m^3. This corresponds to 83.33 W for the numerical geometry and 500 W for a set of nine jets, as examined in the group's past experimental studies. This is a simplification of the experimental geometry used in those studies, replacing the eight cylindrical cartridge heaters used to apply heat. The heat generation is embedded approximately the same distance under the impingement surface such that no difference is observed at the impingement surface due to the differing heat generation geometry between the model and the cylindrical cartridge heaters the geometry is based on. The model used symmetry boundary conditions on either side, reducing the model to a half-row of three jets. While half of the full experimental geometry would have provided a more accurate comparison, this would have drastically increased the number of elements, increasing the required computational time and resources beyond those available.

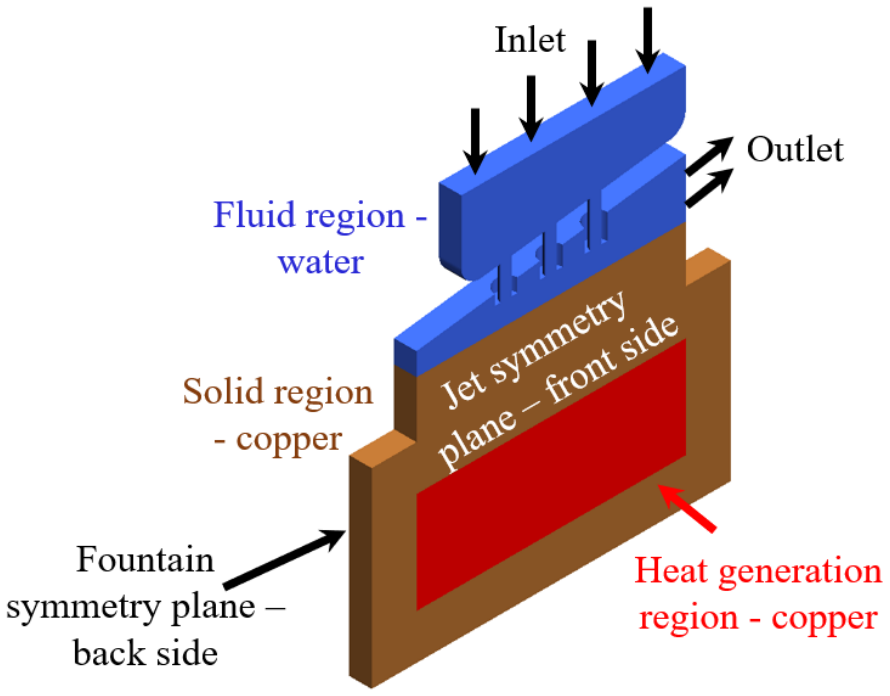

Figure 3-11: Numerical model geometry

The bodies in the numerical geometry were designed to mimic that of the experimental design used in past experimental work in the group and in the PIV experiments, as displayed in

Figure 3-12. The transparent grey components are the modular jet array used in the PIV experiments. The solid blue region is the fluid body of the numerical model.

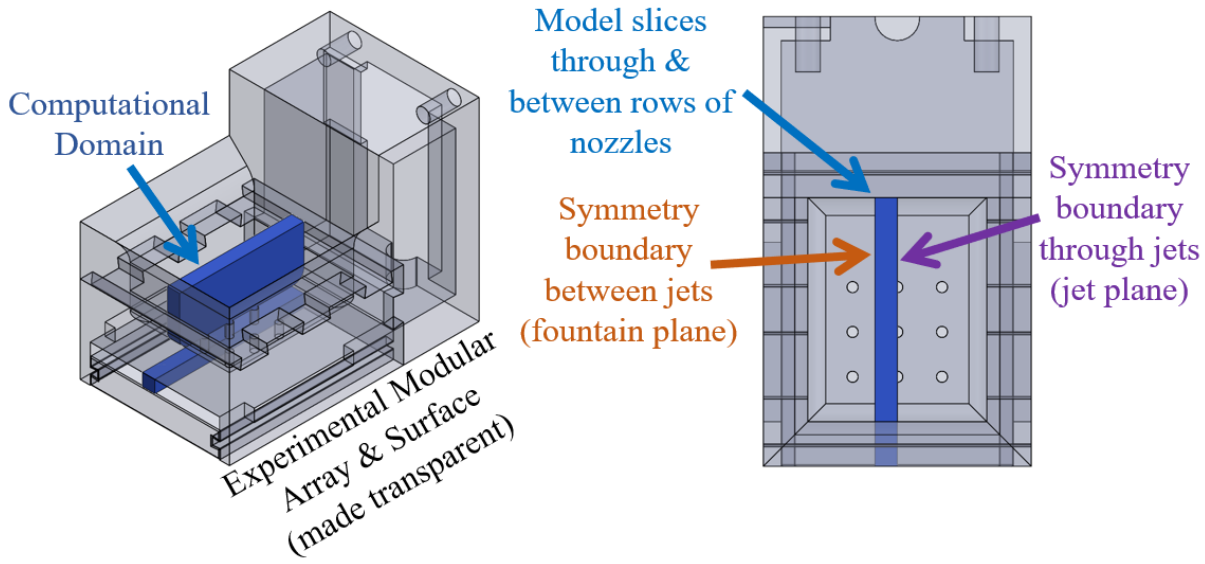

Figure 3-12: Comparison of the numerical model geometry (blue) and PIV modular nozzle array (transparent grey)

3.3.2 Meshing, Grid Independence, and Uncertainty Analysis

Meshing was completed using the workflow provided in ANSYS Fluent (with Fluent meshing). Meshing was completed using polyhedral elements, as shown in Figure 3-13. Element sizes were imposed on the walls of the fluid region, the fluid-surface interface of the impingement surface, and the bodies of the solid regions. Boundary inflation was applied to the walls in the fluid region to resolve the boundary layers.

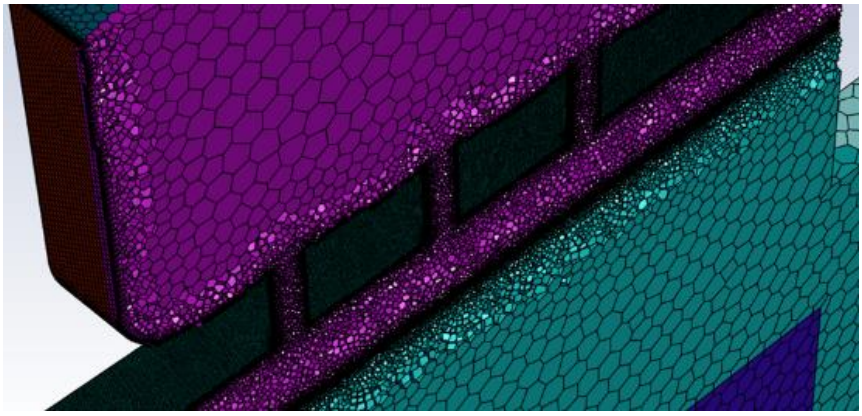

Figure 3-13: Sample mesh using polyhedral elements

Grid independence was examined using an angled confining wall without surface modifications. All element sizes on the walls were decreased to 66.7% and increased to 150% of the values intended for the study. Comparison of these cases yielded highly similar results, suggesting grid independence was achieved. A sample set of data plots in the jet plane is displayed in Figure 3-14. Averaging the heat transfer coefficient across the surface yielded values of 11.56, 11.48, and 11.50kW/m^{2}K for the larger element grid, middle element grid, and smaller element grid, respectively.

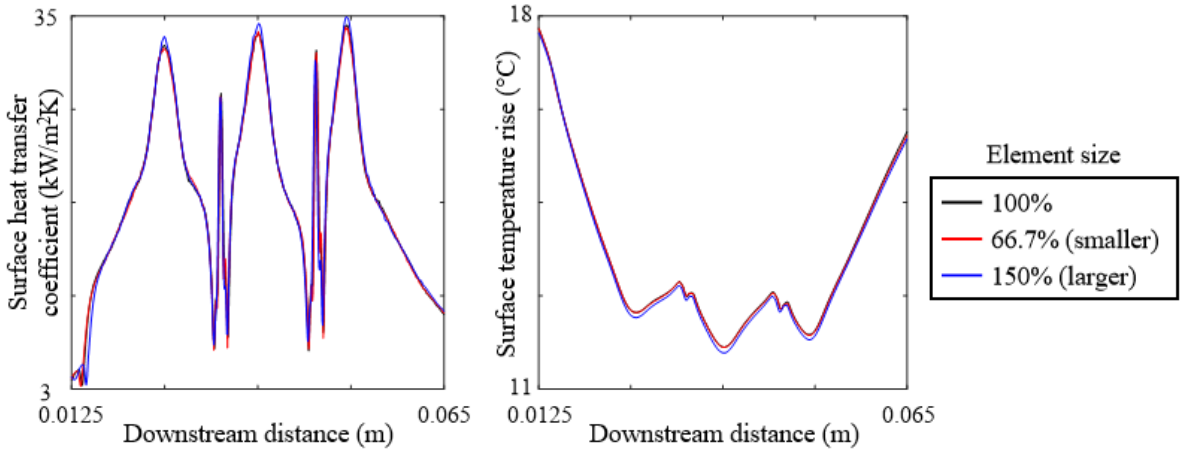

Figure 3-14: Grid independence results for the numerical model in the jet plane

Uncertainty analysis was also completed using Roache's grid convergence index, the details of which can be found in Appendix D [56]. This approach was applied to various local and average values calculated from the same case as the grid independence study. Applying this approach to local values typically yielded uncertainties of less than 30%, with increased uncertainties occurring in locations of flow separation from the surface. Calculating the grid convergence index for the average surface heat transfer coefficient yielded a value of 0.34%. This indicates that the numerical model's results are sufficiently validated.

3.3.3 Turbulence Modelling

All cases examined in this effort were in the turbulent regime. As such, a turbulence model needed to be selected. Due to the scale of the model geometry and quantity of cases analyzed, transient models which provide the best results, including direct numerical simulation (DNS) and large eddy simulation (LES), were inapplicable due to requiring very small elements and long

computational time and resources. Therefore, a Reynolds-averaged Navier-Stokes (RANS) model was to be selected. These models provide a time-averaged result, like the results from the PIV experiments, which are far less computationally expensive or time consuming. Table 2-1 below displays a comparison of common turbulence models used in jet impingement modelling, as examined by Zuckerman and Lior [57].

Table 3-1: A comparison of turbulence models used for jet impingement cases [57]

Turbulence Model	Computational cost (time required)	Impingement Nusselt number prediction accuracy	Ability to predict secondary peak
k-ε	★★★★ Low cost	★ Poor: *Nu* error of 15-60%	★ Poor
k-ω	★★★★ Low-moderate	★★ Poor-fair: anticipate *Nu* errors of at least 10-30%	★★ Fair: may have incorrect location or magnitude
Realizable *k-ε* and other *k-ε* variations	★★★★ Low	★★ Poor-fair: expect *Nu* errors of at least 15-30%	★★ Poor-fair: may have incorrect location or magnitude
Algebraic stress model	★★★★ Low	★★ Poor-fair: anticipate *Nu* errors of at least 10-30%	★ Poor
Reynolds stress model	★★ Moderate-high	★ Poor: anticipate *Nu* errors of 25-100%	★★ Fair: may have incorrect location or magnitude
SST, hybrid method	★★★ Low -moderate	★★★ Good: typical *Nu* errors of 20-40%	★★ Fair
$\boldsymbol{v^2 f}$	★★★ Moderate	★★★★ Excellent: anticipate *Nu* errors of 2-30%	★★★★ Excellent
DNS/LES transient models	★ Extremely high	★★★★ Good-excellent	★★★★ Good-excellent

Many of these were used by the authors of reviewed research efforts in their numerical models. Of particular interest are the *k-ε* and *k-ω* models, as these are frequently used as building blocks for other, more complicated models. The *k-ε* model performs well in the free-stream, away from wall effects, but introduces error when viscous effects are significant. Conversely, the *k-ω* model performs well near walls and when viscous effects dominate but does a poor job modelling free-stream behaviors. In jet impingement modelling, both free-stream mechanics and viscous

effects are significant in certain regions, in particular the potential core and stagnation regions, respectively. As a result, neither of these models are particularly accurate models of impingement behaviors.

To alleviate this, shear stress transport (SST) models are often used when neither the *k-ε* nor *k-ω* models are ideal. These SST models use a blending function to weigh the *k-ε* nor *k-ω* models depending on the proximity to a wall; near a wall, the blending function allows the *k-ω* model to dominate, while it allows the *k-ε* model to dominate in the free-stream [58]. The most common SST models are the SST *k-ω* model and the Transition SST model. The SST *k-ω* model is a simple weighting of the *k-ε* and *k-ω* models as previously described. The Transition SST model, however, enables an intermittency term, which specifies the amount of time the flow in an element behaves as laminar or turbulent. This adds complexity to the model, but more accurately models transitional flow and the viscous sub-layer. As this model provides reasonable accuracy for free-stream flow, viscous effects, and transitional behaviors, it was selected as the turbulence model for this research effort. Also of note was the $v^2\boldsymbol{f}$ model, which is shown in Table 3-1 to model jet impingement better than SST models at slightly higher computational cost. This model was removed from ANSYS Fluent slightly prior to the start of numerical calculations in this effort and was not available as a result.

The Transition SST model begins with the mass, momentum, and energy conservation equations, respectively shown in Equations 3.2-3.4 below.

$$\frac{\partial \rho}{\partial t} + \nabla \cdot (\rho \vec{u}) = S_m \tag{3.2}$$

$$\frac{\partial}{\partial t}(\rho \vec{u}) + \nabla \cdot (\rho \vec{u}\vec{u}) = -\nabla p + \nabla \cdot (\bar{\bar{\tau}}) + \rho \vec{g} + \vec{F} \tag{3.3}$$

$$\frac{\partial}{\partial t}(\rho E) + \nabla \cdot [\vec{u}(\rho E + p)] = \nabla \cdot \left[k_{eff} \nabla T - \sum_j h_j \overrightarrow{J_J} + \left(\overline{\overline{\tau_{eff}}} \cdot \vec{u} \right) \right] + S_h \tag{3.4}$$

The Transition SST model is a modified version of the SST *k-ω* model [58]. Hence, it begins with the transport equation for the turbulent kinetic energy, shown in Equation 3.5.

$$\frac{\partial}{\partial t}(\rho K) + \frac{\partial}{\partial x_i}(\rho K u_i) = \frac{\partial}{\partial x_i}\left(\Gamma_K \frac{\partial K}{\partial x_i} \right) + \widetilde{G_K} - Y_K + S_K \tag{3.5}$$

The remaining equation for the *k-ω* model is the specific dissipation rate of kinetic energy transport equation, shown in Equation 3.6.

$$\frac{\partial}{\partial t}(\rho\omega) + \frac{\partial}{\partial x_i}(\rho\omega u_i) = \frac{\partial}{\partial x_i}\left(\Gamma_\omega \frac{\partial \omega}{\partial x_i}\right) + G_\omega - Y_\omega + D_\omega + S_\omega \tag{3.6}$$

In these equations, *K* is the turbulent kinetic energy, which scales with the square of the velocity fluctuations created by turbulence, while *ω* is the specific turbulence dissipation rate. The turbulence dissipation rate defines the rate at which the turbulent kinetic energy is transformed into heat. In equations 3.4 and 3.5, the left-hand side defines the rate of transport of each variable into or out of each element by transient effects and fluid motion. Each term in the right-hand side of the equations specify various ways in which these parameters are generated or diffused by certain effects [58]. *Γ* represents the effective diffusivity of each parameter due to viscous effects, while *G* represents generation caused by mean velocity gradients. *Y* is the dissipation of each parameter due to turbulence, while *S* is a user-defined source term, which is not used in this effort.

If only these previous equations were used, then the result for the SST k-ω model would be calculated. The transition SST model adds two additional transport equations to improve the accuracy of the results. The first equation defines the transport of the intermittency term, γ. The intermittency defines both the flow regime of that point and the weighing of the *k-ω* and modified *k-ε* models. The intermittency scales from zero (fully laminar) to one (fully turbulent). Since the flow is fully laminar very close to the walls, where the no-slip condition results in shear stress dominating the flow, a low intermittency value will cause the *k-ω* model to dominate. When the intermittency approaches one, the modified *k-ε* model will be much more heavily weighted. This is completed through the following intermittency transport equation, displayed in Equation 3.7.

$$\frac{\partial}{\partial t}(\rho\gamma) + \frac{\partial}{\partial x_i}(\rho\gamma u_i) = S_{\gamma \mathrm{a}} - S_{\gamma a} + R_{\gamma a} - R_{\gamma b} + \frac{\partial}{\partial x_i}\left[\left(\mu + \frac{\mu_t}{\sigma_\gamma}\right)\frac{\partial \gamma}{\partial x_i}\right] \tag{3.7}$$

The fourth and final transport equation for the transition SST model is the transport equation for the momentum thickness Reynolds number ($\widetilde{Re_{\theta t}}$), displayed in Equation 3.8.

$$\frac{\partial}{\partial t}\left(\rho\widetilde{Re_{\theta t}}\right)+\frac{\partial}{\partial x_i}\left(\rho\widetilde{Re_{\theta t}}u_i\right)=S_{\theta t}+\frac{\partial}{\partial x_i}\left[\sigma_{\theta t}(\mu+\mu_t)\frac{\partial\widetilde{Re_{\theta t}}}{\partial x_i}\right] \tag{3.8}$$

3.4 Summary

In this effort, PIV flow visualization and numerical modelling will be utilized to examine effects of modified surface structures and an angled confining wall on the flow mechanics and thermal characteristic if an impinging water jet array. PIV flow visualization will enable experimental investigation into flow mechanics within the array, while the numerical model will simultaneously provide flow and thermal information. Based on literature and past work completed in this group, the Transition SST model was chosen for use in the numerical modelling.

Chapter 4: Results

4.1 Baseline

Prior to application of the modified surfaces, it is essential that results from a flat, baseline surface are analyzed. These will be used as the primary points of comparison for the modified surface cases. As both the PIV experiments and numerical model provide flow data, discussion would be repetitive if these methods were discussed separately. Thus, flow mechanics will be discussed with both the PIV and numerical results in conjunction. As the thermal performance of an impinging jet array is inherently tied to the flow, thermal characteristics from the numerical model will be discussed after flow has been analyzed. To elucidate the many geometric variations examined, Table 4-1 below summarizes the variables that will be examined in the course of the results.

Table 4-1: Independent variables examined in this effort

Variable	Dimensional value(s) examined	Non-dimensional value(s) examined
Jet diameter	3.18mm	-
Nozzle-to-surface distance	6.35mm	2 jet diameters
Jet spacing	12.7mm	4 jet diameters
Flow rate/ Reynolds number	2GPM	5600
	3GPM	8400
	4GPM	11200
	5GPM	14000
Modification base dimension	3.18mm	1 jet diameter
Modification height	1.59mm	½ jet diameter
	3.18mm	1 jet diameter
Modification type	Cones under jets (jet cones)	
	Ribs aligned with outflow (streamwise ribs)	
	Ribs normal to outflow (transverse ribs)	
	Cones between jets in the outflow direction (offset cones)	
Confining wall angle	Flat (0°)	
	Angled (7.5°)	

4.1.1 Baseline – Flow Mechanics

Figure 4-1 displays flow fields from both the PIV and numerical approaches in the jet plane for a baseline surface under a flat confining wall, with the PIV contour placed above the numerical contour. To aid in legibility, both contours share the same velocity scale, shown at the bottom of

the figure. The arrow lengths are normalized to be uniform; when scaled with length, arrows in locations with low velocity became illegible, so the arrow lengths have been made uniform and only the background contour color indicates the velocity magnitude. This will be the case for all contours displayed in figures. There is no objective method to align the PIV contours with each other or the numerical contours since the location of the camera was not the same each time. As such, PIV contours have simply been aligned as closely as possible to where they appear to match other contours in the same figure.

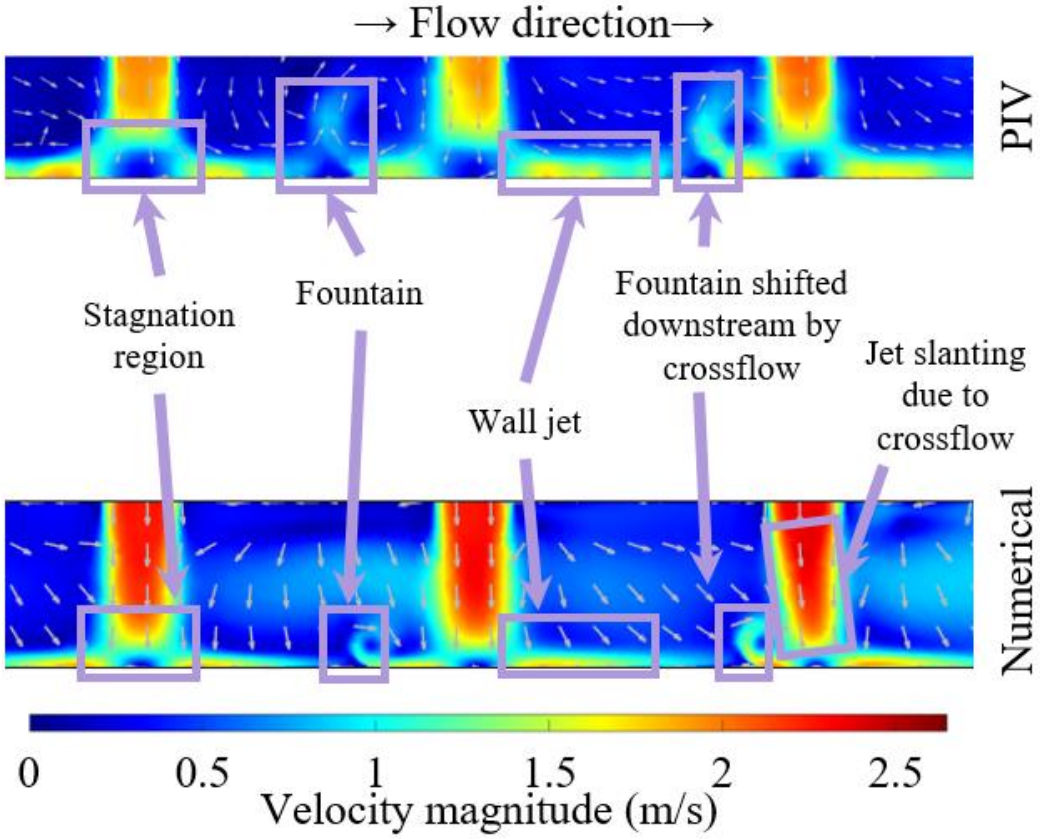

Figure 4-1: Jet plane velocity vector fields and contours for an unmodified surface under a flat confining wall at a jet Reynolds number of 5600

In the jet plane, both the PIV and numerical results display expected flow mechanics. Each of the three jets flow through their respective nozzles. Some shearing is visible as the jet passes through the surrounding water, but this is minimal for this spacing. The jets decelerate as the approach the impingement surface, indicating the stagnation region, where the bulk of heat dissipation will be expected from the surface. The jets are deflected parallel to the surface, creating the wall jet region. Adjacent wall jets interact, deflecting fluid vertically from the surface; this

deflection is limited by the confining wall just above the contours. As a result, spent fluid from the upstream jets must pass by the downstream jets. This results in a downstream shift in the fountain created by the right two jets. Furthermore, in the numerical model, slanting of the downstream jet is visible, indicating that crossflow effects may occur in jet arrays as small as three jets.

In Figure 4-1, crossflow effects are more detrimental in the numerical results. This is most likely caused by differences between the numerical model geometry and the experimental geometry. The physical experiment only used a three-by-three array of jets with excess space to either side. This design was made to mimic the existing experimental setup used in prior research within the group, which was made to accommodate larger arrays than those studied in this effort. In contrast, the numerical model used symmetry to reduce the computational domain, meaning it is modelling an infinite array of jets normal to the plane. As a result, the model predicts that the fountains are heavily impacted by crossflow, with the downstream fountain directly impacting the jet. Meanwhile, crossflow in the PIV experiments has only slightly deflected the right-hand fountain slightly downstream and effects on the jet are minimal.

Visually comparing the contours in Figure 4-1, the PIV results display lower velocities than the numerical results; this will hold true for all flow fields. This is most likely due to imperfect fitting of components allowing some fluid flow around the arrays, not through the nozzles, as well as imperfect spatial calibration. While much effort went into minimizing gaps between the nozzle array and impingement chamber walls, some leakage was inevitable. Since the pump was set to 2GPM for all PIV experiments, the true flow rate through the nozzles was necessarily less than that. However, during initial research stages, it was determined both experimentally and numerically that the flow rate has little effect on qualitative flow behaviors and primarily affects the scale. As such, the PIV results may be considered valuable in regard to wider trends but should not be considered infallible. Regardless of these errors, the experimental and numerical results are largely in agreement regarding these wider trends. Each major difference between the two approaches is readily explainable by errors inherent to experimental measurements and the simplified, idealized numerical geometry.

As each methodological approach was seen to provide reasonable results in the jet plane, the fountain plane will now be analyzed. Figure 4-2 below displays vector fields and velocity contours for the fountain region under a flat confining wall.

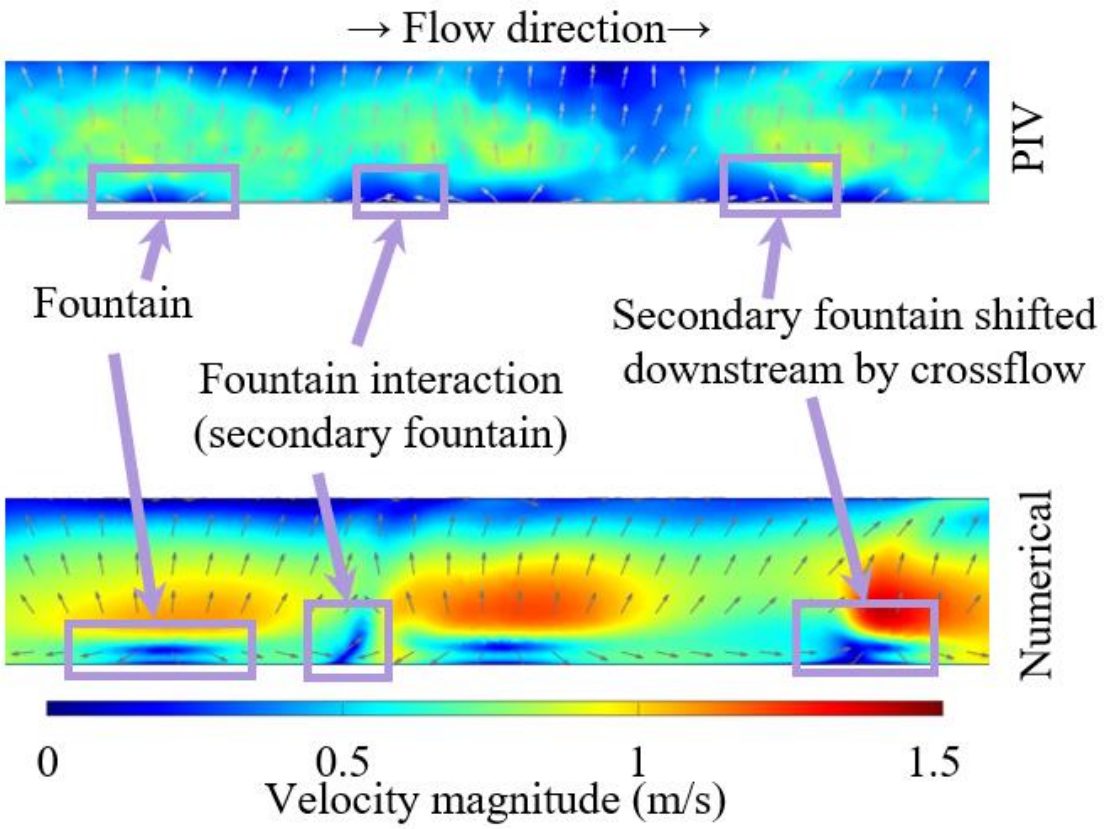

Figure 4-2: Fountain plane velocity vector fields and contours for an unmodified surface under a flat confining wall at a jet Reynolds number of 5600

In the fountain plane, wall jets are interacting normal to the plane, creating fountains that now appear as points of divergence just above the surface. This interaction creates small-scale mixing near the surface visible in the numerical model. This behavior is too small to be observed by the PIV system. The fountains meet and interact, creating a plume of fluid, or a secondary fountain. As these secondary fountains are created by interactions between two fountains, they are highly susceptible to crossflow, especially in the numerical model. Of the fluid that flows through a given jet, only a fraction of it interacts with another jet to create a fountain. This fountain deflects fluid from the surface, leaving an even smaller amount to create a secondary fountain. As a result, crossflow is particularly detrimental to these interactions. While they may be weak, secondary fountains occur at a large distance from the impinging jets; thus, improving surface temperature uniformity necessitates promoting these interactions, even though the magnitude of their thermal performance can be expected to be far less than that of the jets or fountains. As there is a lack of clear trends to visualize the location of these fountains and secondary fountains in these contours,

Figure 4-3 below provides a perspective from above the nozzles to highlight their locations on the surface.

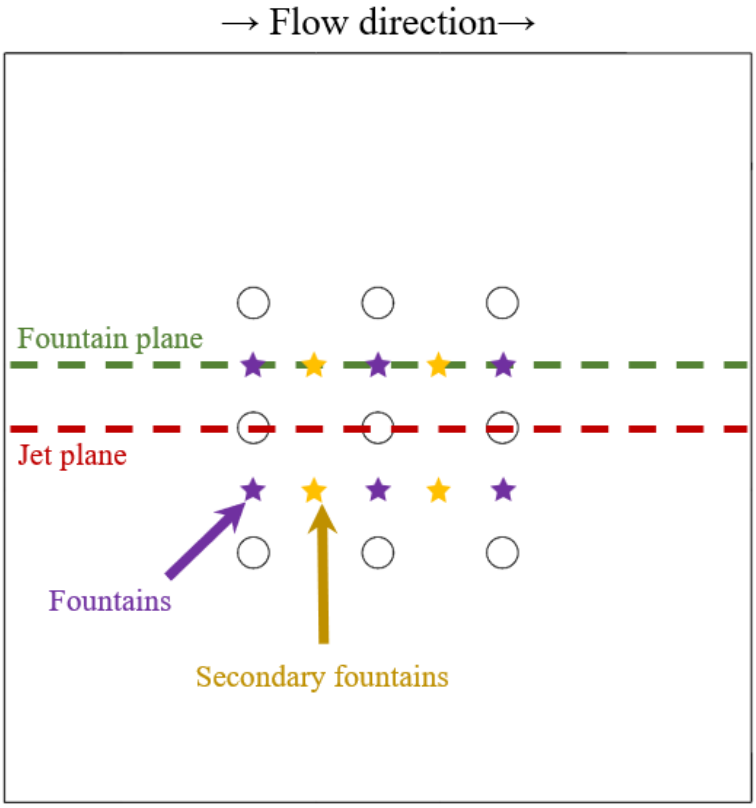

Figure 4-3: Locations of fountains and secondary fountains in the fountain plane viewed from above

A visual comparison of the contours in Figure 4-2 shows that there is far less agreement between the PIV and numerical approaches in the fountain plane. This is attributable to the previously discussed issues in the jet plane, as well as asymmetry in the experimental array. The three-by-three array is symmetric in the jet plane, but highly asymmetric in the fountain plane, as there is only one row of jets to one side and empty space beyond them, which can be seen previously in Figure 3-4 and Figure 4-3. Meanwhile, the numerical geometry models a large array in the transverse direction. As a result, contours will continue to show much less agreement between the PIV experiments and numerical model in the fountain plane than the jet plane.

Velocity vector fields for the jet plane under a confining wall angled at 7.5° are shown in Figure 4-4. While there is space for fluid above the jet inlets, the PIV system could not illuminate that region, as the laser sheet was blocked by the lowest part of the array. As a result, the visual window is the same as the flat wall. While data is available for the entirety of the numerical model,

it has been cropped to display the same region as the PIV visual window for ease of comparison. No noteworthy effects were seen outside of this range, so this does not affect discussion.

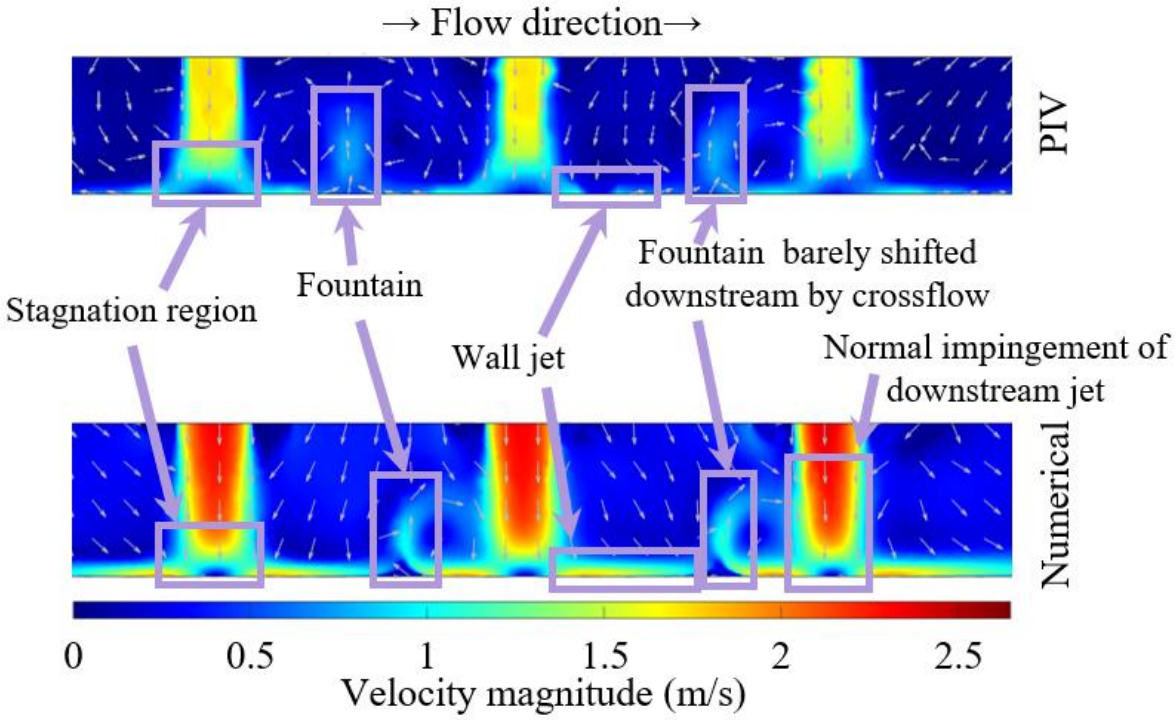

Figure 4-4: Jet plane velocity vector fields and contours for an unmodified surface under an angled confining wall at a jet Reynolds number of 5600

Each of the common flow features seen under the flat wall, including the stagnation region, wall jet, and fountain interaction are still prominent here, under the angled wall. Crossflow is visually less impactful under the angled wall. As there is space above the nozzle outlet, spent fluid is able to flow towards the outlet with less impact on downstream jets. As a result, fountain interactions are much more pronounced, and little-to-no deflection of the downstream fountain occurs. Furthermore, the furthest downstream jet is able to impinge normal to the surface in the numerical model, indicating effective spent fluid management.

Finally, velocity vector fields and contours in the fountain plane under an angled confining wall are shown in Figure 4-5.

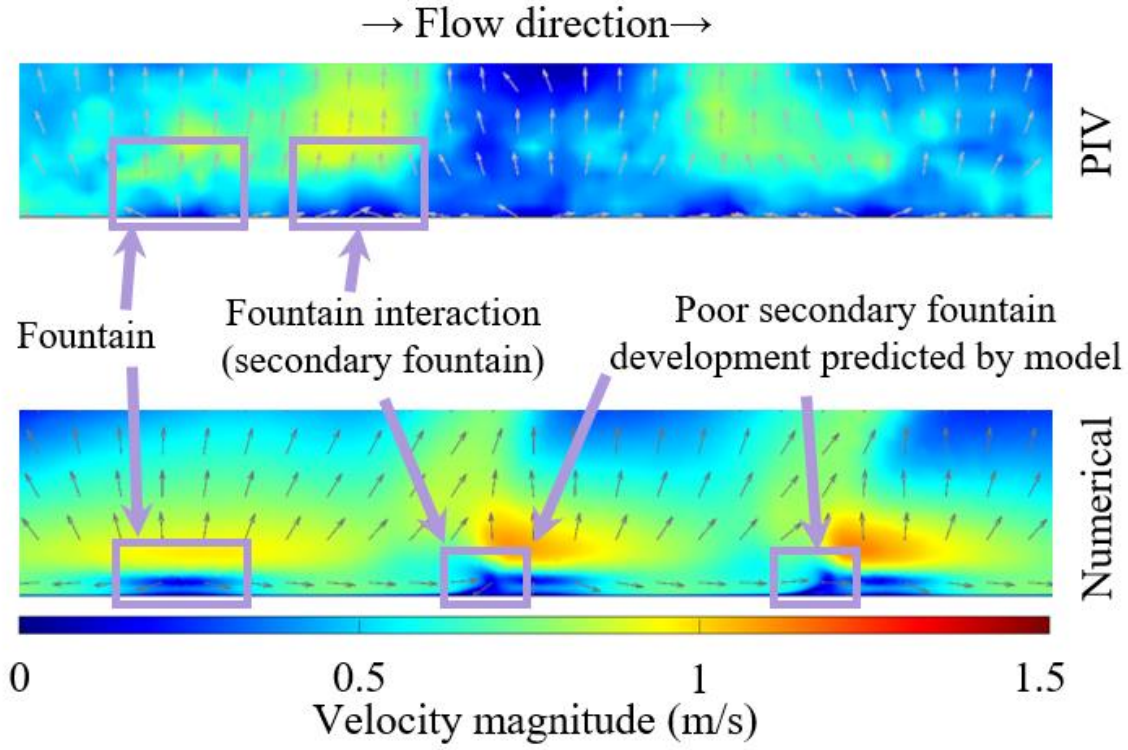

Figure 4-5: Fountain plane velocity vector fields and contours for an unmodified surface under an angled confining wall at a jet Reynolds number of 5600

Fountain and secondary fountains are also visible under the angled wall. These interactions are weaker than they were under the flat wall. Due to the additional space between the surface and angled confining wall, more fluid is deflected from the surface, reducing the fluid sent horizontally to generate a secondary fountain. As a result, the numerical model predicts highly suppressed secondary fountains. However, they are present and centrally-located in the PIV results. This is also likely due to asymmetry in the experimental design and total symmetry in the model resulting in increased crossflow effects.

Regarding pressure losses, the PIV experiments did not measure pressure changes. In the numerical model, applying the angled wall reduced the pressure loss by 5.1% from the flat wall case. This is to be expected. There is a larger gap between under the angled wall, reducing fluid velocity as the spent fluid moves towards the outlet. This reduces the velocity gradients on the wall and, hence, reduces pressure losses. This trend will hold when modifications are applied.

4.1.2 Baseline – Thermal Characteristics

Contours of the local surface heat transfer coefficient were generated from the numerical model for each geometry. This was completed using Equation 4.1 below. All values in this equation were either exported directly from Fluent or defined as a constant.

$$h_l = \frac{\dot{q}_l''}{(T_l - T_{in})} \tag{4.1}$$

As previously discussed, flow trends varied little with the jet Reynolds number. Similarly, surface contour trends from the numerical model varied little with the jet Reynolds number. As such, surface contours for the lowest jet Reynolds number of 5600 are shown, since this value yields the most legible trends. Figure 4-6, shown below, displays the surface heat transfer coefficient contours from the numerical model under both the flat and angled confining walls. In these surface contours, the jet plane pictured previously cuts through each while the fountain plane is on the top and bottom, as indicated in the top contour for the flat confining wall case. Key features on the surface are labelled and corresponding flow mechanics that result in the highlighted surface trends are displayed.

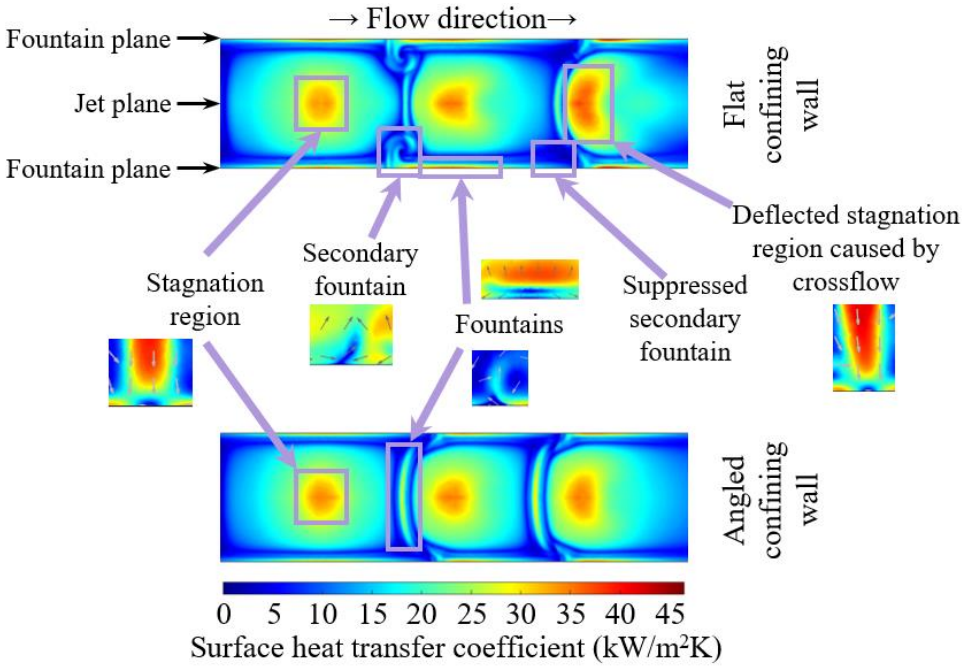

Figure 4-6: Surface heat transfer coefficient contours from the numerical model for an unmodified surface under a flat (top) and angled(bottom) confining wall for a jet Reynolds number of 5600

In each contour, three large regions of high heat transfer coefficient are seen, each of which corresponds to a stagnation region in the jet array. These regions are where the bulk of heat is dissipated from the surface. As the fluid is directed peripherally and develops into the wall jet, the surface heat transfer coefficient decreases with distance from the stagnation region. Once these wall jets meet, mixing near the surface creates long, thin regions of increased heat transfer coefficients, indicating the presence of a fountain. Under the flat wall, fountains in the fountain plane are notably stronger than those in the jet plane. Due to crossflow directing more fluid from the second and third jets downstream than upstream, the fountains generated in the jet plane are weakened, while those in the fountain plane are less affected. A secondary fountain is present under the flat wall, as indicated by a light-blue swirl. While this may seem insignificant, light blue represents upwards of an order of magnitude increase in the surface heat transfer coefficient when compared to the surrounding, dark blue regions. The secondary fountain between the downstream jets was seen in Figure 4-2 to be suppressed, and the effect of that is seen here, as a dark blue region of inefficient heat transfer is visible. Finally, crossflow is seen to affect the downstream jet's stagnation region. It is seen to shift downstream due to oblique impingement caused by crossflow of spent fluid. In this geometry, the issue is not seen to result in reduced thermal performance, but it could become problematic in larger arrays with more rows of jets.

Under the angled wall, the stagnation and fountain regions are also visible. It is noteworthy that, in this case, fountains generated in the jet plane are more prominent than those generated in the fountain plane. As the angled wall reduces crossflow, fluid from each jet is more evenly deflected radially by the impingement surface. As a result, the fountain in the jet plane becomes more pronounced since more fluid from downstream jets may flow upstream. This has the effect of weakening the fountains between rows of jets and the secondary fountains, since less fluid is sent transversely. It is also observed that the downstream stagnation region no longer experiences slanting since crossflow is less powerful than under the flat wall. It can be concluded that the angled confining wall is an effective spent fluid management strategy, though its implementation does come at the cost of some local performance reductions, and its application should be carefully considered based on the size and scale of the jet array. These observations are confirmed with Figure 4-7 below.

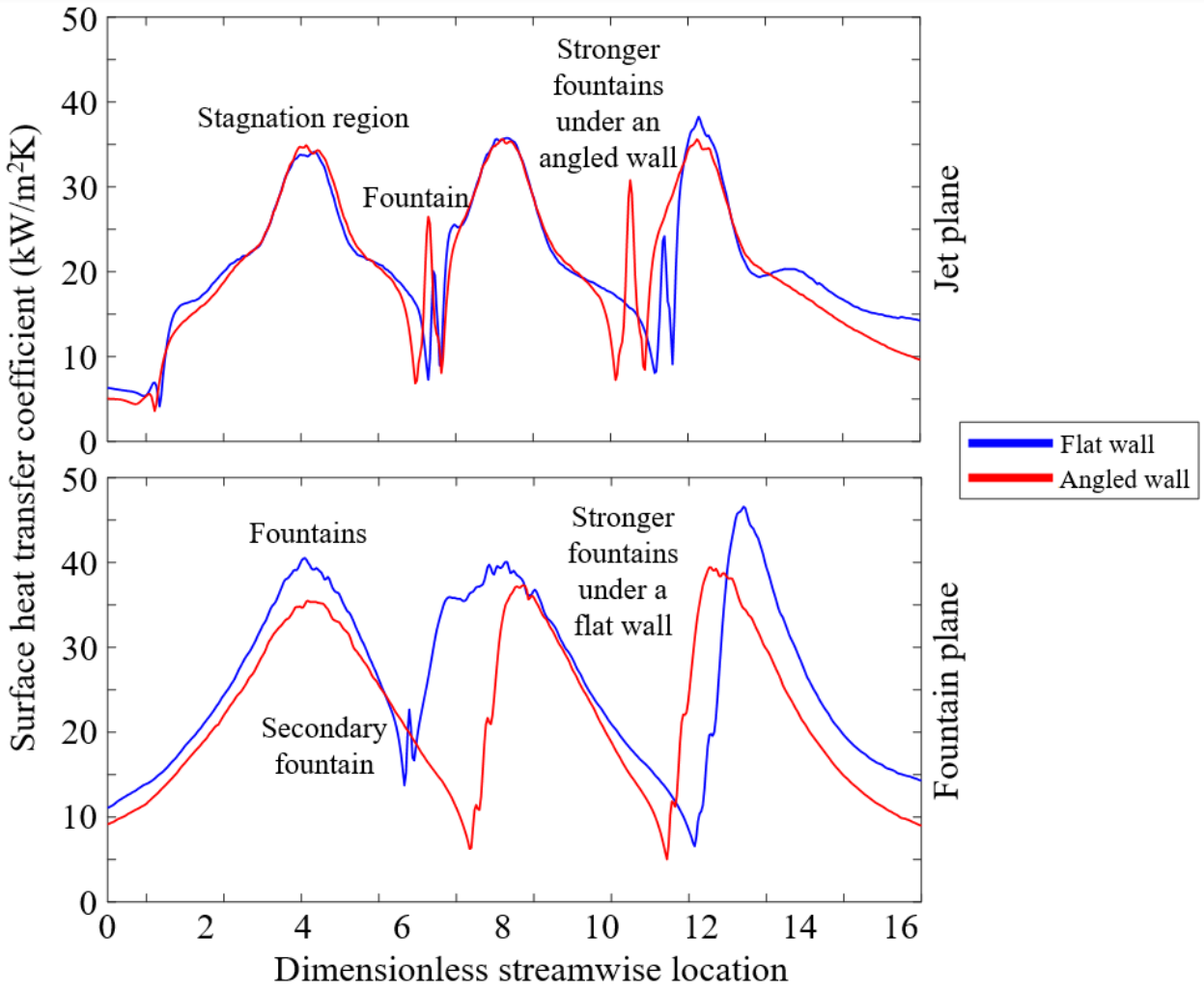

Figure 4-7: Surface heat transfer versus streamwise location plots from the numerical model in the jet and fountain planes for both confining wall angles

In the jet plane, wide peaks are observed in the stagnation regions, while the fountains create thin, sharp peaks between them. Fountains under the angled confining wall (red) are approximately 25% stronger and visually more centralized between the jets than those under the flat wall (blue). In the fountain plane, fountains create wide peaks which are observably stronger under the flat wall. A secondary fountain is observed between the upstream fountains under the flat wall, approximately doubling the local surface heat transfer coefficient, but they are suppressed in all other locations. This results in very low heat transfer coefficients where secondary fountains are lacking.

Finally, Figure 4-8 displays the surface temperature rise contours for the same geometries and jet Reynolds number. The surface temperature rise is defined as temperature difference

between the local or average surface temperature and the inlet water temperature of 30°C. In this effort, these surface temperature rise contours will not always provide meaningful findings and may not be shown for all geometries.

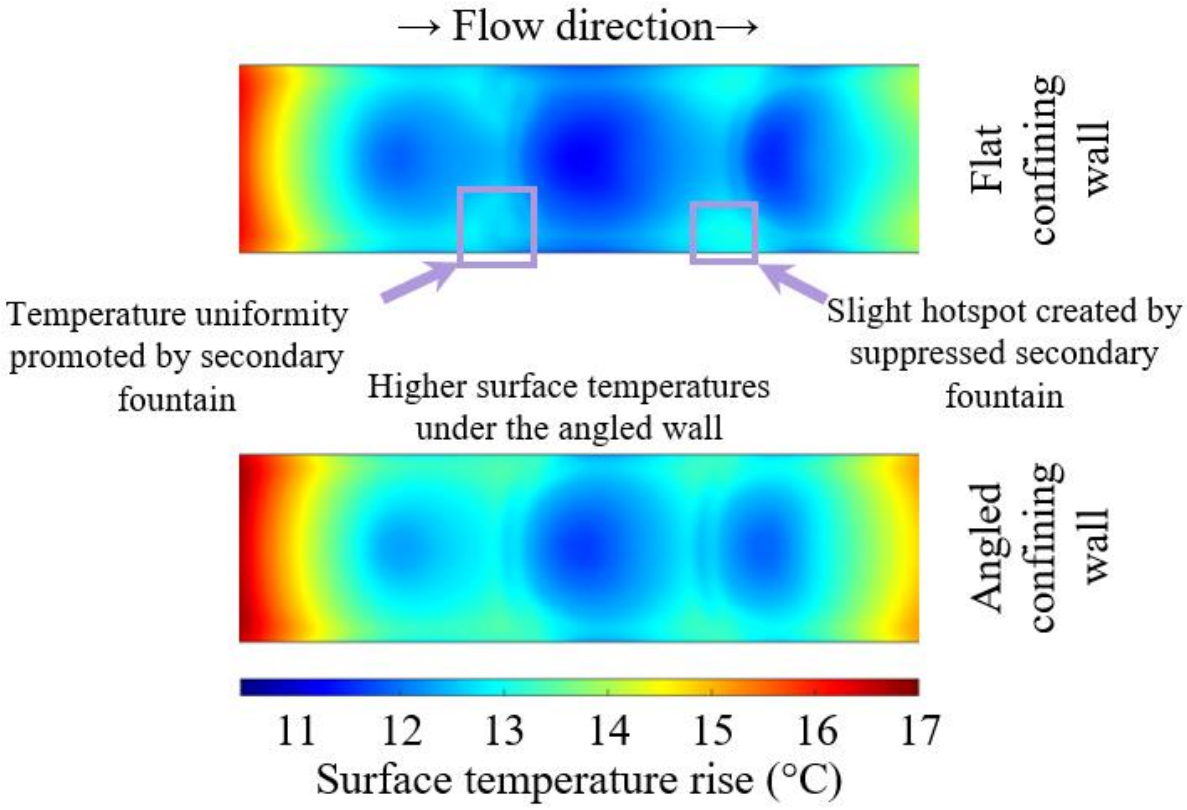

Figure 4-8: Surface temperature rise contours from the numerical model for an unmodified surface under a flat (top) and angled(bottom) confining wall for a jet Reynolds number of 5600

It is seen from these contours that the surface temperature is the lowest in the stagnation regions. Thin regions of reduced temperature are also seen under fountain interactions. Under the flat wall, the secondary fountain has prevented the development of a hotspot, which can be seen downstream and under the angled confining wall, where secondary fountains did not develop. While these hotspots are only about 1-2°C higher in temperature than the surrounding surface, this is primarily due to the surface material being copper, which has a high thermal conductivity. If a similar jet array were applied on a silicon substrate or a PCB, the reduced thermal conductivity could cause these hotspots to become greater, potentially resulting in thermal stresses and device damage. Thus, promoting these secondary fountains or otherwise enabling increased heat dissipation in these regions can be essential to maintaining device performance and longevity.

When surface modifications are applied, the average surface heat transfer coefficient and temperature rise values for these baseline cases will be necessary for analysis and comparison. These values are tabulated below, in Table 4-2.

Table 4-2: Average thermal performance parameters for a baseline surface

Wall angle	Re_j	Average surface heat transfer coefficient (kW/m^2K)	Average surface temperature rise (°C)
Flat (0°)	5600	12.1	14.2
	8400	16.2	10.7
	11200	19.8	8.7
	14000	23.4	7.4
Angled (7.5°)	5600	11.5	15.0
	8400	15.1	11.4
	11200	18.4	9.3
	14000	21.7	8.0

As previously discussed, varying the flow rate primarily affected the magnitude of the flow fields and surface contours, as shown in Figure 4-9. Slight differences arise from the increased fluid velocity, but trends including the stagnation regions and fountains remain consistent. Additional comparisons of flow fields and contours with varying jet Reynolds number are displayed in Appendix E.

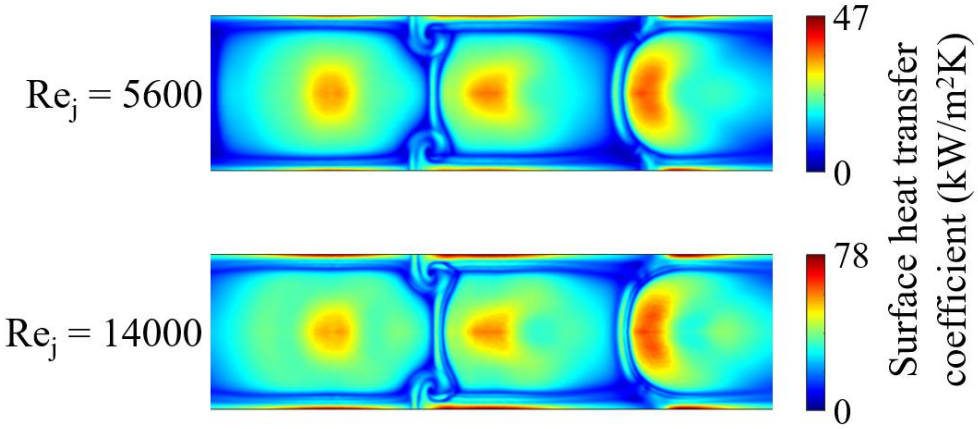

Figure 4-9: Surface heat transfer coefficient contour comparison from the numerical model for the lowest and highest jet Renolds numbers for an unmodified surface under a flat confining wall

4.2 Jet Cones

Having examined the results using a baseline surface, modifications can now be examined. The most obvious location for an extended surface would be in the stagnation region, where heat transfer is most efficient. To accomplish this, cones are placed directly under each nozzle. These cones all have base diameters equal to the jet diameter of 3.18mm and varied heights of one-half and one jet diameter. The primary aim of this design is to aid in distribution of fluid radially from the stagnation region. If more fluid from the downstream jet can move upstream and allow the fountain interaction to be centralized between the jets, thermal improvements could be achieved.

In the PIV experiments, the impingement surfaces were 3D printed using resin. This material is semitransparent. As a result, the laser sheet is sufficiently bright to shine through the surface modifications when the plane of interest intersects with a modification, albeit at a reduced intensity. In each PIV contour, graphics have been overlaid to indicate the location and size of the modifications. Due to the small distance between the camera and laser sheet, two rows of jet cone modifications obstruct the gathered images. Images were captured in a dark enclosure, leaving little visual reference with which to place the modifications within the contours. While the regions immediately surrounding the modifications are illuminated, their results are less reliable. Light reflected or refracted into the camera prevents accurate analysis, and when the laser sheet shines behind the modifications, particles passing behind the modifications may not be detected correctly. As such, results immediately surrounding the modifications are less reliable than regions freely illuminated by the laser sheet.

For all sets of modifications, two heights were examined. The general finding of the varied heights was that the tall modifications create similar effects as the short modifications, but more exaggerated and noteworthy. As such, flow fields and surface contours displayed and discussed in this chapter will primarily be those of the large modifications unless a unique result occurs in the short modification case. Any short modification flow field or contour not discussed in text can be found in Appendix E.

4.2.1 Jet Cones – Flow Mechanics

The velocity vector fields and contours in the jet plane when tall jet cones are applied are displayed in Figure 4-10. In the PIV contours, the grey triangles indicate the visual blockages caused by the cone modifications. Since two rows of jets block the reflected laser light, the near cones are colored lighter than the far cones. Because the nearest row of jets are closer to the camera, they appear more spread out than the central set of jets.

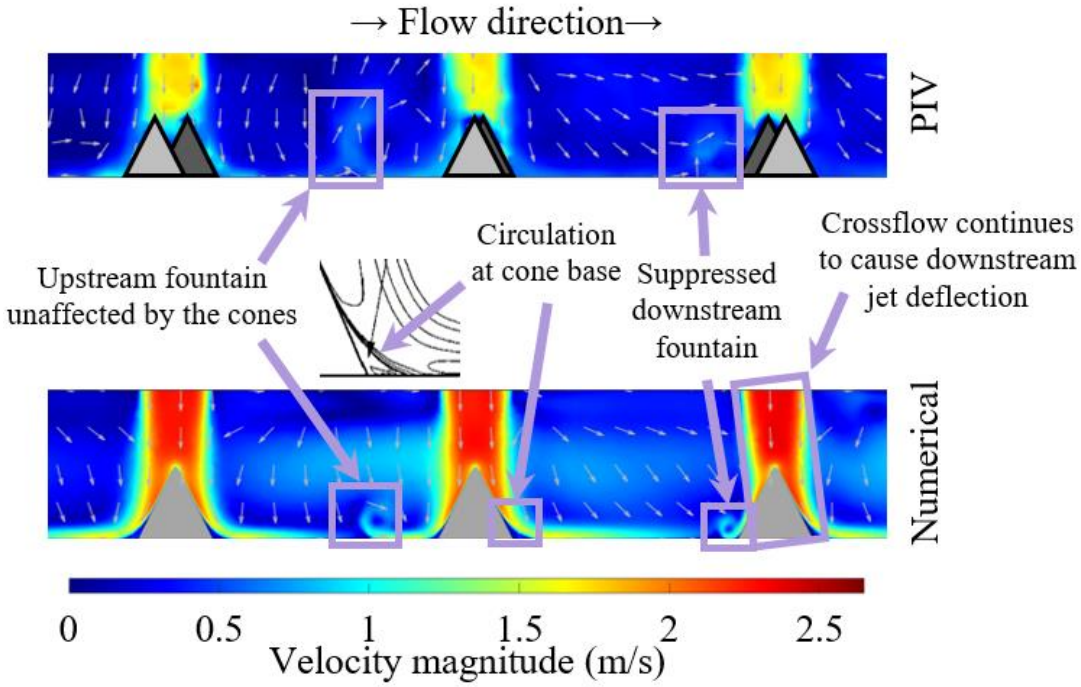

Figure 4-10: Jet plane velocity vector fields and contours for tall jet cones under a flat confining wall at a jet Reynolds number of 5600

The cone modifications resulted in little effect on the jet flows. The first two jets impinge normally, now onto cone structures. In the numerical model, jet slanting still occurs in the downstream jet due to crossflow, indicating that these cones do not provide any crossflow mitigation. Since the first two jets impinge normally onto the cone, the fountain between them is still well pronounced. However, the downstream fountain is far less developed than it was in the unmodified case. Since the downstream jet is still being deflected by crossflow, the cone structure sends the bulk of the fluid downstream. As a result, less fluid moves upstream weakening the wall jet and fountain interaction. This is expected to reduce the thermal performance between the two downstream jets, as most of this area is covered by the wall jet from the central jet, which will

perform worse far away from the jet. At the base of the cones, the numerical model shows a small region of fluid circulation, similar to that observed by King and Chandratilleke, as shown in Figure 2-4 and indicated within Figure 4-10 [44]. This is expected to inhibit heat dissipation from this region, as the fluid is not immediately swept away into the wall jet.

The fountain plane contours for the tall cones under a flat wall are displayed in Figure 4-11. For the numerical contour, triangle graphics have been added to indicate the location of the jet cones, though they are not present in the fountain plane.

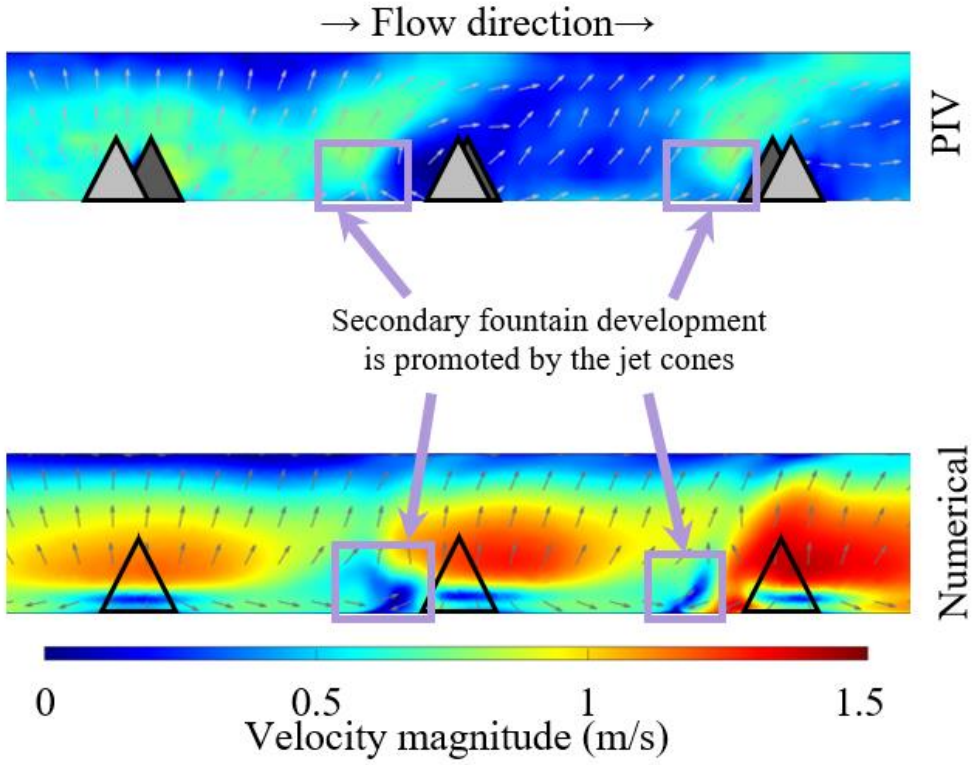

Figure 4-11: Fountain plane velocity vector fields and contours for tall jet cones under a flat confining wall at a jet Reynolds number of 5600

Little effect is observed in the fountain behaviors in this plane as a result of applying the jets. However, the secondary fountains are more clearly developed, particularly between the downstream set of jets. As a result, some thermal benefits are to be expected in this region, as the downstream secondary fountain was highly suppressed in the unmodified surface case.

Having examined the flat wall flow behaviors, the jet region contours for the tall cones under an angled wall are shown in Figure 4-12.

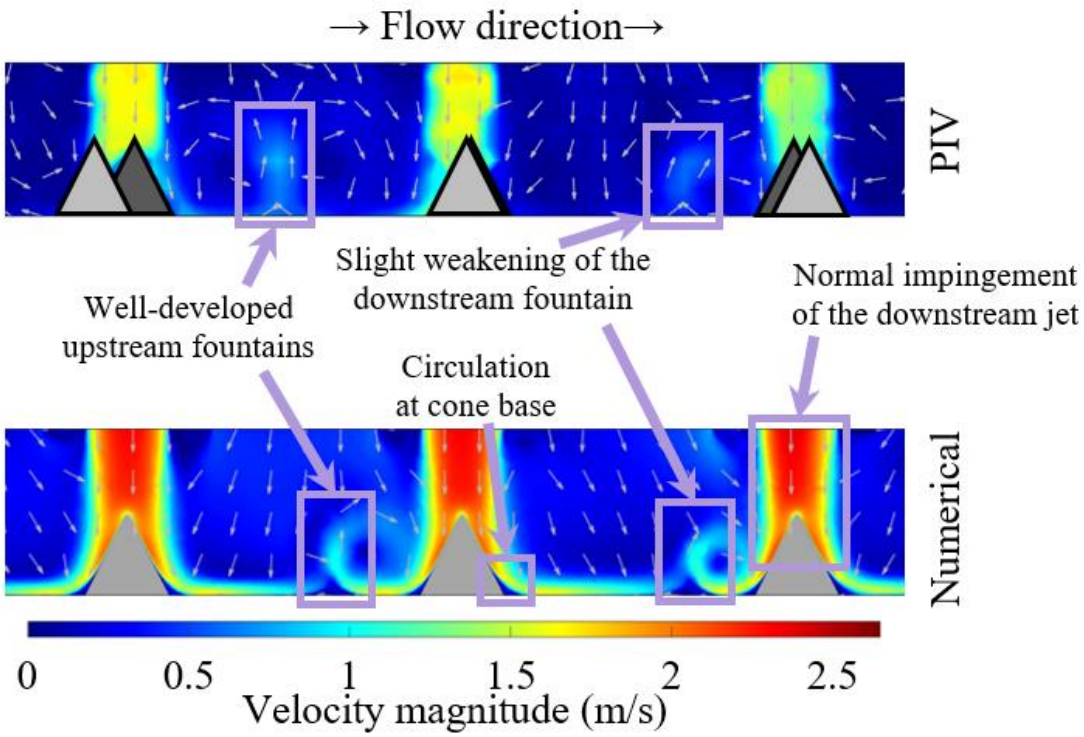

Figure 4-12: Jet plane velocity vector fields and contours for tall jet cones under an angled confining wall at a jet Reynolds number of 5600

As the angled wall provides space for spent fluid above the nozzle outlets, all jets impinge normally onto the cones. This has resulted in far more pronounced fountain interactions than those under the flat wall. Some weakening can be observed in the downstream fountain, but it is minimal. In the numerical model, this weakening is mostly attributable to crossflow. While crossflow is less powerful under the angled wall, it is still present to some extent and still causes some effects on the downstream jet and fountain. For the PIV contour, it is more likely that the weakening is caused by misalignment of the nozzle and cone. Since the PIV array is only a three-by-three array of jets and an angled confining wall is applied, crossflow is nearly negligible. However, alignment of the cones with the nozzles is challenging and even a slight misalignment would result in uneven radial deflection of fluid from the jet. Circulation is once again observed at the base of the cone, indicating that this trend is independent of spent fluid management or crossflow, which is not surprising.

The fountain plane contours for the tall cones under an angled wall are displayed in Figure 4-13.

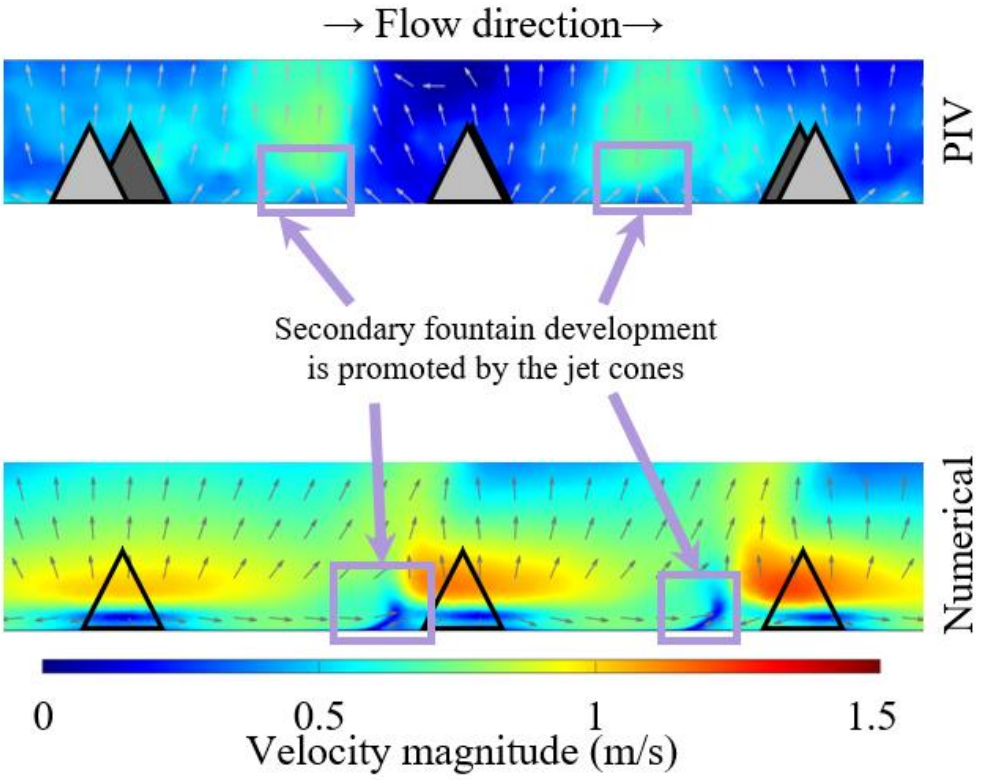

Figure 4-13: Fountain plane velocity vector fields and contours for tall jet cones under an angled confining wall at a jet Reynolds number of 5600

Like under the flat wall, little effect is observed in the fountain mechanics due to applying the cone structures. However, the numerical results show that secondary fountains are seen to be developed better with cones than they were without them, suggesting that these modifications may improve thermal performance away from the stagnation region.

Regarding pressure losses, the jet cones had a negligible effect, despite adding surface area in the stagnation region. All cases yielded changes of less than 1% from their respective unmodified surface case.

4.2.2 Jet Cones – Thermal Characteristics

Regarding the thermal effects of these jet cones, Figure 4-14 below displays the surface heat transfer coefficient contours from the numerical model using the tall cones under both a flat and angled confining wall. Due to the local heat transfer coefficient on the cone tips being far greater than the values on the surrounding surface, scaling the contours natively would result in

illegible trends. As such, the same scale as that used in the baseline surface cases will be used for all modified surface contours. This means that a deep red indicates local surface heat transfer coefficient values greater than those obtained for an unmodified surface.

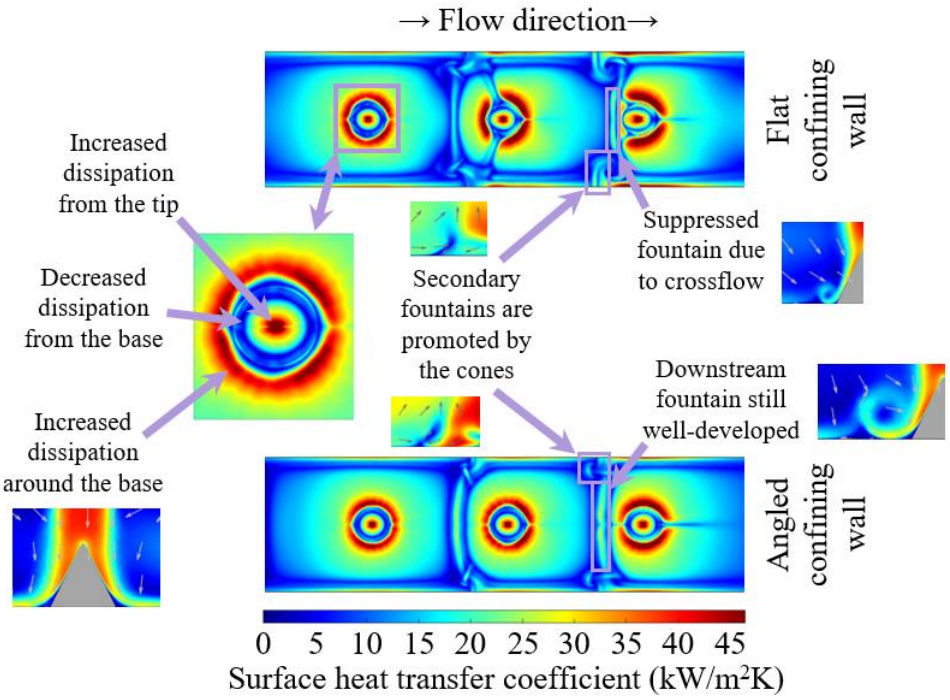

Figure 4-14: Surface heat transfer coefficient contours from the numerical model for tall jet cones under a flat (top) and angled (bottom) confining wall for a jet Reynolds number of 5600

On and surrounding the cones, three regions of interest are visible. First, very high heat transfer coefficients are achieved at the cone tips. This is to be expected, as the tip pierces the impinging jet, being exposed to the cold fluid directly. At the base, the fluid circulation observed from the velocity vector fields results in very low values. This circulation region holds hot fluid at the surface, creating a region of poor thermal performance. This circulation could be reduced by introducing a fillet to the cone base, as also suggested by King and Chandratilleke [44]. This would enable a smoother transition from the flow across the cone's surface to that of the flat impingement surface. Surrounding the base cone is a ring of high heat dissipation. This indicates the end of the circulation and the beginning of oblique impingement from the jet after being deflected by the cone structure. While oblique impingement is typically less effective than normal impingement, the cone structure appears to have disrupted the thermal boundary layer, enabling highly efficient heat transfer on the flat surface immediately surrounding the cone. This trend is well-developed in

the upstream jet for under the flat wall and all jets under the angled wall. However, crossflow under the flat wall inhibits this ring on the upstream side of the central and downstream jets. Furthermore, the fountain between the downstream jets under the flat wall is under-developed due to the cone deflecting more fluid downstream than upstream. Finally, it is noteworthy that the cones aid in development of secondary fountains under both wall angles, though they appear more powerful under the flat wall.

Local surface temperature trends for these and the remaining modifications were not meaningful beyond the discussion enabled by the surface heat transfer coefficient contours, but average effects across the surface are more revealing. Table 4-3 below displays the average surface parameters that result from applying jet cones to the impingement surface.

Table 4-3: Average thermal performance parameters for the jet cone modifications

Wall angle	Cone height	Re_j	Percent change in the surface area from the baseline case	Average surface heat transfer coefficient (kW/m^2K)	Percent change in the surface heat transfer coefficient from the baseline case	Average surface temp. rise (°C)	Percent reduction in the surface temp. rise from the baseline case	Percent of thermal improvement not attributable to increased surface area
Flat (0°)	Short	5600	1.0	12.6	3.8	13.6	4.6	78.3
		8400		16.6	2.6	10.3	3.5	71.7
		11200		20.4	2.9	8.4	3.8	73.7
		14000		24.1	3.0	7.1	3.9	74.0
	Tall	5600	3.0	12.7	4.6	13.2	7.2	59.4
		8400		16.8	4.0	9.9	6.6	55.9
		11200		20.7	4.6	8.1	7.2	59.4
		14000		24.6	5.0	6.8	7.5	61.2
Angled (7.5°)	Short	5600	1.0	11.5	0.28	14.8	1.3	20.6
		8400		15.2	0.65	11.2	1.6	38.2
		11200		18.5	0.15	9.2	1.2	14.0
		14000		21.5	-0.71	7.9	0.3	<0
	Tall	5600	3.0	11.4	-1.2	14.7	1.8	<0
		8400		14.9	-1.0	11.2	1.9	<0
		11200		18.3	-0.96	9.2	2.0	<0
		14000		21.4	-1.0	7.8	1.9	<0

Under the flat wall, increases in the average surface heat transfer coefficient of 2.6-5.0% are achieved. However, applying the cones under the angled wall results in negligible changes for the short cones and slight decreases for the tall cones. Application of the short and tall cones results in a 1.0% and 3.0% increase in the total surface area available for heat transfer when compared to the baseline surface. Despite this, average surface temperature rise reductions of 3.5-7.5% are

achieved under the flat wall, indicating that thermal improvements under the flat wall are not solely attributable to increasing the surface area. These effects are seen graphically in Figure 4-15.

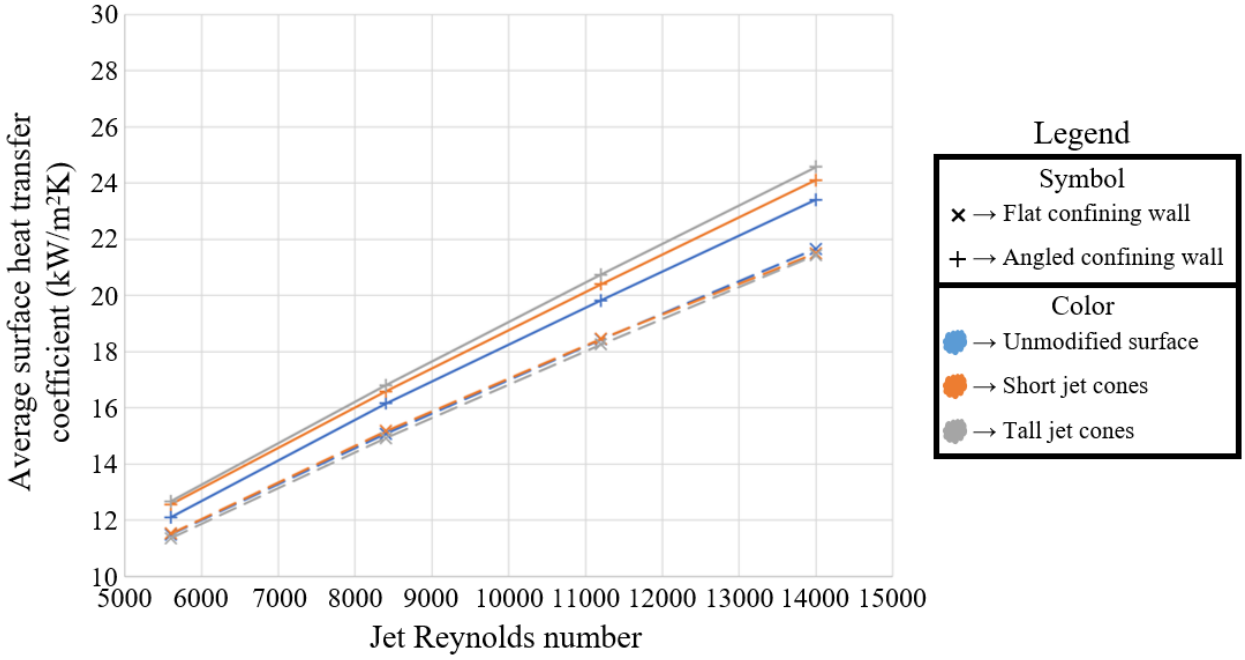

Figure 4-15: Surface heat transfer coefficient versus jet Reynolds number from the numerical model for all baseline and jet cone cases

Using the process detailed in Appendix C, it can be determined that 56-78% of the thermal improvements created by the jet cones under a flat wall are not attributable to increased surface area, but rather to improvements in the flow mechanics and/or the location and design of the extended surface. In this case, the primary reason for this value is likely that the added area is focused in the stagnation region, where heat transfer is most efficient. Meanwhile, surface temperature rise reductions under the angled wall are similar or less than the surface area increases, indicating that thermal improvements are similar or less than trivially increasing the surface area. Only up to 38% of the surface temperature rise reduction can be attributed to other effects than increased surface area, while in most cases the cones perform worse. As the calculations used to populate the right-hand column of Table 4-3 are inapplicable when the modified surface performs worse than expected based on the surface area increase, numerical values are not provided when this occurs. This poor performance is most likely due to the cones causing reduced fountain performance in the jet plane. While secondary fountains were improved, evidently this improvement did not outweigh the negative impact on the fountain. Furthermore, flow effects

under the angled wall were less pronounced, which explains why this percentage is lower or negative for these cases.

Based on these results, it can be concluded that the jet cones are only selectively beneficial. In the absence of crossflow, they provide improved performance on and immediately surrounding the cone, with a resolvable circulation issue at the cone base. However, results in an array are mixed. Without spent fluid management, crossflow deflects jets downstream, which results in more fluid motion downstream than upstream, negatively affecting fountain interactions. When spent fluid management is applied, the cones affect the flow less dramatically, causing less improvement. Furthermore, PIV analysis shows that highly accurate alignment of the cones to the nozzles is essential to maintaining desired flow mechanics in an array, which would be very difficult to accomplish. Thus, these cones could be beneficial for single jet systems or hotspot applications, where jet array interactions are insignificant. However, when distributed heating must be dissipated using an array of jets, they are likely impractical.

4.3 Streamwise Ribs

As the jet cones indicated that surface modifications under the jets may be extremely sensitive to manufacture and positioning tolerances, a variety of surface modifications located between the jets will be examined. The first for analysis are the streamwise ribs, which have a triangular cross-section with bases of one jet diameter and varied heights of one-half and one jet diameter. They are referred to as “streamwise” ribs since they are aligned in the direction of outflow. The intent of this design is to deflect spent fluid from the surface more effectively than the fountains would, while also providing additional surface area for heat dissipation in areas away from the stagnation regions.

4.3.1 Streamwise Ribs – Flow Mechanics

Application of these streamwise ribs in the PIV system severely reduces visibility of the central jet region of interest. While the direct laser light is able to illuminate regions behind the modifications, the light reflected off the seeding particles cannot penetrate the ribs. As a result, only the upper region can be analyzed in the central set of jets, which does not reveal any useful

information regarding flow mechanics that are relevant to thermal performance, those being the stagnation region, wall jet, and fountains. In an attempt to resolve this, PIV analysis was completed using the nearest set of jets, as this set could be fully visualized. This, however, sacrifices symmetry in the results. Figure 4-16 shows the jet plane contours for tall streamwise ribs under a both confining wall angles, where the PIV contours are for the nearest set of jets, not the central set.

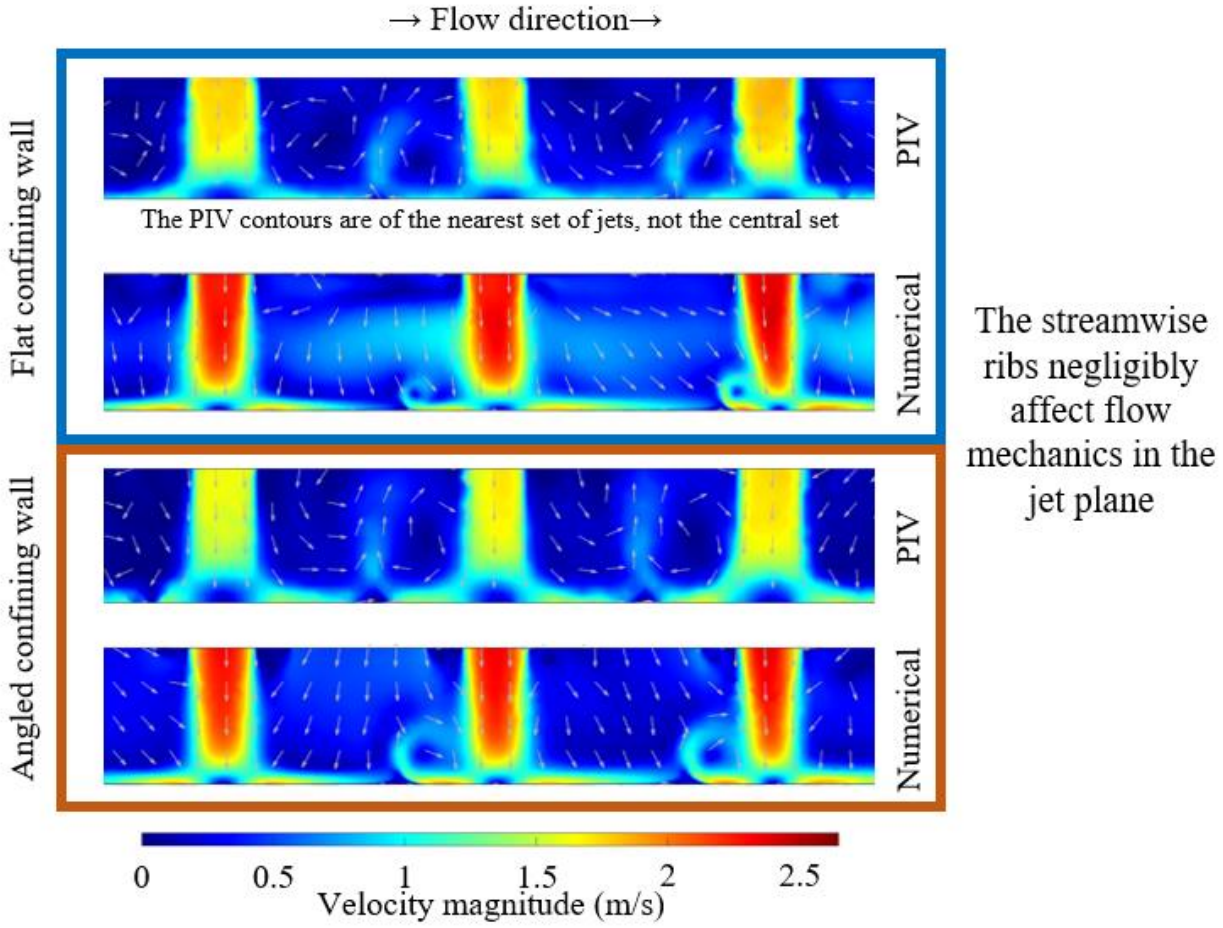

Figure 4-16: Jet plane velocity vector fields and contours for tall streamwise ribs under both confining wall angles at a jet Reynolds number of 5600

The streamwise ribs are not located in this plane and are thus not visualized. All contours were shown together since flow mechanics in the jet plane are nearly unaffected by the streamwise ribs. The flow mechanics in the jet plane are primarily driven by the jet flows and their immediate interactions. None of the stagnation regions or fountain interactions visualized in this plane would be meaningfully affected by surface modifications located entirely out of the plane. It can be

concluded that thermal performances in this plane will be very similar to those of the unmodified surface cases in the jet plane.

The velocity flow fields for the fountain plane with streamwise ribs are shown in Figure 4-17 below.

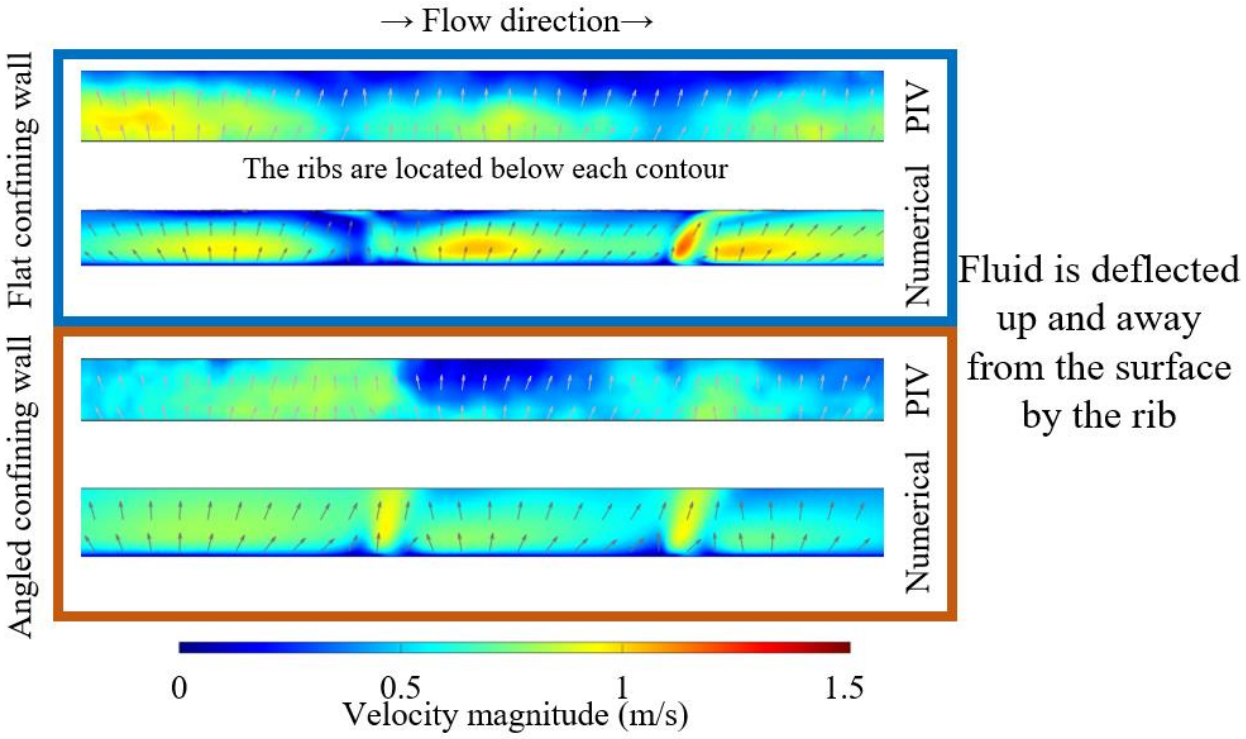

Figure 4-17: Fountain plane velocity vector fields and contours for tall streamwise ribs under both confining wall angles at a jet Reynolds number of 5600

The streamwise ribs lie underneath and parallel to the fountain plane. As a result, the flow field is thinner than the full nozzle-to-surface distance. It should be noted that a lack of any physical object or objectively located fluid motion, such as the jet flow out of the nozzle, makes alignment of the PIV contours very subjective in this case. While the flow in this plane is affected by the ribs, the only key finding to be seen is that fluid is effectively being deflected away from the surface. Interactions such as the fountains and secondary fountains do not exist due to the ribs acting as a physical obstruction where they would otherwise be located. As a result, the obstruction of the view of the flow field close to the surface by the streamwise ribs makes it harder to connect flow mechanics to heat transfer characteristics.

Under the flat wall, the ribs created a slightly increased wetted perimeter and decreased flow area, which resulted in slight increases in pressure losses of 2.5-3.6%. These are minimal and are easily outweighed by the observed thermal improvements created by these ribs. Under the angled wall, these effects were negligible, with the model outputting pressure loss reductions of less than 1% when the ribs were applied.

4.3.2 Streamwise Ribs – Thermal Characteristics

While the flow mechanics when the streamwise ribs were applied in the planes of interest were not especially revealing, their thermal effects can still be examined from the numerical model. Figure 4-18 below displays the surface heat transfer coefficient contours for the tall streamwise ribs.

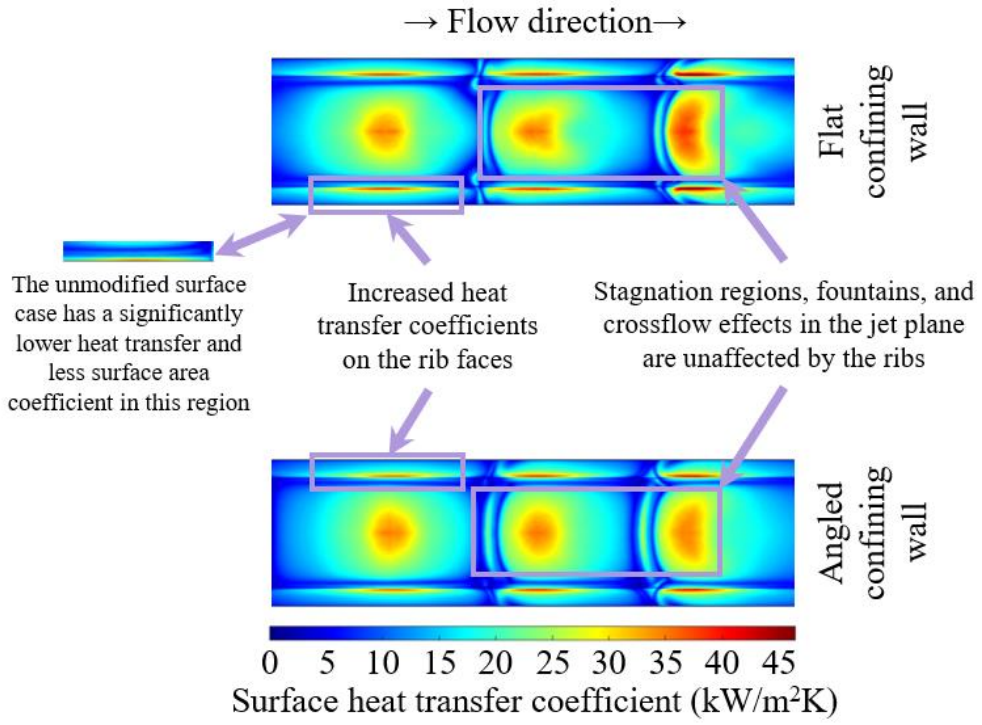

Figure 4-18: Surface heat transfer coefficient contours from the numerical model for tall streamwise ribs under a flat (top) and angled (bottom) confining wall for a jet Reynolds number of 5600

The streamwise ribs are indeed seen to have little-to-no effect on the thermal performance in the jet plane due to having little-to-no effect on the flow mechanics. As a result, crossflow is still an issue in the flat wall case and fountains in the jet plane are still stronger under the angled

wall than the flat wall. In the fountain plane, significantly increased surface heat transfer coefficients are achieved on the rib faces. A thin region near the base provides very high values, while the rest of the face experiences moderately high heat transfer when compared to the same region for the baseline case. To reiterate a previous comment, the light blue color indicates heat transfer coefficients up to an order of magnitude greater than the dark blue color. Most of the region now covered by the ribs was previously dark blue, as indicated in the figure. These greatly increased values are likely the result of the wall jet region, which was moving parallel to the impingement surface, impacting the rib faces, effectively impinging upon them. Not only is the heat transfer coefficient higher, but these values are achieved on the extended surface, which indicates greatly improved cooling effectiveness in this fountain region.

To analyze these thermal improvements in more detail, Table 4-4 below displays the average thermal parameters for the streamwise rib cases.

Table 4-4: Average thermal performance parameters for the streamwise rib modifications

Wall angle	Rib height	Re_j	Percent change in the surface area from the baseline case	Average surface heat transfer coefficient (kW/m^2K)	Percent change in the surface heat transfer coefficient from the baseline case	Average surface temp. rise (°C)	Percent reduction in the surface temp. rise from the baseline case	Percent of thermal improvement not attributable to increased surface area
Flat (0°)	Short	5600	10.4	12.8	5.4	12.2	14.0	33.0
		8400		16.9	4.5	9.2	13.3	29.3
		11200		20.8	4.7	7.5	13.5	30.3
		14000		24.5	4.5	6.4	13.3	29.5
	Tall	5600	30.9	12.5	3.1	10.5	25.9	8.8
		8400		16.5	2.0	8.0	25.1	6.0
		11200		20.2	2.0	6.5	25.1	6.0
		14000		24.0	2.6	5.5	25.5	7.6
Angled (7.5°)	Short	5600	10.4	11.8	2.9	13.2	11.9	21.0
		8400		15.7	3.8	10.0	12.7	26.0
		11200		19.3	4.8	8.1	13.5	30.6
		14000		22.7	5.0	6.9	13.7	31.4
	Tall	5600	30.9	11.3	-1.8	11.7	22.2	<0
		8400		15.0	-0.77	8.8	23.0	<0
		11200		19.1	3.4	6.9	26.2	<0
		14000		21.6	-0.4	6.1	23.3	<0

These ribs create significant surface area increases of 10.4% and 30.9% when compared to the baseline surface. As a result, significant thermal improvement is necessary to justify applying

these modifications. For the short ribs, the surface heat transfer coefficient increases by 4.5-5.4% under the flat wall and 2.9-5.0% under the angled wall, indicating noteworthy improvements. These decrease to 2.0-3.1% and -0.77-3.4% when the tall ribs are applied, suggesting that the tall ribs are needlessly tall. However, the surface temperature rise reductions are significantly greater when using the tall ribs. Reductions of 11.9-14.0% are achieved with the short ribs, while the tall ribs can achieve reductions of 22.2-25.9%. However, most of these improvements are attributable to simply increasing the surface area. For the short ribs, 21-33% of the thermal performance improvements are not attributable to increased surface area. This reduces to 6-8.8% for the tall ribs under the flat wall, and the tall ribs under the angled wall do not meet the expectations of a 30.9% increase in the surface area. Most of the thermal benefit from these modifications comes from the wall jets impacting the rib faces; these results suggest that a greater portion of the short ribs experience this interaction, while only the base of the tall ribs sees benefits.

While most of the thermal benefits created by these streamwise ribs are attributed to increasing the surface area, the surface temperature rise reductions of up to 26.2% are significant and suggest that these are worth further research and consideration in real-world systems. These ribs were seen to create no detriment to the flow mechanics in the jet plane, while significantly increasing the surface heat transfer coefficient and surface area in regions that previously saw very little heat dissipation. Relatively weak fountain and secondary fountain behaviors were replaced with fluid interaction with an extended surface, which results in greatly decreased surface temperatures.

4.4 Transverse Ribs

As the triangular rib structures have been shown to be effective between the jet rows, they have also been examined for use when oriented normal to the outflow, in the transverse direction. Like the streamwise ribs, their intent is to deflect spent fluid from the surface more effectively while also providing additional area for heat transfer in regions away from the jets.

4.4.1 Transverse Ribs – Flow Mechanics

Figure 4-19 below displays the flow fields for the tall streamwise ribs under a flat confining wall.

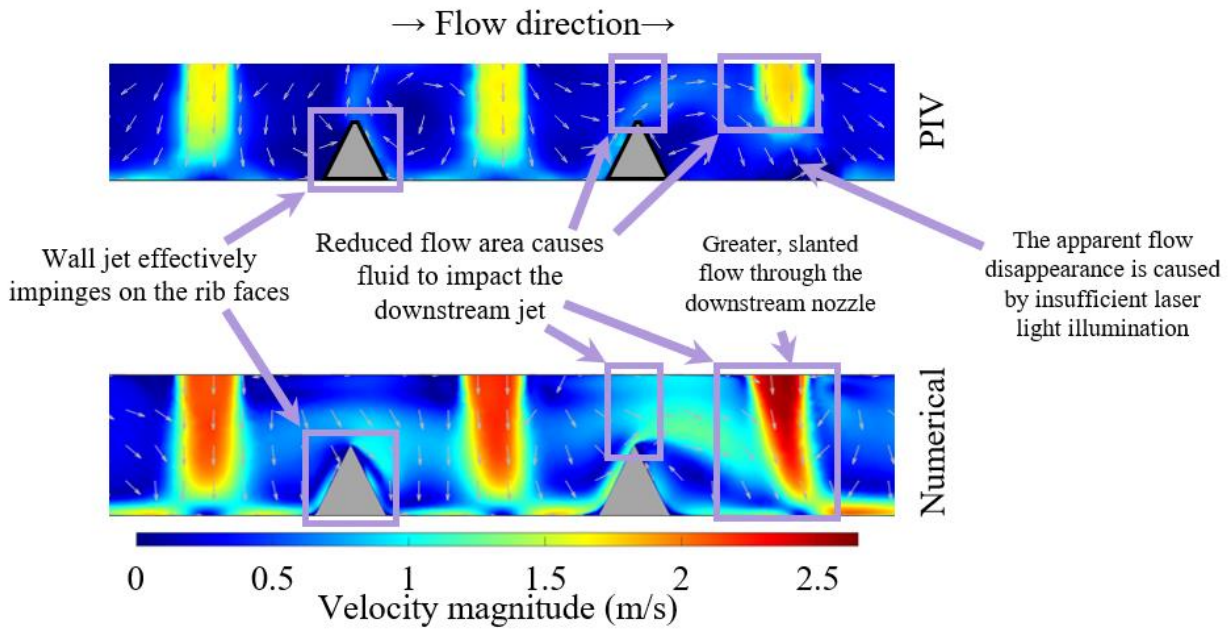

Figure 4-19: Jet plane velocity vector fields and contours for tall transverse ribs under a flat confining wall at a jet Reynolds number of 5600

Between the two upstream jets, the wall jet regions from each jet are seen to effectively impinge on the rib's base. This lends credence to the findings in the streamwise rib investigation that the cause of increased heat dissipation from the rib faces was due to the wall jet's interaction with the rib. As such, increased heat transfer from these transverse ribs can also be expected due to this flow behavior. While this is a good indication, a problem arises in the application of these ribs under the flat confining wall. Since these tall ribs cut the cross-sectional area of the channel in half, flow separation occurs from the top of the ribs. This has the unintended effect of increasing crossflow effects. In the numerical contour, the central jet is seen to be slightly slanted, but the downstream jet in both contours is greatly affected by this separation. The furthest downstream jet is seen to be greatly deflected downstream by flow from above the rib, resulting in highly oblique impingement on the surface. Furthermore, uneven flow is seen from the jets, with a greater velocity magnitude observed for the downstream jet. This corresponds with increased pressure losses. Application of these tall transverse ribs under the flat confining wall increased pressure losses by

over 9% for all flow rates. This suggests that the pressure at the downstream jet is lower than at either of the upstream jets, resulting in a greater flow rate through the downstream nozzle.

These findings are similarly observed in the fountain plane, as shown in Figure 4-20.

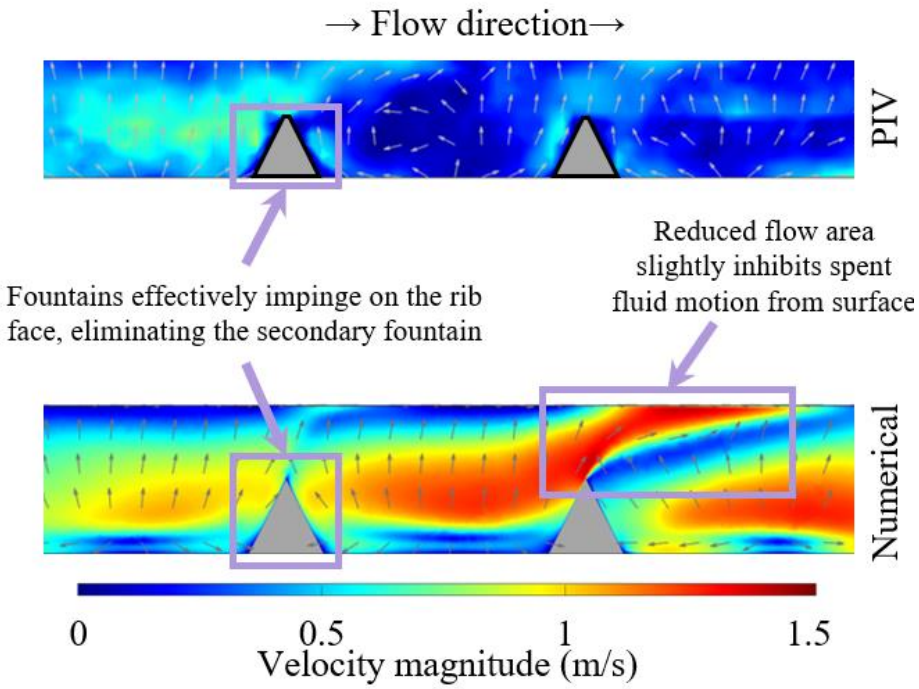

Figure 4-20: Fountain plane velocity vector fields and contours for tall transverse ribs under a flat confining wall at a jet Reynolds number of 5600

The fountains now effectively impinge on the rib faces, but at a much lower velocity. This interaction replaces the very weak secondary fountains that were easily suppressed by crossflow with an unmodified surface. While this is beneficial, reduced flow area again creates a problematic flow behavior downstream. The flow separation results in spent fluid from the downstream fountain not being deflected from the surface as effectively. This, however, is not as substantial of a problem as the behavior observed in the jet plane.

These findings suggest that these transverse ribs could be effective if applied in an array with some form of spent fluid management, but are inapplicable under a flat confining wall, where crossflow may be significant. To confirm this, Figure 4-21 below displays the jet plane contours for the tall transverse ribs under an angled confining wall.

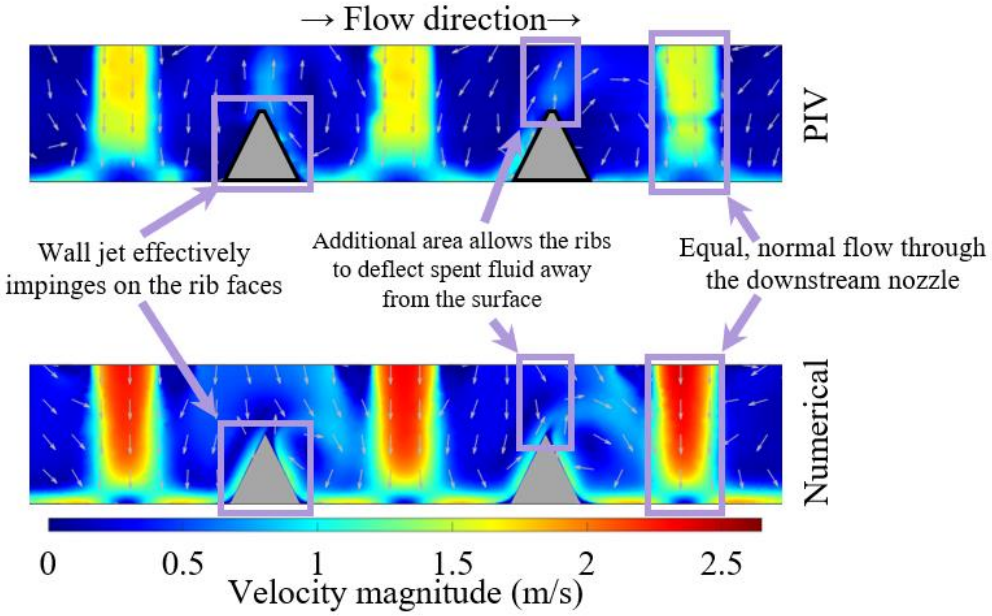

Figure 4-21: Jet plane velocity vector fields and contours for tall transverse ribs under an angled confining wall at a jet Reynolds number of 5600

The wall jet regions still impinge on the ribs faces, which is expected to improve thermal performance. However, since space is available for spent fluid above the nozzle outlets, flow separation from the rib tips is far less powerful. Normal impingement of an equal flow rate is seen from all jets, indicating that the angled wall has resolved the problem. This is fully confirmed by examining the fountain plane contours, as shown in Figure 4-22.

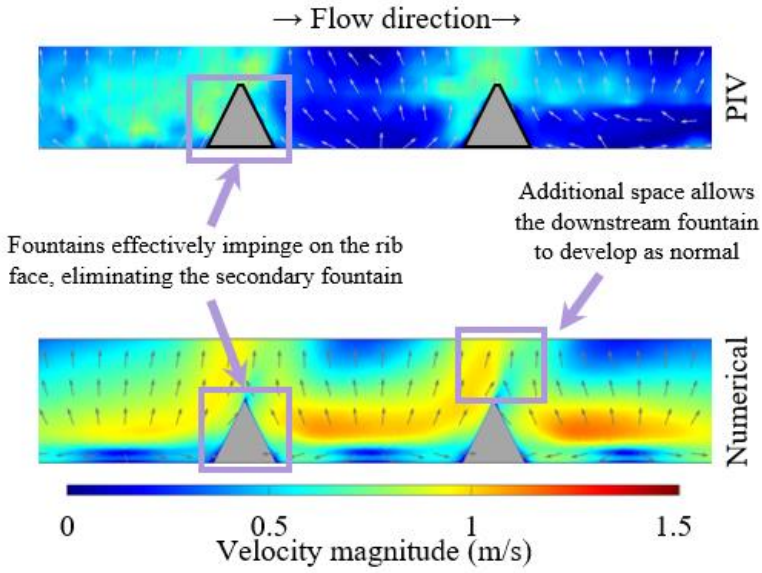

Figure 4-22: Fountain plane velocity vector fields and contours for tall transverse ribs under an angled confining wall at a jet Reynolds number of 5600

As before, secondary fountains are effectively replaced with impingement on the rib face, suggesting thermal improvements will follow. The additional area provided by the angled wall allows spend fluid to be deflected away from the surface. As a result, the downstream fountain develops normally.

As previously stated, pressure losses were increased by over 9% when the tall cones were applied under a flat confining wall. Under the same wall, the short cones also increased pressure losses, but to a lesser extent of 1.6-2%. However, as the angled confining wall resolved the issue of reduced cross-sectional area for flow, the transverse ribs had negligible effects of -0.3-1.4% when applied under an angled confining wall.

4.4.2 Transverse Ribs – Thermal Characteristics

Figure 4-23 below displays the surface heat transfer coefficient contours for the tall transverse ribs under both confining wall angles.

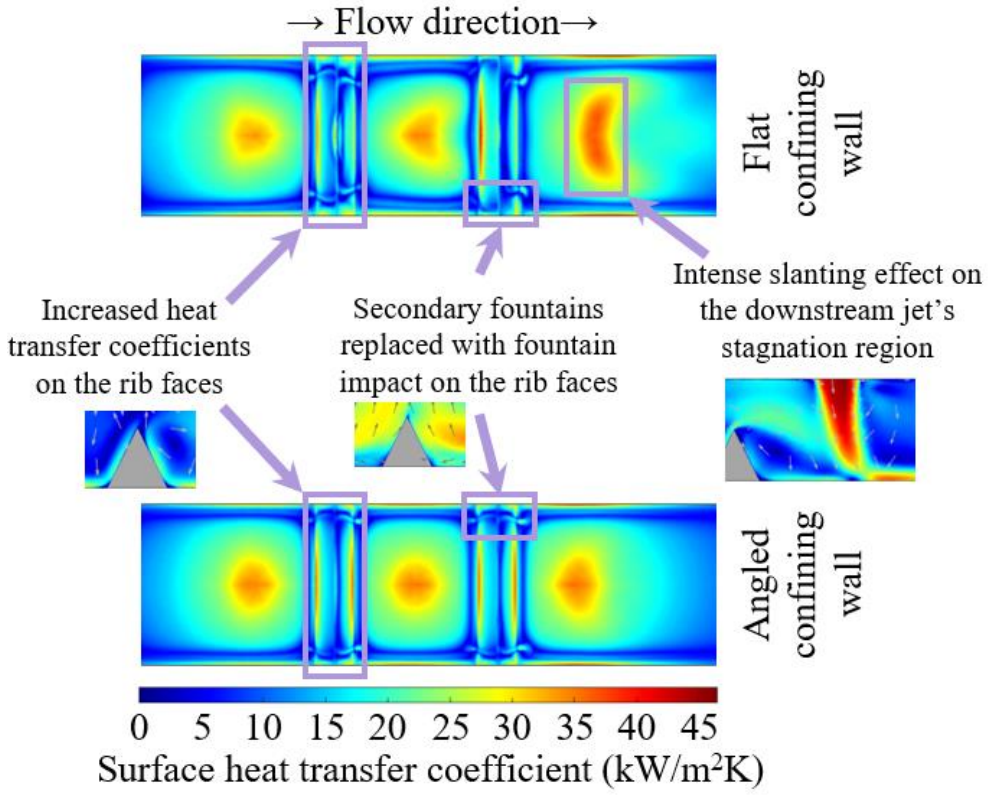

Figure 4-23: Surface heat transfer coefficient contours from the numerical model for tall transverse ribs under a flat (top) and angled (bottom) confining wall for a jet Reynolds number of 5600

Increased heat transfer coefficient values are indeed observed on the rib faces as a result of the wall jet's interaction with the structure. This is particularly strong at the base, since the wall jet region is very thin relative to the height of these tall ribs. In the fountain plane, slight improvements are observed at the rib, where the fountain flows interact with the ribs. This replaces the secondary fountain interactions seen in the unmodified and jet cone surfaces. As those secondary fountains were observed to be very weak and susceptible to crossflow effects, this is a noteworthy improvement. However, under the flat confining wall, greater slanting is observed in the downstream fountain's secondary fountain due to the flow separation problem that was found. In this case, the region provides efficient heat dissipation across a wide area, but this is not a good result. This is primarily the result of greater mass flow through the downstream nozzle created by increased pressure losses. This comes at the cost of reduced performance of the upstream jets, and the issue would become increasingly problematic in larger jet arrays. As such, these transverse ribs are not practical without some mechanism for spent fluid management.

Finally, Table 4-5 below displays the average thermal performance parameters for the transverse rib modification cases.

Table 4-5: Average thermal performance parameters for the transverse rib modifications

Wall angle	Rib height	Re_j	Percent change in the surface area from the baseline case	Average surface heat transfer coefficient (kW/m^2K)	Percent change in the surface heat transfer coefficient from the baseline case	Average surface temp. rise (°C)	Percent reduction in the surface temp. rise from the baseline case	Percent of thermal improvement not attributable to increased surface area
Flat (0°)	Short	5600	3.5	12.5	2.9	13.4	6.1	45.0
		8400		16.5	1.9	10.1	5.1	34.9
		11200		20.6	3.8	8.1	6.9	51.3
		14000		24.2	3.4	6.9	6.5	48.4
	Tall	5600	10.3	12.4	2.1	12.6	11.2	16.6
		8400		16.6	2.4	9.4	11.5	18.6
		11200		20.4	3.1	7.6	12.1	22.7
		14000		24.1	3.0	6.5	12.0	22.0
Angled (7.5°)	Short	5600	3.5	11.8	2.4	14.1	5.6	39.9
		8400		15.4	2.1	10.8	5.2	36.4
		11200		18.7	1.6	8.9	4.8	30.8
		14000		21.9	1.0	7.6	4.3	22.2
	Tall	5600	10.3	11.8	2.4	13.3	11.4	18.3
		8400		15.4	2.1	10.1	11.2	16.6
		11200		18.7	1.6	8.3	10.8	13.3
		14000		21.9	1.1	7.1	10.3	9.6

The short and tall rib modifications created surface area increases of 3.5 and 10.3%, respectively. While the rib structures under the flat wall provided surface heat transfer coefficient increases of 1.9-3.8% and temperature rise reductions of 5.1-12.1%, these results do not supersede the previous findings. These structures, particularly the tall version, need a spent fluid management strategy to provide the best performance. Under the angled confining wall, these structures provided similar improvements of 1-2.4% in the surface heat transfer coefficient and 4.3-11.4% in the surface temperature. These are also the first modifications examined to yield benefits beyond a surface area increase for all angled wall cases, highlighting their benefits when combined with effective spent fluid management. While improvements are achieved in some cases, the streamwise ribs are more promising, as shown in Figure 4-24.

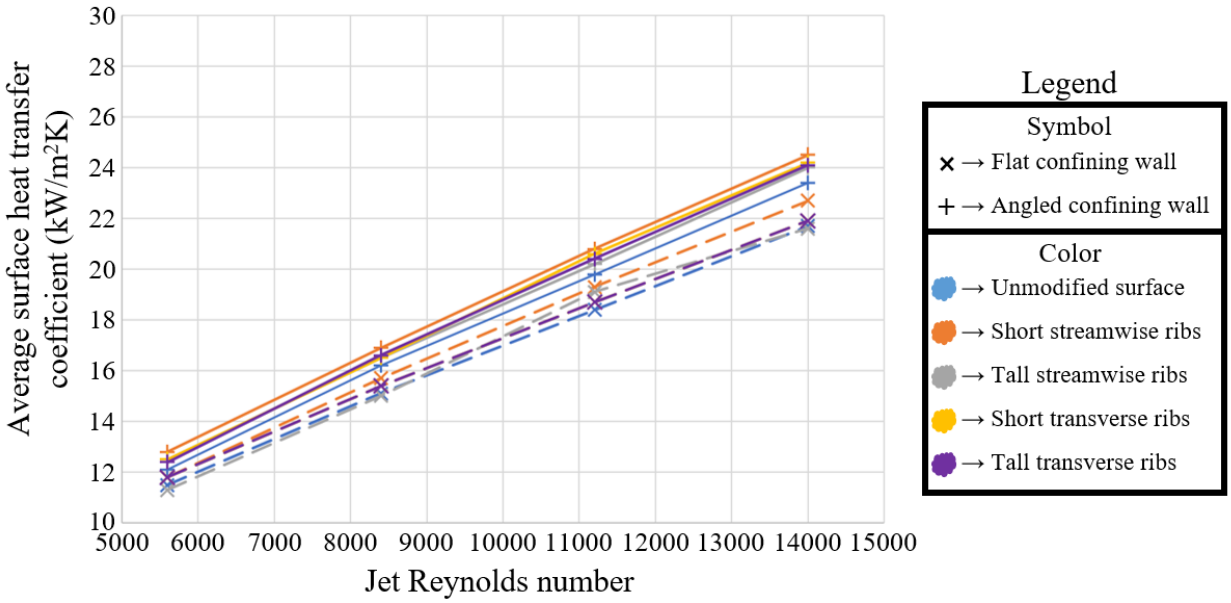

Figure 4-24: Surface heat transfer coefficient versus jet Reynolds number from the numerical model for the both the streamwise and transverse ribs

Regardless of the wall angle, the short transverse ribs provide the greatest heat transfer coefficient increases. While the tall streamwise ribs create the lowest improvements, this is primarily due to them increasing the total surface area by the greatest amount. Meanwhile, the transverse ribs provide marginal improvements in all cases, with detrimental flow effects occurring under the flat wall. As such, while the transverse ribs are beneficial under an angled confining wall, the streamwise ribs are more flexible and promising in their application.

These transverse ribs were observed to be effective at increasing heat transfer from regions away from the impinging jets. The wall jets effectively impinge on the rib faces, providing increased surface heat transfer coefficients on the extended surface. However, reduced cross-sectional area when applied under the angled wall had a negative impact on the array's performance. Pressure losses were increased by over 9% and flow through the nozzles was uneven. However, applying the ribs under the angled wall resulting in improved thermal performance without negatively impacting the flow mechanics. As such, these transverse ribs can be applied to jet impingement arrays with some form of crossflow management, but would not be ideal when crossflow effects are significant.

4.5 Offset Cones

As the transverse ribs were observed to be only applicable in conjunction with spent flow management, their applications are limited. However, their ability to enable wall jet interactions with the rib faces were promising. The source of the problem seen under the flat confining wall was reduced cross-sectional area for flow. Rather than applying ribs across the entire cross-section, cone structures, similar to the jet cones, could be applied between jets in the outflow direction. In doing so, Wall jet interactions could be centralized between jets without increasing crossflow effects. These structures will be referred to as "offset" cones, as they are offset from the nozzles in the outflow direction.

4.5.1 Offset Cones – Flow Mechanics

Figure 4-25 below displays the flow fields in the jet plane when tall offset cones are applied under a flat wall.

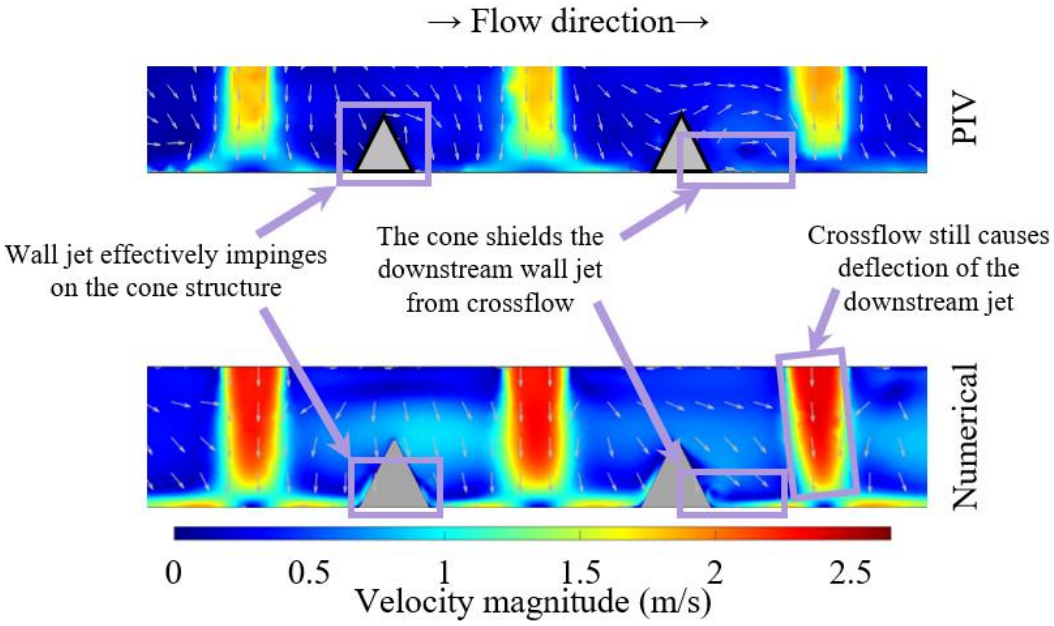

Figure 4-25: Jet plane velocity vector fields and contours for tall offset cones under a flat confining wall at a jet Reynolds number of 5600

At the base of the cones, the wall jet regions still effectively impinge on the cone's face. This will increase heat transfer from this area, though to a lesser extent than the ribs. Downstream, the cone is seen to shield the wall jets from crossflow effects, allowing more fluid from the furthest downstream jet to move upstream and interact with the cone. Due to this shielding, increased heat dissipation can be expected not only from the cone, but also in the space between the furthest downstream cone and jet. Since the cones do not extend across the entire cross-section, there is sufficient area for fluid motion around the cones, avoiding the flow separation problem created by the transverse ribs. It is noteworthy that, despite the flow benefits provided by these cones, crossflow effects are still evident in the downstream jet. It can be concluded the surface structure modifications are not effective crossflow mitigation strategies. Successful crossflow diverters investigated by He et al. and Madhavan et al. spanned the entire nozzle-to-surface distance [31, 33]. Crossflow diverter designs examined in these studies spanned the entire nozzle-to-surface distance, providing full coverage of downstream jets. Evidently, these surface structures that only cover a portion of this distance are not as effective at reducing crossflow effects on the downstream jets.

Figure 4-26 shows the flow fields in the fountain plane for the offset cones under a flat wall. Though the cones are not in this plane, their locations are indicated in the numerical contour with triangles.

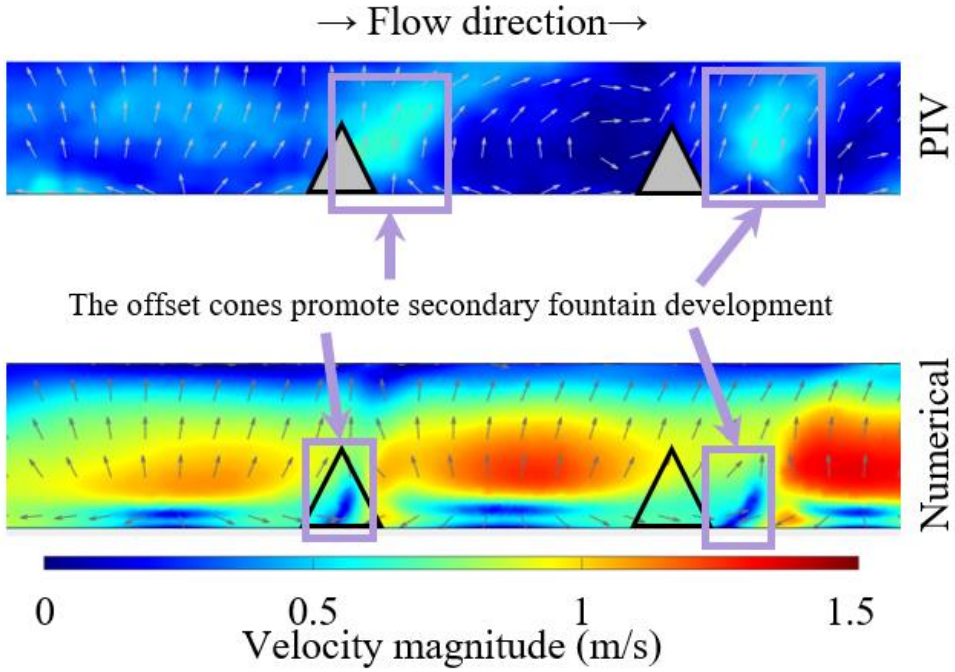

Figure 4-26: Fountain plane velocity vector fields and contours for tall offset cones under a flat confining wall at a jet Reynolds number of 5600

In this plane, the fountains are developing as normal. Notably, secondary fountain interactions are well-developed between both sets of jets. These were readily suppressed by crossflow for the unmodified surface case, indicating that these offset cones are providing flow benefits across the surface.

Flow behaviors for the offset cones under the angled wall in both the jet and fountain planes are displayed in Figure 4-27.

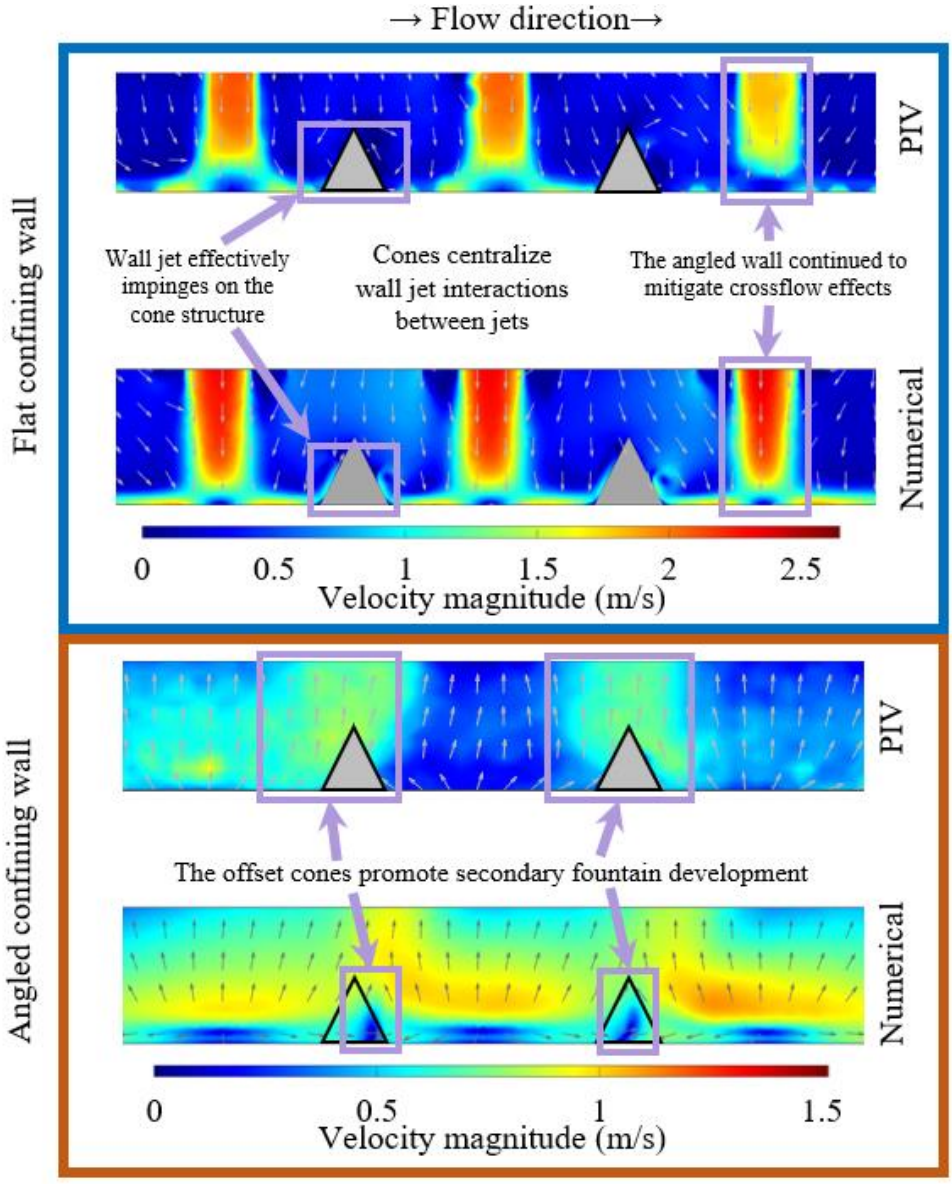

Figure 4-27: Jet and fountain plane velocity vector fields and contours for tall offset cones under an angled confining wall at a jet Reynolds number of 5600

In the jet plane, wall jet interactions are observed on the cone structures, as was the case under the flat wall and for the transverse ribs under the angled wall. Crossflow is again reduced by the angled wall. These results were expected based on prior findings. Of more import is that secondary fountains are also well-developed in the fountain plane, indicating that this improvement is not exclusive to the flat confining wall. As such, these cones appear promising, regardless of the confining wall angle or spent fluid management strategy.

As might be expected of these structures, pressure loss effects were negligible. Under the flat confining wall, pressure gains were all less than 1%. The short offset cones caused pressure loss variations of less than 0.2% under the angled wall; however, the tall offset cones under the angled wall reduced pressure losses by 1.1-1.9%, though this is still minimal.

4.5.2 Offset Cones – Thermal Characteristics

The offset cones show promising results in flow mechanic improvements. The surface heat transfer coefficient contours for the tall offset cones are shown in Figure 4-28.

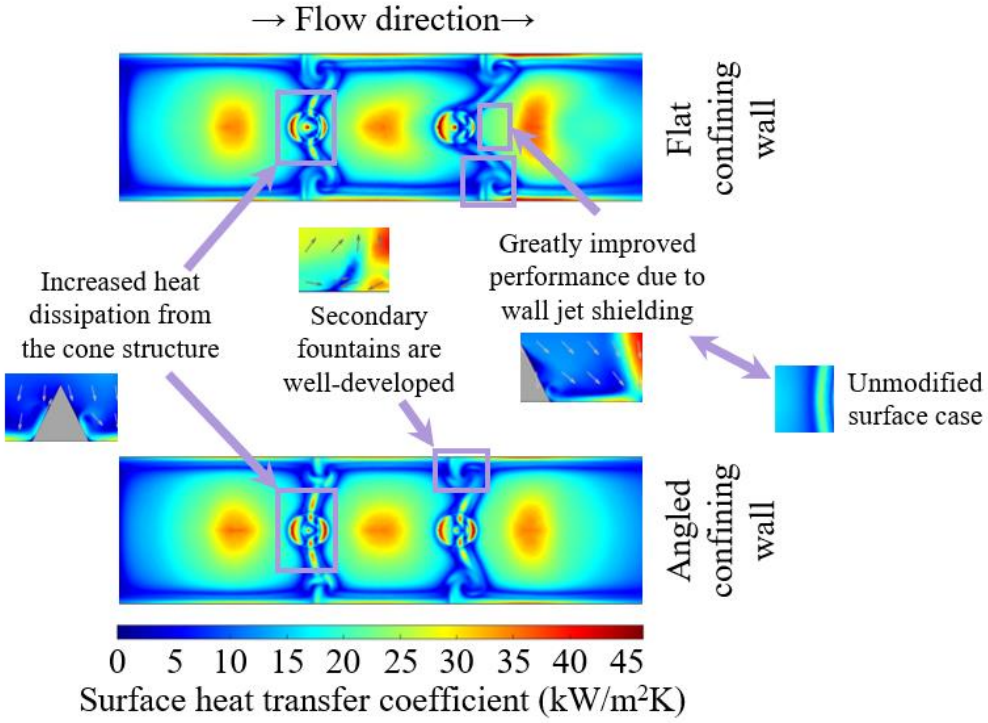

Figure 4-28: Surface heat transfer coefficient contours from the numerical model for tall offset cones under a flat (top) and angled (bottom) confining wall for a jet Reynolds number of 5600

Similar to the transverse ribs, increased heat transfer coefficients are achieved at the bases of the cones due to the wall jet's interaction with the structure. These cones act as a shield for the wall jet regions from jets downstream. This results in greatly increased performance in the area just downstream of the cones, in particular that of the downstream cone under the flat confining wall. As discussed and observed previously, thermal performance degrades with distance from the impinging jet. Under the flat confining wall with no modifications, this region was dominated by

the wall jet region from the central jet, which is much further away. By shielding the downstream wall jet, performance is greatly improved. Finally, secondary fountain interactions are apparent in the fountain regions, providing slight improvements transversely from the cones. By applying these offset cones, three improvements have been achieved in different locations across the surface, which previously saw relatively poor performance.

Finally, to examine the performance of these cones across the surface, Table 4-6 displays the average thermal surface parameters for these cases.

Table 4-6: Average thermal performance parameters for the offset cone modifications

Wall angle	Rib height	Re_j	Percent change in the surface area from the baseline case	Average surface heat transfer coefficient (kW/m²K)	Percent change in the surface heat transfer coefficient from the baseline case	Average surface temp. rise (°C)	Percent reduction in the surface temp. rise from the baseline case	Percent of thermal improvement not attributable to increased surface area
Flat (0°)	Short	5600	0.67	12.3	1.2	14.0	1.9	64.0
		8400		16.4	1.7	10.4	2.3	71.2
		11200		20.4	1.3	8.5	1.9	65.6
		14000		24.0	1.0	7.2	1.7	60.5
	Tall	5600	2.0	12.4	2.4	13.5	4.3	54.3
		8400		16.4	1.6	10.3	3.5	43.9
		11200		20.4	3.0	8.3	4.8	59.0
		14000		24.0	2.7	7.0	4.6	56.9
Angled (7.5°)	Short	5600	0.67	11.6	1.0	14.7	1.6	58.5
		8400		15.3	1.5	11.2	2.1	68.1
		11200		18.7	1.6	9.1	2.3	70.4
		14000		22.0	1.5	7.8	2.1	68.1
	Tall	5600	2.0	11.5	-0.39	14.7	1.6	<0
		8400		14.9	-0.93	11.3	1.0	<0
		11200		18.1	-1.45	9.3	0.53	<0
		14000		21.2	-2.1	8.0	-0.12	<0

These offset cones result in the smallest increases in the surface area of any observed in this effort; the short cones yield an increase of 0.67% while the tall cones increase the area by 2%. Despite the small increases in area, the average surface heat transfer coefficient increases by 1.0-1.7% for the short cones and 1.6-3% for the tall cones under the flat wall. These result in very small surface temperature reductions of 1.7-4.8%, 48-71% of which is not attributable to increased surface area. Unlike the jet cones, this additional area is not located in a region that experiences efficient heat transfer, indicating that these improvements are primarily the result of the improved flow mechanics observed for these structures. However, these improvements are less significant

under the angled wall, with improvements of less than 2.3%. The short cones were still effective at improving performance, with over half their thermal benefits arising from effects other than increased area, the tall cones under the angled wall performed far worse. The average surface heat transfer coefficient decreased when compared to the unmodified case. At low flow rates the surface temperature still decreased, but at the highest flow rate, a slight increase was observed. While the short cones provided some benefit under the angled wall, the tall cones had an excess of height, and the additional area was wasted in that location. In contrast, benefits are achieved under the flat wall regardless of the cone height, indicating that the flow improvements achieved are still noteworthy when additional height is added.

Finally, the two cone structures examined in this effort, the jet and offset cones, are compared in Figure 4-29.

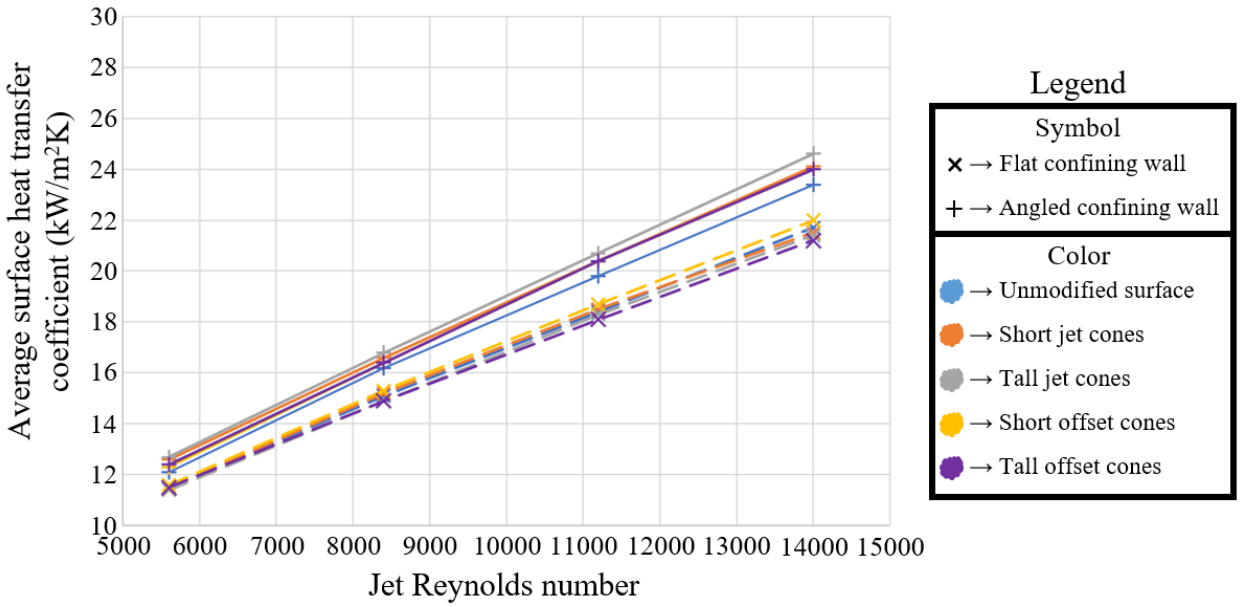

Figure 4-29: Surface heat transfer coefficient versus jet Reynolds number from the numerical model for the both the jet and offset cones

Under the flat wall, the tall jet cones provide the greatest heat transfer coefficient improvements, while the short jet cones and both heights of the offset cones provide similar, lesser improvements. However, it was observed that the jet cones showed high sensitivity to crossflow effects and misalignment. As such, the benefits afforded by the offset cones can be expected to be more reliable than those generated by the jet cones. Under the angled wall, the short offset cones are the only structures observed to provide improvement at all jet Reynolds numbers. However,

the tall cones performed worse due to the excess area penetrating above the wall jets and not effectively increasing heat dissipation. From this, it can be concluded that the offset cones are more likely to provide benefits to a variety of systems, as they have been observed to provide thermal improvements under both wall angles without any negative effect on flow mechanics.

These offset cones have been shown to be effective particularly under the flat confining wall. While their total thermal improvements are small relative to those of the other examined modified surfaces, the benefits achieved by the offset cones are primarily the result of improved flow mechanics. Wall jet interactions with the cones increase dissipation from the structure. Shielding of the wall jet region created by the downstream jet significantly increases the heat transfer coefficient immediately downstream of each cone. Finally, the promotion of secondary fountain development increases heat dissipation transversely from each cone, in a region that previously experienced poor performance. While the tall cones were excessive under the angled confining wall, the short cones were also effective, suggesting that these cones can provide benefits in a variety of systems.

4.6 Streamwise Ribs and Offset Cones

Based on the results from the individual surface modification testing, it was determined that a combination of the streamwise ribs and offset cones would be most promising for further analysis. While the jet cones provided notable thermal benefits by increasing the surface area in the stagnation region, their alignment under the jets required high precision and they would unequally deflect fluid radially in slight crossflow. Meanwhile, the transverse ribs reduced the cross-sectional area for outflow, resulting in magnified crossflow effects and increased pressure losses. However, the streamwise ribs provided significant benefits near the fountain plane due to wall jet interactions with the rib face with a negligible effect on pressure losses, and the offset cones shielded downstream wall jets and promoted secondary fountains, improving performance downstream and transversely from each cone. Combinations of these modifications were examined with the same base and height dimensions examined previously. The short cones were combined with the short ribs and the tall cones were examined with the tall ribs; mismatched modification height cases were not examined.

PIV analysis was not completed using this combined surface. As previously discussed, the streamwise ribs would block visualization near the surface for the central set of jets, requiring visualization of the nearest set of jets to be completed, which would reduce the significance of the gathered data. It was also anticipated that a combination of these structures would have little effect on the flow mechanics in the jet plane, regardless. The streamwise ribs had negligible effects on flow mechanics in the jet plane, and this was expected to remain true. Finally, by applying the streamwise ribs, the results in the fountain plane would be less meaningful, as flow effects detected above the ribs would be far less impactful on the thermal performance. As such, analysis of this combination case was only completed using the numerical model.

It was observed that flow behaviors under the flat confining wall were indeed found to change negligibly. Flow mechanics in the jet plane closely followed those seen for the offset cone case, while mechanics in the fountain plane followed those in the streamwise ribs case. This, however, was not the case for the combination under the angled confining wall, as shown in Figure 4-30.

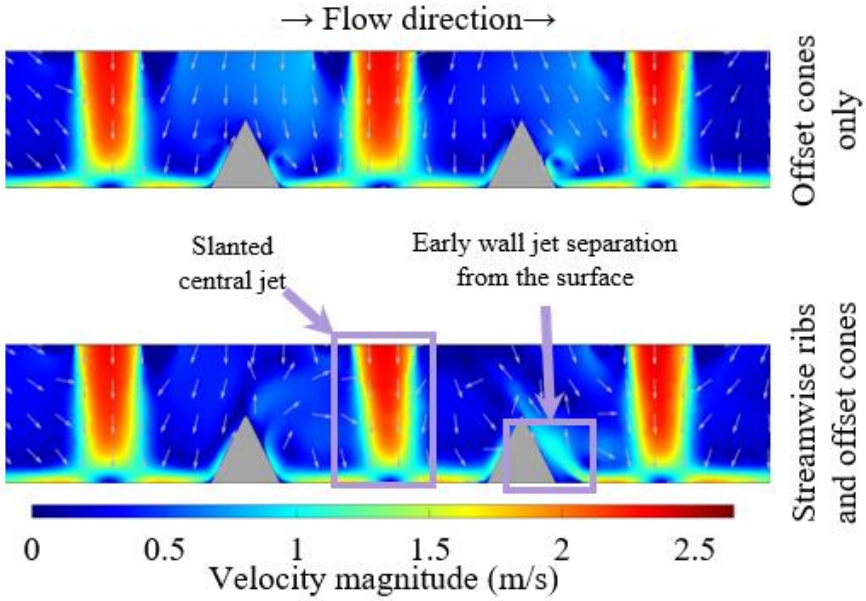

Figure 4-30: Comparison of the numerically calculated jet plane flow behaviors for the tall offset cones and the combination of the tall offset cones and tall streamwise ribs under an angled confining wall for a jet Reynolds number of 5600

Comparing the combination case to the offset cones only reveals two key differences: slanting of the central jet and early separation of the wall jet from the surface for the downstream jet. These behaviors can be expected to have negative impacts on the thermal performance for this

case, but the reason for their appearance could not be determined. The streamwise ribs were not observed to affect the jet plane in any meaningful way except in this case, combined with the offset cones under an angled confining wall. While flow behaviors were affected in the jet plane, the fountain plane trends did not vary in any meaningful manner.

Pressure losses changed little when the combination was applied. Under the flat wall, pressure losses were increased by 3-3.6%, likely due to the combination creating a reduction in the flow area in two locations. Under the angled wall, negligible pressure loss reductions of less than 1.3% resulted in each case.

The surface heat transfer coefficient contours for the combined surface are shown in Figure 4-31.

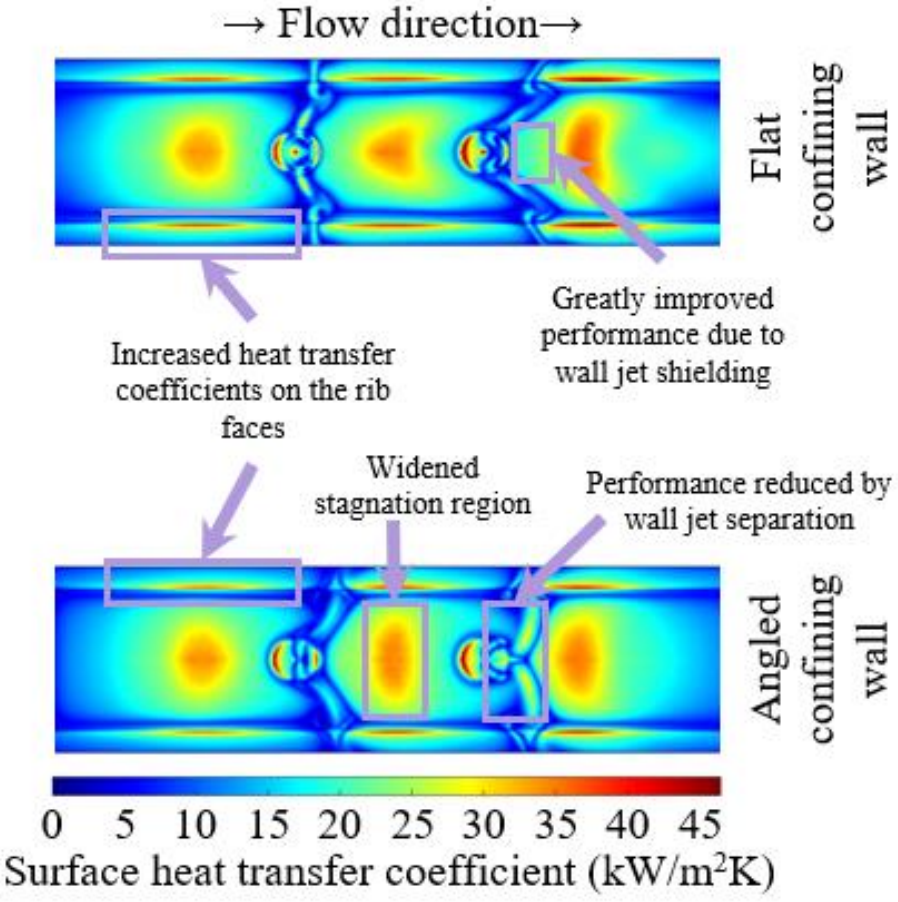

Figure 4-31: Surface heat transfer coefficient contours from the numerical model for combined tall offset cones and tall streamwise ribs under a flat (top) and angled (bottom) confining wall for a jet Reynolds number of 5600

As seen prior, thermal improvements are achieved on the rib faces for both wall angles and downstream of the cones under the flat wall. Under the angled wall, the central jet's stagnation region has widened and performance downstream of the second cone is reduced due to the trends seen in Figure 4-30. Once again, the reason for these discrepancies is not apparent in these trends. As such, it is concluded that this combination is primarily beneficial under the flat confining wall but creates unpredictable effects under the angled wall. Average thermal performance across the surface when these combinations are applied are compiled in Table 4-7.

Table 4-7: Average thermal performance parameters for the combined offset cones and streamwise ribs

Wall angle	Rib height	Re_j	Percent change in the surface area from the baseline case	Average surface heat transfer coefficient (kW/m^2K)	Percent change in the surface heat transfer coefficient from the baseline case	Average surface temp. rise (°C)	Percent reduction in the surface temp. rise from the baseline case	Percent of thermal improvement not attributable to increased surface area
Flat (0°)	Short	5600	11	12.9	6.9	12.0	15.7	36.9
		8400		17.1	6.0	9.0	15.0	34.0
		11200		21.0	6.2	7.4	15.2	34.5
		14000		24.8	6.0	6.3	15.0	33.7
	Tall	5600	33	12.7	5.1	10.2	28.4	12.8
		8400		16.9	4.3	7.7	27.9	11.1
		11200		20.8	4.9	6.2	28.2	12.3
		14000		24.6	5.3	5.3	28.5	13.2
Angled (7.5°)	Short	5600	11	11.9	3.2	13.1	12.8	22.1
		8400		15.6	3.7	9.9	13.1	24.3
		11200		19.2	4.1	8.1	13.5	26.2
		14000		21.1	-2.6	7.4	7.5	<0
	Tall	5600	33	11.2	-2.7	11.6	22.7	<0
		8400		15.0	-0.36	8.6	24.5	<0
		11200		18.7	1.2	6.9	25.6	3.4
		14000		22.0	1.6	5.9	25.9	4.5

Combining the offset cones and streamwise ribs results in surface area increases of 11% and 33%, depending on the modification height. Under the flat wall, the average surface heat transfer coefficient increases by 4.3-6.9%, while the average surface temperature rise reduces by 15-28.5%. These represent the best thermal improvements achieved in this effort, reflecting the surface temperature reductions afforded by the streamwise ribs and the flow benefits provided by the offset cones when applied under a flat wall. While a significant amount of these thermal improvements is attributable to increased surface area, this is to be expected based on the results

from the streamwise ribs cases. Performance under the angled wall is inconsistent, with some cases resulting in decreased heat transfer coefficients. This is likely connected to the unexpected and undesired effects observed in the flow mechanics in the jet plane. Based on these results, the transverse ribs may perform better than these offset cones when applied in combination with the streamwise ribs.

4.7 Summary

Crossflow effects under the flat confining wall were effectively managed by implementing an angled confining wall, but thermal benefits were not actualized. Modifications were more successful under the flat confining wall, likely due to them having less effect on the flow mechanics when applied under the angled wall. The jet cones improved performance under and around the jets, suggesting promising applications in hotspot cooling applications. The streamwise ribs improved performance through interaction of the wall jet regions with the rib faces, greatly reducing surface temperature rises. The transverse ribs magnified detrimental crossflow effects under the flat wall, while the offset cones were effective at shielding the wall jet region created by downstream jets. Additional results not previously displayed are shown in Appendix E, including flow fields and surface contours for the short modifications and a summary data table for the numerical calculations.

Chapter 5: Conclusions

Developments in active automotive systems, including autonomous driving, are expected to create a rise in power draw for onboard devices. Furthermore, advances in heterogeneous integration and stacked electronics limit the area available for heat dissipation while heat generation continues to increase. As a result, more aggressive thermal management strategies are required to handle anticipated heat loads. Jet impingement cooling is particularly attractive in automotive applications due to ready application in the existing water-antifreeze flow loop. Jet impingement is applicable with minimal added components, while maintaining flow rates and pressure losses within the same order of magnitude already achieved in current systems.

Thermal performance of jet impingement cooling is inherently tied to the local behaviors created by the flow. A column of fluid is directed normal to a heated surface. The fluid decelerates as it approaches the surface, forming the stagnation region. The normal motion of fluid toward the surface mitigates the thermal boundary layer, creating a zone of highly efficient heat transfer. The fluid is deflected peripherally, referred to as the wall jet, where the fluid motion becomes parallel to the surface. Heat dissipation in this wall jet decreases, as the fluid motion no longer reduces the thermal boundary layer. In arrays of impinging jets, wall jets from adjacent jets interact, mixing near the surface and deflecting heated, spent fluid from the surface in what is called a fountain. This mixing behavior results in increased heat dissipation from this interaction. While this fountain interaction was seen to cover significantly less area than the stagnation region, their location between jets promotes surface temperature uniformity. Similarly, these fountains can interact, creating a secondary fountain which can aid in achieving improved surface temperature uniformity. Finally, spent fluid from each jet must be removed from the impingement area. In the simplest systems, this spent fluid must pass by jets placed downstream. This crossflow results in deflection and oblique impingement of downstream jets, reducing performance. As such, spent fluid must be managed to achieve best performance in arrays of many jets.

This effort investigated the use of mesoscale surface modifications with the intention of promoting desired flow behaviors, mitigating crossflow effects, and providing additional area for heat dissipation. Each modification was examined under both a flat confining wall and a confining wall angled at 7.5° from the impingement surface. The angled wall was intended to provide space for spent fluid to move towards the exit without affecting downstream jets, reducing detrimental

crossflow effects. A three-by-three array of impinging deionized water jets were used for all cases. Four modification designs were investigated: cone structures under each nozzle, triangular ribs placed between the nozzles oriented parallel and normal to the outflow direction, and cone structures placed between the nozzles in the outflow direction, respectively referred to as jet cones, streamwise ribs, transverse ribs, and offset cones. The most promising two designs, the streamwise ribs and offset cones, were also combined.

Each geometry was analyzed experimentally using particle image velocimetry (PIV) flow visualization and numerically using the Transition SST model in ANSYS Fluent. PIV analysis allowed experimental flow fields to be generated for each geometry in two regions of interest: through the central row of jets in the "jet plane" and between rows of jets in the "fountain plane". The numerical model was used to generate flow fields in these same regions of interest and to analyze thermal performance across the surface.

While the angled wall was observed to effectively manage spend fluid and mitigate crossflow effects, each angled wall case performed worse than the respective flat wall case from a thermal perspective. This may be the result of applying the angled wall in a relatively small, three-by-three array, where crossflow effects are observable but not especially detrimental. This falls in line with past findings of in the group [59]. The angled confining wall increased the average surface heat transfer coefficient for a nozzle spacing of four jet diameters and a nozzle-to-surface distance of one jet diameter, a condition in which crossflow would be more impactful. However, increasing the jet spacing to six jet diameters resulted in similar performance for all wall angles, while increasing the nozzle-to-surface distance caused reduced heat transfer coefficients when the wall angled was applied. While the angled wall would have been better applied with a smaller nozzle-to-surface distance, this would have severely reduced the PIV visual window and made the modifications much more obstructive to the laser sheet; as such, a larger gap was a necessity for this effort. Furthermore, the modified surfaces provided less benefits to the angled wall cases. This is likely due to them not impacting flow mechanics as strongly as they did under the flat wall. Due to the additional space between the surface and confining wall, flow mechanics were less sensitive to surface modifications on the scale of those examined. Under the angled wall, small-scale structures or surface roughening would likely be more effective at improving thermal performance.

The jet cones were successful in increasing heat dissipation from under each jet but resulted in mixed results in other regions. In the experimental cases, even very small misalignment of the cones with the jets caused uneven deflection of fluid by the cones, weakening fountain interactions. Crossflow effects in the numerical model caused a similar problem under the flat confining wall. However, these cones were successful in promoting secondary fountain interactions, improving performance in certain regions away from the jets. The average surface heat transfer coefficient was increased by up to 5% and the average surface temperature rise was reduced by up to 7.5%. Under the flat wall, most of this performance improvement was not attributable to increased surface area, but rather that the additional area was focused in the stagnation region, where heat transfer was most efficient. Under the angled wall, the cones provided negligible effects on the heat transfer coefficient and most of the surface temperature reduction was attributed to increasing the surface area. This was likely the result of the modifications having less dramatic effects on the flow behaviors when applied under the angled wall. It can be concluded that these cones are best applied in hotspot applications, where jet interactions and crossflow effects are insignificant.

The streamwise ribs successfully increased heat dissipation in the fountain plane. This was accomplished through a combination of two effects. The wall jet region, which moved parallel to the impingement surface, would impact the rib face, effectively impinging upon it. This resulted in very efficient heat transfer from the rib base. Combined with the additional surface area, this resulted in significantly improved heat dissipation in regions that previously saw relatively poor performance. They were particularly effective in reducing the average surface temperature rise, achieving reductions of up to 26.2% when compared to the corresponding baseline, unmodified surface case. However, most of the benefits provided by these modifications was the result of adding additional surface area for heat transfer, especially for the tall ribs. As these benefits were achieved under both wall angled and with negligible changes to pressure losses, these ribs are very promising for in-line jet arrays.

The transverse ribs benefited from the same interaction with the wall jet regions, creating efficient heat transfer from their bases. However, they significantly reduced the cross-sectional area of the impingement channel when applied under a flat confining wall. This resulted in two problems. First, flow separation from the cones impacted jets downstream, essentially magnifying crossflow effects. Second, pressure losses were increased by over 9%, which also resulted in

uneven flow through the nozzles. Under the angled confining wall, this issue was resolved. Since additional space was available between the rib tips and the confining wall, the cross-sectional area reduction was less impactful, and the ribs were able to effectively deflect spent fluid away from the surface. As such, it is concluded that these transverse ribs are only applicable when some method of spent fluid management is applied.

As the transverse ribs were only selectively successful, cone structures were instead applied between the jets in the streamwise direction, termed the offset cones. These provided the benefit of shielding the wall jet regions of downstream jets from crossflow effects, allowing more fluid to move upstream. This resulted in greatly increased local heat transfer coefficients downstream of each cone. Furthermore, secondary fountain interactions were strengthened by the cones, providing improvements transversely. As a result, average surface temperature rise reductions of up to 4.8% were achieved, despite only increasing the surface area by 2%. This thermal benefit was primarily attributable to the flow mechanics improvements enabled by the cones, rather than simply increasing the surface area. While they performed better under the flat wall, they also provided some improvements under the angled wall, leading to them being considered a potential benefit to jet arrays.

Finally, the streamwise ribs and offset cones were examined together in the numerical model, as they were the most promising under both wall angles. The offset cones provided the most visually observable flow improvements while the streamwise ribs enabled the largest thermal benefits. Under the flat wall, this combination resulted in the best thermal performances in this effort, with the average surface heat transfer coefficient increasing by up to 6.9% and the average surface temperature rise reduced by up to 28.5%, when compared to the corresponding unmodified surface cases. However, an unexpected change in the flow mechanics was observed under the angled wall, which reduced performance. This supports the conclusion that these structures are more impactful on the flat wall case. Since there is less space between the impingement surface and the confining wall, these modifications were more impactful, resulting in more dramatic changes in the flow behaviors and more significant thermal improvements.

As automotive computational requirements increase, the heat generation in the power electronics will increase significantly. Application of jet impingement on the backside of the substrate has the potential to enable increased heat dissipation from these devices with minimal

added components under-the-hood. In such an array, the streamwise ribs and offset cones examined in this effort have the potential to provide significant thermal benefits with a negligible increase in pressure losses.

5.1 Suggestions for Future Work

This effort examined the application of four surface modifications under two confining wall angles. The greatest weakness of this effort is the lack of experimental validation of the thermal results. At the inception of this effort, it was intended to use an experimental system created and used in prior stages of this group's research. However, for reasons discussed in Appendix F, this was not possible. As such, it would be wise for these modified surfaces to be rigorously examined in experimental trials where thermal performance can be examined.

While the flat confining wall enabled discussion of crossflow effects, the actual crossflow created in this effort was relatively small. Some modifications, including the jet cones and transverse ribs, were readily seen to perform poorly in even slight crossflow. However, the streamwise rib and offset cone designs could be examined under increased crossflow conditions to examine their performance in larger jet array systems. This is particularly pertinent for the offset cones, as their primary benefit was shielding the downstream wall jet regions from crossflow effects.

All the modifications examined in this effort were cones and triangular ribs, which are not necessarily the best form factor for these structures. The streamwise ribs may see improved performance if a fillet was added to the base or they were changed to fins with a parabolic profile. Furthermore, the offset cones might be improved if they were changed to cylinders or dimples, which might shield the downstream jets from crossflow more effectively. These designs were seen to provide noteworthy benefits across the surface, and optimizing the form factor of these modifications can be expected to provide further benefits.

The jets examined in this effort all had a diameter of 3.18mm, but jet arrays analyzed in electronics thermal management studies are often of a much smaller scale [14, 15, 16, 19, 22, 24]. In these microjet arrays, surface modifications can be expected to have much greater effects on

thermal performance. As such, the streamwise rib and offset cone concepts should be examined in microjet arrays, as they may be more effective in arrays with a smaller scale.

Finally, research has shown that surface microstructures, including roughening, coatings, and microfins, are effective at improving thermal performance in jet impingement [49, 50, 51, 52]. However, there is a lack of studies on a combination of mesoscale and microscale structures in jet impingement. Further analysis of these structures in conjunction with micro-scale surface modification could yield an optimized surface design for thermal improvements. The mesoscale structures can be used to enable desired flow mechanics, such as wall jet interactions of the streamwise ribs or shielding provided by the offset cones. Meanwhile, microscale modifications on the rest of the surface can maximize heat dissipation from the portion of the impingement surface that does not benefit from mesoscale structures. While manufacturing of such a surface could propose a challenge, such a surface would likely yield optimized heat dissipation for an impinging jet array.

References

[1] S. Lohrasbi, R. Hammer, W. Essl, G. Reiss, S. Defregger and W. Sanz, "A Comprehensive Review on the Core Thermal Management Improvement Concepts in Power Electronics," *IEEE Access,* vol. 8, pp. 166880-166906, 2020.

[2] S. Zhang, L. Zhenfeng, H. Zhou, R. Li, S. Wang, K. Paik and P. He, "Challenges and recent prospectives of 3D heterogeneous integration," *e-Prime - Advances in Electrical Engineering, Electronics and Energy,* vol. 2, pp. 1-14, 2022.

[3] S. S. Iyer, "Heterogeneous Integration for Performance and Scaling," *IEEE Transactions on Components, Packaging, and Manufacturing Technology,* vol. 6, no. 7, pp. 973-982, 2016.

[4] T. L. Bergman, A. S. Lavine, F. P. Incropera and D. P. DeWitt, Fundamentals of Heat and Mass Transfer, 8th Edition, New Your: Wiley, 2017.

[5] "arrow.com," 31 Oct 2019. [Online]. Available: https://www.arrow.com/en/research-and-events/articles/understanding-heat-sinks-functions-types-and-more. [Accessed 27 Sept 2023].

[6] G. Moreno, S. Narumanchi, X. Feng, P. Anschel, S. Myers and P. Keller, "Electric-Drive Vehicle Power Electronics Thermal Management: Current Status, Challenges, and Future Directions," *Journal of Electronic Packaging,* vol. 114, no. 1, pp. 011004-1 to 011004-11, 2022.

[7] J. Broughton, V. Smet, R. R. Tummala and Y. K. Joshi, "Review of Thermal Packaging Technologies for Automotive Power Electronics for Traction Purposes," *Journal of Electronic Packaging,* pp. 1-11, 2017.

[8] S. Sarkar, R. Gupta, T. Roy, R. Ganguly and C. M. Megaridis, "Review of jet impingement cooling of electronic devices: Emerging role of surface engineering," *International Journal of Heat and Mass Transfer,* vol. 206, pp. 123888-1 to 123888-23, 2023.

[9] G. Wang, P. Cheng and A. E. Bergles, "Effects of inlet/outlet configurations on flow boiling instability in parallel microchannels," *International Journal of Heat and Mass Transfer,* vol. 51, no. 9-10, pp. 2267-2281, 2008.

[10] N. Fallahtafti, S. Rangarajan, Y. Hadad, C. Arvin, K. Sikka, C. H. Hoang, G. Mohsenian, V. Radmard, S. Schiffres and B. Sammakia, "Shape optimization of hotspot targeted micro pin fins for heterogeneous integration applications," *International Journal of Heat and Mass Transfer,* vol. 192, pp. 1-18, 2022.

[11] S. Jones-Jackson, R. Rodriguez, Y. Yang, L. Lopera and A. Emadi, "Overview of Current Thermal Management of Automotive Power Electronics for Transaction Purposes and Future Directions," *IEEE Transactions on Transportation Electrification,* vol. 8, no. 2, pp. 2412-2028, 2022.

[12] Y. Han, B. L. Lau, G. Tang and H. Chen, "Si Micro-fluid Cooler with Jet-Slot Array for Server Processor Direct Liquid Cooling," *IEEE Transactions on Components, Packaging and Manufacturing Technology,* vol. 10, no. 2, pp. 255-262, 2020.

[13] Y. Han, B. L. Lau, G. Tang, S. M. Low and J. Goh, "Package-level Si Micro-fluid Cooler with Enhanced Jet Array for High Performance 3D Systems," *IEEE Electronics Components and Technology Conference,* vol. 67, pp. 1-6, 2017.

[14] S. M. Walsh, B. A. Malouin, E. A. Browne, K. R. Bagnall, E. N. Wang and J. P. Smith, "Embedded Microjets for Thermal Management of High Power-Density Electronic Devices," *IEEE Transactions on Components, Packaging and Manufacturing Technology,* vol. 9, no. 2, pp. 269-278, 2019.

[15] T. Wei, H. Oprins, V. Cherman, J. Qian, I. De Wolf, E. Beyne and M. Baelmans, "High-Efficiency Polymer-Based Direct Multi-Jet Impingement Cooling Solution for High-Power Devices," *IEEE Transactions on Power Electronics,* vol. 34, no. 7, pp. 6601-6612, 2018.

[16] G. Elsinger, H. Oprins, V. Cherman, G. Van der Plas, E. Beyne and I. De Wolf, "Micro-Scale Jet Cooling: A Numerical Study on Improvement Options," *2023 22nd IEEE Intersociety*

Conference on Thermal and Thermomechanical Phenomena in Electronic Systems (ITherm), vol. 22, pp. 1-10, 2023.

[17] J. Jörg, S. Taraborelli, E. Sabelberg, R. Kneer, R. D. Doncker and W. Rohlfs, "Hot spot removal in power electronics by means of direct liquid jet cooling," *2017 16th IEEE Intersociety Conference on Thermal and Thermomechanical Phenomena in Electronic Systems (ITherm),* vol. 16, pp. 471-481, 2017.

[18] S. Jones-Jackson, R. Rodriguez, M. Gokhale and A. Emadi, "Numerical Investigation of Liquid Jet Impingement for Power Electronics Cooling in Electrified Transportation," *IEEE ITHERM Conference,* vol. 20, pp. 229-236, 2021.

[19] K. Agbim, D. Pahinkar and S. Graham Jr., "Integration of Jet Impingement Cooling with Direct Bonded Copper Substrates for Power Electronics Thermal Management," *IEEE Transactions on Components, Packaging and Manufacturing Technology,* pp. 1-10, 2018.

[20] R. Leena, G. Syamkumar and M. J. Prakash, "Experimental and Numerical Analyses of Multiple Jets Impingement Cooling for High-Power Electronics," *IEEE Transactions on Components, Packaging and Manufacturing Technology,* vol. 8, no. 2, pp. 210-215, 2018.

[21] P. A. de Oliviera and J. R. Barbosa Jr., "Novel two-phase jet impingement heat sink for active cooling of electronic devices," *Applied Thermal Engineering,* vol. 112, pp. 952-964, 2017.

[22] L. E. Paniagua-Guerra, S. Sehgal, C. U. Gonzalez-Valle and B. Ramos-Alvarado, "Fractal channel manifolds for microjet liquid-cooled heat sinks," *International Journal of Heat and Mass Transfer,* vol. 138, pp. 257-266, 2019.

[23] A. Kaood, I. O. Elhagali and M. A. Hassan, "Investigation of high-efficiency compact jet impingement cooling modules for high-power applications," *International Journal of Thermal Sciences,* vol. 184, pp. 108006-1 to 108006-13, 2023.

[24] R. Kempers, J. Colenbrander, W. Tan, R. Chen and A. J. Robinson, "Experimental characterization of a hybrid impinging microjet-microchannel heat sink fabricated using

high-volume metal additive manufacturing," *International Journal of Thermofluids,* Vols. 5-6, pp. 100029-1 to 100029-11, 2020.

[25] B. Kwon, T. Foulkes, T. Yang, N. Miljkovic and W. P. King, "Air Jet Impingement Cooling of Electronic Devices Using Additively Manufactured Nozzles," *IEEE Transactions on Components, Packaging and Manufacturing Technology,* vol. 10, no. 2, pp. 220-229, 2010.

[26] A. Pappaterra, B. Vandevelde, M. Nazemi, W. Verleysen and H. Oprins, "Advanced (Metal 3D-Printed) Direct Liquid Jet-Impingement Cooling Solution for Autonomous Driving High-Performance Vehicle Computer (HPVC)," *International Conference on Thermal, Mechanical and Multi-Physics Simulation and Experiments in Microelectronics and Microsystems,* vol. 22, pp. 1-14, 2021.

[27] T. Wei, H. Oprins, V. Cherman, S. Yang, I. De Wolf, E. Beyne and M. Baelmans, "Experimental Characterization of a Chip-Level 3-D Printed Microjet Liquid Impingement Cooler for High-Performance Systems," *IEEE Transactions on Components, Packaging and Manufacturing Technology,* vol. 9, no. 9, pp. 1815-1824, 2019.

[28] N. T. Obot and T. A. Trabold, "Impingement Heat Transfer within Arrays of Circular Jets: Part 1 - Effects of Minimum, Intermediate, and Complete Crossflow for Small and Large Spacings," *Transactions of the ASME,* vol. 109, pp. 872-879, 1987.

[29] C. Corvera and S. Mahjoob, "Analysis of Jet and Cross Flow Interaction with Application in Hotspot Electronics Cooling," *2022 21st IEEE Intersociety Conference on Thermal and Thermomechanical Phenomena in Electronic Systems (iTherm),* pp. 1-9, 2022.

[30] C. Corvera and S. Mahjoob, "Thermal-Fluid Study of Jet-in-Crossflow Cooling in Comparison with Pure Jet Impingement and Pure Crossflow Cooling Methods Applicable in Hotspot Treatment," *2023 22nd IEEE Intersociety Conference on Thermal and Thermomechanical Phenomena in Electronic Systems (ITherm),* vol. 22, pp. 1-9, 2023.

[31] J. He, Q. Deng, K. Xiao and Z. Feng, "Heat Transfer Enhancement of Impingement Cooling by Different Crossflow Diverters," *Journal of Heat Transfer,* vol. 144, no. 4, pp. 1-53, 2022.

[32] J. F. Fan, W. K. Ding, J. F. Zhang, Y. L. He and W. Q. Tao, "A performance evaluation plot of enhanced heat transfer techniques oriented for energy-saving," *International Journal of Heat and Mass Transfer,* vol. 52, pp. 33-44, 2009.

[33] S. Madhavan, K. R. Ramakrishnan, P. Singh and S. Ekkad, "Jet Impingement Heat Transfer Enhancement by U-Shaped Crossflow Diverters," *ASME. J. Thermal Sci. Eng. Appl.,* vol. 12, no. 4, pp. 041005-1 to 041005-9, 2020.

[34] N. R. Arens, M. P. Morem, J. Doom and G. J. Michna, "Reducing Crossflow Effects in Arrays of Impinging Jets," *ASME 2017 Summer Heat Transfer Conference,* pp. 1-8, 2017.

[35] M. Forster and B. Weigand, "Experimental and numerical investigation of jet impingement cooling onto a concave leading edge of a generic gas turbine blade," *International Journal of Thermal Sciences,* vol. 164, pp. 1-18, 2021.

[36] A. J. Onstad, C. J. Elkins, R. J. Moffat and J. K. Eaton, "Full-Field Flow Measurements and Heat Transfer of a Compact Jet Impingement Array With Local Extraction of Spent Fluid," *ASME. J. Heat Transfer.,* vol. 131, no. 8, pp. 082201-1 to 082201-8, 2009.

[37] D. Hobby, T. Walker, A. Rattner, C. Jacobsen, D. Sherrer and T. Bandhauer, "Comparison of Experimental and Computational Heat Transfer Characterization of Water Jet Impingement Array with Interspersed Fluid Extraction," *Heat Transfer Engineering,* vol. 42, no. 6, pp. 549-564, 2021.

[38] A. S. Rattner, "General Characterization of Jet Impingement Array Heat Sinks With Interspersed Fluid Extraction Ports for Uniform High-Flux Cooling," *ASME. J. Heat Transfer.,* vol. 139, no. 8, pp. 082201-1 to 082201-11, 2017.

[39] S. V. Ekkad and D. Kontrovitz, "Jet Impingement Heat Transfer on Dimpled Target Surfaces," *International Journal of Heat and Fluid Flow,* vol. 23, pp. 22-28, 2001.

[40] K. Kanokjaruvijit and R. F. Martinez-Botas, "Heat transfer correlations of perpendicularly impinging jets on a hemispherical-dimpled surface," *International Journal of Heat and Mass Transfer,* vol. 53, pp. 3045-3056, 2010.

[41] T. A. Trabold and N. T. Obot, "Impingement Heat Transfer within Arrays of Circular Jets: Part II - Effects of Crossflow in the Presence of Roughness Elements," *Transactions of the ASME,* vol. 109, pp. 594-601, 1987.

[42] H. A. El-Sheikh and S. V. Garimella, "Heat Transfer from Pin-Fin Heat Sinks under Multiple Impinging Jets," *IEEE Transactions on Advanced Packaging,* vol. 23, no. 1, pp. 113-120, 2000.

[43] L. G. Hansen and B. W. Webb, "Air Jet Impingement Heat Transfer from Modified Surfaces," *International Journal of Heat and Mass Transfer,* vol. 36, no. 4, pp. 989-997, 1991.

[44] A. J. C. King and T. T. Chandratilleke, "Heat Transfer Enhancement in Impinging Jets by Surface Modification," *Electronics Packaging Technology Conference,* pp. 270-272, 2004.

[45] P. Govindaraju, N. Pundir and J. Alvarado, "Numerical and experimental investigation of multi jet impingement cooling system with optimized heat sinks," *2023 22nd IEEE Intersociety Conference on Thermal and Thermomechanical Phenomena in Electronic Systems (ITherm),* vol. 22, pp. 01-09, 2023.

[46] W. Gao, J. F. Zhang, Z. G. Qu and W. Q. Tao, "Numerical investigations of heat transfer in hybrid microchannel heat sink with multi-jet impinging and trapezoidal fins," *International Journal of Thermal Sciences,* vol. 164, 2021.

[47] H. C. Cui, J. H. Xie, R. Z. Zhao, M. Z. Wang, Z. C. Liu and W. Liu, "Thermal-hydraulic performance analysis of a hybrid micro pin–fin, jet impingement heat sink with non-uniform heat flow," *Applied Thermal Engineering,* vol. 208, 2022.

[48] N. Celik, "Effects of the surface roughness on heat transfer of perpendicularly impinging co-axial jet," *Heat and Mass Transfer,* vol. 47, pp. 1209-1217, 2011.

[49] S. Madhavan, P. Singh and S. Ekkad, "Jet Impingement Heat Transfer Enhancement by Packing High Porosity Thin Metal Foams Between Jet Exit Plane and Target Surface," *ASME. J. Thermal Sci. Eng. Appl.,* vol. 11, no. 6, pp. 061016-1 to 061016-9, 2019.

[50] V. Radmard, S. Azizi, S. Rangarajan, N. Fallahtafti, C. H. Hoang, G. Mohsenian, K. Nemati, S. N. Schiffres and B. Sammakia, "Performance Analysis of Impinging Chip-Attached Micro Pin Fin Direct Liquid Cooling Package for Hotspot Targeted Applications," *2021 20th IEEE Intersociety Conference on Thermal and Thermomechanical Phenomena in Electronic Systems (iTherm),* vol. 20, pp. 220-228, 2021.

[51] S. K. Waye, S. .. Narumanchi, M. Mihalic, G. Moreno, K. Bennion and J. Jeffers, "Advanced liquid cooling for a traction drive inverter using jet impingement and microfinned enhanced surfaces," *Fourteenth Intersociety Conference on Thermal and Thermomechanical Phenomena in Electronic Systems (ITherm),* pp. 1064-1073, 2014.

[52] G. Moreno, S. Narumanchi, T. Venson and K. Bennion, "Microstructured Surfaces for Single-Phase Jet Impingement Heat Transfer Enhancement," *Journal of Thermal Science and Engineering Applications,* vol. 5, no. 3, pp. 1-9, 2013.

[53] J. F. Maddox, R. W. Knight and S. H. Bhavnani, "Liquid Jet Impingement with an Angled Confining Wall for Spent Flow Management for Power Electronics Cooling with Local Thermal Measurements," *ASME Journal of Electronic Packaging,* vol. 137, no. 3, pp. 031025-1 to 031015-9, 2015.

[54] M. A. Henry, K. E. Reid, S. H. Bhavnani, R. W. Knight, J. F. Maddox and W. D. Brannon, "Staggered and In-line Submerged Jet Arrays for Power Electronics using Variable Area Discharge Manifolds: Part I - Experimental," *2018 17th IEEE Intersociety Conference on Thermal and Thermomechanical Phenomena in Electronic Systems (ITherm),* vol. 17, pp. 410-416, 2018.

[55] K. E. Reid, M. A. Henry, R. W. Knight, S. H. Bhavnani and J. F. Maddox, "Staggered and In-line Submerged Jet Arrays for Power Electronics Using Variable Area Discharge Manifolds: Part II - Numerical," *17th Intersociety Conference on Thermal and Thermomechanical Phenomena in Electronic Systems,* vol. 17, pp. 417-423, 2018.

[56] P. J. Roache, "Perspective: A Method for Uniform Reporting of Grid Refinement Studies," *ASME. J. Fluids Eng.,* vol. 116, no. 3, pp. 405-413, 1994.

[57] N. Zuckerman and N. Lior, "Jet impingement heat transfer: Physics, correlations, and," *Advances in Heat Transfer,* vol. 39, no. 6, pp. 565-631, 2006.

[58] ANSYS, Inc., "ANSYS Fluent 12.0 Theory Guide," 23 01 2009. [Online]. Available: https://www.afs.enea.it/project/neptunius/docs/fluent/html/th/main_pre.htm.

[59] J. F. Maddox, "Liquid Jet Impingement with Spent Flow Management for Power Electronics," Ph.D. dissertation, Dept. of Mech. Eng., Auburn Univ., Auburn, Alabama, 2015.

[60] A. Sciacchitano, "Uncertainty quantification in particle image velocimetry," *Meas. Sci. Technol.,* vol. 30, pp. 092001-1 to 092001-31, 2019.

[61] T. C. Lau and G. J. Nathan, "Influence of Stokes number on the velocity and concentration distributions in particle-laden jets," *Journal of Fluid Mechanics,* vol. 757, pp. 432-457, 2014.

Appendices

Appendix A: Mechanical Drawings

The following figures are mechanical drawings of all components required to fabricate the impingement chamber used in the PIV experiments. Components that were 3D printed my have some features without dimensions. In these parts, many of the features were added and designed purely based on fitting the modular assembly together and into the chamber; these features and their dimensions are not universal and may require adjustment or improvement, depending on the machine used to manufacture them.

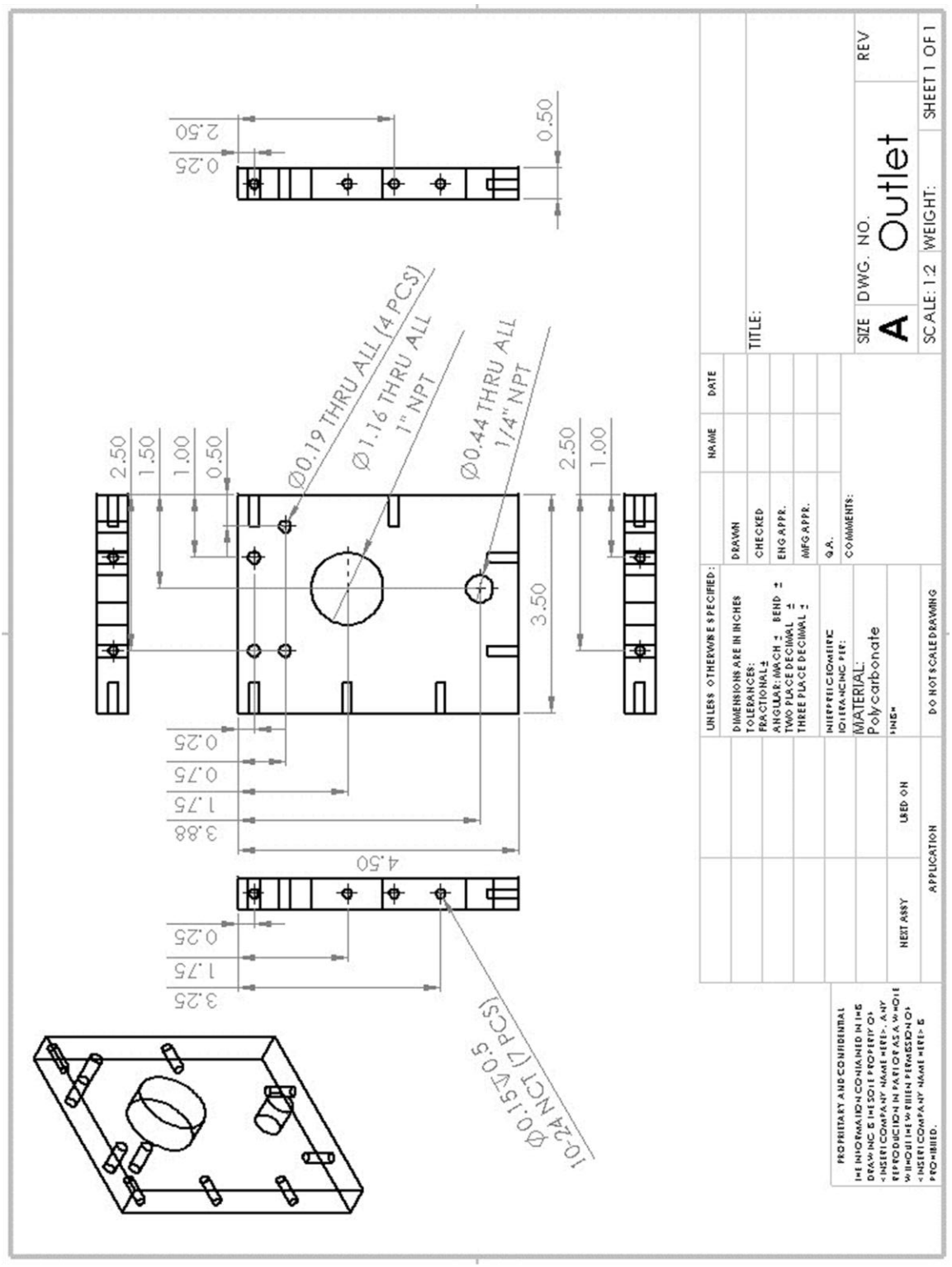

Figure A-1: Back wall mechanical drawing

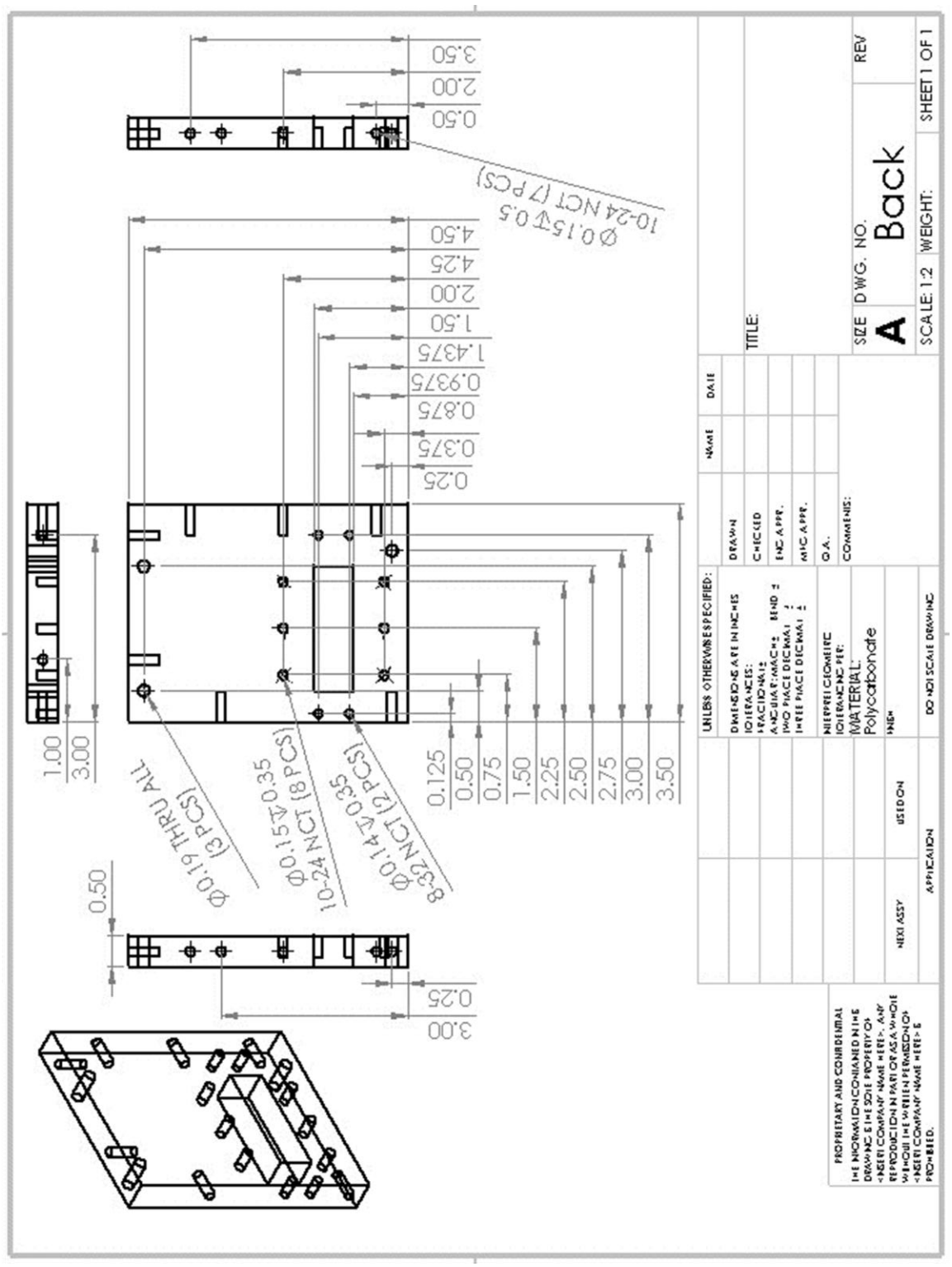

Figure A-2: Front wall mechanical drawing

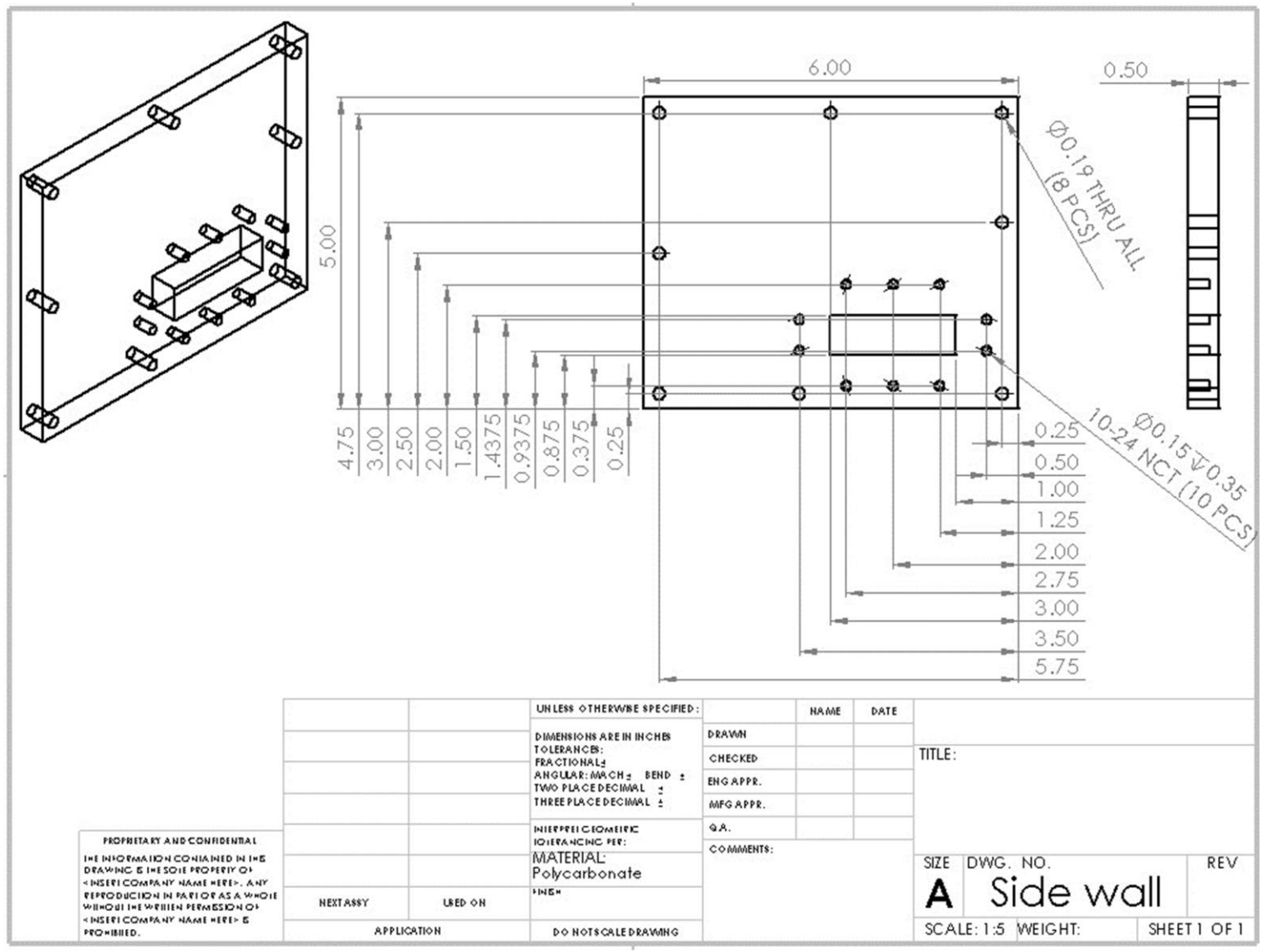

Figure A-3: Side wall mechanical drawing

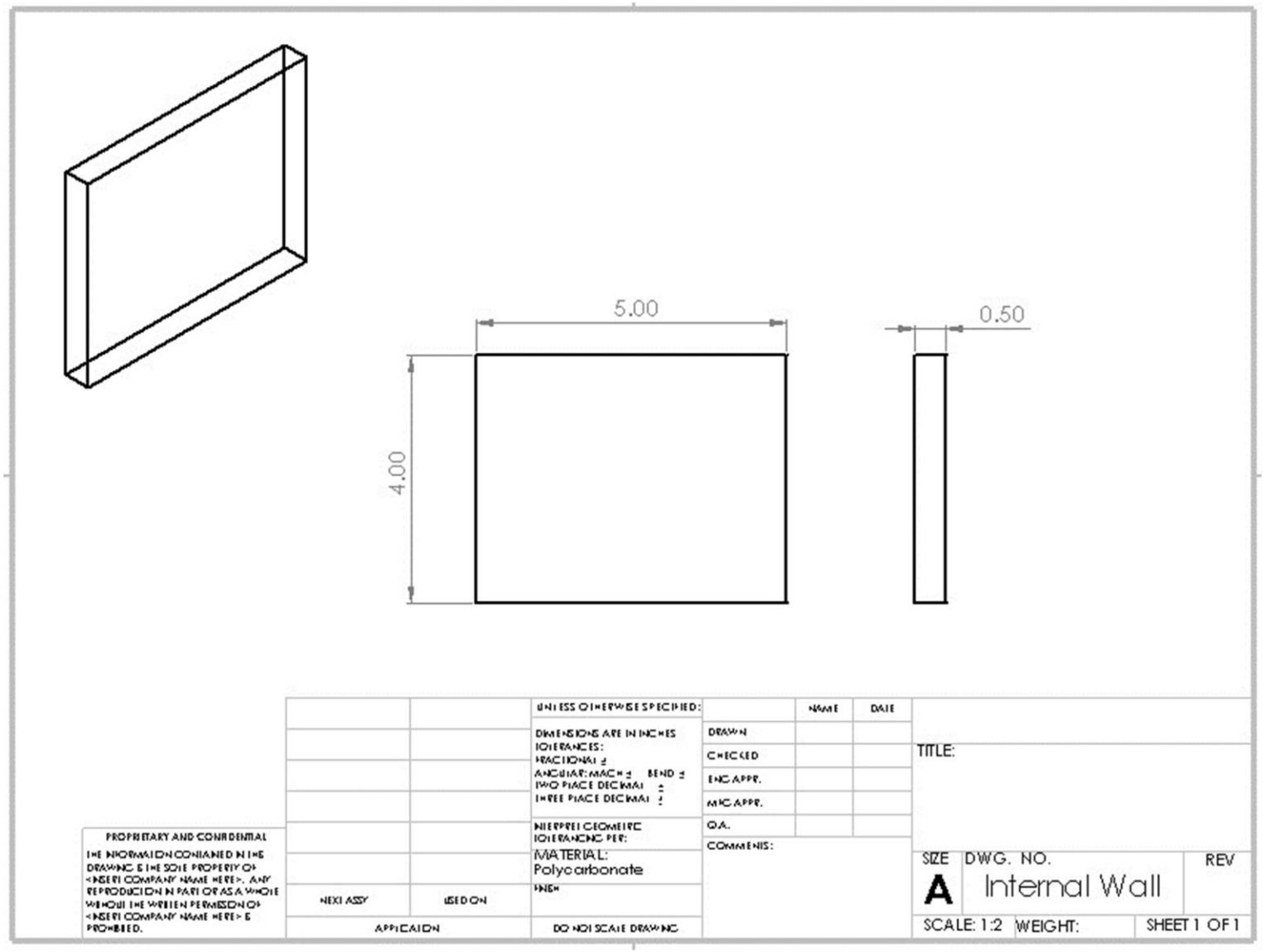

Figure A-4: Internal wall mechanical drawing

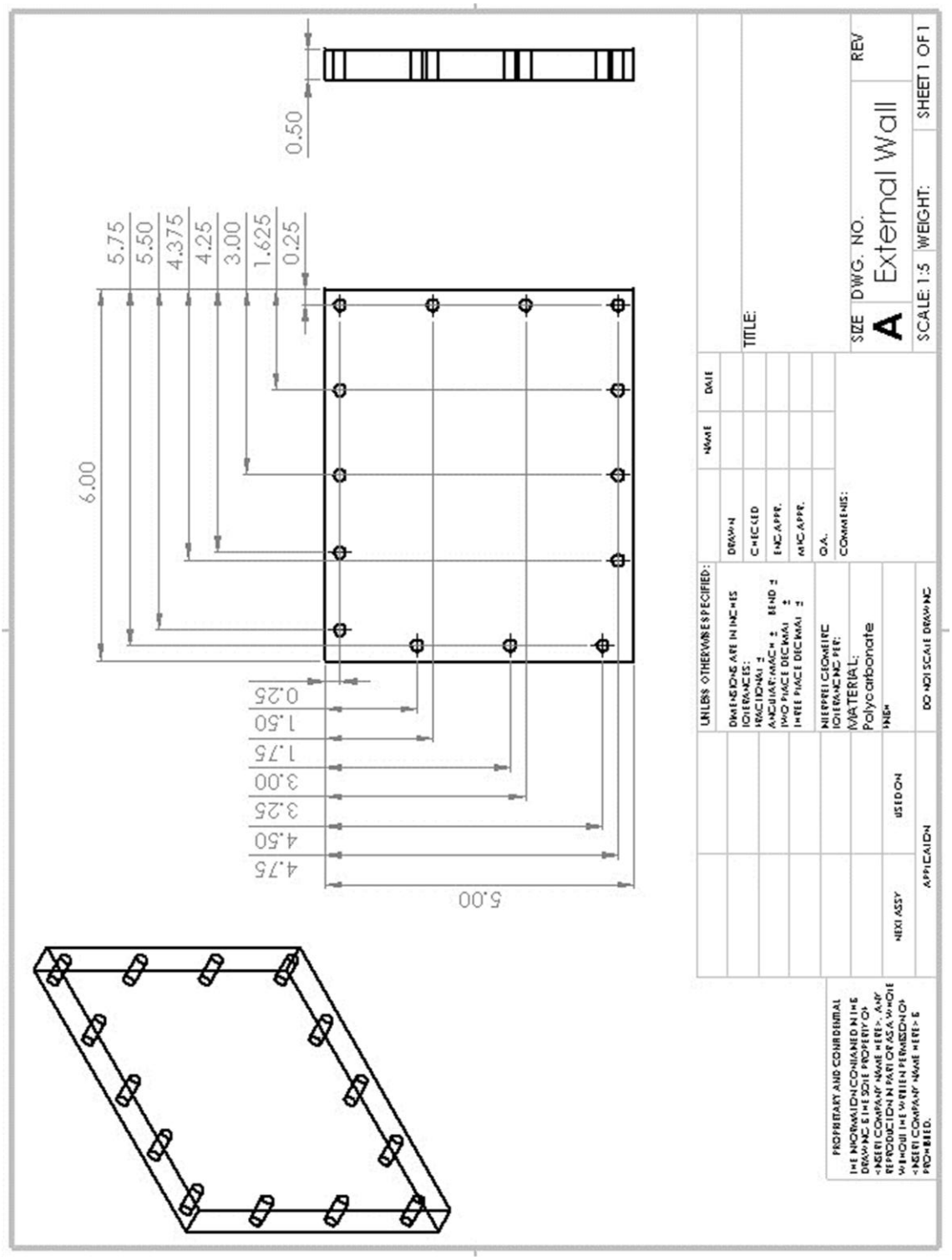

Figure A-5: External wall mechanical drawing

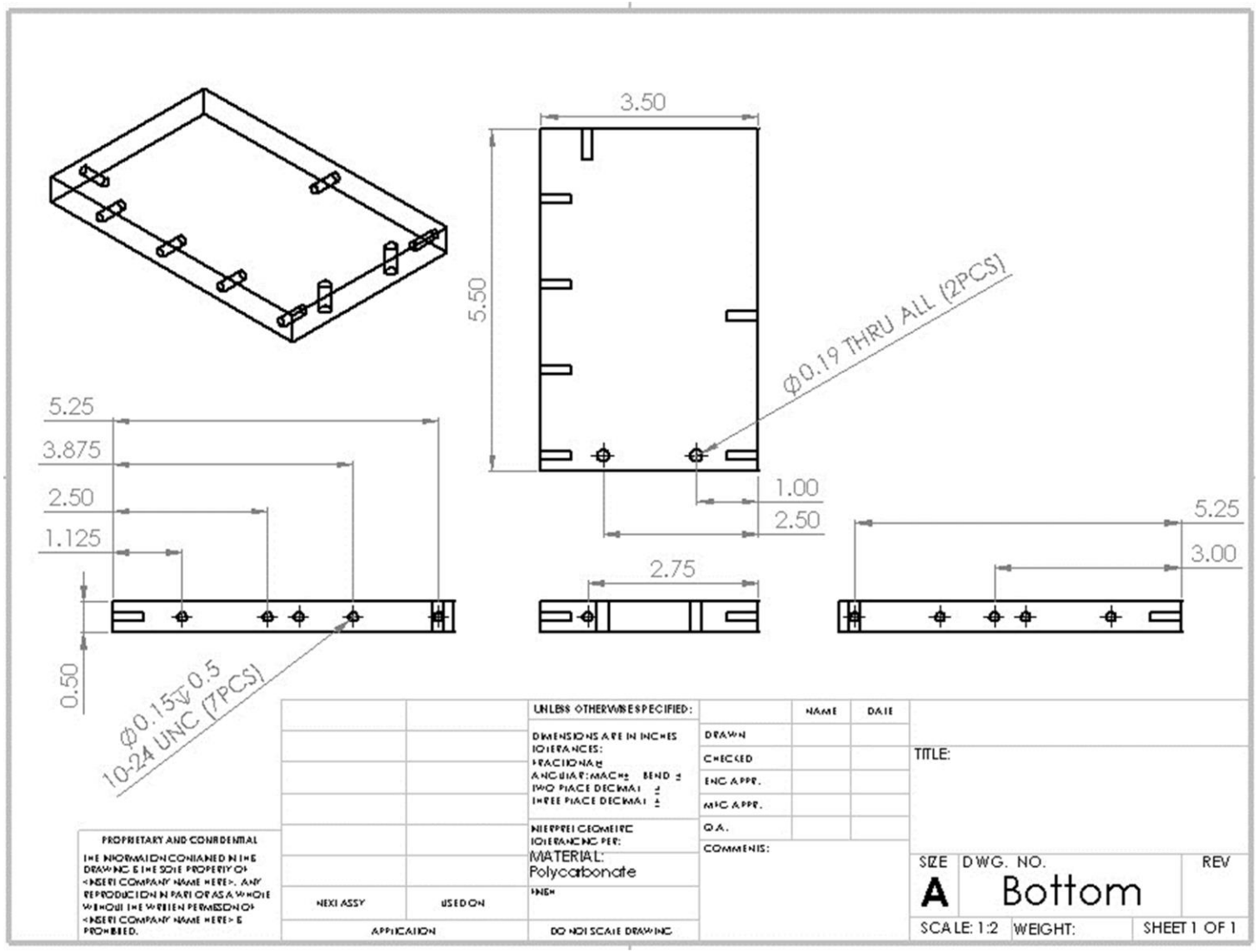

Figure A-6: Bottom wall mechanical drawing

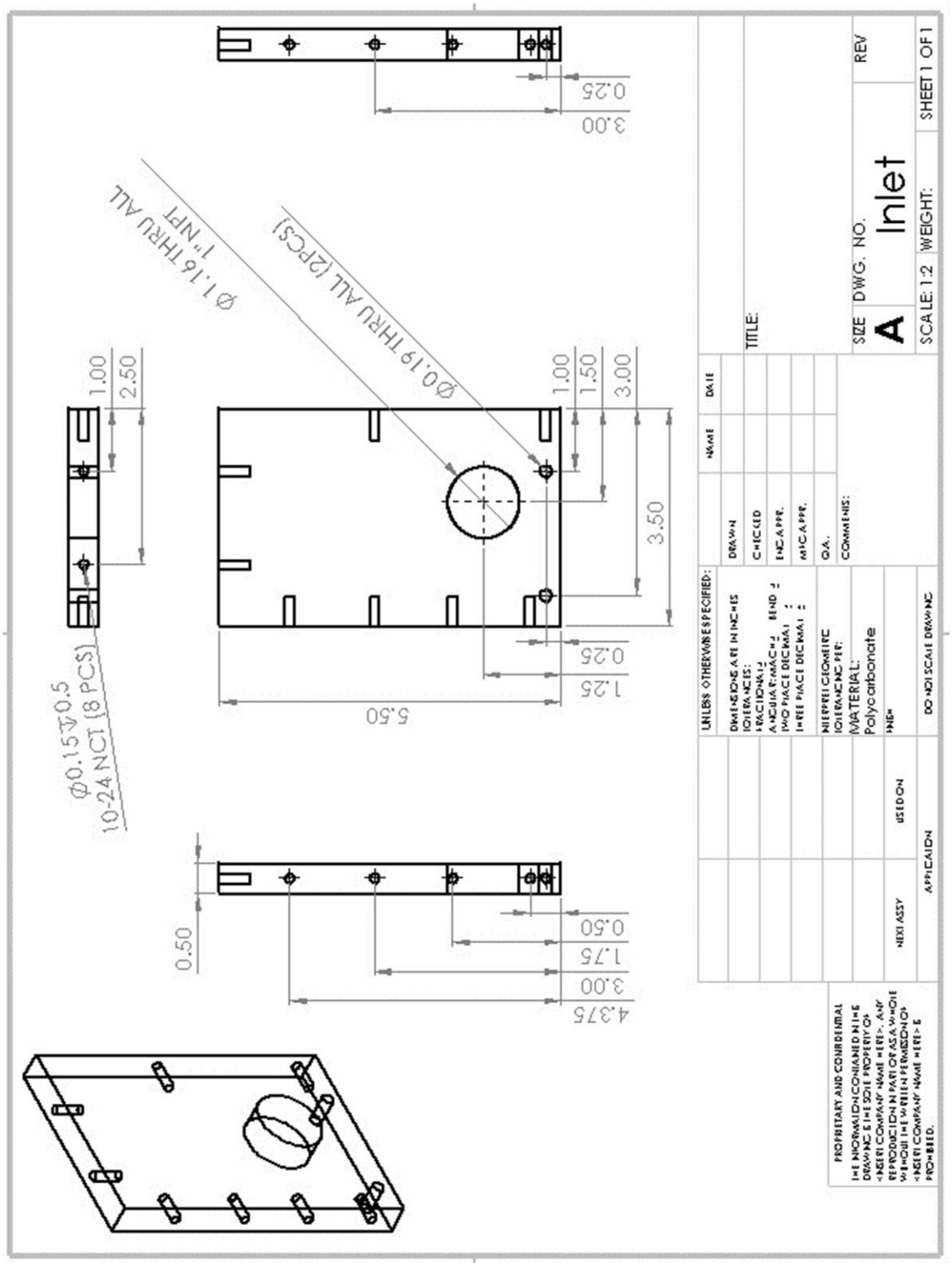

Figure A-7: Top wall mechanical drawing

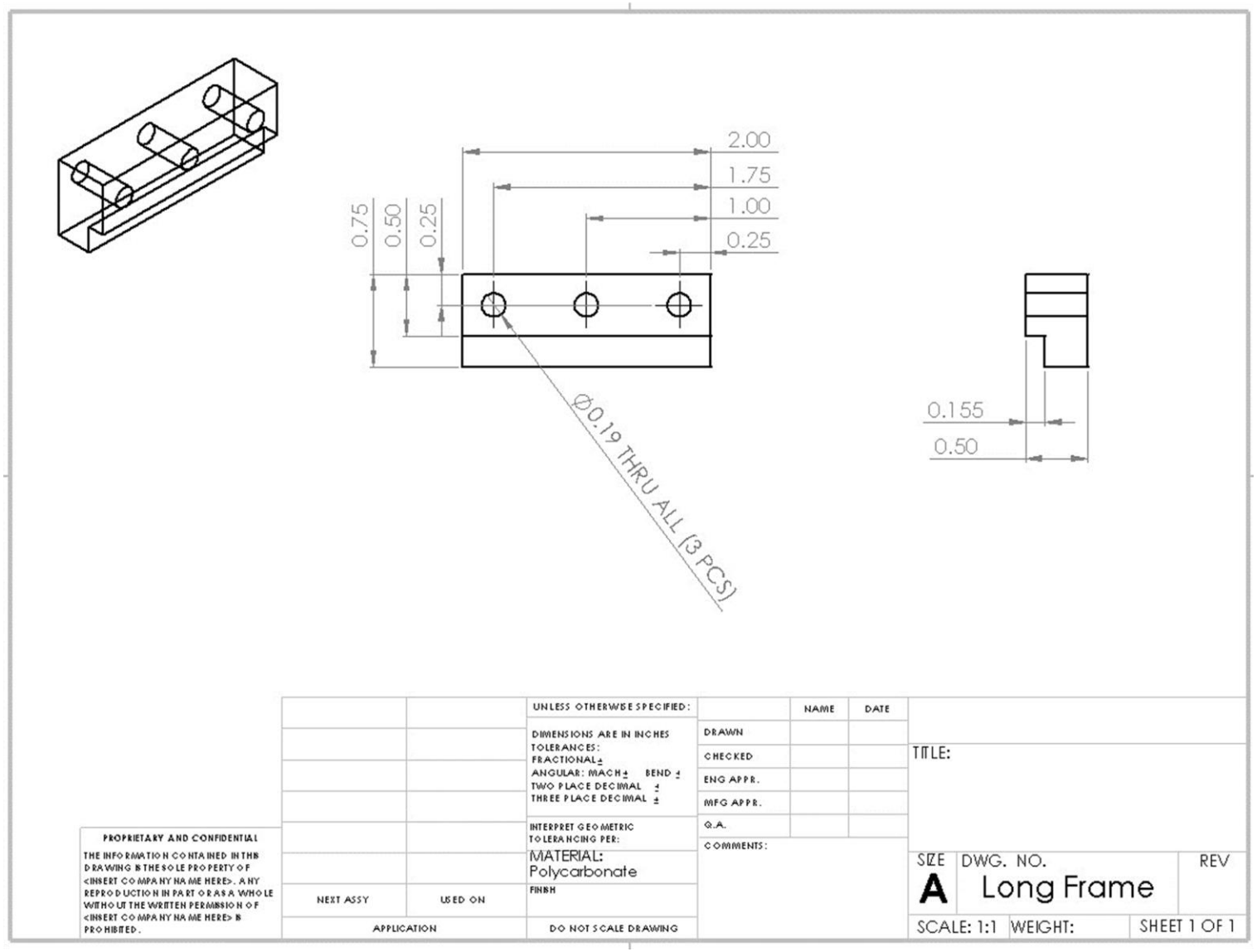

Figure A-8: Long window frame piece mechanical drawing

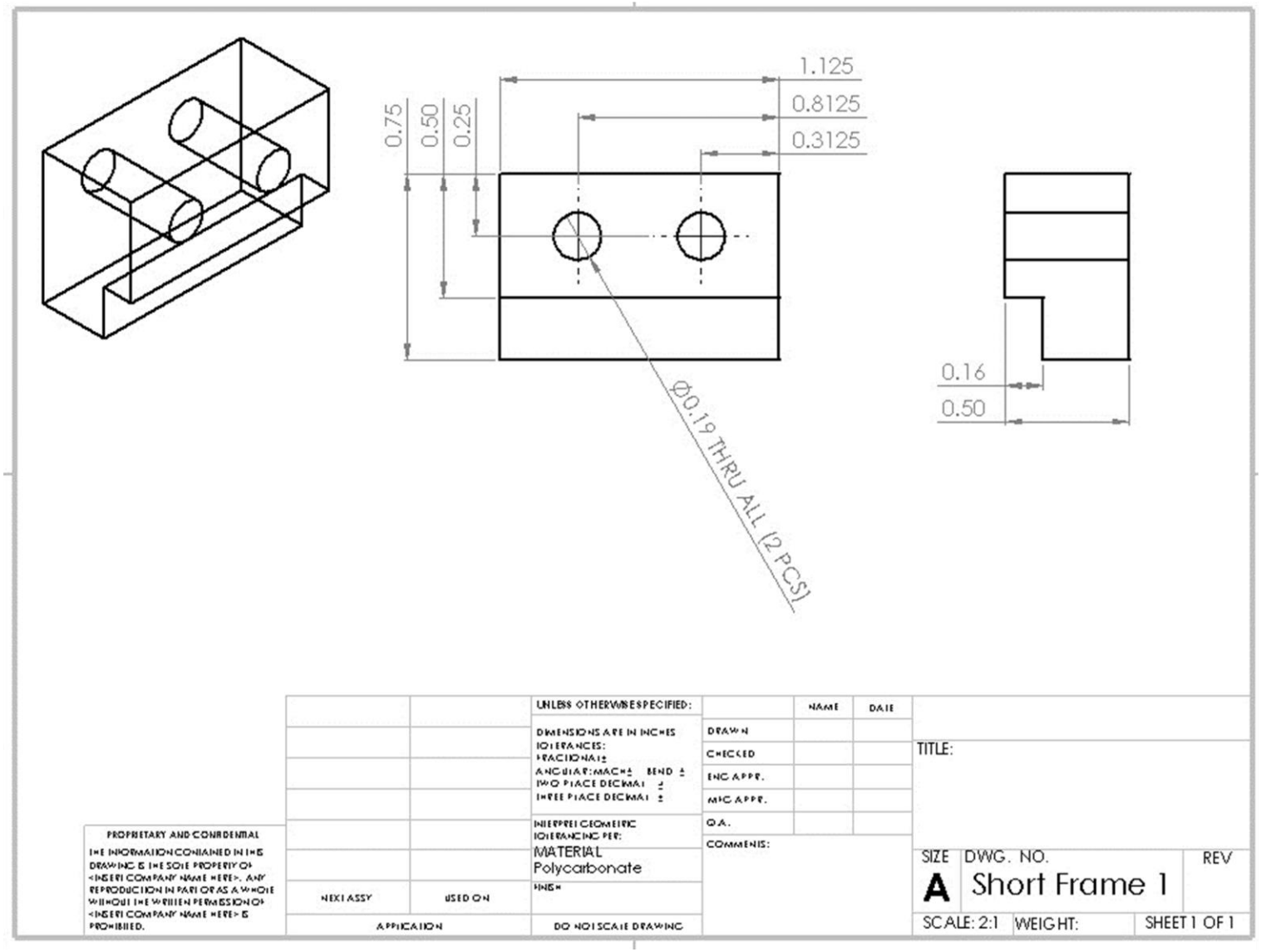

Figure A-9: Short window frame piece #1 mechanical drawing

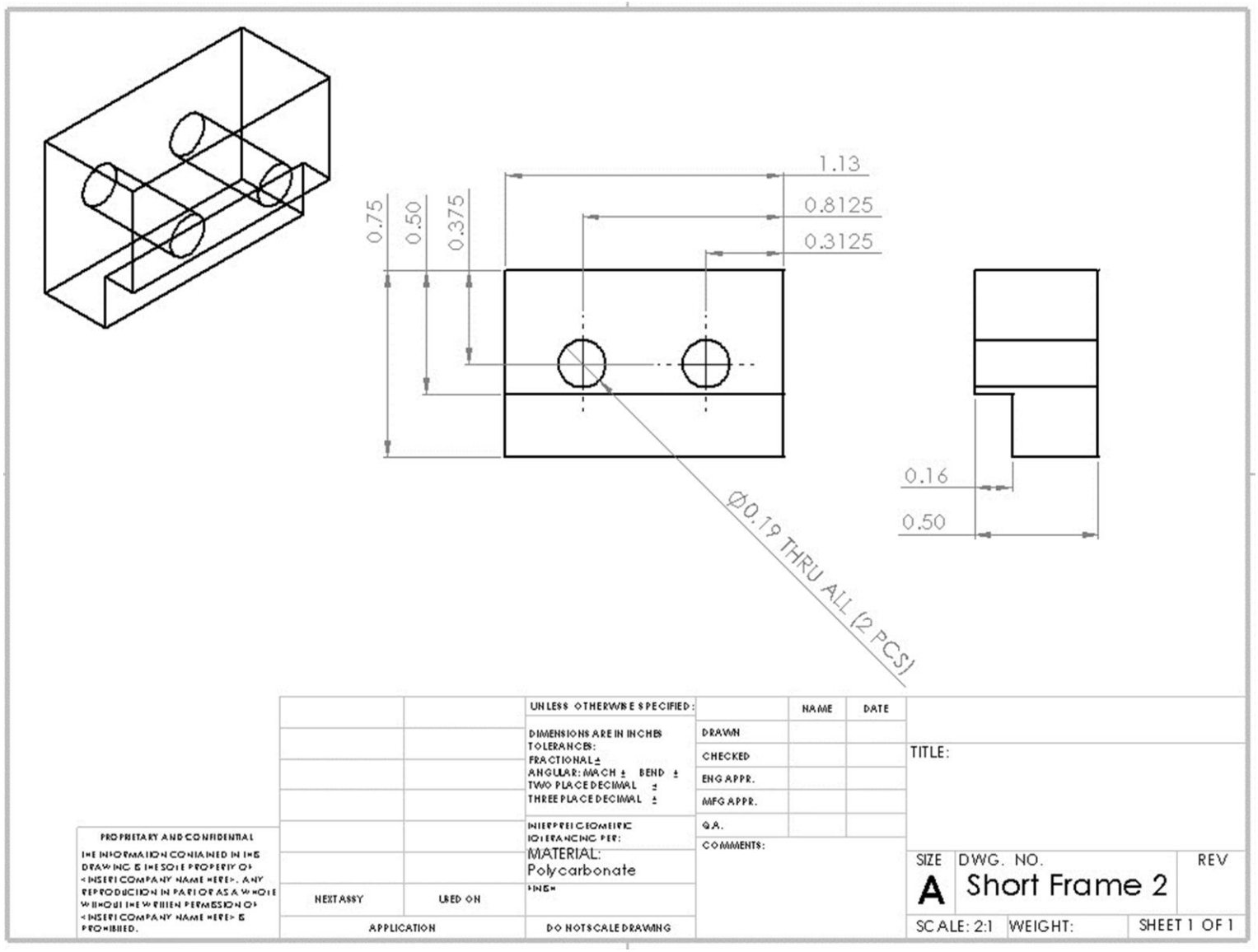

Figure A-10: Short window frame piece #1 mechanical drawing

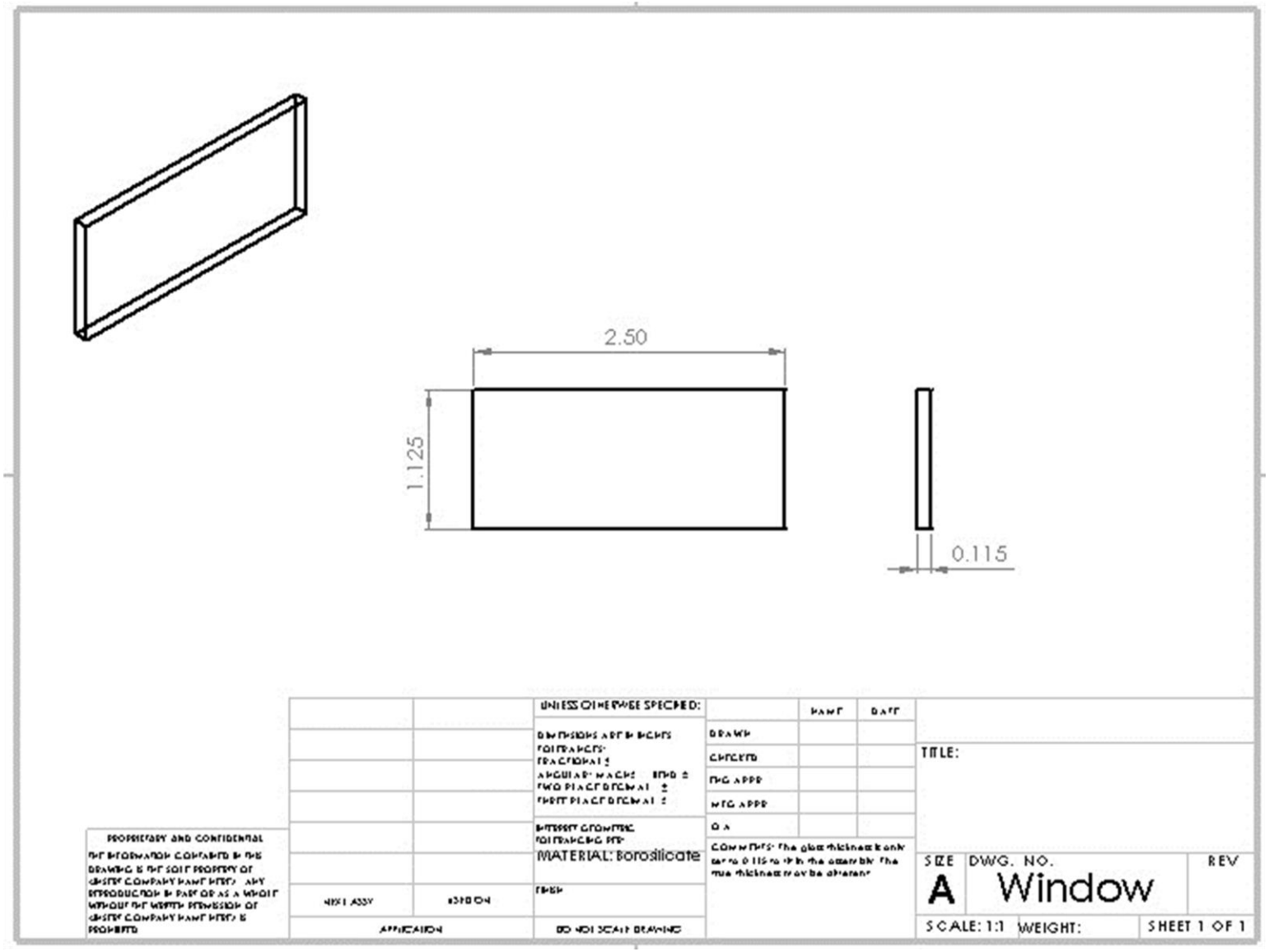

Figure A-11: Borosilicate glass window mechanical drawing

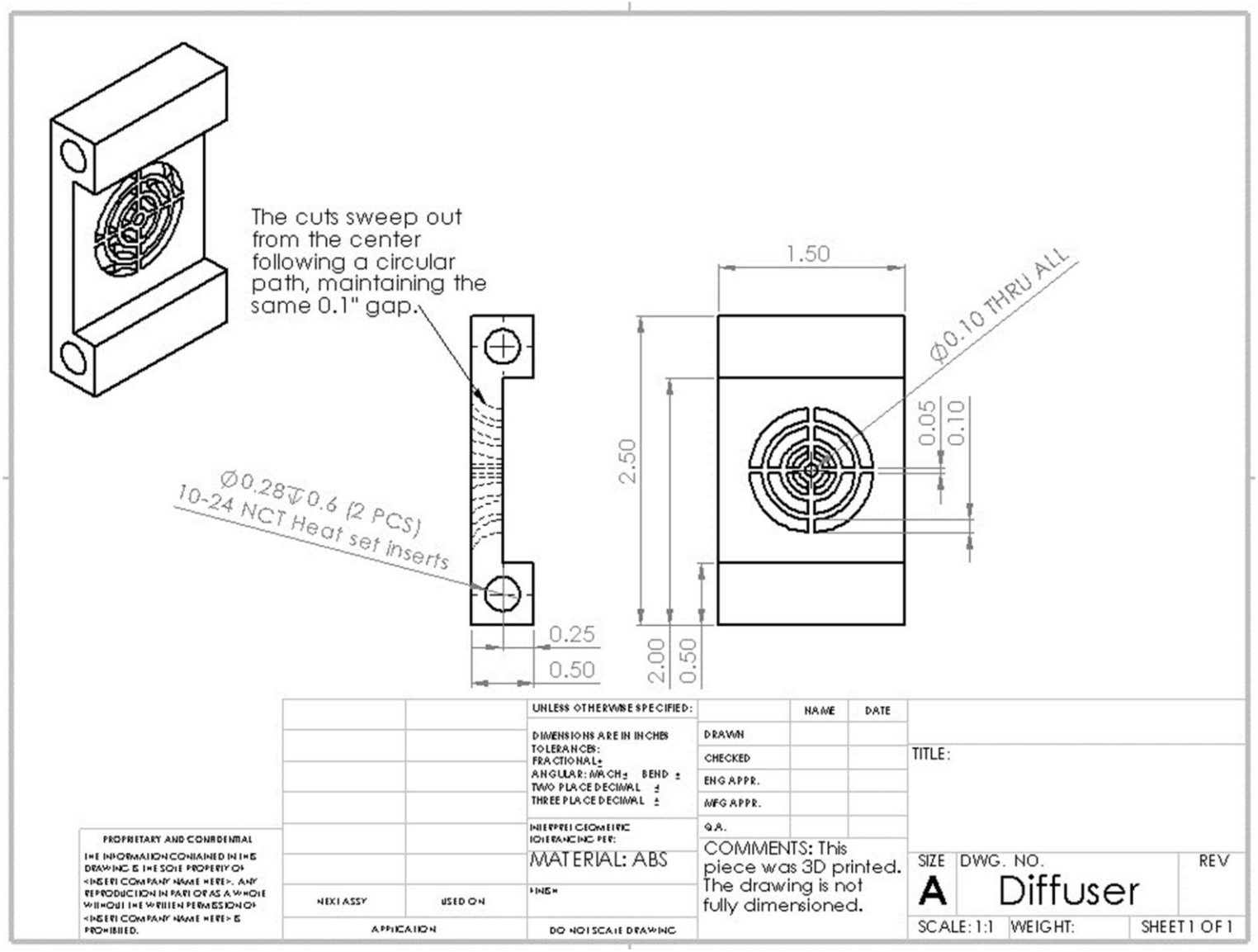

Figure A-12: Borosilicate glass window mechanical drawing

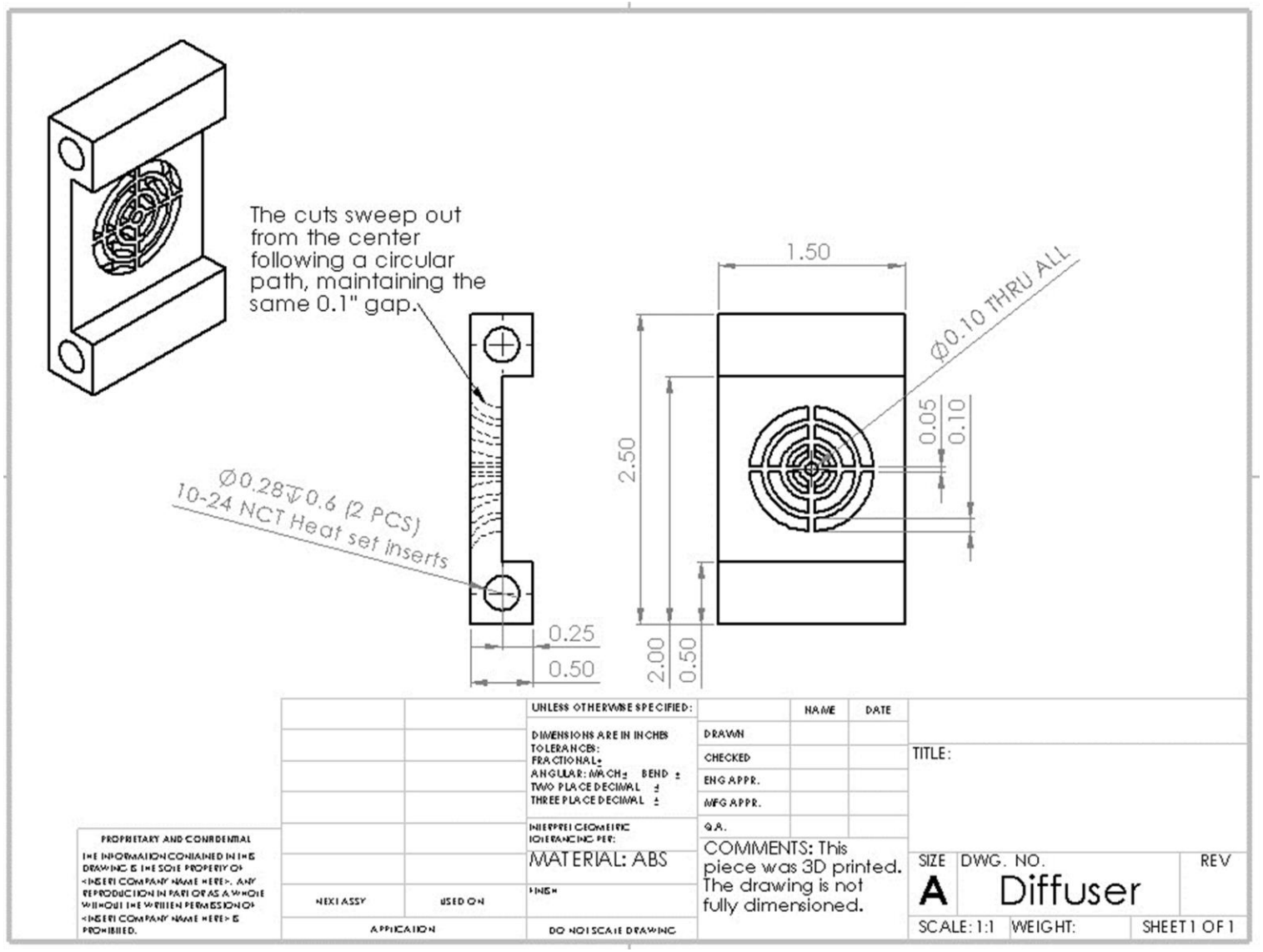

Figure A-13: Flow diffuser mechanical drawing

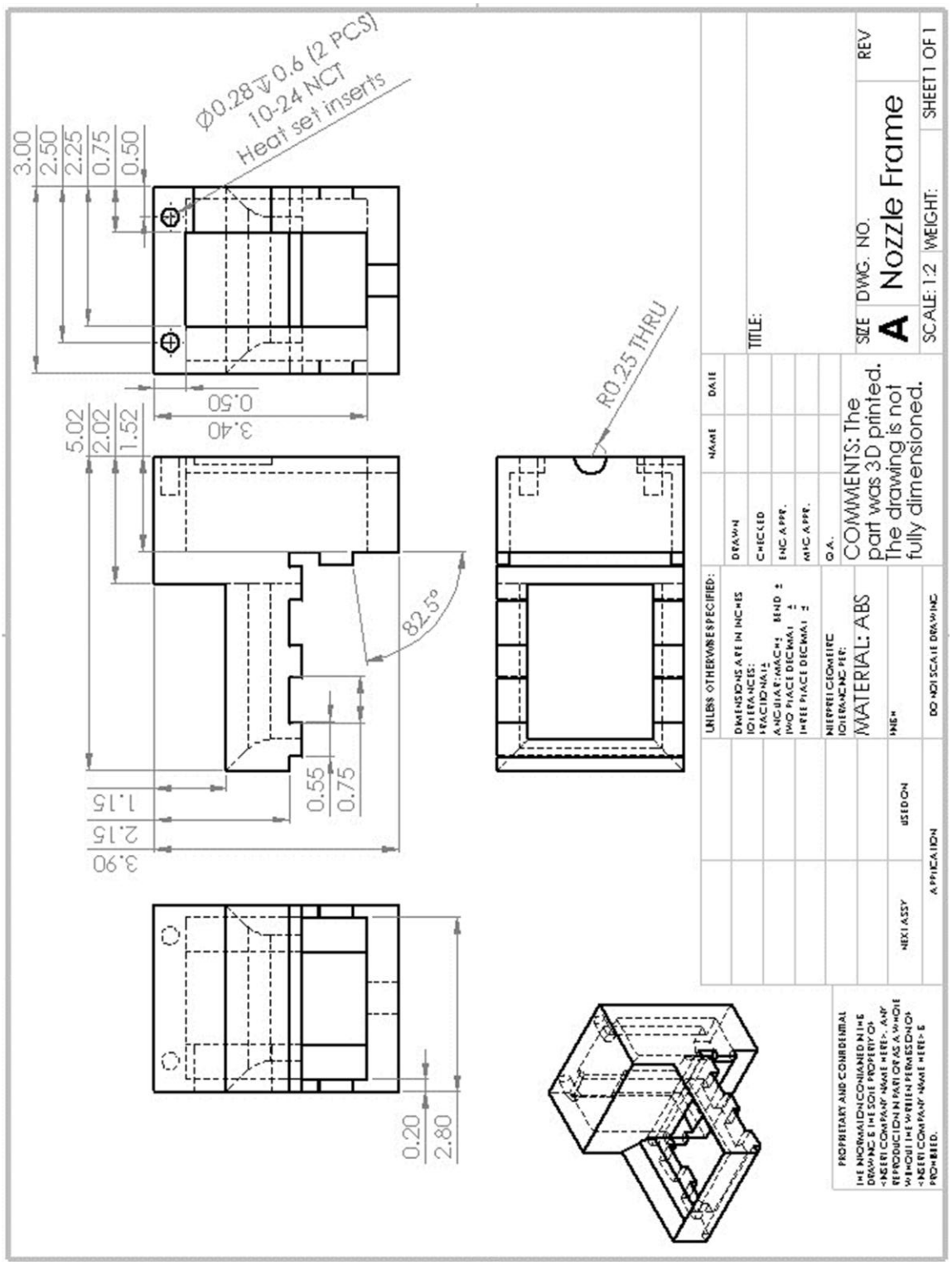

Figure A-14: Modular nozzle frame mechanical drawing

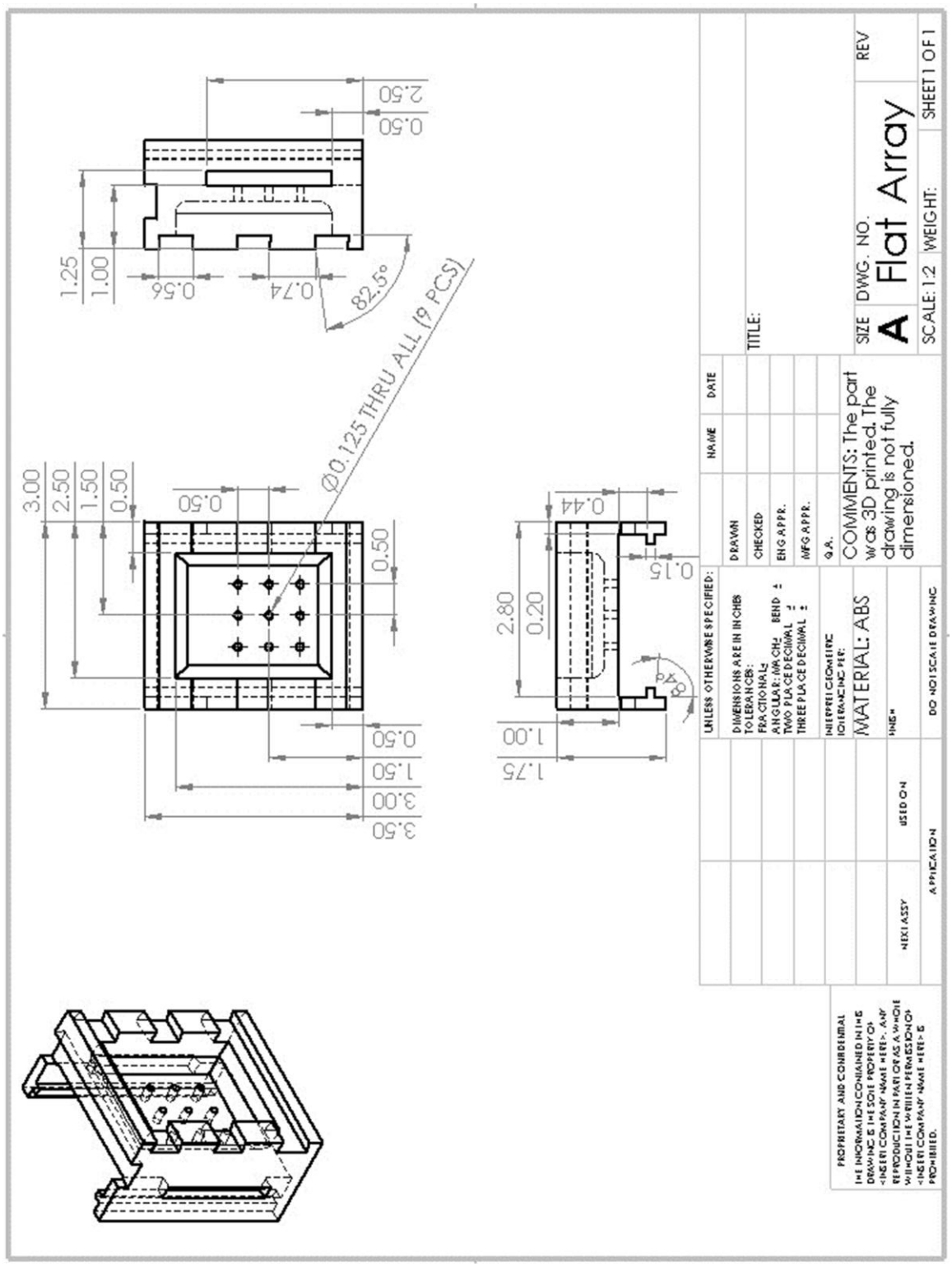

Figure A-15: Modular nozzle array with a flat confining wall mechanical drawing

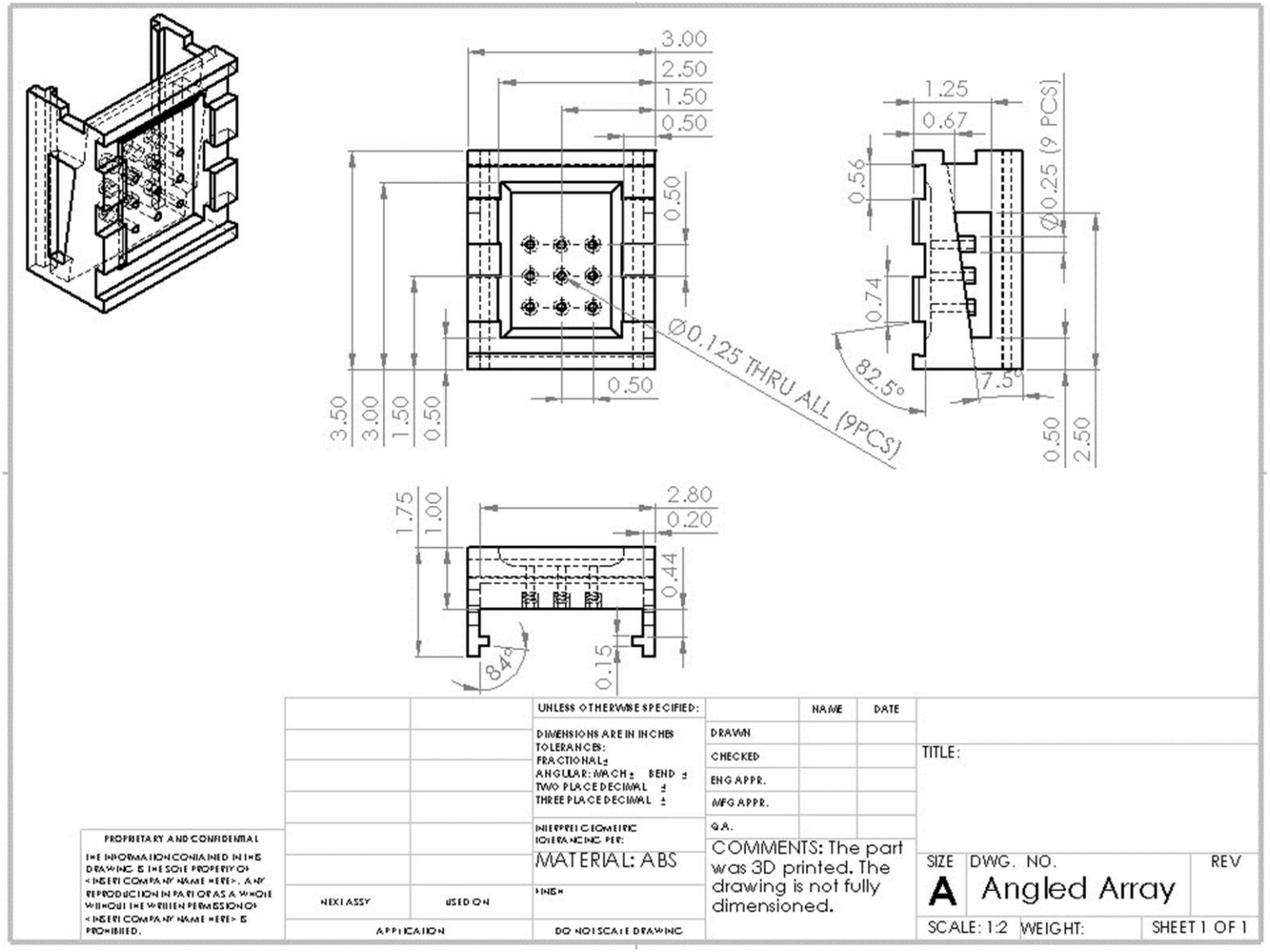

Figure A-16: Modular nozzle array with an angled confining wall mechanical drawing

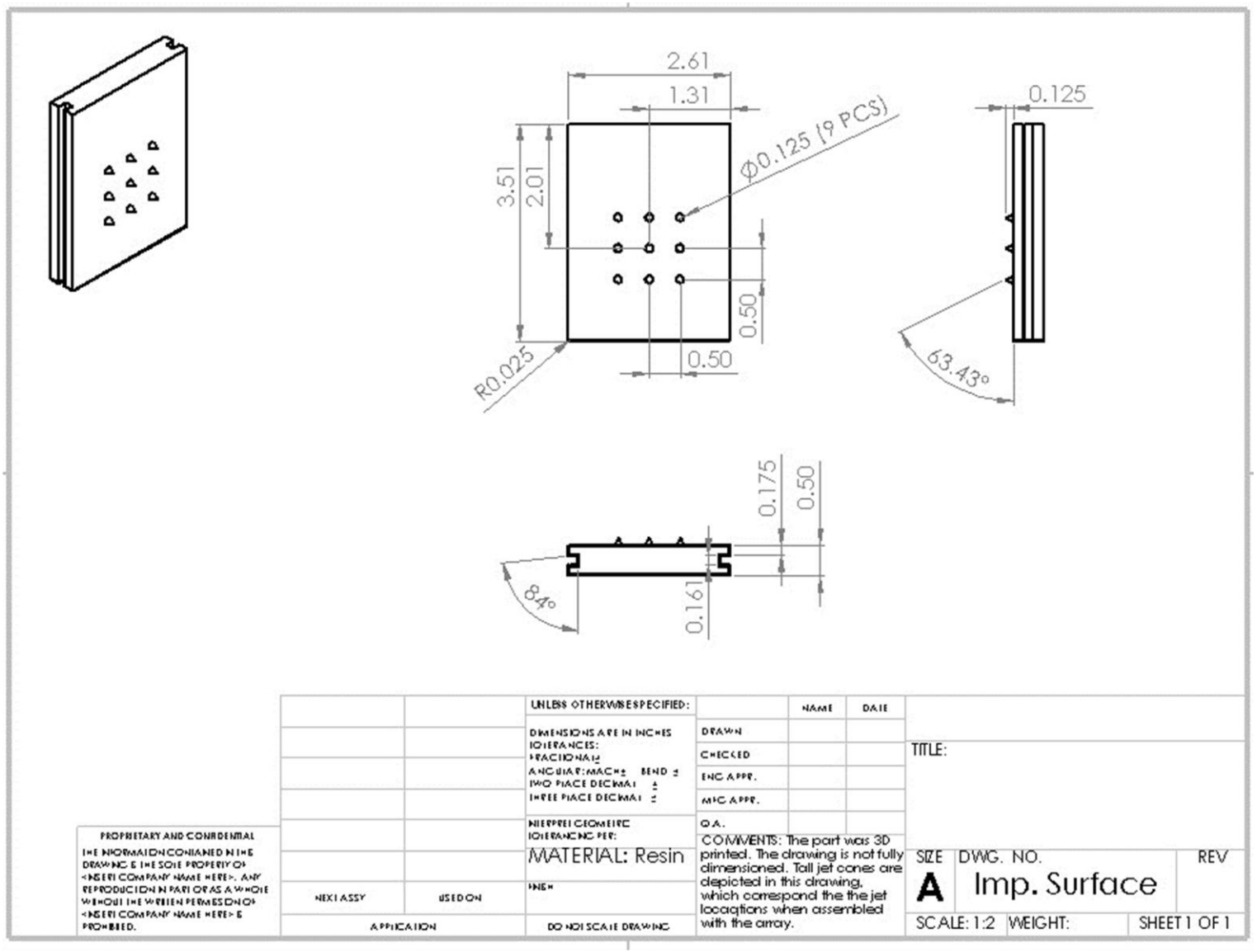

Figure A-17: Modular impingement surface with tall jet cones mechanical drawing

Appendix B: Detailed Logistics of the Study

This appendix will discuss the procedure taken to gather data from the PIV experiments and to setup, calculate, and export results for the numerical model.

B.1 PIV

The data acquisition process for the PIV system was discussed in section 3.2.3. Here, ordered instructions are provided regarding the PIV data acquisition process, such that the procedure taken in this effort can be fully repeated.

A. Prepare necessary equipment
    1. Gather the impingement chamber, internal and external side walls, nozzle frame, nozzle array, impingement surface, fasteners, a screwdriver, and the working fluid near the flow loop
    2. Assemble the modular nozzle array using the dovetail grooves, as shown in Figure A-14 through Figure A-17
    3. Attach the impingement chamber to the flow loop and tighten the connections using a screwdriver
    4. Place the chamber at the lowest point in the system, facing the open side upwards
        i. This was done over a tray to catch any spilled fluid during the assembly process

B. Assemble the impingement chamber
    1. Block the holes in the impingement chamber walls used to attach the modular nozzle frame to the chamber
        i. This was typically done using the fingers of one hand, while the other followed the next steps until the nozzle frame was attached
    2. Fill the impingement chamber with the working fluid
        i. It is necessary to fill the chamber with fluid before inserting the nozzle array to minimize the air in the chamber
    3. Insert the modular nozzle array and fasten it to the chamber using a screw, washer, and gasket

4. Wait a few minutes, occasionally agitating the impingement chamber, to release as much air as possible
5. Insert the internal sidewall into the chamber
6. Fasten the external sidewall to the chamber using screws and washers
    i. Do not move the chamber from its low point at this time

C. Fill the system with the working fluid
1. Fill the rest of the system from the reservoir
2. Maneuver air bubbles caught in the system to the atmosphere:
    i. Maneuver bubbles caught in the tubes to the reservoir or liquid-air separator
    ii. Maneuver bubbles caught in the impingement chamber into the inlet or outlet tubes and, again, maneuver them to the reservoir or liquid-air separator
    iii. Maneuver the liquid-air separator to force bubbles to its top
3. Place the impingement chamber on its stand in front of the PIV laser sheet
4. Top off the reservoir with fluid if it has drained due to the removal of bubbles

D. Remove bubbles from the pump
1. Take the tube connected to the top of the liquid-air separator, open the ball valve at its end, and place it in the fluid reservoir
    i. This valve need not be removed from this location at any point and any reference of opening this valve indicates that it is still present in the reservoir
2. Activate the Arduino Uno used to measure the flow rate measured by the turbine flow meter
3. Using the variable frequency drive, activate the pump at a flow rate sufficient to move water through the tube and into the reservoir, bypassing the impingement chamber
    i. Due to buoyancy forces, this flow will carry the vast majority of air from the pump to the reservoir, where it will be removed from the system to the atmosphere
    ii. At a sufficiently high flow rate, fluid will flow out of a tube connected just after the pump; close the valve at this tube's end
4. Wait for the flow of bubbles to cease
5. Using the variable frequency drive, increase the flow rate of the pump
    i. This will cause more bubbles to depart from the pump

6. Repeat steps D3 and D4 until the flow rate well exceeds the highest flow rate that will be required of the pump during the experiments
7. Close the ball valve connected to the liquid air separator
    i. Upon closing the ball, the flow rate will decrease; thus, it is necessary to exceed the desired flow rate during the air removal process

E. Initialize the system
1. Using the variable feed drive, adjust the flow rate from the pump until it reaches the desired value
    i. This will need to be monitored throughout the experiments, as slight changes in the flow rate may arise while the pump runs
2. Ensure that the lab space is locked, external windows are covered, an external warning light is activated, the impingement chamber and laser head are covered by a shroud of fabric, and safety glasses are prepared for the experiments
    i. Wear safety glasses at all times, except when changing to and from alignment and full coverage glasses
3. Activate supply power to the laser head and prepare it for use
    i. Turn the key, activating the power supply and chill water
    ii. Activate the supply voltage to the laser using the power supply
    iii. Turn the shutters on each of the laser sheets to allow illumination
    iv. Remove the lens cap from the laser head
4. Connect the camera used to capture the snapshots to the computer and its power supply; remove the lens cap and point the camera into the impingement chamber
5. Activate the computer used to control the laser and gather the data
6. In the computer, activate the Insight 4G software
7. Specify a new or existing run within the software for the current experiment

F. Align the PIV system and seed the fluid
1. Cover any rounded, reflective surfaces on the impingement chamber facing the laser head, but leave the flat walls exposed
2. Ensure that alignment safety glasses are worn and a piece of cardboard is prepared for use in the alignment process

3. In the software, move to the “Capture” tab, Figure B-1 below displays the settings available when capturing images

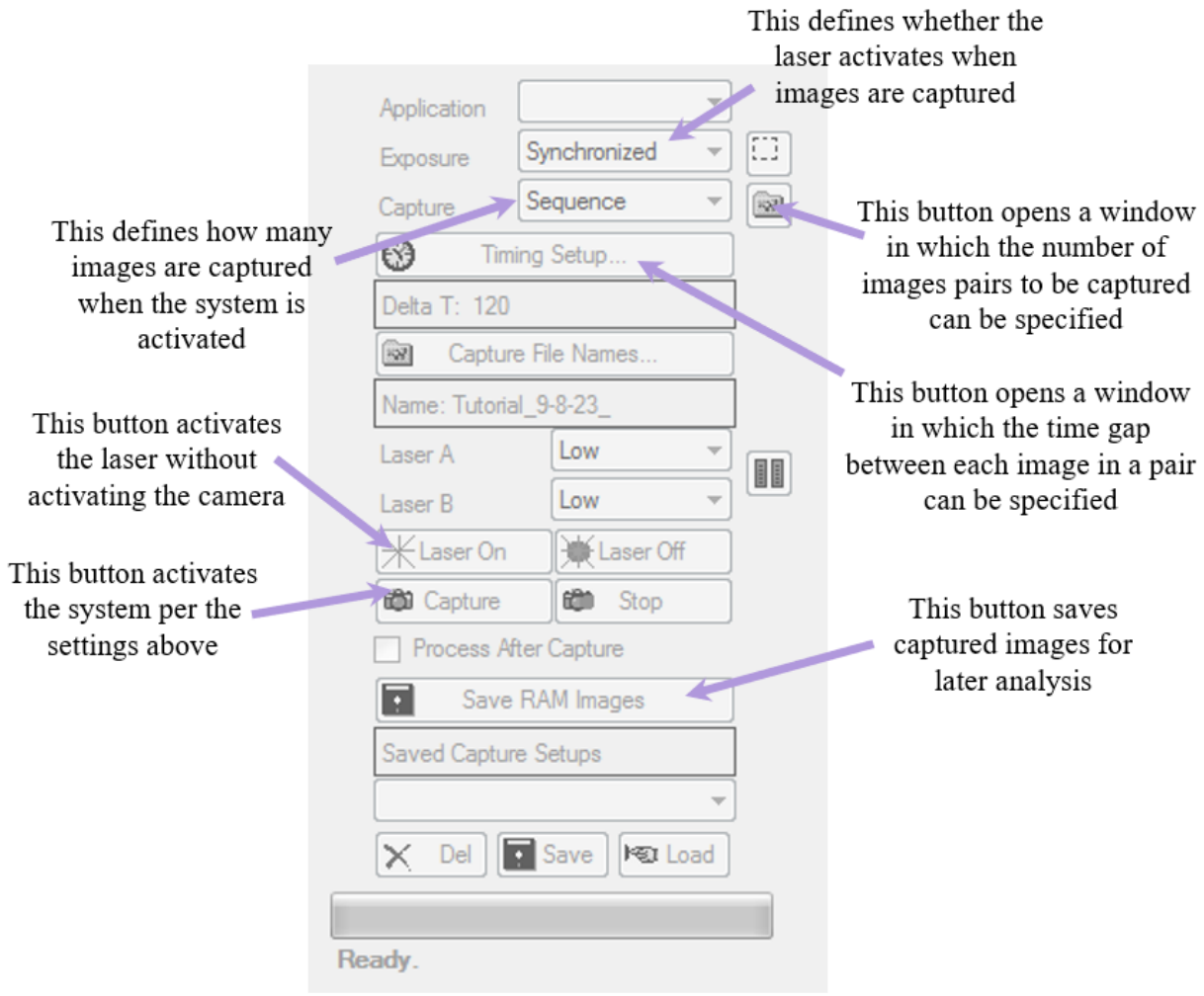

Figure B-1: PIV software capture settings

4. Using the software, activate the laser sheet using the “Laser On” button
5. Holding the cardboard just above the laser head, slightly lift the fabric shroud
    i. The flat walls of the impingement chamber will reflect the laser sheet back, onto the cardboard
    ii. If the laser sheet does not shine normal to the impingement chamber’s wall, the reflected laser sheet will be seen to one side of the laser head’s lens
6. Deactivate the laser and adjust the rotation of the impingement chamber based on the location that the laser sheet reflected onto the cardboard
7. Repeat steps F3-F5 until the laser sheet’s reflection lies over the lens

8. Cover all reflective surfaces in front of the laser head
9. Ensure that full coverage safety glasses are worn for the remainder of the experiments, unless otherwise stated or this process is repeated
10. Add seeding particles to the fluid reservoir and mix them in
11. Open the ball valve connected to the liquid-air separator, mixing the highly-seeded fluid in the reservoir into the system, then close the valve when well mixed
12. Setting the laser and camera to continuous captures, activate the laser and camera
    i. This continuous setting causes the laser and camera to capture and display synchronized images until stopped by the user
13. Adjust the zoom and aperture on the camera to obtain clean images of the region illuminated by the laser light
14. Deactivate the laser and camera
15. Adjust the amount of seeding particles in the fluid until the particles densely cover the visual window without fully attenuating the light deep into the fluid
    i. Increase the amount of seeding particles by following steps F8 and F9
    ii. Decrease the amount of seeding particles by removing seeded fluid from the reservoir, adding unseeded fluid to the reservoir, opening the valve connected to the liquid-air separator, allowing the unseeded fluid to mix into the system, and reclosing the valve
16. Once the fluid is adequately seeded, change the software settings to take a sequence of captures and capture a few synchronized images
    i. The synchronized setting captures a set number of image pair for analysis; the captures will automatically cease when the specified number of image pairs is reached
    ii. Only a few image pairs are required in this step, as the laser sheet is not likely to be aligned with the region of interest
17. In the software, move to the “Processing” tab, Figure B-2 below shows the settings available when processing the results

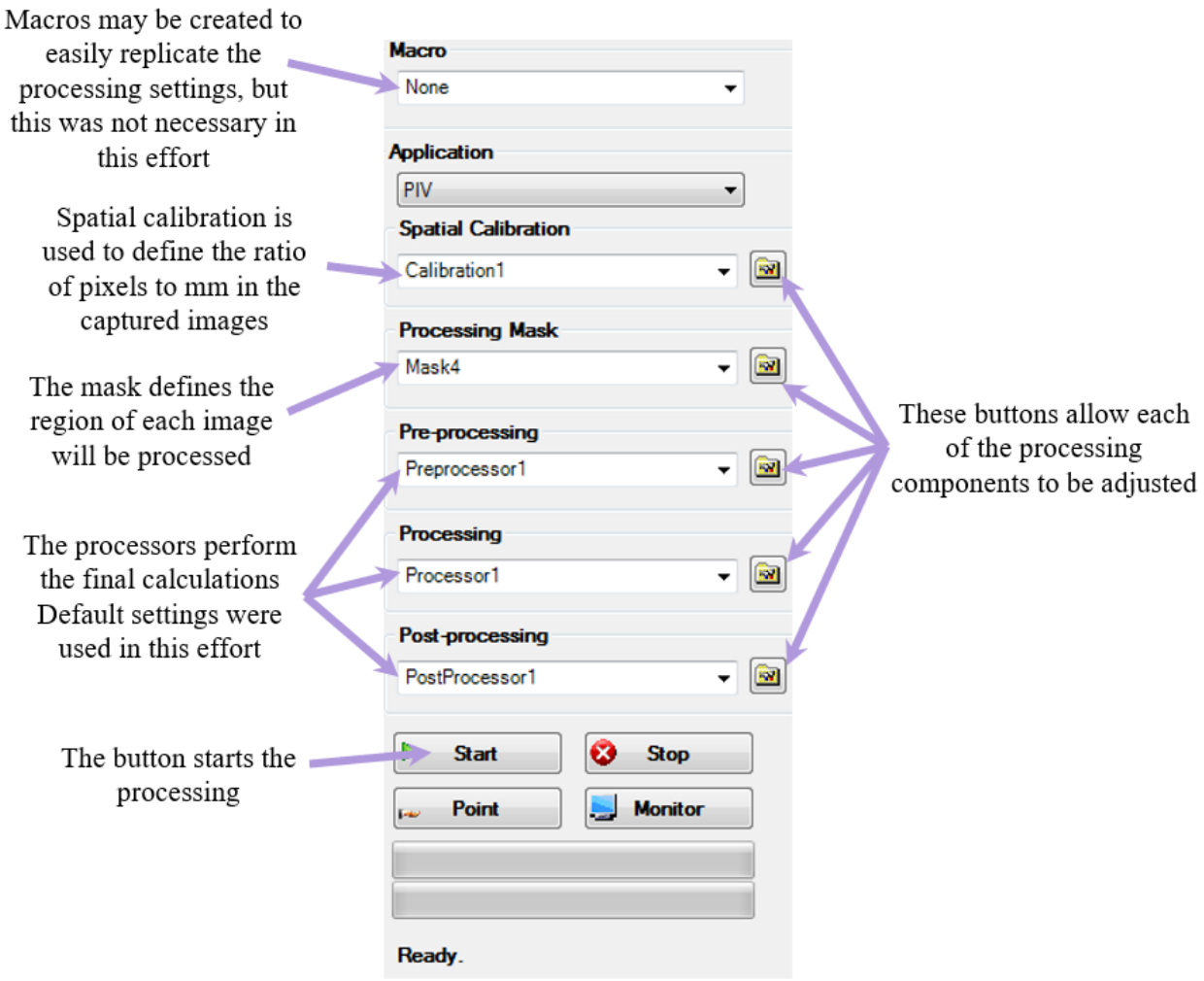

Figure B-2: PIV software processing settings

18. Using the processing window, process the results to generate a preliminary flow field
    i. Adjust the processing mask to only cover the region of the frame containing seeding particles
    ii. Instruct the software to process the images
    iii. It is not necessary to adjust the spatial calibration at this point
19. Observe the resulting flow field for desired flow behaviors or physical structures expected in the region of interest
    i. Optionally, take a screenshot of the flow field for later comparison
20. Using the knob on the laser head, translate the laser head to a new location
    i. One full turn of the know on the laser head used in this effort corresponded to a translation of 1mm in the direction following the right-hand-rule

ii. There is no objective method to determine the required direction of translation; it may be determined from experience after running these experiments many times, by wearing alignment glasses and observing where the laser sheet illuminates the covered impingement chamber, or by guessing and checking

21. As necessary, change the software to capture and display continuously and refocus the camera
22. Repeat steps F15-F19 until the laser sheet illuminates the region of interest
    i. In this effort, this was done by adjusting the location until the jet inflow was at its widest

G. Capture the final snapshots

1. Change the number of snapshot pairs to the total number desired for the final analysis
2. Capture the snapshots
3. Click "Save RAM Images" to ensure that the results are saved for later analysis, if needed
4. In the processing window, ensure that the processing mask covers only the region of the frames that contain seeding particles
5. Adjust the spatial calibration settings
    i. In the spatial calibration window, use the mouse to measure a known distance in a frame; the software will automatically input the distance in pixels
    ii. Specify the length of the indicated distance in mm
    iii. In this effort, the space between the top of the laser sheet and the impingement surface was set to 6.35mm
6. Process the images
7. Examine the results for quality
    i. If there was an issue, resolve it as required, delete the previous images, and repeat steps G1-G6 until the results appear reasonable
8. Using the Tecplot window, shown below in Figure B-3, export the final data to a text file for analysis in Matlab; this button can be accessed from either the "Capture" or "Processing" tab

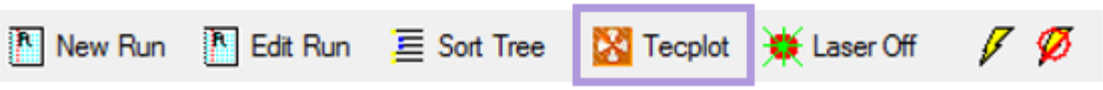

Figure B-3: Tecplot button in the PIV software

H. Further measurements
    1. If further measurements are needed for the current geometry, they can be taken in the same data collection session
    2. If the flow rate needs to be changed, adjust the variable frequency drive until the new desired flow rate is reached, then repeat steps G1-G8
    3. If a new region of interest is to be examined, use the translation knob on the laser head to illuminate the appropriate region
        i. Repeat steps F11 and F12 to refocus the camera
        ii. Repeat steps G1-G8 to capture the new data

I. System shutdown
    1. When all data is collected, deactivate the laser's power supply, close the shutters, and replace the lens cap
        i. At this point the external warning light should be deactivated and, optionally, safety glasses may be removed, the lab door may be unlocked, windows may be uncovered, and the shroud may be removed
    2. Deactivate the software and shutdown the computer
    3. Disconnect the camera from its power supply

J. Disassemble the impingement chamber
    1. Open the ball valves connected to the tube after the pump and the liquid-air separator
    2. Drain the system into a container using the drain port on the impingement chamber
        i. Maneuver any liquid trapped in the tubes, liquid-air separator, or impingement chamber out of the system
    3. Disconnect the impingement chamber from the system using a screwdriver
    4. Place the impingement chamber on a towel or tray to handle water spills and remove the external sidewall using a screw driver
    5. Remove the internal sidewall

6. Disconnect the modular nozzle assembly using a screw driver and remove it from the impingement chamber
7. In a sink, rinse off the modular nozzle assembly and impingement chamber of any residual seeding particles
8. Disassemble the modular nozzle assembly
9. Place the impingement chamber and modular nozzle assembly components out to dry
10. Dispose of the used and seeded working fluid

B.2 Numerical Model

This section reviews the process taken to calculate the solution for the numerical model. The instructions will explain the process as completed in this effort.

A. Generate the model geometry

1. In this effort, this was completed using SolidWorks, but it could be completed within ANSYS
2. Generate each part individually and combine them in an assembly
    i. As shown in Figure B-4 below, this assembly was created out of the following parts: (1) the fluid region starting at the inlet and ending at the start of the nozzles, (2-4) three nozzle sections connecting the inlet region to the impingement region, (5) the impingement region, (6) the solid body upon which the fluid impinges, and (7) another solid region in which heat generation is applied that is embedded in solid part (6)

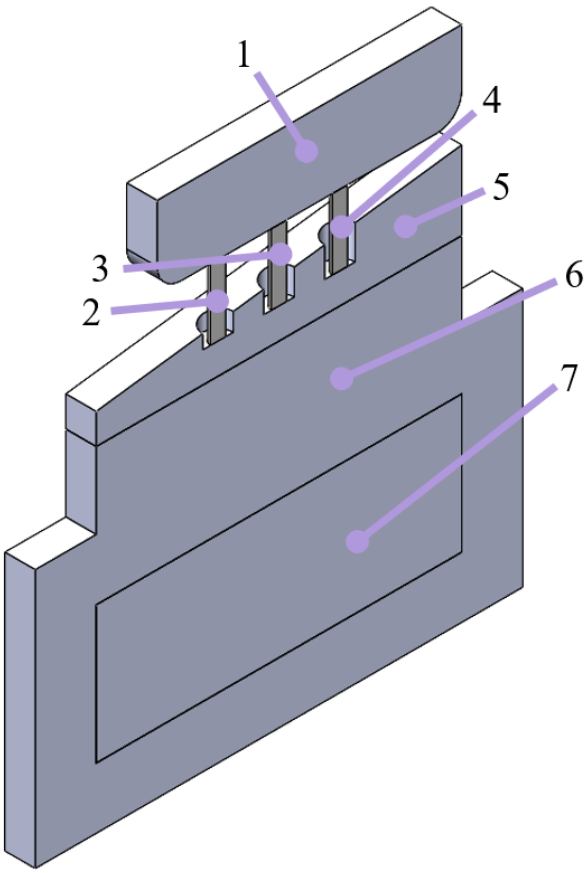

Figure B-4: Numerical model assembly in SolidWorks, with all parts identified by number

ii. Ensure any impingement surface modifications are applied both to the solid surface and working fluid parts

3. The tall cone structures caused divergence at the tip, so they were rounded slightly
4. Export the assembly of the desired geometry as an IGES file

B. Import the geometry into ANSYS and generate the named sections

1. In a new ANSYS workbench, create a "Geometry" module
2. Right-click the module and import the IGES file
3. Right-click and open the geometry module
4. Within the DesignModeler that opens, create the following named sections for the bodies of the model:
   i. Name the heat generation part "gen"
   ii. Name the solid part upon which the fluid impinges "solid"
   iii. Name the fluid entry part "fluidentry"

iv. Name the upstream nozzle part “fluidnozus”
v. Name the central nozzle part “fluidnozcen”
vi. Name the downstream nozzle part “fluidnozds”
vii. Name the fluid impingement region part “fluidimp”

5. Hide all fluid bodies and create the following named sections for certain faces in the solid bodies:
    i. Name the face of the heat generation body in the symmetry boundary on the jet plane side “symmetrygenjet”
    ii. Name the face of the heat generation body in the symmetry boundary on the fountain plane side “symmetrygenftn”
    iii. Name the face of the solid body upon which the fluid impinges in the symmetry boundary on the jet plane side “symmetrysolidjet”
    iv. Name the face of the solid body upon which the fluid impinges in the symmetry boundary on the fountain plane side “symmetrysolidjet”
    v. Name all faces that contact the fluid body “contactsolid”
    vi. Name all external faces of the solid body upon which the fluid impinges that are neither symmetry boundaries nor in contact with the fluid region “adiabats”
6. Hide all solid bodies and create the following named sections for certain faces in the fluid bodies:
    i. Name all faces on the jet plane side “symmetryfluidjet”
    ii. Name all faces on the fountain plane side “symmetryfluidftn”
    iii. Name all faces that contact the solid body “contactfluid”
    iv. Name the inlet face “inlet”
    v. Name the outlet face “outlet”
    vi. Name the walls on the interior of the nozzles “wallsmall”
    vii. Name the walls in the impingement body “wallmedium”
    viii. Name the walls in the inlet body “walllarge”
7. Close out the DesignModeler

C. Meshing

1. Add the “Fluent (with Fluent Meshing)” module to the workbench, connecting the “Geometry” module to the meshing portion of the Fluent module

2. Right-click the meshing section and open it
3. In the window that opens, do the following:
    i. Ensure that “Double Precision” is enabled
    ii. Ensure that parallel processing is active
    iii. Set the number of parallel processes to 12
    iv. Click “OK”
4. In the window that opens, ensure that the “Watertight Geometry” is selected and import the geometry
5. Insert local sizing for the following bodies and faces:
    i. For the gen body, set a size of 0.004m and check the box labeled “Repair Body”
    ii. For the solid body, set a size of 0.0024m and check the box labeled “Repair Body”
    iii. For the contactfluid, contaqctsolid, and wallsmall faces, set a size of 7.5e-5m
    iv. For the wallmedium faces, set a size of 0.00015m
    v. For the walllarge faces, set a size of 0.0004m
6. In the “Create Surface Mesh” section, complete the following:
    i. Set the minimum feature size to 7.5e-5m
    ii. Set the maximum feature size to 0.004m
    iii. Set the cells per gap to 3
    iv. Set the “Scope Proximity to” option to “faces and edges”
    v. Generate the surface mesh
7. In the “Describe Geometry” window, select the options that the model contains fluid and solid regions and that share topology will be applied
8. In the Share Topology window, change the maximum gap value to 0 and regenerate the surface mesh
9. The next few windows should automatically populate themselves correctly; double check these settings to confirm until the “Add Boundary Layers” window is reached
10. In the “Add Boundary Layers” window, complete the following:
    i. Change the setting to apply boundary layers on selected labels
    ii. Set the number of layers to 10
    iii. Select the following labels: contactfluid, wallsmall, wallmedium, walllarge

iv. Continue to the next window

11. In the “Create Volume Mesh” window, change the mesh type to polyhedral
12. Generate the volume mesh, an example of which is shown below in Figure B-5

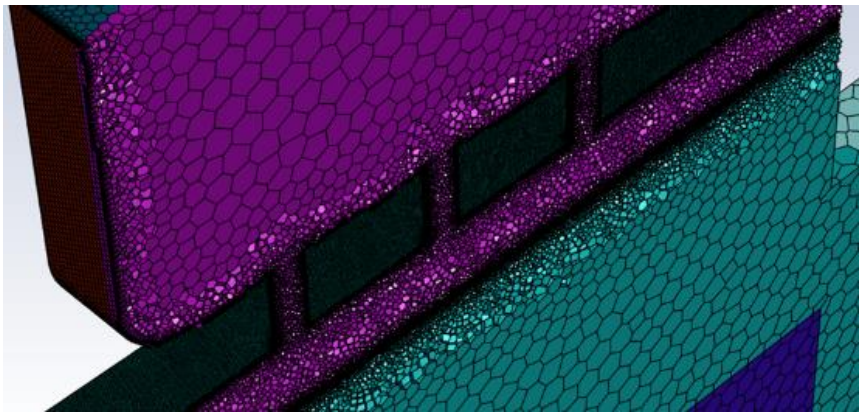

Figure B-5: Example volume mesh of the numerical model

13. Check that the mesh sizing and boundary layers appear correct
14. Click “Switch to Solution”

D. Setting up the calculation

1. Click “Check Mesh”
    i. Optionally, check the mesh quality; a value above 0.1 is generally desired, but this is not essential
2. Click the physics window
3. Ensure that the “Steady”, “Pressure-Based”, and “Energy” settings are selected
4. Click the “Viscous…” button
    i. In the window that opens, select the “Transition SST (4 eqn)” option
    ii. Close the window
5. Under the “Materials” header, click the “Create/Edit…” button
    i. In the window that opens, click the “Fluent Database…” button
    ii. In the second window, find copper under the solids section and add it
    iii. Change the section to fluids, find liquid water, and add it
    iv. Close both the “Fluent Database” and “Create/Edit Materials” windows
6. Under the “Zones” header, click the “Cell Zones” button
7. In the sub-window that opens, select the “gen” label, then click the “Edit…” button
    i. In the window that opens, change the material to copper

ii. Click the “Source Terms” button

iii. In the Source Terms” window, create a volumetric heat generation of 6027036W/m^3

iv. Close the window

8. Similarly, change the solid body to copper and all five fluid bodies to liquid water, but do not change any other settings for these bodies
9. Under the “Zones” header, click the “Boundaries” button
10. In the sub-window that opens, select the “inlet” label, then click the “Edit…” button
    i. In the window that opens, change the velocity magnitude to the desired value:
        - $Re_j = 5600 \rightarrow V_{in} = 0.052197$m/s
        - $Re_j = 8400 \rightarrow V_{in} = 0.078296$m/s
        - $Re_j = 11200 \rightarrow V_{in} = 0.10439$m/s
        - $Re_j = 14000 \rightarrow V_{in} = 0.13049$m/s
    ii. Change the turbulence intensity to the desired value:
        - $Re_j = 5600 \rightarrow I = 5.33\%$
        - $Re_j = 8400 \rightarrow I = 5.07\%$
        - $Re_j = 11200 \rightarrow I = 4.89\%$
        - $Re_j = 14000 \rightarrow I = 4.75\%$
            - These values are the result of Equation B.1 below [58]. This equation is for developed duct flow, but will likely provide a more accurate estimate of the true intensity than the default value of 5%

$$I = 0.16\left(Re_{D_H}\right)^{-1/8} = 0.16\left(\frac{\rho \bar{u} D_H}{\mu}\right) \quad \text{(B.1)}$$

    iii. Change the third inlet boundary condition to “Hydraulic Diameter” and set it to 0.127m
    iv. Change to the “Thermal” tab and change the temperature to 303K
    v. Close the window
11. Click the “Solving” button

12. Under the “Solution” heading, click the “Methods” button
13. In the sub-window that opens, complete the following:
    i. Set the scheme to “Coupled”
    ii. Set the gradient setting to “Green-Gauss Node Based”
    iii. Set the pressure setting to “PRESTO!”
    iv. Set the momentum setting to “Third-Order MUSCL”
    v. Set the turbulent kinetic energy, specific dissipation rate, intermittency, momentum thickness Re, and energy settings to “Second Order Upwind”
    vi. Activate the “Pseudo Transient” and “High Order Term Relaxation” settings
        - If the calculation fails to converge, click the “Options…” button next for the high order term relaxation and reduce the value in the window that opens
14. Click the “Initialize” button
15. Click the “Check Case” button
    i. No issues should be identified
16. Set the number of iterations to some value at or above 1000
    i. If the high order term relaxation value was reduced, it will likely take more iterations for the solution to converge

E. Calculation
1. Click “calculate”
2. Monitor the residuals occasionally as the calculation progresses; the momentum residual is most likely the last to converge
    i. Convergence will be achieved when the energy residual is less than 10^{-6} and all other residuals are less than 10^{-3}
    ii. If the residuals oscillate in a repeating pattern every few iterations without meeting the convergence criteria, then the solution did not converge; adjust the settings and recalculate
    iii. If the number of iterations specified is reached without convergence, the calculation will stop; if the residuals are not following an oscillatory pattern every few iterations, continue the calculation until it converges or oscillates
3. When convergence is achieved, save the ANSYS Workbench project

F. Exporting the solution data into text files
    1. Click “File”, “Export”, and “Solution” data
    2. In the window that opens, change the file type to ASCII
    3. In the middle sub-window, select the five symmetryfluidjet labels
    4. In the right sub-window, select the “Velocity Magnitude”, “X-Velocity”, “Y-Velocity”, and “Z-Velocity” parameters
    5. Write the text file to a known location
    6. In the middle sub-window, deselect the previous labels and select the two symmetryfluidftn labels
    7. Write the text file to a known location
        i. The velocity options will still be selected in the right sub-window
    8. In the middle sub-window, deselect the previous labels and select the contactfluid label
    9. In the right sub-window, deselect the previous parameters and select the “Static Temperature” and “Total Surface Heat Flux” parameters
        i. These values will be later used in a Matlab script to calculate the local surface heat transfer coefficient. This Matlab script is shown later in Appendix C. The local surface heat transfer coefficient was calculated using Equation 4.1
    10. Write the text file to a known location

G. Calculate average surface characteristics
    1. In the “Results” tab, click the “Surface Integrals” button
    2. In the window that opens, find the “Surfaces” sub-window and select the “contactfluid…” surface
    3. In the “Report Type” box, select “Area”
    4. Click “Compute”
    5. The impingement surface’s area in m^2 will be reported to the command window, copy this result to an Excel spreadsheet
    6. In the “Report Type” box, select “Area-Weighted Average”
    7. In the “Field Variable” box, select “Temperature…”
    8. In the unlabeled box just under the “Field Variable” box, select “Static Temperature”
    9. Click “Compute”

10. The impingement surface's average temperature in K will be reported to the command window, copy this result to an Excel spreadsheet
11. In the "Report Type" box, select "Integral"
12. In the "Field Variable" box, select "Wall Fluxes…"
13. In the unlabeled box just under the "Field Variable" box, select "Total Surface Heat Flux"
14. Click "Compute"
15. The total heat dissipated through the impingement surface in W will be reported to the command window, copy this result to an Excel spreadsheet
    i. This value should be near 83.33W, but will vary slightly
16. A Matlab script in Appendix C will use these three values to calculate the average surface heat transfer coefficient using Equation B.2 below

$$\bar{h} = \frac{Q_T}{A(\bar{T} - T_{in})} \tag{B.2}$$

H. Close out ANSYS Fluent

1. Make sure the solution data is saved prior to closing the workbench

Appendix C: Numerical Data Reduction

Data reduction of flow data gathered from either the PIV or numerical approaches did not require reduction. The only manipulation of this data was cubic smoothing of the contours in the Matlab scripts. As such, this section will not review any data reduction of the flow fields.

Rather, further analysis of the numerical thermal surface contours is required. The local surface temperature and heat flux were gathered directly from the model's solution data. However, calculations were required to find the local surface heat transfer coefficients and average surface characteristics. This section will review the calculations completed to obtain these values.

C.1 Calculating the Local Surface Heat Transfer Coefficient

The only local thermal parameter calculated in this effort was the local surface heat transfer coefficient. This was completed using Equation 4.1, which is repeated below. This equation only uses values taken directly from the numerical model.

$$h_l = \frac{\dot{q}_l''}{(T_l - T_{in})} \tag{4.1}$$

Consider a point on the impingement surface which the numerical model has determined to have a temperature of 41.3°C with a local heat flux of 400kW/m^2; this data was taken from the central stagnation region of the baseline surface under a flat confining wall at a jet Reynolds number of 5600. The inlet temperature for all cases was set to 30°C. Thus, the local surface heat transfer coefficient can be calculated as such:

$$h_l = \frac{\dot{q}_l''}{(T_l - T_{in})} \tag{4.1}$$

$$h_l = \frac{\left(400\,\frac{kW}{m^2}\right)}{(41.3°C - 30°C)}$$

$$h_l = 35.4\,\frac{kW}{m^2K}$$

This was the only data reduction completed using local values.

C.2 Calculating Average Surface Values

Many average surface values were calculated starting with the local surface values. Table C-1 displays five datapoints that will be used to walk through the process for calculating the average surface parameters. The local surface temperature and local surface heat flux were taken across the surface for the baseline surface under the flat confining wall at a jet Reynolds number of 5600. However, the local surface area values were adjusted to add up to the surface area of the baseline surface. This was done to maintain the results of the sample calculations within the order of magnitude of the values reported in the results section, but the values calculated in this section are not representative of the actual results. The local surface area values provided in the table were set to be approximately the same value, as this was the case in the numerical model; sizing controls were applied to the surface, keeping the element size on the impingement surface close to equal. The sum of these areas is $4.84*10^{-4}m^2$, which equals the surface area for the baseline surface.

Table C-1: Sample dataset for data reduction calculations

Data point number	Local surface temperature (°C)	Local surface heat flux (kW/m^2)	Local surface area (m^2)
1	41.3	400	$9.47*10^{-5}$
2	42.0	268	$9.68*10^{-5}$
3	42.7	322	$9.77*10^{-5}$
4	42.9	293	$9.89*10^{-5}$
5	43.5	123	$9.59*10^{-5}$

The first value to be calculated was the total heat dissipation. As a constant heat generation rate was applied to the same volume in all cases, this value was a nearly constant 83.3W, which corresponds to 500W for a three-by-three array of jets. This value was internally calculated and reported directly by ANSYS Fluent, not through an external software. For the sample dataset displayed above, this value is calculated as follows using Equation C.1:

$$Q_T = \sum_{i=1}^{n} \dot{q}''_{l,i} A_{l,i} \tag{C.1}$$

$$Q_T = \left(400\frac{kW}{m^2}\right)(9.47 * 10^{-5}m^2) + \left(268\frac{kW}{m^2}\right)(9.68 * 10^{-5}m^2) + \cdots$$

$$Q_T = 0.136kW = 136W$$

The total heat dissipated from this dataset is calculated to be greater than that of the actual model. This is reasonable, given the simplifications taken in generating the sample dataset. To reiterate, the values reported in this set of sample calculations are not representative of the final reported values displayed in Table 4-2 through Table 4-7 in Chapter 4, or in Table E-1 displayed in Appendix E.

The next value to be calculated is the average surface temperature, which was again internally calculated and outputted by ANSYS Fluent. This was done through an area-weighted average of the local surface temperature, as shown in Equation C.2. A sample calculating for this value follows:

$$\overline{T_s} = \frac{\sum_{i=1}^{n} T_{l,i}A_{l,i}}{\sum_{i=1}^{n} A_{l,i}} \tag{C.2}$$

$$\overline{T_s} = \frac{(41.3°C)(9.47 * 10^{-5}m^2) + (42°C)(9.68 * 10^{-5}m^2) + \cdots}{9.47 * 10^{-5}m^2 + 9.68 * 10^{-5}m^2 + \cdots}$$

$$\overline{T_s} = 42.5°C$$

The average surface temperature rise ($\overline{\Theta_s}$) was then calculated by subtracting the inlet temperature of 30°C from the average surface temperature. In this sample case, the resulting average surface temperature rise is 12.5K.

Using these values, the average surface heat transfer coefficient can be calculated using Equation C.3, as follows:

$$\overline{h_s} = \frac{Q_T}{\overline{\Theta_s}A_T} \tag{C.3}$$

$$\overline{h_s} = \frac{136W}{(42.5K)(4.84 * 10^{-4}m^2)}$$

$$\overline{h_s} = 22500\frac{W}{m^2K} = 22.5\frac{kW}{m^2K}$$

This concludes the data reduction process for analyzing a single case. However, further data reduction was completed to enable comparisons between surfaces and confining wall angles. To illustrate these additional calculations, consider the sample dataset presented in Table C-2. The baseline surface values are those calculated previously in this section. The modified surface values have been changed in the same proportion to how the short streamwise ribs changed each parameter under a flat confining wall at a jet Reynolds number of 5600; in other words, the average surface temperature was decreased by 14%, the average surface heat transfer coefficient was increased by 5.4%, and the surface area was increased by 10.4%, as indicated in Table 4-4.

Table C-2: Sample dataset for comparisons of different geometries

Surface	Average surface temperature rise (°C)	Average surface heat transfer coefficient (kW/m^2K)	Total surface area (m^2)
Baseline	12.5	22.5	$4.84*10^{-4}$
Modified	10.7	23.7	$5.34*10^{-4}$

Since the model used a constant supply heat condition and the surface area varied with the modification type and size, a direct comparison of the average surface temperature rise or average surface heat transfer coefficient does not directly identify the relative significance of the increased surface area versus changes in the flow mechanics. This proportion can be calculated in one equation, but it will be discussed in multiple steps to help make the process clearer. First, the surface temperature that would result from the same proportional increase in surface area without affecting flow behaviors is calculated. This is obviously not possible, but calculating this value indicates how much surface temperature reduction can be expected due only to the effect of increasing surface area. This is calculated as shown below, starting with Equation C.4:

$$\overline{\Theta_A} = \overline{\Theta_B}\frac{A_B}{A_M} \tag{C.4}$$

$$\overline{\Theta_A} = (12.5°C)\frac{4.84 * 10^{-4}m^2}{5.34 * 10^{-4}m^2}$$

$$\overline{\Theta_A} = 11.3°C$$

Now, knowing the average surface temperature of the baseline case, the modified surface case, and the resulting value due only to increasing surface area, the proportion of the thermal performance of the modified case that is attributed to increasing the surface area can be calculated as such, using Equation C.5:

$$r_A = \frac{\overline{\Theta_B} - \overline{\Theta_A}}{\overline{\Theta_B} - \overline{\Theta_M}} \tag{C.5}$$

$$\overline{\Theta_A} = \frac{12.5°C - 11.3°C}{12.5°C - 10.7°C}$$

$$\overline{\Theta_A} = 0.673 = 67.3\%$$

From this, it is concluded that 67.3% of the thermal improvement provided by the hypothetical modified surface in this sample dataset is the result of increasing area. Conversely, 32.7% of the improvement cannot be attributable to increased area. This process does not prescribe the reason for this proportion of the improved performance, but merely eliminates increasing the surface area for 32.7% of the thermal benefit provided by the modifications. The two effects to which this additional improvement could most likely be attributed would be improvements in the flow mechanics and the location of the added surface area. Analysis of the modification design, location, and flow effects would be required to determine which one is the primary benefactor.

C.3 Matlab Scripting

Matlab scripts were used to generate all contours presented in this effort. This section will display the most pertinent scripts used.

C.3.1 PIV Contour Script

The following code was used to generate all PIV contours. Portions highlighted in yellow are changed depending on the case being examined. It should be noted that the use of the xlsread function is highly inefficient and should be replaced with the readtable function. The xlsread function was used in prior researchers' works and carried over, but it significantly slows the codes.

```
clear all
clc
%clf
```

```
% Specify geometry
wall = 1;   % set to 2 if the angled wall is used and a plot of the
            % y-velocity at the top of the contour is desired

% Read data from Excel
x = xlsread('Angled Re-5600 Ftn OC0.5 mps.xlsx','sheet','A:A');
y = xlsread('Angled Re-5600 Ftn OC0.5 mps.xlsx','sheet','B:B');
u = -xlsread('Angled Re-5600 Ftn OC0.5 mps.xlsx','sheet','C:C');
v = xlsread('Angled Re-5600 Ftn OC0.5 mps.xlsx','sheet','D:D');
mag = xlsread('Angled Re-5600 Ftn OC0.5 mps.xlsx','sheet','E:E');

% Redefine x & y arrays
x = max(x)-x; y = y-min(y);

% Remove redundant data - the text file is populated with data across the
    % entire image frame, even though only a portion of the image viewed
    % the seeded particles. This section removes the fluff.
for i = linspace(length(x),1,length(x))
    if u(i) == 0 && v(i) == 0
        x(i) = []; y(i) = []; u(i) = []; v(i) = []; mag(i) = [];
    else
    end
end

% Define key parameters
xmin = min(x); xmax = max(x);
ymin = min(y); ymax = max(y);

% Define bounds
xlow = xmin; xhigh = xmax; xinc = 2; dx = xhigh - xlow;
ylow = ymin; yhigh = ymax; yinc = 2; dy = yhigh - ylow;

% Determine increment
xinc_mm = 0; yinc_mm = 0; index = 2;
while xinc_mm == 0
    xinc_mm = abs(x(index)-x(index-1));
    index = index+1;
end

index = 2;
while yinc_mm == 0
    yinc_mm = abs(y(index)-y(index-1));
    index = index+1;
end

%% Meshgrid data
xd = xlow:xinc_mm:xmax;
yd = ylow:yinc_mm:ymax;
[xi,yi] = meshgrid(xd,yd);
fprintf('Finished meshgrid of xi and yi\n')
ui = griddata(x,y,u,xi,yi,'cubic');
vi = griddata(x,y,v,xi,yi,'cubic');
magi = griddata(x,y,mag,xi,yi,'cubic');
fprintf('Finished making zi\n')
```

```
Vlow = 0; Vhigh = max(max(magi));
    % These values cover the range of all figures:
    % j-e-t plane: 2.65   fountain plane: 1.514
%Vlow = 0; Vhigh = 1.514;

%% Image processing
% Generate velocity magnitude contour
[C,h] = contourf(xi,yi,magi,256);
w = h.LineStyle;
h.LineStyle = 'none';
title('Velocity Magnitude Contour in the Ftn Symmetry Plane for
Re=5600','FontSize',12)
xlabel('-> Flow Direction ->','FontSize',12,'FontWeight','bold')
% ylabel(' <-Downstream    Upstream->','FontSize',12,'FontWeight','bold')
axis([xlow xhigh ylow yhigh])
xlabels = linspace(xlow,xhigh,xinc);
ylabels = linspace(ylow,yhigh,yinc);
set(gca,'XTick',xlabels)
set(gca,'YTick',ylabels)
set(gca,'FontSize',10)
colormap('jet')
caxis([Vlow Vhigh])
% axis equal
c = colorbar;
c.Label.String = 'Velocity Magnitude (m/s)';
c.Label.FontSize = 11;
c.Label.FontWeight = 'bold';
axis equal
colorbar('southoutside')
fprintf('Finished making contour\n')

% Impose quiverplot
steps_q = 5;
nx_q = round(steps_q*(dx/dy));
ny_q = steps_q;
xd_q = linspace(xlow,xhigh,nx_q);
yd_q = linspace(ylow,yhigh,ny_q);
[xi_q,yi_q] = meshgrid(xd_q,yd_q);
fprintf('Finished meshgrid of xi and yi for quiver plot\n')
ui_q = griddata(x,y,u,xi_q,yi_q,'cubic');
vi_q = griddata(x,y,v,xi_q,yi_q,'cubic');
% wi_q = griddata(x,y,w,xi_q,yi_q,'cubic');
magi_q = griddata(x,y,mag,xi_q,yi_q,'cubic');
fprintf('Finished making zi for quiver plot\n')

    % Normalize vector lengths
ui_n = ui_q./sqrt(ui_q.^2+vi_q.^2);
vi_n = vi_q./sqrt(ui_q.^2+vi_q.^2);

hold on
quiver(xi_q,yi_q,ui_n,vi_n,0.5,'Color',[0.72 0.72 0.72],'LineWidth',1)
set(gca,'Color',[0.65 0.65 0.65])
ylim([ylow yhigh])
hold off
```

```
%% Output parameters to command window
fprintf('Vmin = %5.3f\n',min(min(magi)))
fprintf('Vmax = %5.3f\n',max(max(magi)))

%% Plot the y-velocity of the top row of the data
switch wall
    case 2
        figure
        plot(xi(size(xi,1),:)-xmin,vi(size(vi,1),:),LineWidth=1.5)
        xlim([0,xmax-xmin])
        title('Angled Wall y-velocity of the Top Row in the Ftn Plane')
        ylabel('y-velocity (m/s)');xlabel('Location (mm)')
        fprintf('Max y-vel of the top row: %4.3f\n',max(vi(size(vi,1),:)))
        fprintf('Min y-vel of the top row: %4.3f\n',min(vi(size(vi,1),:)))
    otherwise
end
```

C.3.2 Numerical Jet Plane Flow Field Contours

Two slightly different scripts were used to generate flow fields in the jet plane: one was for the flat wall while the other was for the angled wall. For brevity, only the flat wall script is shown here. Portions highlighted in yellow are changed depending on the case being examined. Portions highlighted in cyan are to be edited to change the scope and scale of the flow field.

```
clear all
clc
clf

% Specify geometry
% Set each value to 1 if a short modification is applied and 2 if a tall
% modification is applied. Any other value indicated no modification of
% that type. jc=Jet Cone     tr=Tansverse Rib   oc=Offset Cone
jc = 3; tr = 3; oc = 3;

% Read data from Excel
x = xlsread('Flat Re-5600 OC-05.xlsx','sheet','D:D');
y = xlsread('Flat Re-5600 OC-05.xlsx','sheet','C:C');
u = -xlsread('Flat Re-5600 OC-05.xlsx','sheet','H:H');
v = xlsread('Flat Re-5600 OC-05.xlsx','sheet','G:G');
mag = xlsread('Flat Re-5600 OC-05.xlsx','sheet','E:E');
fprintf('Finished reading Excel document\n')

% Redefine x & y arrays
x = max(x)-x; y = y-min(y);

% Define key parameters
xmin = min(x); xmax = max(x);
ymin = min(y); ymax = max(y);
```

```
% Define bounds
xlow = 0.0125; xhigh = 0.065; xinc = 2; dx = xlow - xhigh;
ylow = 0; yhigh = 0.00635; yinc = 2; dy = ylow - yhigh;
% xlow = xmin; xhigh = xmax; xinc = 2; dx = xlow - xhigh;
% ylow = ymin; yhigh = ymax; yinc = 2; dy = ylow - yhigh;

% Meshgrid data
steps = 700;
nx = round(steps*(dx/dy));
ny = steps;
xd = linspace(xlow,xhigh,nx);
yd = linspace(ylow,yhigh,ny);
[xi,yi] = meshgrid(xd,yd);
fprintf('Finished meshgrid of xi and yi\n')
ui = griddata(x,y,u,xi,yi,'cubic');
vi = griddata(x,y,v,xi,yi,'cubic');
magi = griddata(x,y,mag,xi,yi,'cubic');
fprintf('Finished making zi\n')

% Exclude extraneous data - the meshgrid process fills all empty spaces in
% the data, even where there is no fluid. This section removes the fluff.
for i = 1:nx
    for j = 1:ny
        if yi(j,i)>0.00635 && xi(j,i)<0.0127
            magi(j,i) = NaN; ui(j,i) = NaN; vi(j,i) = NaN; wi(j,i) = NaN;
        elseif yi(j,i)>0.00635 && yi(j,i)<0.0127 && xi(j,i)<0.023815
            magi(j,i) = NaN; ui(j,i) = NaN; vi(j,i) = NaN; wi(j,i) = NaN;
        elseif yi(j,i)>0.00635 && yi(j,i)<0.0127 && xi(j,i)>0.026988 &&
xi(j,i)<0.036513
            magi(j,i) = NaN; ui(j,i) = NaN; vi(j,i) = NaN; wi(j,i) = NaN;
        elseif yi(j,i)>0.00635 && yi(j,i)<0.0127 && xi(j,i)>0.039688 &&
xi(j,i)<0.049213
            magi(j,i) = NaN; ui(j,i) = NaN; vi(j,i) = NaN; wi(j,i) = NaN;
        elseif yi(j,i)>0.00635 && yi(j,i)<0.0127 && xi(j,i)>0.052388
            magi(j,i) = NaN; ui(j,i) = NaN; vi(j,i) = NaN; wi(j,i) = NaN;
        elseif xi(j,i)>0.0127 && xi(j,i)<0.01778 && yi(j,i)>0.00635 &&
yi(j,i)<0.01778-sqrt(0.00508^2-(xi(j,i)-0.01778)^2)
            magi(j,i) = NaN; ui(j,i) = NaN; vi(j,i) = NaN; wi(j,i) = NaN;
        elseif xi(j,i)>0.07112 && xi(j,i)<0.0762 && yi(j,i)>0.00635 &&
yi(j,i)<0.01778-sqrt(0.00508^2-(xi(j,i)-0.07112)^2)
            magi(j,i) = NaN; ui(j,i) = NaN; vi(j,i) = NaN; wi(j,i) = NaN;
        end
        switch jc
            case 2
                if xi(j,i)>0.023813 && xi(j,i)<0.025308 && yi(j,i)<(jc*xi(j,i)-
jc*0.023813)
                    magi(j,i) = NaN; ui(j,i) = NaN; vi(j,i) = NaN; wi(j,i) = NaN;
                elseif xi(j,i)>0.025492 && xi(j,i)<0.026988 && yi(j,i)<(-
jc*xi(j,i)+jc*0.026988)
                    magi(j,i) = NaN; ui(j,i) = NaN; vi(j,i) = NaN; wi(j,i) = NaN;
                elseif xi(j,i)>0.025308 && xi(j,i)<0.025492 &&
yi(j,i)<0.002945+sqrt(0.000103^2-(xi(j,i)-0.0254)^2)
                    magi(j,i) = NaN; ui(j,i) = NaN; vi(j,i) = NaN; wi(j,i) = NaN;
                elseif xi(j,i)>0.036513 && xi(j,i)<0.038008 && yi(j,i)<(jc*xi(j,i)-
jc*0.036513)
```

```
                    magi(j,i) = NaN; ui(j,i) = NaN; vi(j,i) = NaN; wi(j,i) = NaN;
                elseif xi(j,i)>0.038192 && xi(j,i)<0.039688 && yi(j,i)<(-
jc*xi(j,i)+jc*0.039688)
                    magi(j,i) = NaN; ui(j,i) = NaN; vi(j,i) = NaN; wi(j,i) = NaN;
                elseif xi(j,i)>0.038008 && xi(j,i)<0.038192 &&
yi(j,i)<0.002945+sqrt(0.000103^2-(xi(j,i)-0.0381)^2)
                    magi(j,i) = NaN; ui(j,i) = NaN; vi(j,i) = NaN; wi(j,i) = NaN;
                elseif xi(j,i)>0.049213 && xi(j,i)<0.050708 && yi(j,i)<(jc*xi(j,i)-
jc*0.049213)
                    magi(j,i) = NaN; ui(j,i) = NaN; vi(j,i) = NaN; wi(j,i) = NaN;
                elseif xi(j,i)>0.050892 && xi(j,i)<0.052388 && yi(j,i)<(-
jc*xi(j,i)+jc*0.052388)
                    magi(j,i) = NaN; ui(j,i) = NaN; vi(j,i) = NaN; wi(j,i) = NaN;
                elseif xi(j,i)>0.050708 && xi(j,i)<0.050892 &&
yi(j,i)<0.002945+sqrt(0.000103^2-(xi(j,i)-0.0508)^2)
                    magi(j,i) = NaN; ui(j,i) = NaN; vi(j,i) = NaN; wi(j,i) = NaN;
                end
            case 1
                if xi(j,i)>0.023813 && xi(j,i)<0.0254 && yi(j,i)<(jc*xi(j,i)-
jc*0.023813)
                    magi(j,i) = NaN; ui(j,i) = NaN; vi(j,i) = NaN; wi(j,i) = NaN;
                elseif xi(j,i)>0.0254 && xi(j,i)<0.026988 && yi(j,i)<(-
jc*xi(j,i)+jc*0.026988)
                    magi(j,i) = NaN; ui(j,i) = NaN; vi(j,i) = NaN; wi(j,i) = NaN;
                elseif xi(j,i)>0.036513 && xi(j,i)<0.0381 && yi(j,i)<(jc*xi(j,i)-
jc*0.036513)
                    magi(j,i) = NaN; ui(j,i) = NaN; vi(j,i) = NaN; wi(j,i) = NaN;
                elseif xi(j,i)>0.0381 && xi(j,i)<0.039688 && yi(j,i)<(-
jc*xi(j,i)+jc*0.039688)
                    magi(j,i) = NaN; ui(j,i) = NaN; vi(j,i) = NaN; wi(j,i) = NaN;
                elseif xi(j,i)>0.049213 && xi(j,i)<0.0508 && yi(j,i)<(jc*xi(j,i)-
jc*0.049213)
                    magi(j,i) = NaN; ui(j,i) = NaN; vi(j,i) = NaN; wi(j,i) = NaN;
                elseif xi(j,i)>0.0508 && xi(j,i)<0.052388 && yi(j,i)<(-
jc*xi(j,i)+jc*0.052388)
                    magi(j,i) = NaN; ui(j,i) = NaN; vi(j,i) = NaN; wi(j,i) = NaN;
                end
            otherwise
        end
        switch tr
            case 3
            otherwise
                if xi(j,i)>0.0301625 && xi(j,i)<0.03175 && yi(j,i)<(tr*xi(j,i)-
tr*0.0301625)
                    magi(j,i) = NaN; ui(j,i) = NaN; vi(j,i) = NaN; wi(j,i) = NaN;
                elseif xi(j,i)>0.03175 && xi(j,i)<0.0333375 && yi(j,i)<(-
tr*xi(j,i)+tr*0.0333375)
                    magi(j,i) = NaN; ui(j,i) = NaN; vi(j,i) = NaN; wi(j,i) = NaN;
                elseif xi(j,i)>0.0428625 && xi(j,i)<0.04445 && yi(j,i)<(tr*xi(j,i)-
tr*0.0428625)
                    magi(j,i) = NaN; ui(j,i) = NaN; vi(j,i) = NaN; wi(j,i) = NaN;
                elseif xi(j,i)>0.04445 && xi(j,i)<0.0460375 && yi(j,i)<(-
tr*xi(j,i)+tr*0.0460375)
                    magi(j,i) = NaN; ui(j,i) = NaN; vi(j,i) = NaN; wi(j,i) = NaN;
                end
```

```
        end
        switch oc
            case 2
                if xi(j,i)>0.0301625 && xi(j,i)<0.0316581 && yi(j,i)<(oc*xi(j,i)-
oc*0.0301625)
                    magi(j,i) = NaN; ui(j,i) = NaN; vi(j,i) = NaN; wi(j,i) = NaN;
                elseif xi(j,i)>0.0318419 && xi(j,i)<0.0333375 && yi(j,i)<(-
oc*xi(j,i)+oc*0.0333375)
                    magi(j,i) = NaN; ui(j,i) = NaN; vi(j,i) = NaN; wi(j,i) = NaN;
                elseif xi(j,i)>0.0316581 && xi(j,i)<0.0318419 &&
yi(j,i)<0.002945+sqrt(0.000103^2-(xi(j,i)-0.03175)^2)
                    magi(j,i) = NaN; ui(j,i) = NaN; vi(j,i) = NaN; wi(j,i) = NaN;
                elseif xi(j,i)>0.0428625 && xi(j,i)<0.0443581 && yi(j,i)<(oc*xi(j,i)-
oc*0.0428625)
                    magi(j,i) = NaN; ui(j,i) = NaN; vi(j,i) = NaN; wi(j,i) = NaN;
                elseif xi(j,i)>0.0445419 && xi(j,i)<0.0460375 && yi(j,i)<(-
oc*xi(j,i)+oc*0.0460375)
                    magi(j,i) = NaN; ui(j,i) = NaN; vi(j,i) = NaN; wi(j,i) = NaN;
                elseif xi(j,i)>0.0443581 && xi(j,i)<0.0445419 &&
yi(j,i)<0.002945+sqrt(0.000103^2-(xi(j,i)-0.04445)^2)
                    magi(j,i) = NaN; ui(j,i) = NaN; vi(j,i) = NaN; wi(j,i) = NaN;
                end
            case 1
                if xi(j,i)>0.0301625 && xi(j,i)<0.03175 && yi(j,i)<(oc*xi(j,i)-
oc*0.0301625)
                    magi(j,i) = NaN; ui(j,i) = NaN; vi(j,i) = NaN; wi(j,i) = NaN;
                elseif xi(j,i)>0.03175 && xi(j,i)<0.0333375 && yi(j,i)<(-
oc*xi(j,i)+oc*0.0333375)
                    magi(j,i) = NaN; ui(j,i) = NaN; vi(j,i) = NaN; wi(j,i) = NaN;
                elseif xi(j,i)>0.0428625 && xi(j,i)<0.04445 && yi(j,i)<(oc*xi(j,i)-
oc*0.0428625)
                    magi(j,i) = NaN; ui(j,i) = NaN; vi(j,i) = NaN; wi(j,i) = NaN;
                elseif xi(j,i)>0.04445 && xi(j,i)<0.0460375 && yi(j,i)<(-
oc*xi(j,i)+oc*0.0460375)
                    magi(j,i) = NaN; ui(j,i) = NaN; vi(j,i) = NaN; wi(j,i) = NaN;
                end
            otherwise
        end
    end
end
fprintf('Finished excluding extraneous data')

%% Generate velocity magnitude contour
V_max = max(max(magi));
        %V_max = 2.65;
[C,h] = contourf(xi,yi,magi,256);
w = h.LineStyle;
h.LineStyle = 'none';
title('Velocity Magnitude Contour in the Jet Symmetry Plane for
Re=5600','FontSize',12)
xlabel('<-Downstream    Upstream->','FontSize',14,'FontWeight','bold')
axis([xlow xhigh ylow yhigh])
xlabels = linspace(xlow,xhigh,xinc);
ylabels = linspace(ylow,yhigh,yinc);
set(gca,'XTick',xlabels)
```

```
set(gca,'YTick',ylabels)
set(gca,'FontSize',10)
colormap('jet')
caxis([0 V_max])
c = colorbar('southoutside');
c.Label.String = 'Velocity Magnitude (m/s)';
c.Label.FontSize = 11;
c.Label.FontWeight = 'bold';
axis equal
fprintf('Finished making plot\n')

% Impose quiver plot
    % Define looser grid for quiver plot
steps_q = 5;
nx_q = round(steps_q*(dx/dy));
ny_q = steps_q;
xd_q = linspace(xlow,xhigh,nx_q);
yd_q = linspace(ylow,yhigh,ny_q);
[xi_q,yi_q] = meshgrid(xd_q,yd_q);
fprintf('Finished meshgrid of xi and yi for quiver plot\n')
ui_q = griddata(x,y,u,xi_q,yi_q,'cubic');
vi_q = griddata(x,y,v,xi_q,yi_q,'cubic');
magi_q = griddata(x,y,mag,xi_q,yi_q,'cubic');
fprintf('Finished making zi for quiver plot\n')

    % Normalize vector lengths
ui_q_n = ui_q./sqrt(ui_q.^2+vi_q.^2);
vi_q_n = vi_q./sqrt(ui_q.^2+vi_q.^2);
ui_q = ui_q_n; vi_q = vi_q_n;

    % Exclude extraneous data
for i = 1:nx_q
    for j = 1:ny_q
        if yi_q(j,i)>0.00635 && xi_q(j,i)<0.0127
            magi_q(j,i) = NaN; ui_q(j,i) = NaN; vi_q(j,i) = NaN;
        elseif yi_q(j,i)>0.00635 && yi_q(j,i)<0.0127 && xi_q(j,i)<0.023815
            magi_q(j,i) = NaN; ui_q(j,i) = NaN; vi_q(j,i) = NaN;
        elseif yi_q(j,i)>0.00635 && yi_q(j,i)<0.0127 && xi_q(j,i)>0.026988 &&
xi_q(j,i)<0.036513
            magi_q(j,i) = NaN; ui_q(j,i) = NaN; vi_q(j,i) = NaN;
        elseif yi_q(j,i)>0.00635 && yi_q(j,i)<0.0127 && xi_q(j,i)>0.039688 &&
xi_q(j,i)<0.049213
            magi_q(j,i) = NaN; ui_q(j,i) = NaN; vi_q(j,i) = NaN;
        elseif yi_q(j,i)>0.00635 && yi_q(j,i)<0.0127 && xi_q(j,i)>0.052388
            magi_q(j,i) = NaN; ui_q(j,i) = NaN; vi_q(j,i) = NaN;
        elseif xi_q(j,i)>0.0127 && xi_q(j,i)<0.01778 && yi_q(j,i)>0.00635 &&
yi_q(j,i)<0.01778-sqrt(0.00508^2-(xi_q(j,i)-0.01778)^2)
            magi_q(j,i) = NaN; ui_q(j,i) = NaN; vi_q(j,i) = NaN;
        elseif xi_q(j,i)>0.07112 && xi_q(j,i)<0.0762 && yi_q(j,i)>0.00635 &&
yi_q(j,i)<0.01778-sqrt(0.00508^2-(xi_q(j,i)-0.07112)^2)
            magi_q(j,i) = NaN; ui_q(j,i) = NaN; vi_q(j,i) = NaN;
        end
        switch jc
            case 2
```

```
                if xi_q(j,i)>0.023813 && xi_q(j,i)<0.025308 &&
yi_q(j,i)<(jc*xi_q(j,i)-jc*0.023813)
                    magi_q(j,i) = NaN; ui_q(j,i) = NaN; vi_q(j,i) = NaN;
                elseif xi_q(j,i)>0.025492 && xi_q(j,i)<0.026988 && yi_q(j,i)<(-
jc*xi_q(j,i)+jc*0.026988)
                    magi_q(j,i) = NaN; ui_q(j,i) = NaN; vi_q(j,i) = NaN;
                elseif xi_q(j,i)>0.025308 && xi_q(j,i)<0.025492 &&
yi_q(j,i)<0.002945+sqrt(0.000103^2-(xi_q(j,i)-0.0254)^2)
                    magi_q(j,i) = NaN; ui_q(j,i) = NaN; vi_q(j,i) = NaN;
                elseif xi_q(j,i)>0.036513 && xi_q(j,i)<0.038008 &&
yi_q(j,i)<(jc*xi_q(j,i)-jc*0.036513)
                    magi_q(j,i) = NaN; ui_q(j,i) = NaN; vi_q(j,i) = NaN;
                elseif xi_q(j,i)>0.038192 && xi_q(j,i)<0.039688 && yi_q(j,i)<(-
jc*xi_q(j,i)+jc*0.039688)
                    magi_q(j,i) = NaN; ui_q(j,i) = NaN; vi_q(j,i) = NaN;
                elseif xi_q(j,i)>0.038008 && xi_q(j,i)<0.038192 &&
yi_q(j,i)<0.002945+sqrt(0.000103^2-(xi_q(j,i)-0.0381)^2)
                    magi_q(j,i) = NaN; ui_q(j,i) = NaN; vi_q(j,i) = NaN;
                elseif xi_q(j,i)>0.049213 && xi_q(j,i)<0.050708 &&
yi_q(j,i)<(jc*xi_q(j,i)-jc*0.049213)
                    magi_q(j,i) = NaN; ui_q(j,i) = NaN; vi_q(j,i) = NaN;
                elseif xi_q(j,i)>0.050892 && xi_q(j,i)<0.052388 && yi_q(j,i)<(-
jc*xi_q(j,i)+jc*0.052388)
                    magi_q(j,i) = NaN; ui_q(j,i) = NaN; vi_q(j,i) = NaN;
                elseif xi_q(j,i)>0.050708 && xi_q(j,i)<0.050892 &&
yi_q(j,i)<0.002945+sqrt(0.000103^2-(xi_q(j,i)-0.0508)^2)
                    magi_q(j,i) = NaN; ui_q(j,i) = NaN; vi_q(j,i) = NaN;
                end
            case 1
                if xi_q(j,i)>0.023813 && xi_q(j,i)<0.0254 && yi_q(j,i)<(jc*xi_q(j,i)-
jc*0.023813)
                    magi_q(j,i) = NaN; ui_q(j,i) = NaN; vi_q(j,i) = NaN;
                elseif xi_q(j,i)>0.0254 && xi_q(j,i)<0.026988 && yi_q(j,i)<(-
jc*xi_q(j,i)+jc*0.026988)
                    magi_q(j,i) = NaN; ui_q(j,i) = NaN; vi_q(j,i) = NaN;
                elseif xi_q(j,i)>0.036513 && xi_q(j,i)<0.0381 &&
yi_q(j,i)<(jc*xi_q(j,i)-jc*0.036513)
                    magi_q(j,i) = NaN; ui_q(j,i) = NaN; vi_q(j,i) = NaN;
                elseif xi_q(j,i)>0.0381 && xi_q(j,i)<0.039688 && yi_q(j,i)<(-
jc*xi_q(j,i)+jc*0.039688)
                    magi_q(j,i) = NaN; ui_q(j,i) = NaN; vi_q(j,i) = NaN;
                elseif xi_q(j,i)>0.049213 && xi_q(j,i)<0.0508 &&
yi_q(j,i)<(jc*xi_q(j,i)-jc*0.049213)
                    magi_q(j,i) = NaN; ui_q(j,i) = NaN; vi_q(j,i) = NaN;
                elseif xi_q(j,i)>0.0508 && xi_q(j,i)<0.052388 && yi_q(j,i)<(-
jc*xi_q(j,i)+jc*0.052388)
                    magi_q(j,i) = NaN; ui_q(j,i) = NaN; vi_q(j,i) = NaN;
                end
            otherwise
        end
        switch tr
            case 3
            otherwise
                if xi_q(j,i)>0.0301625 && xi_q(j,i)<0.03175 &&
yi_q(j,i)<(tr*xi_q(j,i)-tr*0.0301625)
```

```
                    magi_q(j,i) = NaN; ui_q(j,i) = NaN; vi_q(j,i) = NaN; wi_q(j,i) =
NaN;
                elseif xi_q(j,i)>0.03175 && xi_q(j,i)<0.0333375 && yi_q(j,i)<(-
tr*xi_q(j,i)+tr*0.0333375)
                    magi_q(j,i) = NaN; ui_q(j,i) = NaN; vi_q(j,i) = NaN; wi_q(j,i) =
NaN;
                elseif xi_q(j,i)>0.0428625 && xi_q(j,i)<0.04445 &&
yi_q(j,i)<(tr*xi_q(j,i)-tr*0.0428625)
                    magi_q(j,i) = NaN; ui_q(j,i) = NaN; vi_q(j,i) = NaN; wi_q(j,i) =
NaN;
                elseif xi_q(j,i)>0.04445 && xi_q(j,i)<0.0460375 && yi_q(j,i)<(-
tr*xi_q(j,i)+tr*0.0460375)
                    magi_q(j,i) = NaN; ui_q(j,i) = NaN; vi_q(j,i) = NaN; wi_q(j,i) =
NaN;
                end
        end
        switch oc
            case 2
                if xi_q(j,i)>0.0301625 && xi_q(j,i)<0.0316581 &&
yi_q(j,i)<(oc*xi_q(j,i)-oc*0.0301625)
                    magi_q(j,i) = NaN; ui_q(j,i) = NaN; vi_q(j,i) = NaN;
                elseif xi_q(j,i)>0.0318419 && xi_q(j,i)<0.0333375 && yi_q(j,i)<(-
oc*xi_q(j,i)+oc*0.0333375)
                    magi_q(j,i) = NaN; ui_q(j,i) = NaN; vi_q(j,i) = NaN;
                elseif xi_q(j,i)>0.0316581 && xi_q(j,i)<0.0318419 &&
yi_q(j,i)<0.002945+sqrt(0.000103^2-(xi_q(j,i)-0.03175)^2)
                    magi_q(j,i) = NaN; ui_q(j,i) = NaN; vi_q(j,i) = NaN;
                elseif xi_q(j,i)>0.0428625 && xi_q(j,i)<0.0443581 &&
yi_q(j,i)<(oc*xi_q(j,i)-oc*0.0428625)
                    magi_q(j,i) = NaN; ui_q(j,i) = NaN; vi_q(j,i) = NaN;
                elseif xi_q(j,i)>0.0445419 && xi_q(j,i)<0.0460375 && yi_q(j,i)<(-
oc*xi_q(j,i)+oc*0.0460375)
                    magi_q(j,i) = NaN; ui_q(j,i) = NaN; vi_q(j,i) = NaN;
                elseif xi_q(j,i)>0.0443581 && xi_q(j,i)<0.0445419 &&
yi_q(j,i)<0.002945+sqrt(0.000103^2-(xi_q(j,i)-0.04445)^2)
                    magi_q(j,i) = NaN; ui_q(j,i) = NaN; vi_q(j,i) = NaN;
                end
            case 1
                if xi_q(j,i)>0.0301625 && xi_q(j,i)<0.03175 &&
yi_q(j,i)<(oc*xi_q(j,i)-oc*0.0301625)
                    magi_q(j,i) = NaN; ui_q(j,i) = NaN; vi_q(j,i) = NaN;
                elseif xi_q(j,i)>0.03175 && xi_q(j,i)<0.0333375 && yi_q(j,i)<(-
oc*xi_q(j,i)+oc*0.0333375)
                    magi_q(j,i) = NaN; ui_q(j,i) = NaN; vi_q(j,i) = NaN;
                elseif xi_q(j,i)>0.0428625 && xi_q(j,i)<0.04445 &&
yi_q(j,i)<(oc*xi_q(j,i)-oc*0.0428625)
                    magi_q(j,i) = NaN; ui_q(j,i) = NaN; vi_q(j,i) = NaN;
                elseif xi_q(j,i)>0.04445 && xi_q(j,i)<0.0460375 && yi_q(j,i)<(-
oc*xi_q(j,i)+oc*0.0460375)
                    magi_q(j,i) = NaN; ui_q(j,i) = NaN; vi_q(j,i) = NaN;
                end
            otherwise
        end
    end
end
```

```
hold on
quiver(xi_q,yi_q,ui_q,vi_q,0.5,'Color',[0.72 0.72 0.72],'LineWidth',1)
set(gca,'Color',[0.65 0.65 0.65])
ylim([ylow yhigh])
hold off

%% Output parameters to command window
fprintf('Vmax = %5.3f\n',max(max(magi)))
```

C.3.3 Numerical Fountain Plane Flow Field Contours

Like to the jet plane scripting, separate scripts were used for the flat and angled confining walls in the fountain plane. Again, for brevity, only the flat wall script is shown here. Portions highlighted in yellow are changed depending on the case being examined. Portions highlighted in cyan are to be edited to change the scope and scale of the flow field.

```
clear all
clc
clf

% Specify geometry
% Set each value to 1 if a short modification is applied and 2 if a tall
% modification is applied. Any other value indicated no modification of
% that type. sr=Streamwise Rib     tr=Tansverse Rib
sr = 3; tr = 3;

% Read data from Excel
x = xlsread('Flat Re-5600 OC-05.xlsx','sheet','D:D');
y = xlsread('Flat Re-5600 OC-05.xlsx','sheet','C:C');
u = -xlsread('Flat Re-5600 OC-05.xlsx','sheet','H:H');
v = xlsread('Flat Re-5600 OC-05.xlsx','sheet','G:G');
mag = xlsread('Flat Re-5600 OC-05.xlsx','sheet','E:E');
fprintf('Finished reading Excel document\n')

% Redefine x & y arrays
x = max(x)-x;
switch sr
    case 1
        y = y-min(y)+0.003175/2;
    case 2
        y = y-min(y)+0.003175;
    otherwise
    y = y-min(y);
end

% Define key parameters
xmin = min(x); xmax = max(x);
ymin = min(y); ymax = max(y);
```

```
% Define bounds
xlow = 0.0125; xhigh = 0.065; xinc = 2; dx = xlow - xhigh;
ylow = 0; yhigh = 0.00635; yinc = 2; dy = ylow - yhigh;
% xlow = xmin; xhigh = xmax; xinc = 5; dx = xlow - xhigh;
% ylow = ymin; yhigh = ymax; yinc = 2; dy = ylow - yhigh;

% Meshgrid data
steps = 500;
nx = round(steps*(dx/dy));
ny = steps;
xd = linspace(xlow,xhigh,nx);
yd = linspace(ylow,yhigh,ny);
[xi,yi] = meshgrid(xd,yd);
fprintf('Finished meshgrid of xi and yi\n')
ui = griddata(x,y,u,xi,yi,'cubic');
vi = griddata(x,y,v,xi,yi,'cubic');
magi = griddata(x,y,mag,xi,yi,'cubic');
fprintf('Finished making zi\n')

% Exclude extraneous data - the meshgrid process fills all empty spaces in
% the data, even where there is no fluid. This section removes the fluff.
for i = 1:nx
    for j = 1:ny
        if yi(j,i)>0.00635
            magi(j,i) = NaN; ui(j,i) = NaN; vi(j,i) = NaN; wi(j,i) = NaN;
        end
        switch tr
            case 3
            otherwise
                if xi(j,i)>0.0301625 && xi(j,i)<0.03175 && yi(j,i)<(tr*xi(j,i)-
tr*0.0301625)
                    magi(j,i) = NaN; ui(j,i) = NaN; vi(j,i) = NaN; wi(j,i) = NaN;
                elseif xi(j,i)>0.03175 && xi(j,i)<0.0333375 && yi(j,i)<(-
tr*xi(j,i)+tr*0.0333375)
                    magi(j,i) = NaN; ui(j,i) = NaN; vi(j,i) = NaN; wi(j,i) = NaN;
                elseif xi(j,i)>0.0428625 && xi(j,i)<0.04445 && yi(j,i)<(tr*xi(j,i)-
tr*0.0428625)
                    magi(j,i) = NaN; ui(j,i) = NaN; vi(j,i) = NaN; wi(j,i) = NaN;
                elseif xi(j,i)>0.04445 && xi(j,i)<0.0460375 && yi(j,i)<(-
tr*xi(j,i)+tr*0.0460375)
                    magi(j,i) = NaN; ui(j,i) = NaN; vi(j,i) = NaN; wi(j,i) = NaN;
                end
        end
    end
end

%% Generate velocity magnitude contour
V_max = max(max(magi));
        %V_max = 1.514;
[C,h] = contourf(xi,yi,magi,256);
w = h.LineStyle;
h.LineStyle = 'none';
title('Velocity Magnitude Contour in the Fountain Symmetry Plane for
Re=5600','FontSize',12)
xlabel('<-Downstream    Upstream->','FontSize',14,'FontWeight','bold')
```

```
axis([xlow xhigh ylow yhigh])
xlabels = linspace(xlow,xhigh,xinc);
ylabels = linspace(ylow,yhigh,yinc);
set(gca,'XTick',xlabels)
set(gca,'YTick',ylabels)
set(gca,'FontSize',10)
colormap('jet')
caxis([0 V_max])
c = colorbar('southoutside');
c.Label.String = 'Velocity Magnitude (m/s)';
c.Label.FontSize = 11;
c.Label.FontWeight = 'bold';
axis equal
fprintf('Finished making plot\n')

% Impose quiver plot
    % Define looser grid for quiver plot
steps_q = 5;
nx_q = round(steps_q*(dx/dy));
ny_q = steps_q;
xd_q = linspace(xlow,xhigh,nx_q);
yd_q = linspace(0.0005,yhigh,ny_q);
[xi_q,yi_q] = meshgrid(xd_q,yd_q);
fprintf('Finished meshgrid of xi and yi for quiver plot\n')
ui_q = griddata(x,y,u,xi_q,yi_q,'cubic');
vi_q = griddata(x,y,v,xi_q,yi_q,'cubic');
magi_q = griddata(x,y,mag,xi_q,yi_q,'cubic');
fprintf('Finished making zi for quiver plot\n')

    % Normalize vector lengths
ui_q_n = ui_q./sqrt(ui_q.^2+vi_q.^2);
vi_q_n = vi_q./sqrt(ui_q.^2+vi_q.^2);
ui_q = ui_q_n; vi_q = vi_q_n;

    % Excluse extraneous data
for i = 1:nx_q
    for j = 1:ny_q
        if yi_q(j,i)>0.00635
            magi_q(j,i) = NaN; ui_q(j,i) = NaN; vi_q(j,i) = NaN;
        end
        switch tr
            case 3
            otherwise
                if xi_q(j,i)>0.0301625 && xi_q(j,i)<0.03175 &&
yi_q(j,i)<(tr*xi_q(j,i)-tr*0.0301625)
                    magi_q(j,i) = NaN; ui_q(j,i) = NaN; vi_q(j,i) = NaN; wi_q(j,i) =
NaN;
                elseif xi_q(j,i)>0.03175 && xi_q(j,i)<0.0333375 && yi_q(j,i)<(-
tr*xi_q(j,i)+tr*0.0333375)
                    magi_q(j,i) = NaN; ui_q(j,i) = NaN; vi_q(j,i) = NaN; wi_q(j,i) =
NaN;
                elseif xi_q(j,i)>0.0428625 && xi_q(j,i)<0.04445 &&
yi_q(j,i)<(tr*xi_q(j,i)-tr*0.0428625)
                    magi_q(j,i) = NaN; ui_q(j,i) = NaN; vi_q(j,i) = NaN; wi_q(j,i) =
NaN;
```

```
                elseif xi_q(j,i)>0.04445 && xi_q(j,i)<0.0460375 && yi_q(j,i)<(-
tr*xi_q(j,i)+tr*0.0460375)
                    magi_q(j,i) = NaN; ui_q(j,i) = NaN; vi_q(j,i) = NaN; wi_q(j,i) =
NaN;
                end
        end
    end
end

hold on
quiver(xi_q,yi_q,ui_q,vi_q,0.5,'Color',[0.45 0.45 0.45],'LineWidth',1)
set(gca,'Color',[0.65 0.65 0.65])
ylim([ylow yhigh])
hold off

%% Output parameters to command window
fprintf('Vmax = %5.3f\n',max(max(magi)))
```

C.3.4 Numerical Surface Contours

One script was used to generate all numerical surface contours, as shown below. The script is designed to allow any combination of the numerical cases at the same jet Reynolds number to be juxtaposed in the same contour. Due to the many possible combinations of cases that could be created, this script is very long. It has been abridged here, reducing it to only handle the baseline and jet cone cases under a flat confining wall. To accommodate additional geometries in the script below, the portions highlighted in green and yellow need to be copied and pasted; after pasting, the portions highlighted in green need not be changed, while the portions highlighted in yellow must be changed to accommodate the new geometry. Portions highlighted in cyan are to be edited to change the scope and scale of the contours.

```
clear all
clc

% Specify cases - set to 1 if the case should be added in the contours. Any
% other value will neglect that case
baseline_flat = 1;
jc05_flat = 0;
jc1_flat = 0;

% Define bounds
xlow = 0; xhigh = 0.0063; xinc = 2;
ylow = 0.0125; yhigh = 0.065; yinc = 2;

% Meshgrid data
steps = 500;
nx = round(steps*((xhigh-xlow)/(yhigh-ylow)));
```

```
ny = steps;
xd = linspace(xlow,xhigh,nx);
yd = linspace(ylow,yhigh,ny);
[xi,yi] = meshgrid(xd,yd);

% Initialize variables
Ti_c = []; qi_c = []; hi_c = [];
xi_c = []; yi_c = [];
ind = 0;

% Process data
switch baseline_flat
    case 1
        % Read data from Excel
        x = xlsread('Flat Re-5600 No-Mods.xlsx','sheet','B:B');
        y = xlsread('Flat Re-5600 No-Mods.xlsx','sheet','D:D');
        T = xlsread('Flat Re-5600 No-Mods.xlsx','sheet','E:E') - 273 - 30;
        q = xlsread('Flat Re-5600 No-Mods.xlsx','sheet','F:F');

        % Redefine x & y arrays
        x = x-min(x); y = max(y)-y;

        % Griddata
        Ti = griddata(x,y,T,xi,yi,'cubic');
        qi = griddata(x,y,q,xi,yi,'cubic');

        % Calculate htc
        hi = qi./Ti/1000;

        % Combine data
        Ti_c = [Ti_c Ti flip(Ti,2)];
        qi_c = [qi_c qi flip(qi,2)];
        hi_c = [hi_c hi flip(hi,2)];
        xi_c = [xi_c xi+(ind*xhigh) xi+((ind+1)*xhigh)];
        yi_c = [yi_c yi yi];

        % Increment count (by 2)
        ind = ind+2;
end

switch jc05_flat
    case 1
        % Read data from Excel
        x = xlsread('Flat Re-5600 JC-0.5.xlsx','sheet','B:B');
        y = xlsread('Flat Re-5600 JC-0.5.xlsx','sheet','D:D');
        T = xlsread('Flat Re-5600 JC-0.5.xlsx','sheet','E:E') - 273 - 30;
        q = xlsread('Flat Re-5600 JC-0.5.xlsx','sheet','F:F');

        % Redefine x & y arrays
        x = x-min(x); y = max(y)-y;

        % Griddata
        Ti = griddata(x,y,T,xi,yi,'cubic');
        qi = griddata(x,y,q,xi,yi,'cubic');
```

```
        % Calculate htc
        hi = qi./Ti/1000;

        % Combine data
        Ti_c = [Ti_c Ti flip(Ti,2)];
        qi_c = [qi_c qi flip(qi,2)];
        hi_c = [hi_c hi flip(hi,2)];
        xi_c = [xi_c xi+(ind*xhigh) xi+((ind+1)*xhigh)];
        yi_c = [yi_c yi yi];

        % Increment count (by 2)
        ind = ind+2;
end

switch jc1_flat
    case 1
        % Read data from Excel
        x = xlsread('Flat Re-5600 JC-1.xlsx','sheet','B:B');
        y = xlsread('Flat Re-5600 JC-1.xlsx','sheet','D:D');
        T = xlsread('Flat Re-5600 JC-1.xlsx','sheet','E:E') - 273 - 30;
        q = xlsread('Flat Re-5600 JC-1.xlsx','sheet','F:F');

        % Redefine x & y arrays
        x = x-min(x); y = max(y)-y;

        % Griddata
        Ti = griddata(x,y,T,xi,yi,'cubic');
        qi = griddata(x,y,q,xi,yi,'cubic');

        % Calculate htc
        hi = qi./Ti/1000;

        % Combine data
        Ti_c = [Ti_c Ti flip(Ti,2)];
        qi_c = [qi_c qi flip(qi,2)];
        hi_c = [hi_c hi flip(hi,2)];
        xi_c = [xi_c xi+(ind*xhigh) xi+((ind+1)*xhigh)];
        yi_c = [yi_c yi yi];

        % Increment count (by 2)
        ind = ind+2;
end


%% Generate h contour
hlow = 0; hhigh = 46.58;
figure
[C,h] = contourf(xi_c,yi_c,hi_c,256);
w = h.LineStyle;
h.LineStyle = 'none';
title('HTC Contour of Re=5600','FontSize',12)
ylabel(' <-Upstream    Downstream->','FontSize',14,'FontWeight','bold')
axis([xlow max(max(xi_c)) ylow yhigh])
xlabels = linspace(xlow,max(max(xi_c)),xinc);
ylabels = linspace(ylow,yhigh,yinc);
```

```
set(gca,'XTick',xlabels)
set(gca,'YTick',ylabels)
set(gca,'FontSize',10)
colormap('jet')
caxis([hlow hhigh])
axis equal
c = colorbar;
c.Label.String = 'Heat Transfer Coefficient (kW/Km^2) ';
c.Label.FontSize = 11;
c.Label.FontWeight = 'bold';
fprintf('Finished making htc plot\n')

%% Generate T contour
Tlow = 8.5; Thigh = 15;
figure
[C,h] = contourf(xi_c,yi_c,Ti_c,256);
w = h.LineStyle;
h.LineStyle = 'none';
title('Temp Rise Contour of Re=5600','FontSize',12)
ylabel(' <-Upstream    Downstream->','FontSize',14,'FontWeight','bold')
axis([xlow max(max(xi_c)) ylow yhigh])
xlabels = linspace(xlow,max(max(xi_c)),xinc);
ylabels = linspace(ylow,yhigh,yinc);
set(gca,'XTick',xlabels)
set(gca,'YTick',ylabels)
set(gca,'FontSize',10)
colormap('jet')
caxis([Tlow Thigh])
axis equal
c = colorbar;
c.Label.String = 'Temp Rise (K) ';
c.Label.FontSize = 11;
c.Label.FontWeight = 'bold';
fprintf('Finished making temp plot\n')
```

Appendix D: Uncertainty Analysis

D.1 PIV Uncertainty Analysis

Uncertainty analysis of PIV results is a complex, developing topic with no clear solution in literature [60]. The exact specifications and accuracies achieved by the PIV system varied with each trial ran. Since the laser head, camera, and impingement chamber were independently located and aligned, some differences would arise, primarily based on the location and orientation of the camera relative to the impingement chamber.

PIV analysis is completed by segmenting the images into a grid of interrogation windows; within each interrogation window, the particle motion is examined to determine the local fluid velocity, generating a single vector. Prior to spatial calibration, the interrogation windows used the default size of 32-by-32 pixels for all cases. The spatial calibration varied slightly from one case to another, thus further analysis was completed using the baseline surface under the flat confining wall case; results for other cases would yield similar values. For this case, the interrogation windows were approximately 0.5-by-0.5mm in size after spatial calibration, yielding a conversion factor of 64 pixels per 1mm. In the jet plane, the time gap between each snapshot was set to 80ms. The order of the velocity increment detectable by the system can be estimated as when a particle moves one pixel during this time gap. As such, the velocity increment achieved by the system can be estimated as such:

$$u_{increment} \approx \left(\frac{1pix}{0.08s}\right)\left(\frac{0.001m}{64pix}\right) = 0.0002\frac{m}{s}$$

Thus, the increment of the velocity measurements as generated by the PIV system can be expected to be on the order of 0.0002m/s. This estimate indicates that a reasonable level of accuracy has been achieved by the system in the generation of the experimental flow fields.

Glass spheres with diameters of 55μm were used to seed the fluid. The jet velocities observed in the PIV cases are approximately 2m/s. Using these values and properties of glass and deionized water, the Stokes number for the particles follows in equation D.1 [61].

$$Sk = \frac{\rho_p D_p^2 u}{18\mu_w D_j} \tag{D.1}$$

$$Sk = \frac{\left(2500\frac{kg}{m^3}\right)(55 * 10^{-6}m)^2\left(2\frac{m}{s}\right)}{18\left(10^{-3}\frac{kg}{m*s}\right)(3.18 * 10^{-3}m)}$$

$$Sk = 0.26$$

As the Stokes number is less than unity, it can be concluded that the particles reliably follow the fluid's flow path. This value can be expected to be an overestimate. The true density of the glass particles is lower than the value used above, as the particles are hollow.

D.2 Numerical Model Uncertainty Analysis

Uncertainty analysis on the numerical model was also completed using the grid convergence index (GCI) defined by Roache to compare the final grid design to a smaller element grid, where element sized were reduced by 33.3% [56]. Roache's grid convergence index is defined in equation D.2. In this equation, N_1 indicates a value generated from a small element mesh, while N_2 indicates the corresponding value generated from the large element mesh. The variable $r_{2:1}$ is the ratio of the element sizes in the large mesh to those in the small mesh; as the smaller element mesh used in this calculation had elements two-thirds the size of the large element mesh, this equals 1.5, the inverse of two-thirds. Finally, the variable O indicates the lowest order method used in the calculations; second-order methods were used in all the model calculations. For example, at one location the large grid reported a surface heat transfer coefficient value of 32.7kW/m^{2}K, while the small grid reported a value of 30.5kW/m^{2}K at the same location. The grid convergence index would then be calculated as follows:

$$GCI = \frac{3\left|\frac{f_2 - f_1}{f_1}\right|}{r^O - 1} \tag{D.2}$$

$$GCI = \frac{3\left|\frac{32.7\frac{kW}{m^2K} - 30.5\frac{kW}{m^2K}}{30.5\frac{kW}{m^2K_1}}\right|}{1.5^2 - 1}$$

$$GCI = 0.173 = 17.3\%$$

The index was found for local velocity magnitudes in the jet and fountain planes, and for the surface heat transfer coefficient across the impingement surface using the same case as was analyzed in the grid independence study. The results of these calculations are shown in Figure D-1.

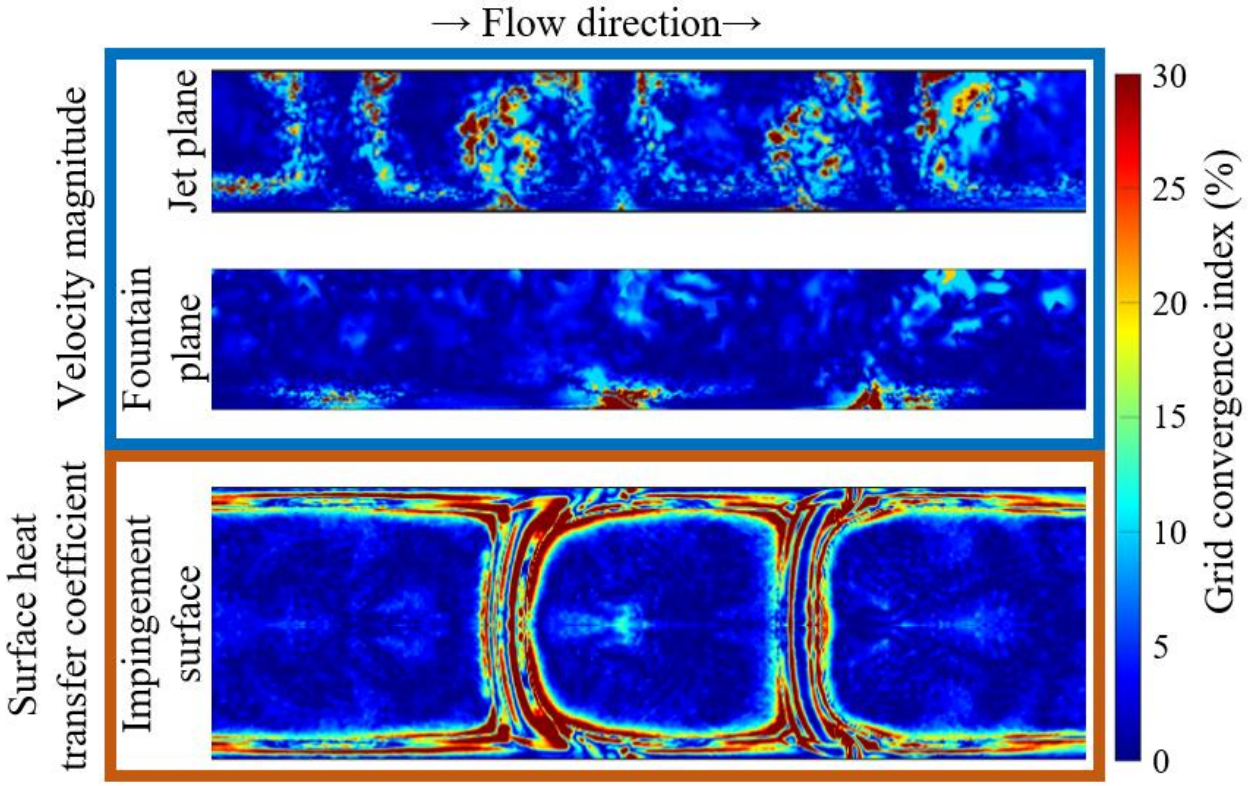

Figure D-1: Grid convergence index contours

For most locations, index values of 10% or less were achieved, indicating highly accurate results. Greater values occur near regions of flow separation from the surface or circulation. In these regions, velocities near zero are observed. While the grids only predicted separation at slightly different locations, comparing two near-zero values in each grid causes very high uncertainties. As a result, the relative error calculated by the index is large, despite the absolute error being very low, possibly negligibly so. Combined with the fact that Roache acknowledges this index as often being overly conservative, it is concluded that the model is adequately verified.

The grid convergence index is also applicable for averaged values. The resulting uncertainty for the average surface heat transfer coefficient for the case examined above is 0.34%. This very low value is to be expected, as localized errors tend to have little effect when integrated

or averaged. As such, it can be concluded that the observed differences in the average surface heat transfer coefficient of up to 6.9% are significant and not the result of error or uncertainty.

Appendix E: Additional Results

E.1 PIV Contours

Additional PIV contours not discussed in the dissertation are displayed here. Figure E-1 displays a comparison of various jet Reynolds numbers for the baseline surface under a flat confining wall, indicating that flow trends vary little with the flow rate. Figure E-2 to Figure E-5 display PIV flow fields for the short modifications.

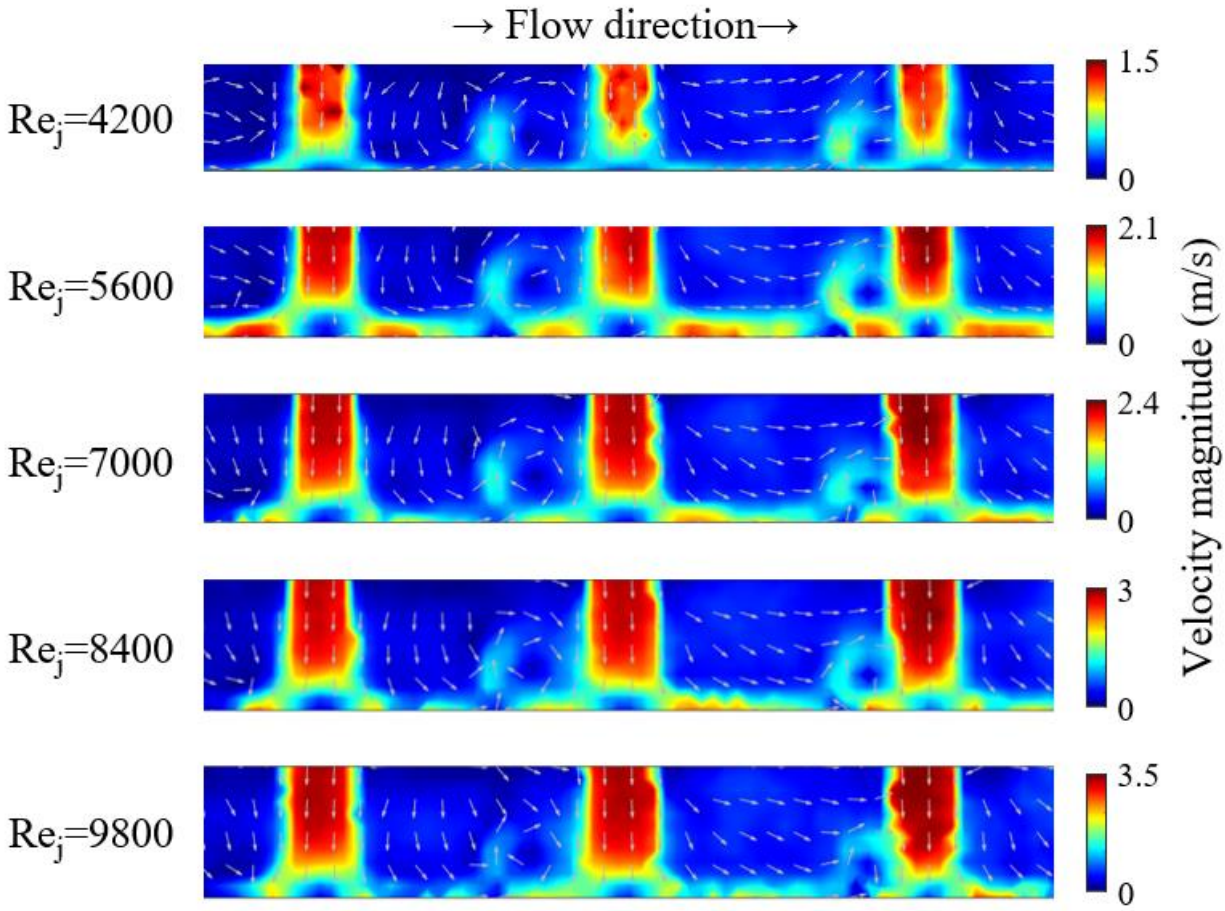

Figure E-1: Comparison of varied jet Reynolds number for the baseline surface under a flat confining wall

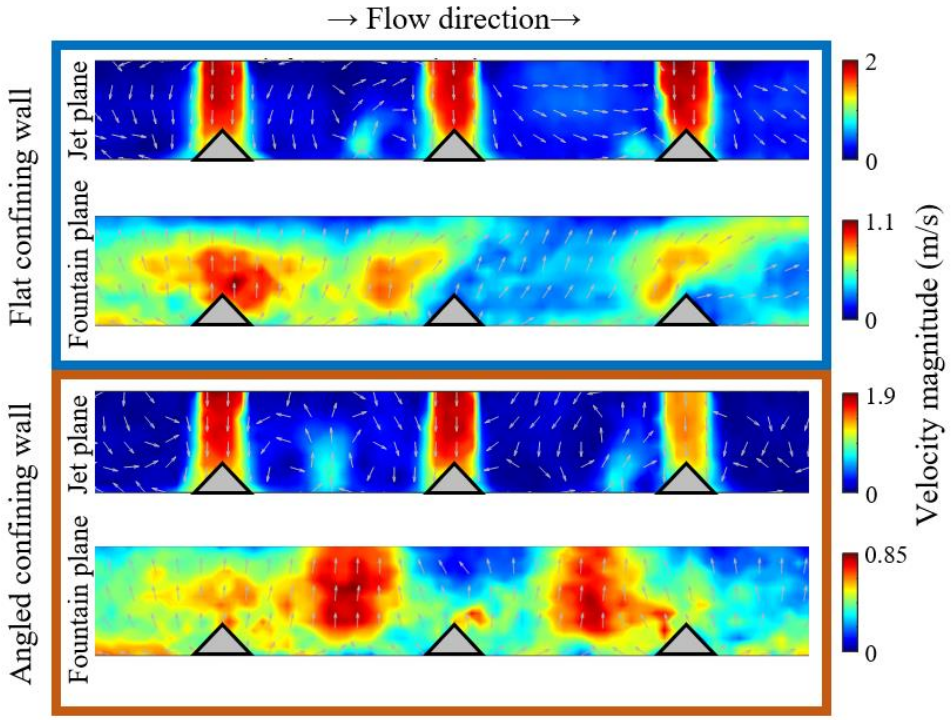

Figure E-2: PIV flow fields for short jet cones at a jet Reynolds number of 5600

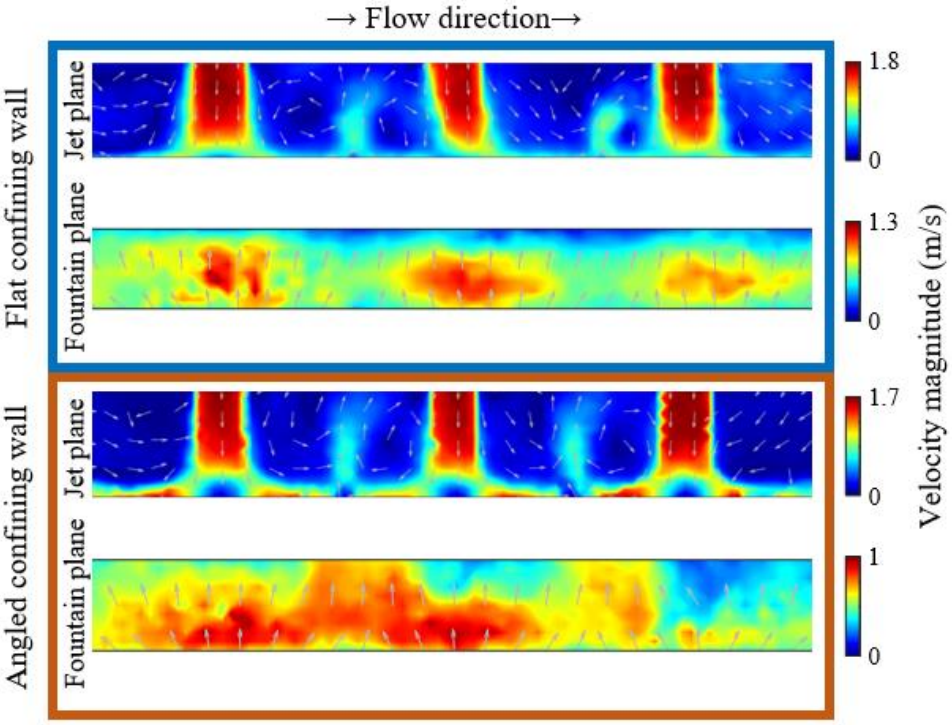

Figure E-3: PIV flow fields for short streamwise ribs at a jet Reynolds number of 5600

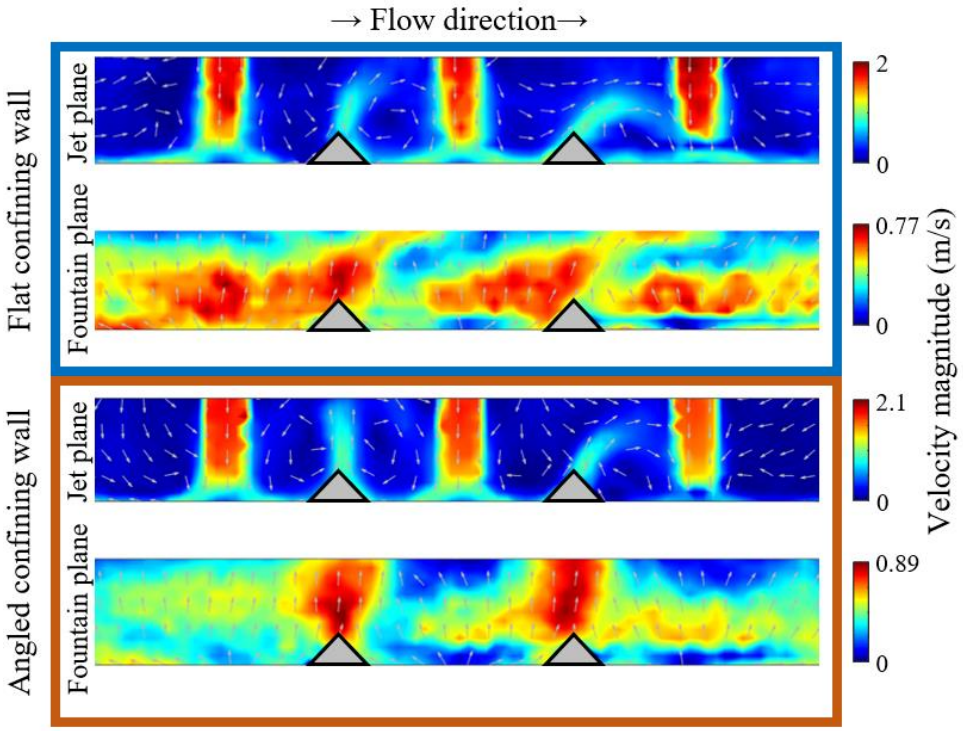

Figure E-4: PIV flow fields for short streamwise ribs at a jet Reynolds number of 5600

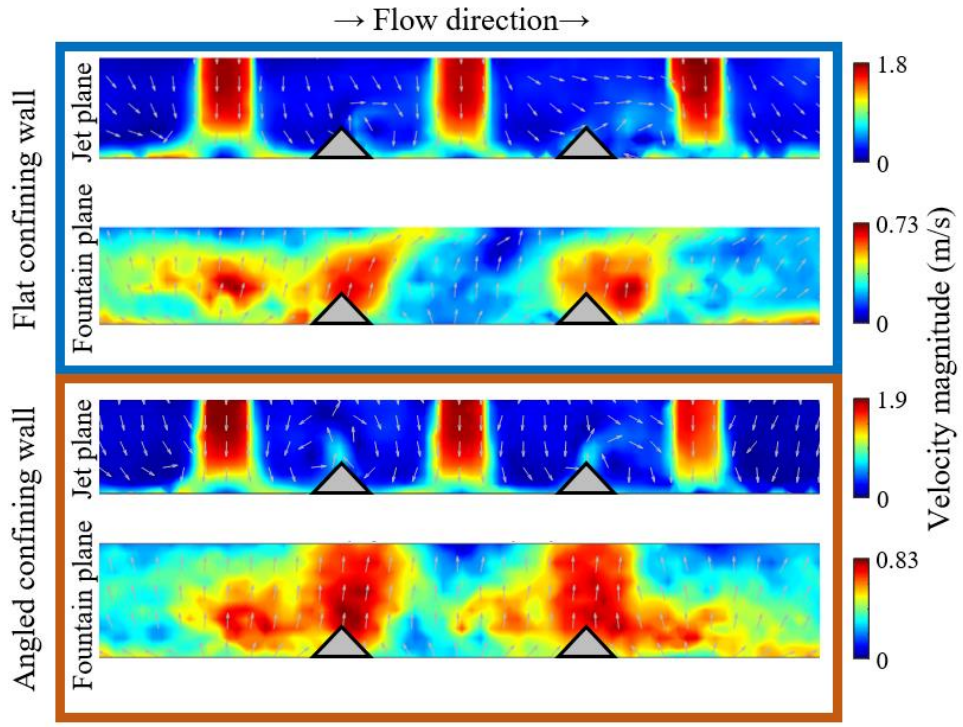

Figure E-5: PIV flow fields for short offset cones at a jet Reynolds number of 5600

E.2 Numerical Contours

Additional numerical contours not discussed in the dissertation are displayed here. Figure E-6 displays a comparison of various jet Reynolds numbers for the baseline surface under a flat confining wall, indicating that flow trends vary little with the flow rate. Figure E-7 to Figure E-10 display numerical flow fields for the short cone and rib modifications. Figure E-11 to Figure E-14 display the surface contours for the short cone and rib modifications.

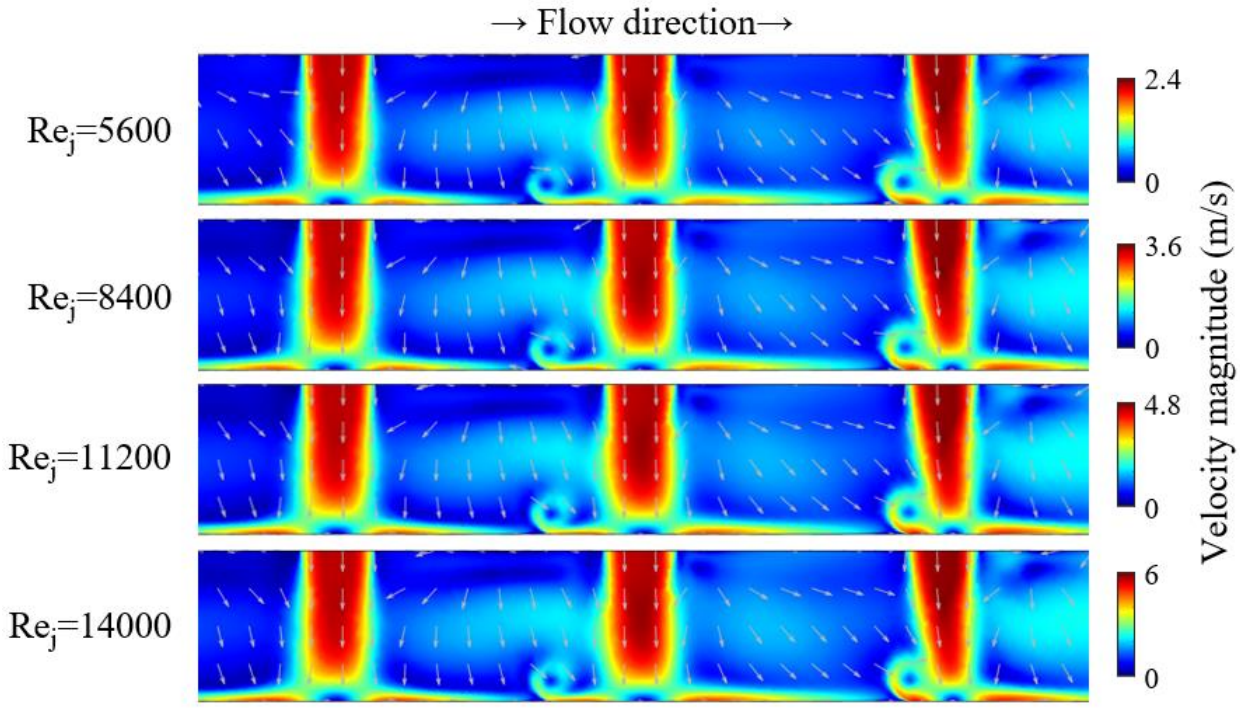

Figure E-6: Comparison of varied jet Reynolds number in the numerical model for the baseline surface under a flat confining wall

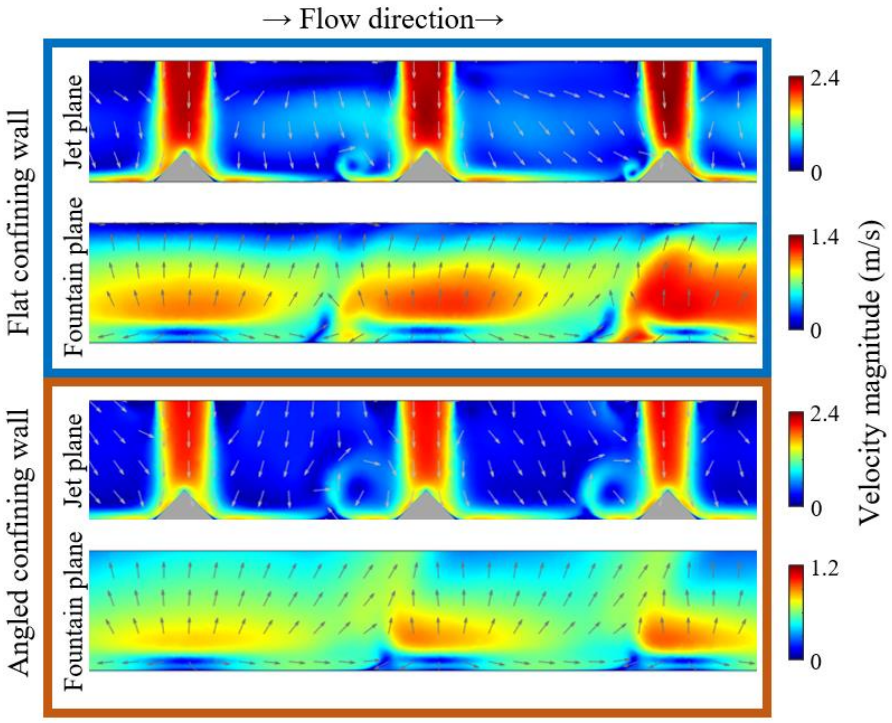

Figure E-7: Numerical model flow fields for short jet cones at a jet Reynolds number of 5600

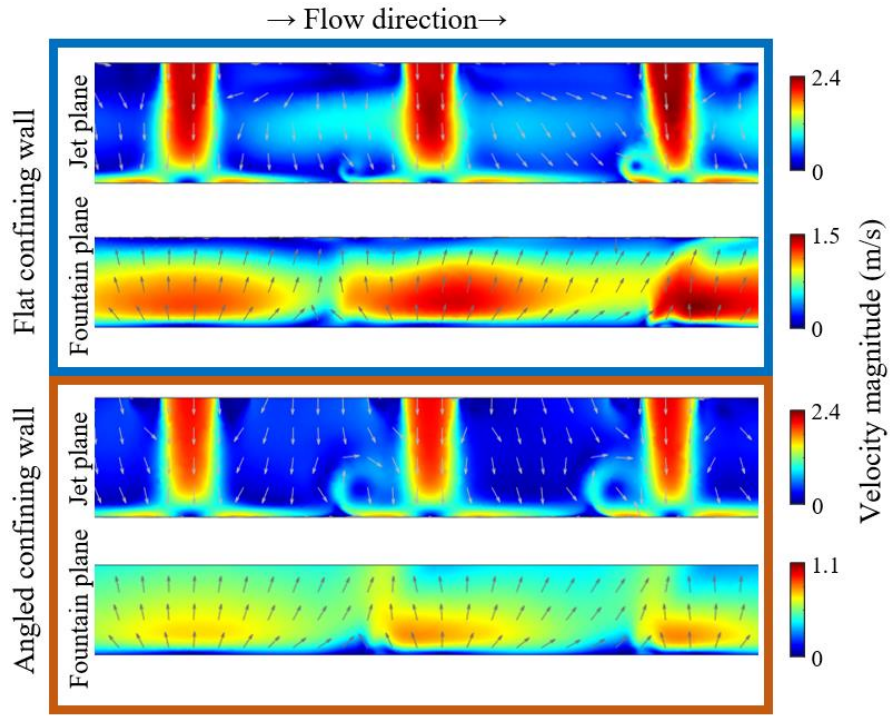

Figure E-8: Numerical model flow fields for short streamwise ribs at a jet Reynolds number of 5600

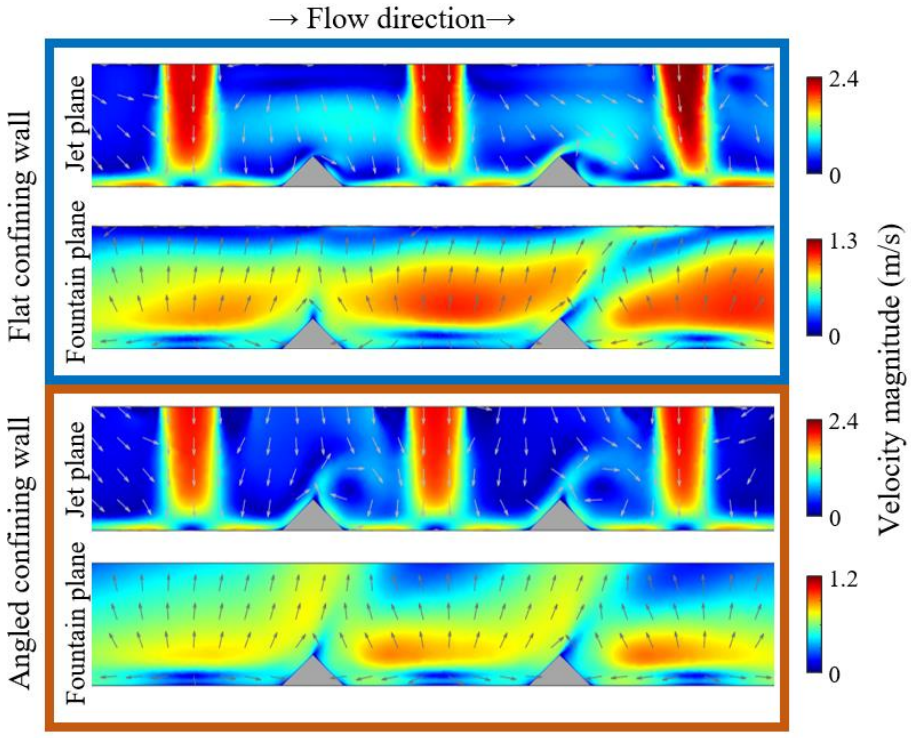

Figure E-9: Numerical model flow fields for short transverse ribs at a jet Reynolds number of 5600

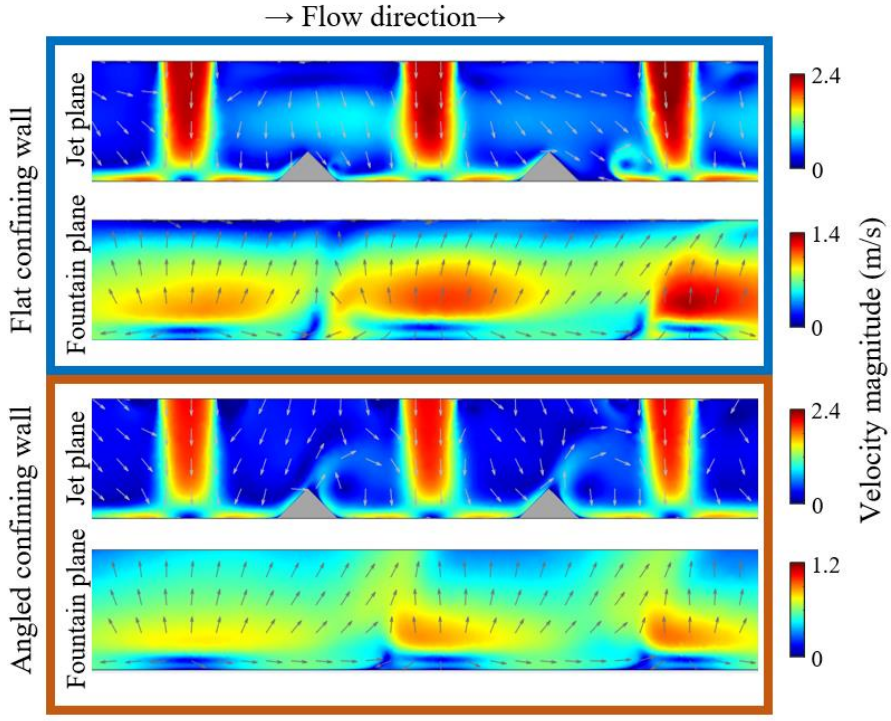

Figure E-10: Numerical model flow fields for short offset cones at a jet Reynolds number of 5600

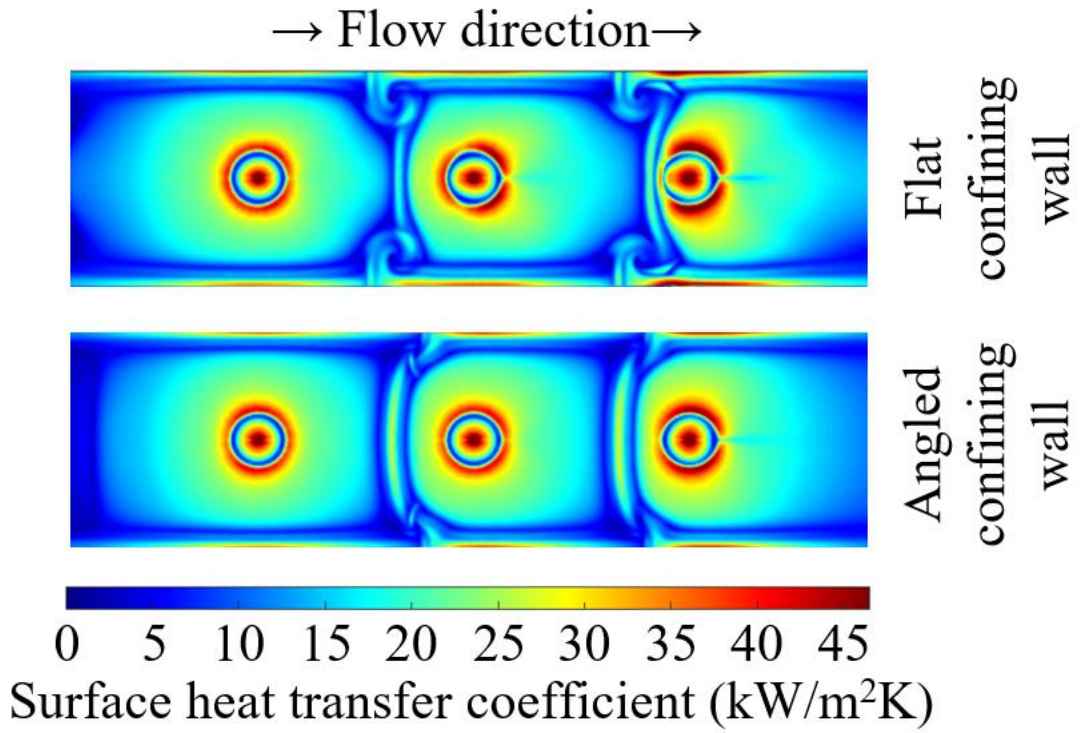

Figure E-11: Numerical model surface contours for short jet cones at a jet Reynolds number of 5600

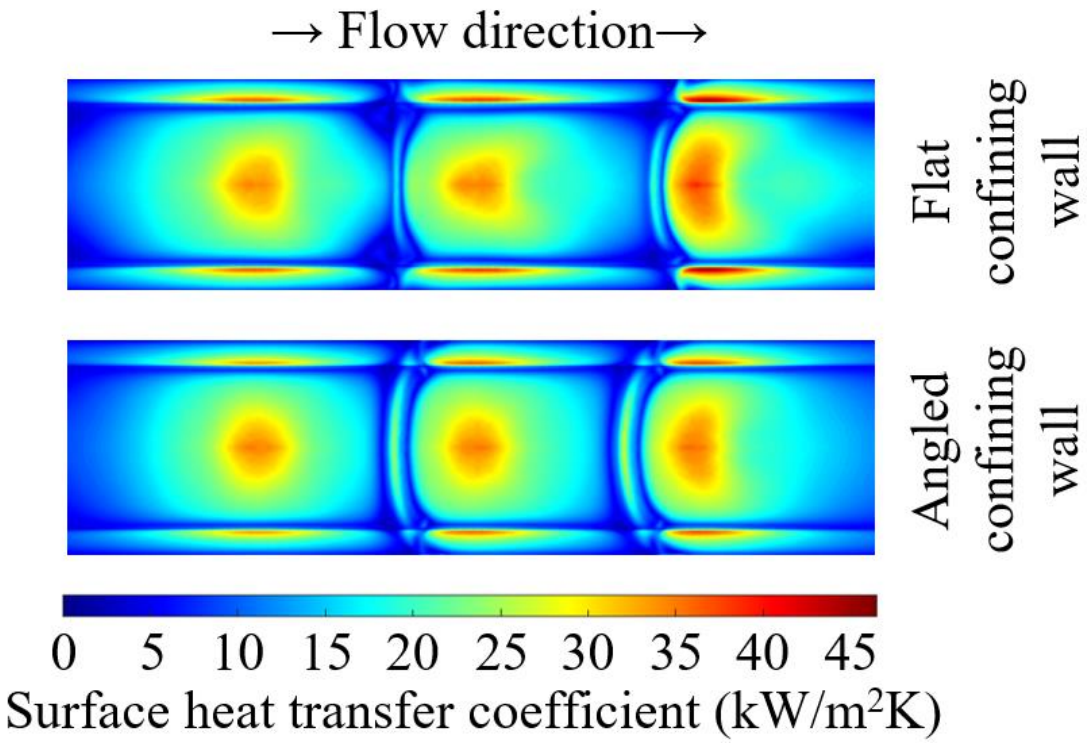

Figure E-12: Numerical model surface contours for short streamwise ribs at a jet Reynolds number of 5600

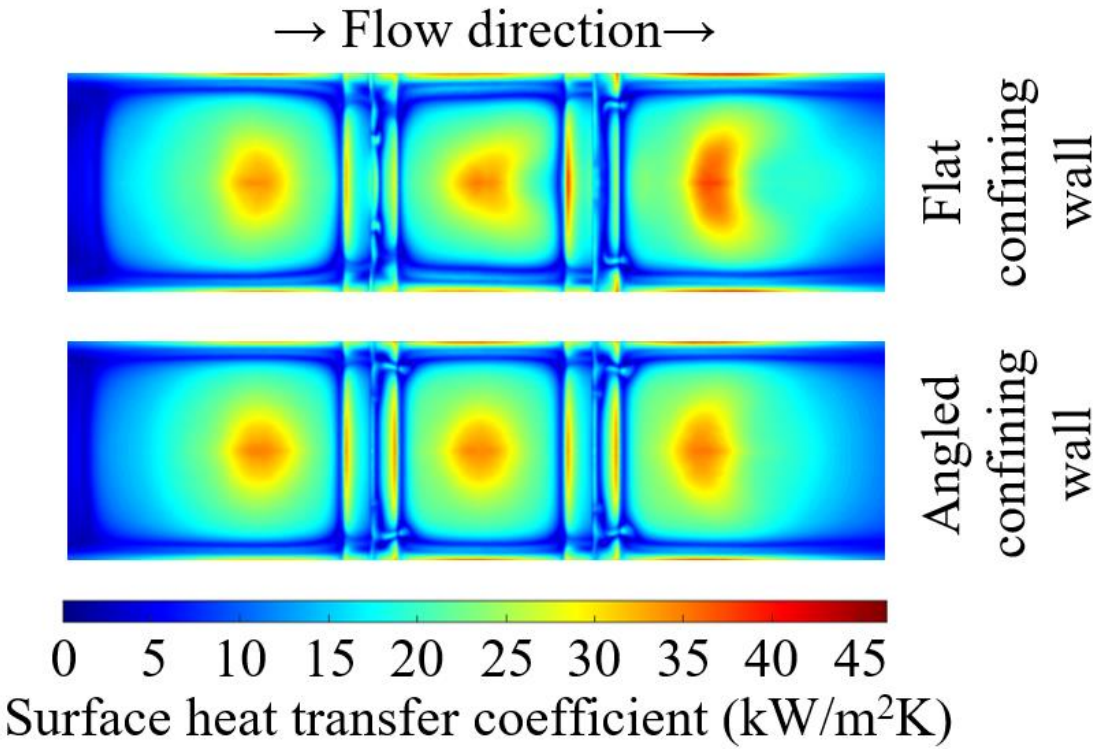

Figure E-13: Numerical model surface contours for short transverse ribs at a jet Reynolds number of 5600

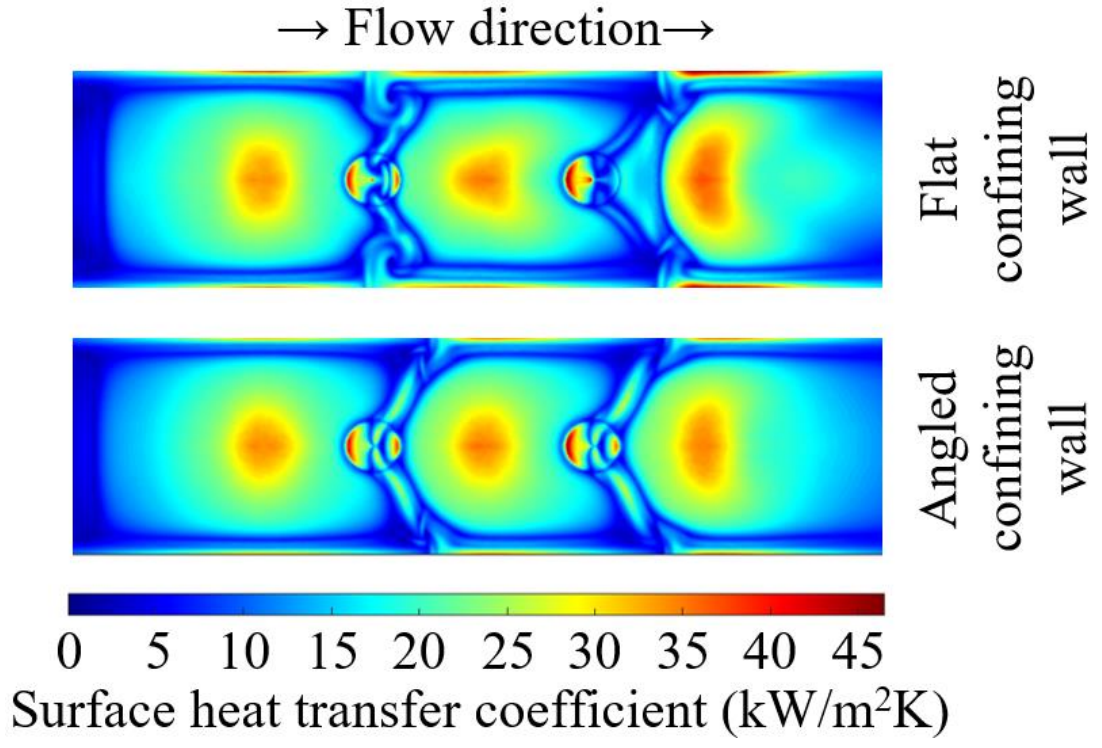

Figure E-14: Numerical model surface contours for short offset cones at a jet Reynolds number of 5600

E.3 Numerical Data Summary

Below displays the average surface characteristics and pressure losses as calculated in the numerical model for all geometries and flow rates. Data from this table is graphically displayed in Figure E-15 through Figure E-18.

Table E-1: Summary of the surface characteristics and pressure losses as calculated by the numerical model

Confining wall angle	Modification	Jet Reynolds number	Average surf. heat transfer coef. (kW/m^{2}K)	Average surf. temp. rise (°C)	Inlet-outlet pressure loss (kPa)
Flat (0°)	Baseline (none)	5600	12.11	14.22	2.805
		8400	16.17	10.65	6.22
		11200	19.82	8.688	11.05
		14000	23.41	7.357	17.29
	Short jet cones	5600	12.57	13.56	2.8
		8400	16.59	10.27	6.195
		11200	20.4	8.358	11.01
		14000	24.11	7.073	17.25
	Tall jet cones	5600	12.67	13.19	2.82
		8400	16.81	9.944	6.234
		11200	20.74	8.062	11.07
		14000	24.58	6.802	17.32
	Short streamwise ribs	5600	12.77	12.22	2.902
		8400	16.89	9.24	6.434
		11200	20.76	7.518	11.44
		14000	24.47	6.378	17.91
	Tall streamwise ribs	5600	12.49	10.54	2.885
		8400	16.49	7.977	6.382
		11200	20.22	6.507	11.32
		14000	24.02	5.478	17.72
	Short transverse ribs	5600	12.47	13.35	2.86
		8400	16.47	10.11	6.32
		11200	20.57	8.093	11.26
		14000	21.19	6.881	17.64
	Tall transverse ribs	5600	12.37	12.63	3.071
		8400	16.56	9.429	6.803
		11200	20.44	7.638	12.11
		14000	24.11	6.476	18.97
	Short offset cones	5600	12.26	13.95	2.813
		8400	16.45	10.4	6.263
		11200	20.08	8.519	11.12
		14000	23.65	7.232	17.4
	Tall offset cones	5600	12.41	13.6	2.828
		8400	16.43	10.28	6.267
		11200	20.41	8.271	11.14
		14000	24.05	7.021	17.41
		5600	12.95	11.98	2.906

	Short combination	8400	17.14	9.049	6.441
		11200	21.04	7.371	11.45
		14000	24.8	6.254	17.91
	Tall combination	5600	12.73	10.18	2.894
		8400	16.86	7.684	6.413
		11200	20.78	6.235	11.37
		14000	24.64	5.258	17.81
Angled (7.5°)	Baseline (none)	5600	11.5	14.97	2.661
		8400	15.08	11.42	5.86
		11200	18.44	9.343	10.3
		14000	21.66	7.951	15.97
	Short jet cones	5600	11.53	14.78	2.65
		8400	15.18	11.23	5.833
		11200	18.46	9.234	10.24
		14000	21.51	7.927	15.88
	Tall jet cones	5600	11.37	14.71	2.647
		8400	14.93	11.2	5.826
		11200	18.26	9.157	10.24
		14000	21.44	7.798	15.88
	Short streamwise ribs	5600	11.83	13.19	2.643
		8400	15.65	9.971	5.822
		11200	19.32	8.079	10.24
		14000	22.74	6.862	15.88
	Tall streamwise ribs	5600	11.29	11.65	2.652
		8400	14.96	8.792	5.821
		11200	19.07	6.899	10.22
		14000	21.57	6.1	15.9
	Short transverse ribs	5600	11.78	14.14	2.663
		8400	15.39	10.82	5.852
		11200	18.72	8.892	10.27
		14000	21.88	7.61	15.92
	Tall transverse ribs	5600	11.78	13.26	2.697
		8400	15.4	10.14	5.931
		11200	18.73	8.337	10.41
		14000	21.9	7.129	16.15
	Short offset cones	5600	11.61	14.73	2.662
		8400	15.3	11.17	5.861
		11200	18.73	9.131	10.29
		14000	21.98	7.784	15.94
	Tall offset cones	5600	11.46	14.73	2.63
		8400	14.94	11.3	5.769
		11200	18.17	9.293	10.11
		14000	21.21	7.96	15.67
	Short combination	5600	11.87	13.06	2.646
		8400	15.64	9.921	5.831
		11200	19.19	8.085	10.25
		14000	21.1	7.353	15.91
	Tall combination	5600	11.19	11.58	2.66
		8400	15.03	8.623	5.846
		11200	18.65	6.947	10.25

		14000	22	5.889	15.77

A plot of the average surface heat transfer coefficient versus the jet Reynolds number for the combination surface is shown in . Corresponding plots for the rib and cone modifications are shown in Chapter 4 in Figure 4-24 and Figure 4-29, respectively.

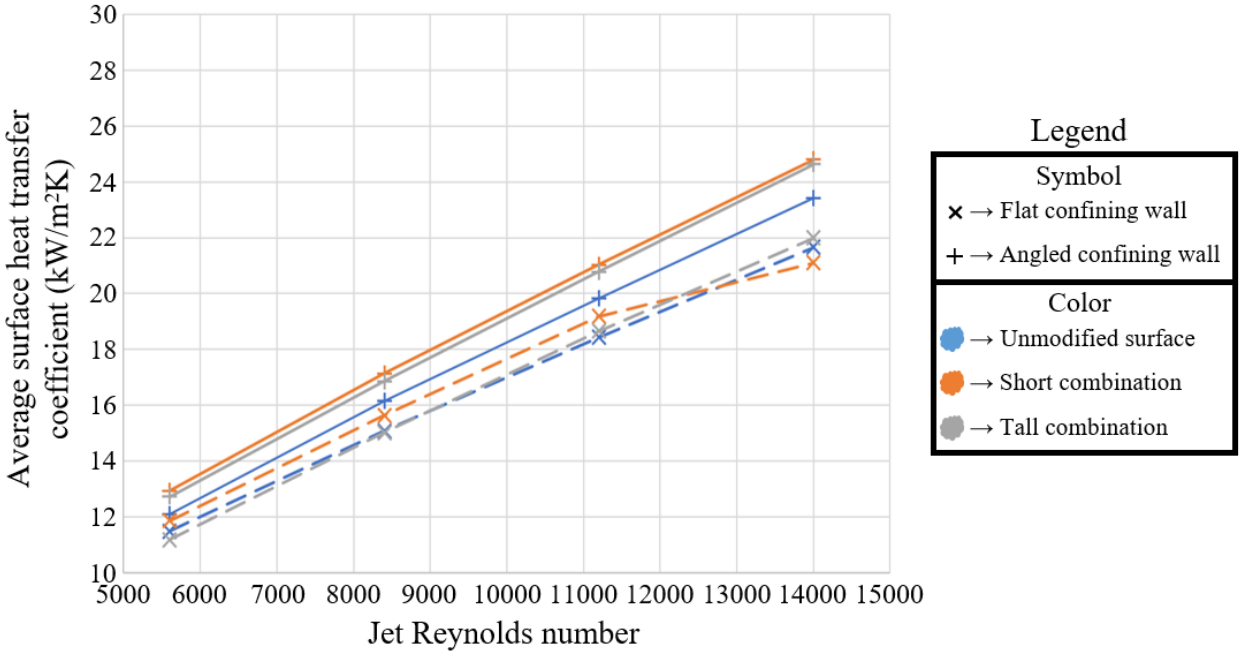

Figure E-15: Surface heat transfer coefficient versus jet Reynolds number from the numerical model for the combination surface

Figure E-16 through Figure E-18 below display plots of the pressure losses with the jet Reynolds number for the cone structures, rib structures, and combination surface.

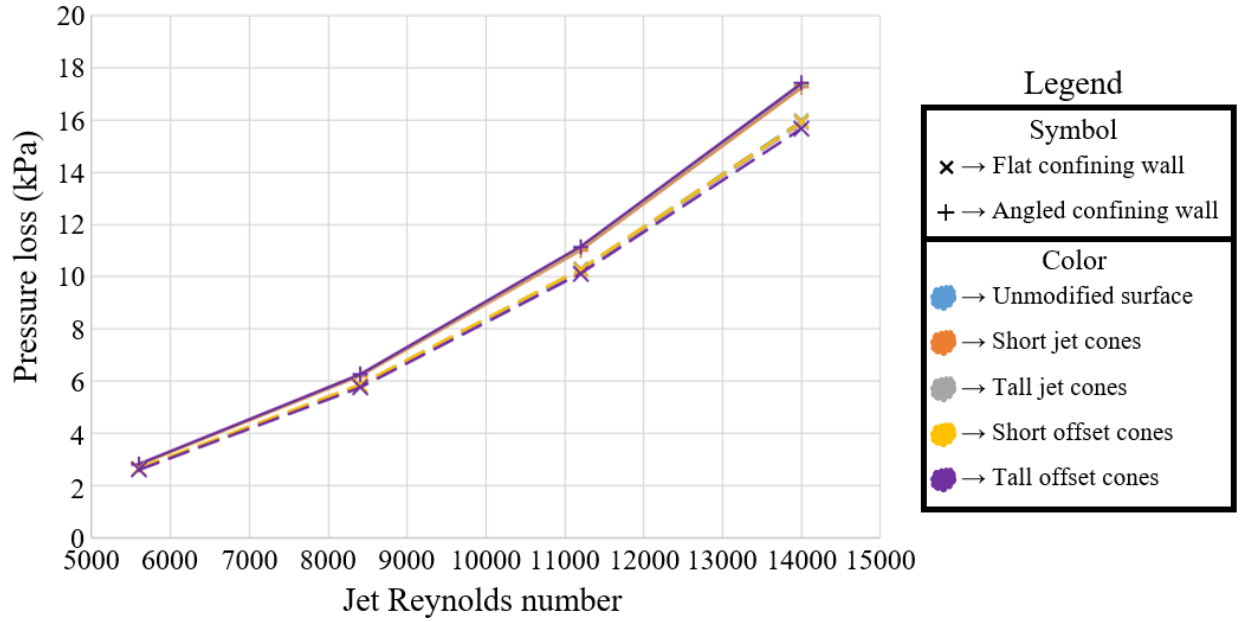

Figure E-16: Pressure loss versus jet Reynolds number from the numerical model for the cone structures

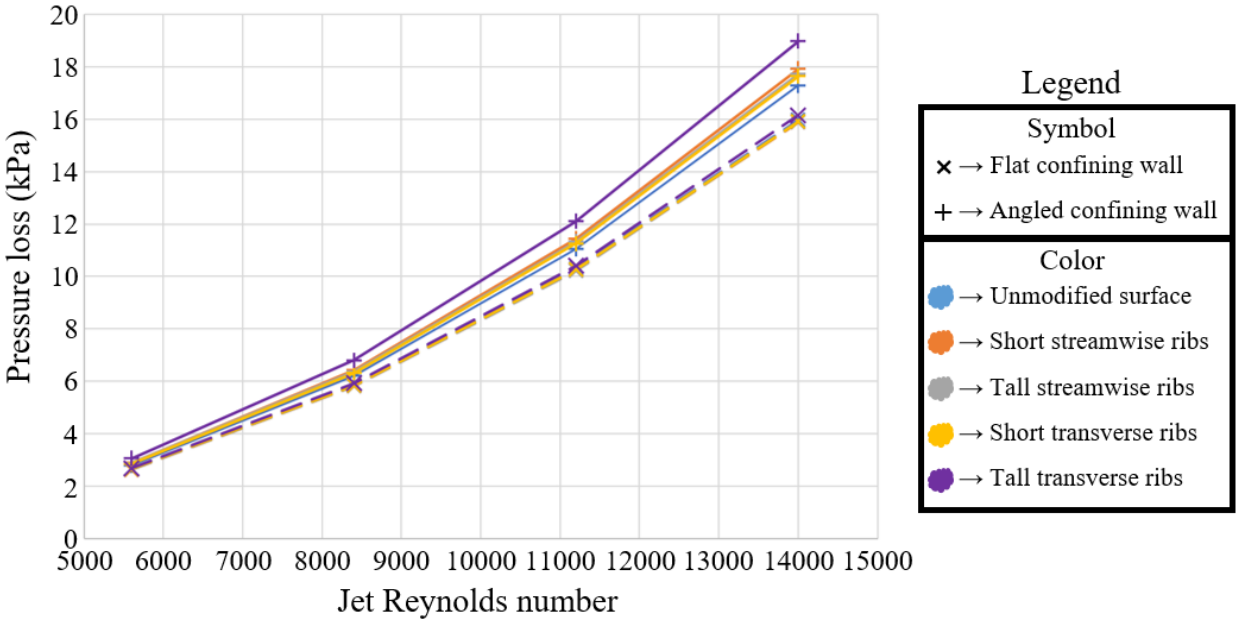

Figure E-17: Pressure loss versus jet Reynolds number from the numerical model for the rib structures

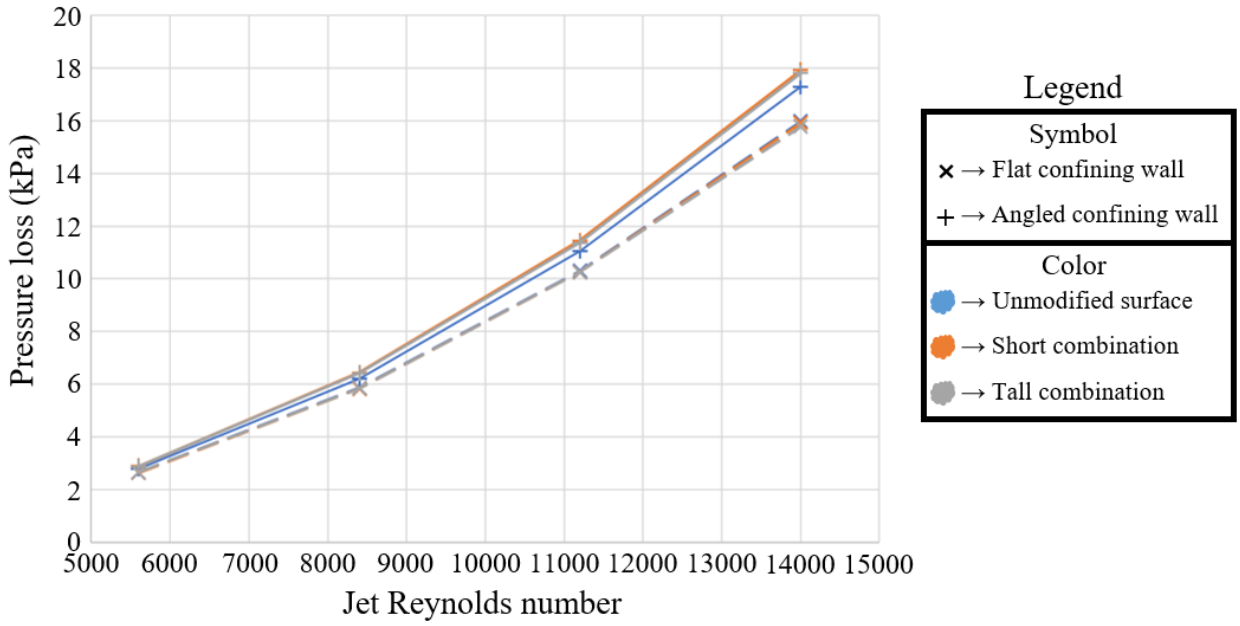

Figure E-18: Pressure loss versus jet Reynolds number from the numerical model for the combination surface

Appendix F: Experimental Surface Contour Results

F.1 System Details

In past stages of this group's research into jet impingement, an experimental system was created to experimentally analyze the performance of deionized water jet arrays, as displayed in Figure F-1, while Figure F-2 displays the internal features of the system [59].

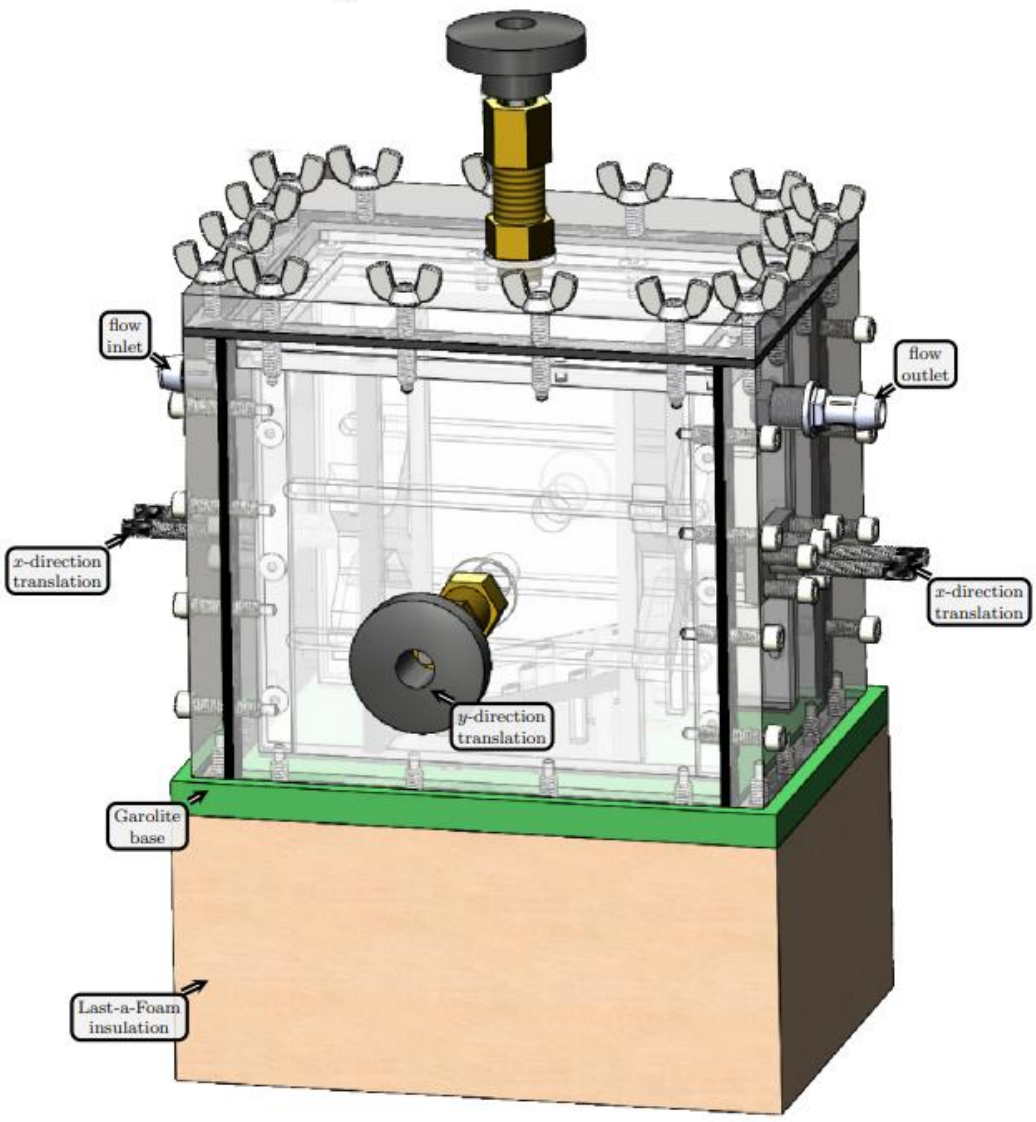

Figure F-1: Experimental jet impingement system used in prior stages of the group's research efforts [59]

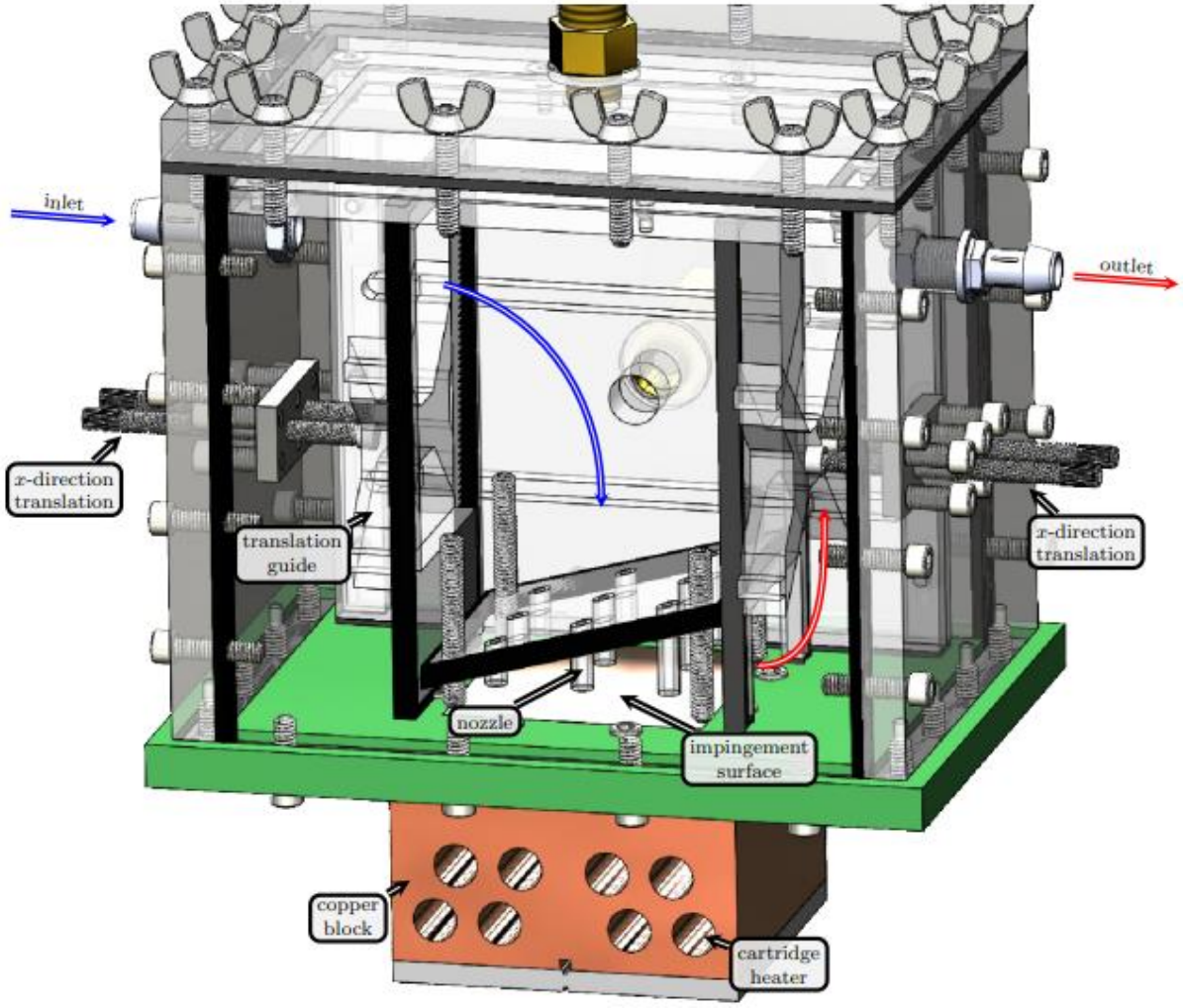

Figure F-2: Internal features of the experimental jet impingement system used in past stages of this group's research efforts [59]

The system was composed of an enclosure within a larger enclosure, such that the nozzle array could be translated to nine locations across the impingement surface. This nozzle array could be manufactured or 3D printed to analyze any design that fits within the 76.2-by-76.2mm footprint of the system. Cold fluid entered the enclosure through the top, was forced through the nozzle array using a set of confinement walls and ejected out the other side of the enclosure. The inlet and outlet temperatures were measured using K-type thermocouples. The internal enclosure, comprised of these confinement walls, couple be translated in two dimensions using a system of screws on the front, back, and sides of the external enclosure. Heat was supplied into a copper block under the nozzle array using eight cartridge heaters, where a DC power supply provided the necessary voltage and current sources. The copper block was surrounded by insulation to minimize heat loss to the environment and force as much of the generated heat through the smooth

impingement surface. Thermocouples embedded within the copper block measured temperature within the copper block in specified locations under the surface, as shown in Figure F-3.

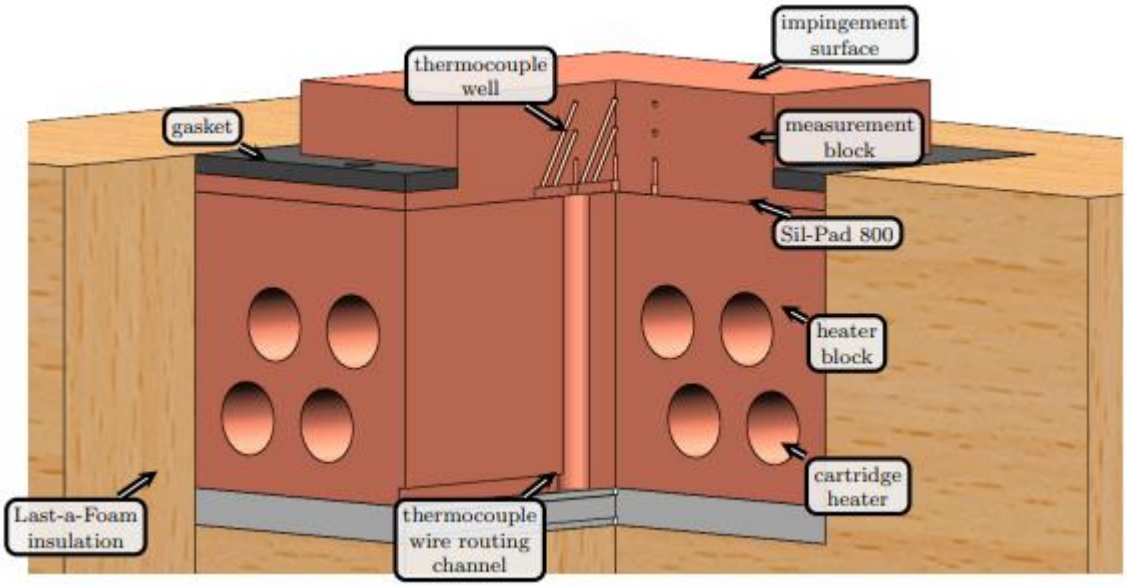

Figure F-3: Internal view of the copper block upon which fluid would impinge in the experimental system used in past stages of this group's research efforts

Four sets of three K-type thermocouples were placed under certain locations at depths of 3mm, 8mm, and 13mm under the impingement surface. Using these values, the local surface temperature rise and heat flux could be estimated, and the local surface heat transfer coefficient could be calculated. Four local measurements were taken for a given nozzle array at a given location, and each nozzle array would be translated using the internal enclosure to nine locations on the impingement surface, allowing a total of 36 local surface temperature, heat flux, and heat transfer coefficient measurements across the surface for a given nozzle array design, from which surface contours and average values could be generated. One final K-type thermocouple was also used to monitor the heater temperatures and avoid accidental overheating.

This enclosure was attached to a flow loop shown in Figure F-4.

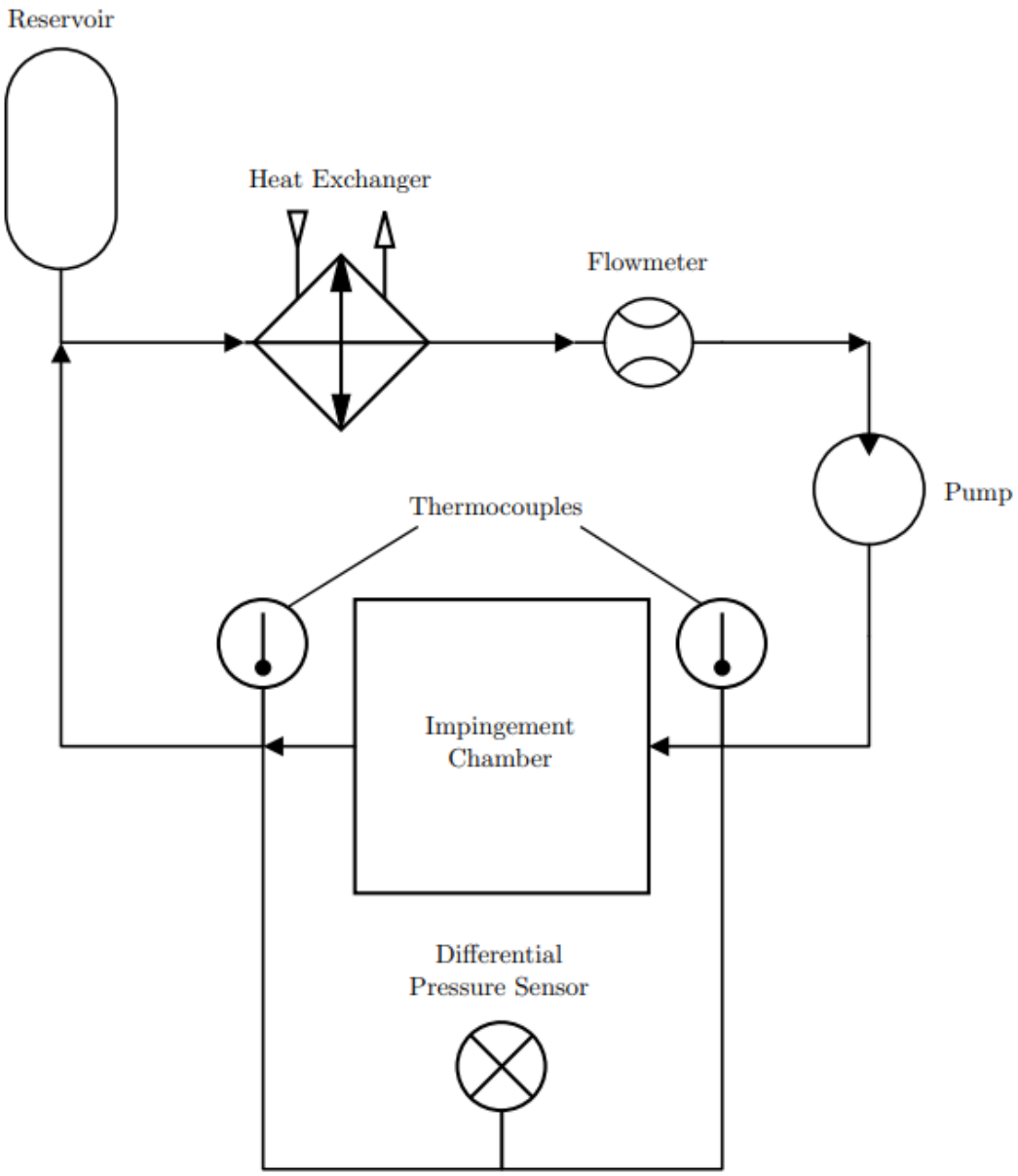

Figure F-4: Flow loop for the experimental jet impingement system used in past stages of this group's research efforts

Flow was generated using an Iwaki magnetic pump controlled by a Lenze SMVector variable frequency drive. The fluid was then forced through the impingement chamber, where it would be heated through the impingement process. The heated fluid was then cooled using a brazed plate heat exchanger connected to a NESLAB RTE-220 chiller, which was used to maintain the inlet temperature at 30°C. Finally, the flow rate was measured using an Omega FTB4700 turbine flow meter. An Arduino Uno was used to supply the required supply voltages to the meter and interpret the output. Temperature measurements were monitored and captured using LabView.

F.2 LabView Scripting

A LabView script was generated to display the readouts from the thermocouples in real time and, when prompted, record the data to a text file for image generation in Matlab; this Matlab code follows a very similar procedure for generating the surface contours as the code displayed in Appendix C.3.4 above, and will thus not be displayed here. As LabView uses a graphical block diagram rather than text, the block diagram will be displayed in figures and complemented with explanations as needed.

The block diagram was composed of three parts: (1) the initialization, (2) the while loop, and (3) the for loop. The first section, the initialization stage, is displayed below in Figure F-5.

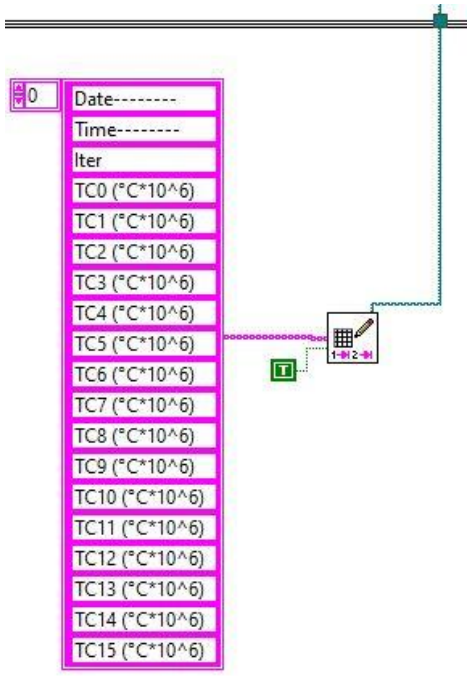

Figure F-5: LabView block diagram - initialization

This section of the block diagram initializes a text file that the data will be reported within. Immediately upon running the script, the user will be prompted to specify the location and name of the text file. Once this is completed, 19 column headers will be generated as shown in the pink table. The first two columns will store the data and time that the row of data was captured. The third column records the iteration number. Finally, the remaining columns store the temperature measurements from each thermocouple. Once this initialization is complete, the script will begin

running the loops in the block diagram. A while loop is embedded within a for loop, resulting in the while loop, shown below in Figure F-6, exclusively repeating until prompted by the user.

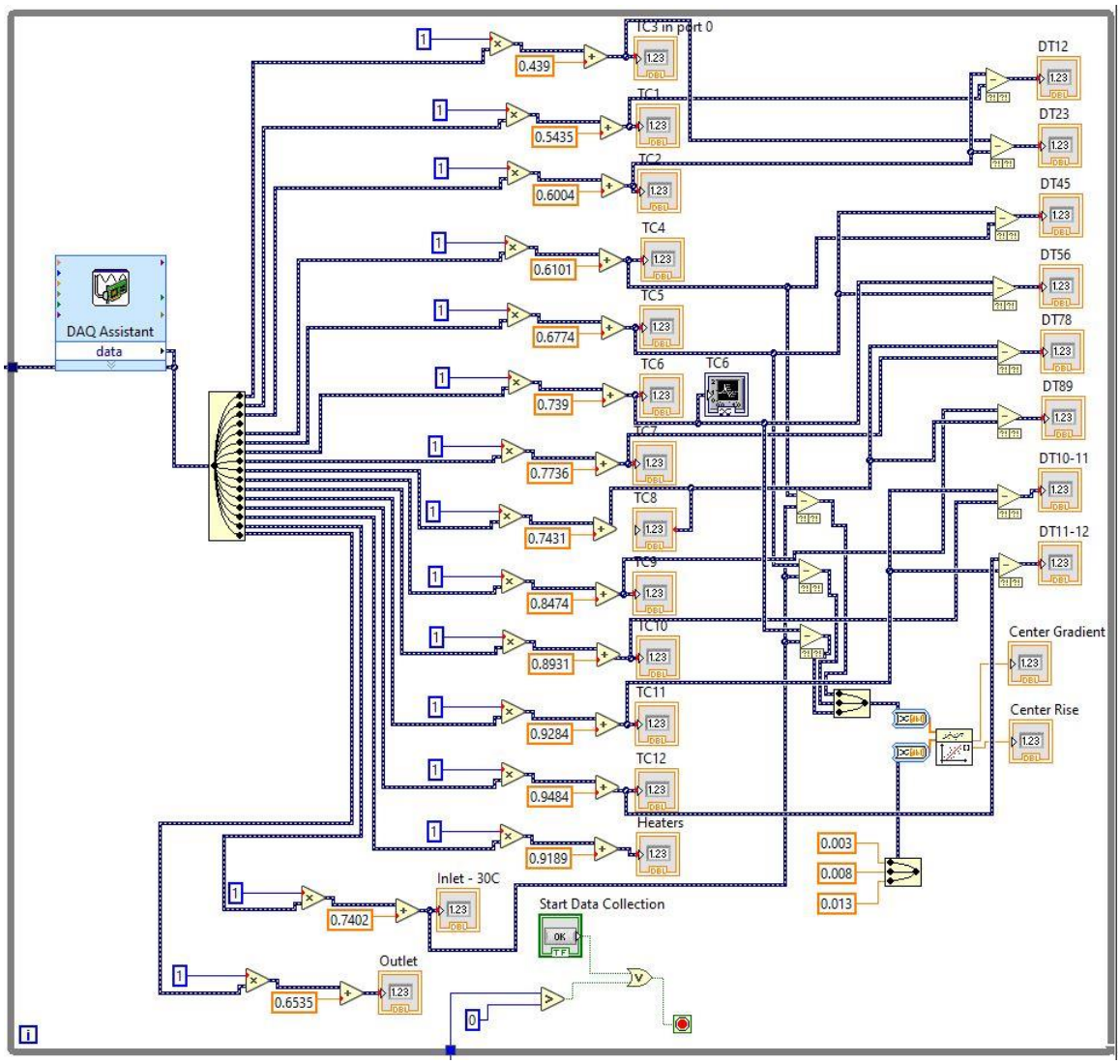

Figure F-6: LabView script - while loop

As previously mentioned, this while loop is embedded within a larger for loop. The vast majority of this while loop is dedicated to displaying the temperature data in real time such that the user can determine when the system has reached steady state. The calibration functions are applied to the raw measurements prior to numerical displays. The deepest thermocouple under the central location (TC6) is also displayed as a graph. A linear regression is applied to difference between the central set of temperatures and the inlet temperature versus their corresponding thermocouple depths. The resulting slope and y-intercept are displayed as the "Central Gradient"

and “Center Rise”, respectively. This loops continuously until the user clicks the “Start Data Collection” button. At this point, the for loop runs. This while loop is also set to terminate if iteration number of the for loop is greater than zero, causing the while loop to be immediately terminated until the script is restarted. The for loop is shown in Figure F-7.

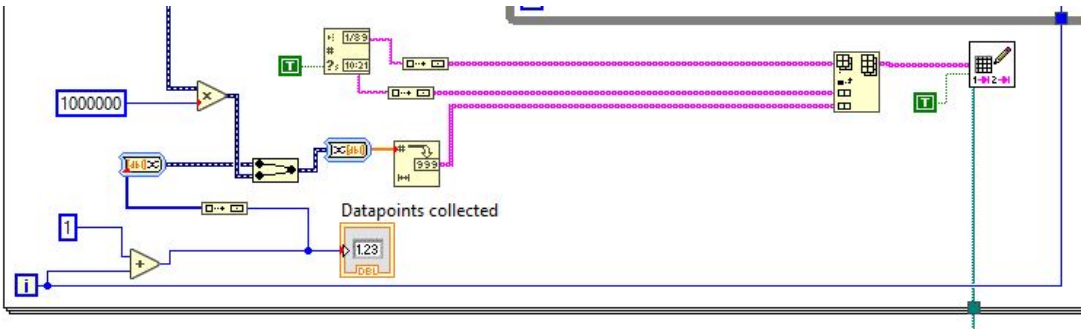

Figure F-7: LabView script - for loop

This for loop takes the thermocouple measurements and stores them in the same text file defined by the user during the initialization stage. This method of recording the data does not record decimal points; to resolve this, all values were multiplied by 10^6, which was accounted for in Matlab scripting. This loop repeats until the specified number of iterations is reached, at which point the entire script terminates. This value was set at 300 during this effort.

F.3 Data Acquisition

The system, as designed by its original researcher, made use of software to automate data acquisition. However, due to its age, the computer originally used in the system ceased functioning and required replacement. Rather than spending the time to return the system to full functionality, it was decided that the system would be simplified, using manual control of processes previously handled by software, as it would take too long to return all aspects of the programming to working order. To gather data for a particular nozzle array in the system’s present condition, the following steps must be performed.

A. Assemble the chamber

1. Insert the required nozzle array into the enclosure on top of the impingement surface, ensuring that a wall with the angled array has the highest side facing the outlet
2. Insert the internal enclosure’s components in the following order:

i. Insert the x-shaped spacers (see Figure F-2) on each side, such that they touch the x-direction translation screws and the extensions are resting in the grooves cut into the internal enclosure's side walls
ii. Insert the spacers in the grooves in the internal enclosure's side walls
iii. Insert the front and back walls between the x-shaped spacers and the nozzle array, such that the cut-out on the inlet side faces up and the cut-out on the outlet side faces down

3. Tighten the x and y-direction translation screws tightly such that the internal closure can no longer be moved by hand, but do not fully tighten the system
4. Fill the chamber with deionized water up to the top of the internal enclosure's walls
5. Inert the internal lit of the enclosure, placing the gasketing material through the screws on the top
6. Cover the enclosure with the external lid
7. Tighten the external lid using a gasket, washer, and nut on all screws
8. Fill the reservoir with water
9. Loosen the screws on the external lid slightly, allowing as much trapped air in the impingement chamber out, then retighten the external lid

B. Translate the internal enclosure to the desired location
1. Using the x-adjustment screws, adjust the location of the internal chamber until it rests where desired in the streamwise direction and pressure is exerted to avoid water leakage bypassing the nozzle array; use calipers to ensure the location is correct
2. Using the y-adjustment screws, adjust the location of the internal chamber until it rests where desired in the transverse direction and pressure is exerted to avoid water leakage bypassing the nozzle array; use calipers to ensure the location is correct
3. Using the screw attached to the external lid, tighten the top to avoid water leakage bypassing the nozzle array

C. Initialize the system
1. Activate the pump using the variable frequency drive
i. Monitor the flow rate repeatedly using the output of the Arduino Uno, adjusting the variable frequency drive to maintain the desired flow rate
2. Activate the water chiller

3. Activate the DC power supply, adjusting the voltage and current until their product equals the desired eat supply in Watts
4. Activate the LabView program
    i. Monitor the inlet temperature repeatedly, adjusting the water chiller to maintain the desired inlet temperature

D. Collect data
1. Allow the system to come to steady-state with the desired flow rate and inlet temperature
2. Activate data collection in the LabView program
3. Wait for the data collection to complete, monitoring the flow rate and inlet temperature during the process
4. If necessary, adjust the variable frequency drive and water chiller to a new flow rate or inlet temperature at the given location and repeat steps C4-D3
5. If additional locations are to be recorded in the same work session, follow these steps:
    i. Deactivate the power supply and allow the system to cool for a few minutes
    ii. Deactivate the pump
    iii. In this order, loosen the top screw, y-adjustment screws, and x-adjustment screws
    iv. Repeat steps B1-D4

E. Disassemble the chamber
1. When data collection is completed for the session, deactivate the DC power supply and allow the system to cool for a few minutes
2. Deactivate the pump and water chiller
3. In this order, loosen the top screw, y-adjustment screws, and x-adjustment screws
4. Drain the reservoir of its water using a siphon, sponges or washcloths
5. Loosen and remove the nuts keeping the external lid attached
6. Remove the external and internal lids
7. Drain the impingement chamber of water using a siphon, sponges or washcloths
8. If data collection will resume at a later time using the same nozzle array, this marks the end of the data collection process; otherwise, follow these steps:

i. Remove the front and back walls presently between the x-shaped spacers and the nozzle array
ii. Remove the spacers presently in the grooves in the internal enclosure's side walls
iii. Remove the x-shaped spacers
iv. Remove the nozzle array

F.4 Data Reduction

Following the data collection process for all locations for a given nozzle array, the raw data needed to be manipulated to yield the desired surface contours and average surface values. For each thermocouple at each translation and flow rate, 300 measurements were taken in steady-state conditions. The average of these values was then taken as the steady-state temperature for that specific nozzle array, translation, and flow rate. The difference between the measurements of each thermocouple and the inlet thermocouple were then taken, resulting in a temperature rise for all twelve thermocouples embedded in the copper block. As discussed prior, four sets of three thermocouples were placed at depths of 3, 8, and 13mm under a certain location under the impingement surface. Each set was plotted as shown in Figure F-8 and a linear regression was applied to the trends.

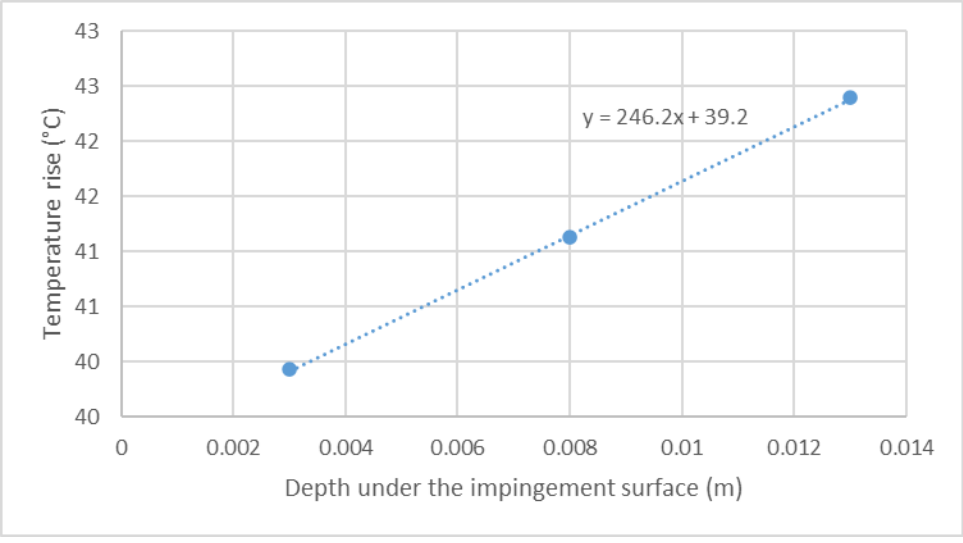

Figure F-8: Example set of measurements from a set of three thermocouples embedded in the copper block at a given location

In the resulting trendline, y=246.2x+39.2, the slope is the temperature gradient through the copper in °C/m, while the y-intercept is the local surface temperature rise. Multiplying the

temperature gradient by the thermal conductivity of copper, 401W/mK, yields the local surface heat flux in W/m^2, in this case $98730W/m^2$ or $98.73kW/m^2$. Using Equation F.1, these values are used to calculate the local surface heat transfer coefficient.

$$h_l = \frac{\dot{q}_l''}{\Theta_l} \tag{F.1}$$

Applying this process across the entire surface, contours of the surface temperature rise, heat flux, and heat transfer coefficient could be generated. To average these values across the surface, the average surface temperature rise was first found by averaging the values across the surface. Next, the total heat dissipated through the surface was calculated using equation F.2.

$$Q_T = \sum \dot{q}_l'' A_l \tag{F.1}$$

The final local values were all spaced 0.003175m apart. Thus, the local area term was equal to $1.01*10^{-5}m^2$. Having found the average surface temperature and the total heat dissipated, the average surface heat transfer coefficient could be calculated using equation F.3.

$$\bar{h} = \frac{Q_T}{\bar{\Theta}} \tag{F.3}$$

F.5 Results

At the inception of this research effort, it was intended to use this experimental system to gather heat transfer data for the most promising surface modifications in this system. However, unexpected problems resulted in completion of this research stage not being possible.

Three attempts were made to calibrate the thermocouples in a calibration oven located in another lab space. Each time, the resulting calibration functions showed good results in the oven, but they stopped yielding accurate results upon returning the system to the lab space; when left for an extended time and allowed to reach room temperature, measurement disagreements of over 2°C after calibration would arise for the thermocouples within the copper block. After each failed attempt to calibrate the thermocouples, the thermocouple reader, docking port, and computer were replaced until the only remaining temperature-reading components that were the same as in the original setup were the thermocouples themselves. Even after fully replacing the hardware and rewiring the thermocouples, the third calibration still failed.

Observations of the failed calibrations showed that the slope corrections for all thermocouples was within 2% of unity, it was decided that calibrations would initially be completed by only correcting the offset error and not the scale errors, which were informally observed to be small. This was done by filling the system with water, insulating the system, and allowing the temperature to equalize for an extended period. The resulting values were then compared to a calibration thermistor to correct for the offset error. While this approach was not perfect, it allowed rudimentary values to be collected and analyzed for observable trends. If data collection was successful, the thermocouples could then be more rigorously calibrated in post, yielding more accurate results.

It was also noticed that one set of thermocouples provided unreasonably larger heat flux measurements when compared to the other sets. This set of thermocouples was removed from analysis. With the rudimentary calibration completed, baseline data was gathered for the nozzle array analyzed in this effort impinging directly on the flat surface of thew copper block. These results are displayed in Figure F-9.

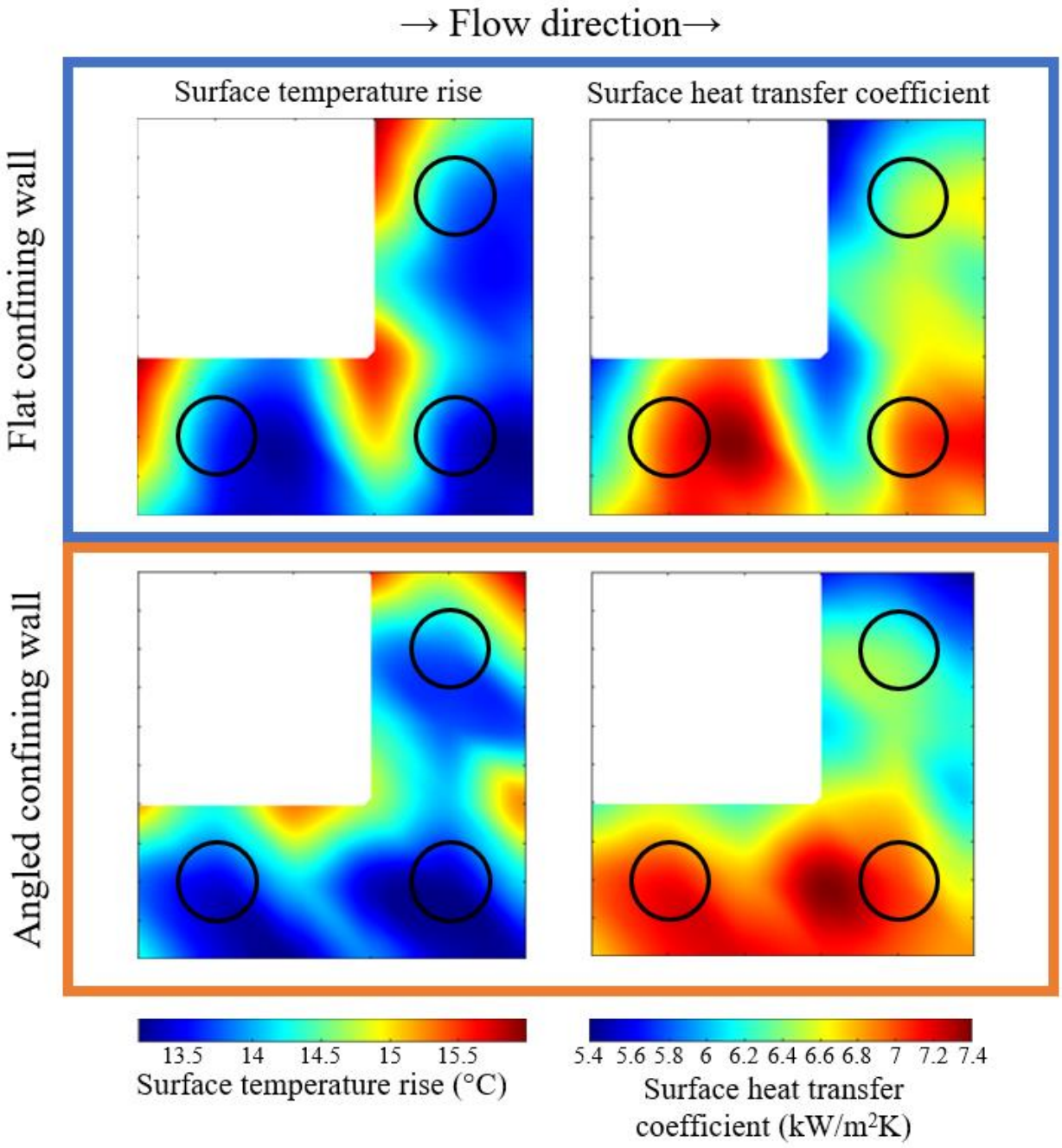

Figure F-9: Baseline case surface contours gathered from the experimental heat transfer system

In these contours, the approximate locations of the jet nozzles are indicated with black circles. In the surface temperature rise contours, cold spots are observable at the approximate locations of the jets and hotspots are seen in spaces between them. Though the alignment of the nozzles and surface is imperfect, the stagnation regions are successfully visualized. However, the accuracy of the surface heat transfer coefficient contours is questionable. As they are calculated

from a derivative, the heat flux, error is relatively high, especially given that these are generated from data based on rudimentary, simplified calibrations. The average surface temperature rise was calculated as 13.8°C under both the flat and angled wall. For the area observed in the experimental setup, this compares to numerical model values of 12.3°C under the flat wall and 12.7°C under the angled wall, which shows decent agreement. However, the average surface heat transfer coefficient results of 6.48 and 6.95W/m^{2}K from the experimental system under the flat and angled wall, respectively, compare very poorly to the numerical model's outputs of 17.3 and 17.8W/m^{2}K.

While these results were not perfect, they were sufficient to move to the next stage. The modified surfaces were machined using copper with a baseplate that was 3mm thick, as displayed in Figure F-10. These were fabricated from copper 110 using computerized numerical control machining.

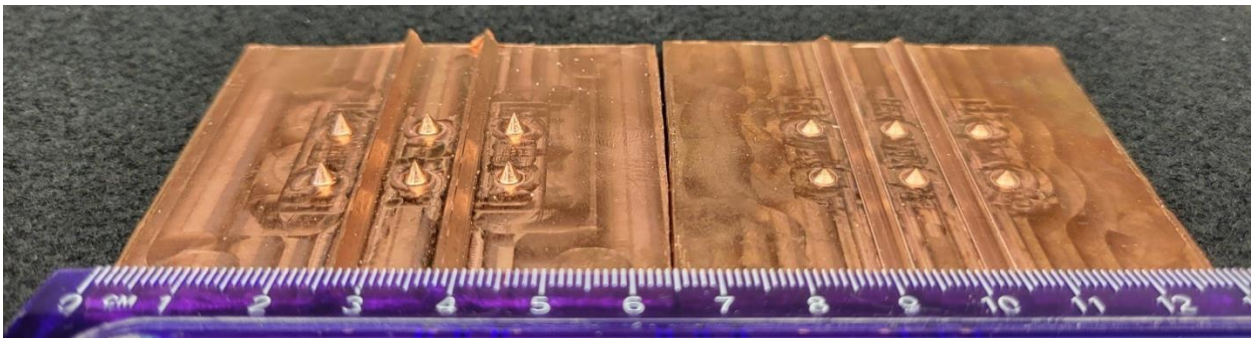

Figure F-10: Modified copper baseplates fabricated through computerized numerical controlled machining for use in the experimental heat transfer system

The modified surfaces were to be attached to the impingement surface using Arctic Silver 5 thermal paste. To analyze the effect of the thermal paste and baseplate, a flat copper plate, 3mm thick was first used in the system under a flat confining wall. Thermal paste was applied in a thin layer on one side of the plate, which was then attached to the surface and weighed down for a time. Data was then collected for this flat plate, the results of which are shown in Figure F-11.

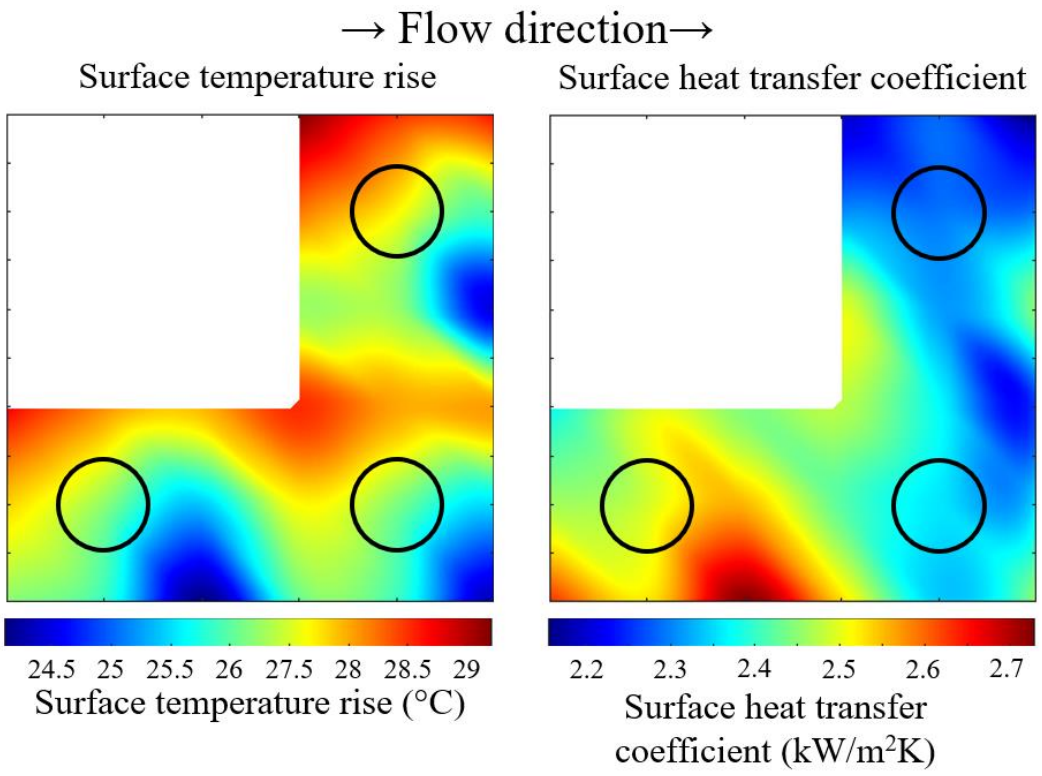

Figure F-11: Surface contours for a flat plate applied by thermal paste

It should be noted that these contours do not purport the true surface characteristics, but rather those of the original impingement surface, now underneath the plate and thermal paste. For preliminary analysis, an attempt was not made to extrapolate the true surface contours without achieving quality results using the same approach as that of the baseline case. Apparent hot and cold spots in the surface temperature contour do not correspond with the location of the impinging jets or flow interactions. Rather, they correspond to the different translations of the nozzle array relative to the surface. As previously explained, these contours were generated by combining data from nine sub-trials where the nozzle array was translated to different locations; the three cold spots correspond to one of these locations, while the three hotspots correspond with another. From this, it is concluded that the observed surface contour variations are not the result of flow mechanics on the surface, but rather differing thickness and application quality of the thermal paste. Furthermore, the range of the surface heat transfer coefficient contour has decreased from 2W/m^{2}K to just over 0.5W/m^{2}K. These results indicate that the added material of the baseplate and thermal paste mask surface characteristics too strongly for them to be observed. Furthermore, the fact that the temperature rise contour's variations are purely the result of the different

translation of the internal enclosure indicate that the thermal paste is too unrepeatable to be used in this system.

Due to many factors, it was decided that the heat transfer experiments could not be completed in this research effort or discussed in the body of this dissertation. As previously explained, the inaccuracy of the calibrations forced a rudimentary offset error adjustment and the use of thermal paste to attach the plates to the impingement surface was not repeatable and introduced substantial error. Furthermore, repeated assembly and disassembly throughout many years of use resulted in wear and damaging of both the internal and external enclosures. Threaded holes were stripped, glued joints failed, and the polycarbonate walls cracked and leaked. Given the inability to gather usable data with the modified surfaces and the continual deterioration of the apparatus, obtaining experimental heat transfer results using this system was viewed as beyond the scope of this effort.